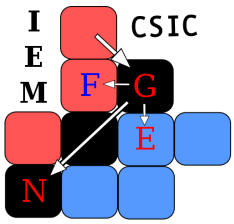

Grupo de Física
Nuclear Experimental

Nuclear Structure of ^{12}C from 3-Body Break-up Studies by Light Ion Reactions in Complete Kinematics

Martín Alcorta Moreno

MEMORIA PRESENTADA PARA LA OBTENCIÓN DEL
TITULO DE DOCTOR EN FÍSICA POR LA U.C.M.

Febrero 2010

Directores
Olof Tengblad and Hans Fynbo

Para la ama y el aita

Contents

List of Figures

List of Tables

Acknowledgements

I want to start off by thinking everybody here at IEM, both the theoreticians and experimentalists. Firstly, to Miguel, who was always willing to help from the first day I arrived (and is still a huge help) both inside and outside the workplace, and for welcoming me to Madrid. To Ricardo for the physics discussions and for helping me get through the physics exams (what a nightmare). To Mario for putting up with my particular moods while writing the thesis and for helping me discover the great Grimbergen they serve at a nearby pub. To Briz and Mariano, for teaching me the proper way to speak English and for the great times had both at work and in Madrid. To Angel many thanks for all the help given here and also for the great time had in GANIL. To Carlos for making me enjoy those Barca victories even more and for making me promise to make a trip out to Granada sometime. To Victor, thanks for the smoke breaks. It was nice to go through the thesis process together and to share the load. To Carlos Pascual, who taught me my first "Hello World" for fortran and helped me a great deal with programming and linux, and also for encouraging me to use OSS whenever possible. To Dani, thanks for inviting me to Lisbon and for all the advice regarding postdocs and in general of life after the PhD. To Arantza, thanks for all the lively discussions. To Manoli, who encouraged me from day one to participate in experiments and who always helped me with the many bureaucratic problems I encountered. To Luis Mario, thanks for the help with the various papers involved in the thesis application and for listening to my many questions at ILL. To the theory group, special thanks to Oscar for the many long conversations we shared, and for the great times in Tokyo. Also to Raquel for the long talks on carbon and for the time had in Aarhus.

Thank you to everybody at the TRIUMF group. To Chris for welcoming me and for taking me out of the lab and showing me what Vancouver has to offer. To Isao, it was a pleasure working with you, and I learned a great deal even though it was only a few months. To Ritu, thank you so much for all your help at TRIUMF and for encouraging me to stick with physics. Thanks also to Nakamura-san for giving me the opportunity to travel to Tokyo and for the opportunity to work together while there.

To the Aarhus group, I cannot thank you enough. Many thanks to both Hans Henrik and Oliver, for making Aarhus feel like a second home. Hans Henrik, thanks for the conversations had over beer all over the world. To Oliver, for your great help in the analysis and for the great times had outside the workplace as well. It was a wonderful experience to work together during these years and your help has been indispensable. Thanks also to Christian and Solveig for the fun at experiments and conferences and for the great help on R-matrix. To Karsten who always found a way to make difficult things sound easy, and for making me realize some seemingly easy questions are in fact quite complicated. Very special thanks to Hans, who has always been extremely patient with the many questions I have had from the first experiment at ILL to the final analysis for the thesis. You always found a way to make physics fascinating since day one, and this could not have been done without you.

Thank you to everyone else I have met or worked with throughout this PhD, with a special thanks to the group at Gotheborg, Elizabeth, Thomas, Bjorn, and Goran. To everybody in the PhD courses, especially Luis, with whom I share much more than a continent. Thanks also to Robert at ANL for taking me under his wing as a young bachelor student and for introducing me to the world of nuclear physics, and for always encouraging me to continue in physics. Without those years at Argonne I probably would not have pursued a PhD, and for that I thank you and also Filip and Ingo for their patience.

A very special thanks to Maria Jose and Olof, without whom this wouldn't have been possible. I was able to travel all over the world at both experiments and conferences, and the experience I gained both here and abroad I owe to the both of you. Thanks for always pushing me to do my best.

Finally, a big thank you to my family. A special thanks to Alvaro, who helped put me in contact with the nuclear physics group in Madrid and who encouraged me to pursue a PhD in Spain. To Idoia for always reminding me there is more to life than physics. Thanks for putting up with my late nights in the office, and in general for putting up with me throughout these years and I hope for many more to come. And finally to my parents, for having faith in me and for always encouraging me to do what I enjoy.

Physics is like sex. Sure, it may give some practical results, but that's not why we do it.

Richard P. Feynman

Preface

The intention of this thesis is to give an overview of the main part of my work as a PhD student. I had the luck of being able to participate in the entire process of a nuclear physics experiment. I was involved with the design phase of the experiment all the way to the final stages of preparing the results obtained for publication. I tried to write this thesis so as to be fairly easy to follow, ordering the chapters chronologically so the reader can get an idea of everything that goes into a nuclear physics experiment. Many times what we see from an experiment is the final results, which usually takes years after the experiment has taken place, not to mention the months or years spent preparing for that experiment. I hope this thesis to, at the least, provide the reader with a general understanding of the many steps which are involved in an experiment and which sometimes may be overlooked. Before discussing the outline of this work, I want to write a few words regarding the nature of our work which I have struggled with at times.

When the inevitable question of what one does for a living comes up, my reply is followed up by one of two responses: "..." or "OK... What is that for? What are the applications?" If it's the latter (the former implies the end of the conversation) most of the times I would mention how the work I do has no immediate practical applications, but that some application may be derived from work similar to mine sometime in the future. I always felt, however, that this was a cheap cop-out. After all, that is not *why* we do it. In other words, if there were no practical applications in the future, would basic research be justified?

Only recently have I been able to respond to this question. Many times I have struggled with thoughts that my work in research had no meaning or purpose. That it was so specific, so specialized, that nothing would come of it. But of course one has to accept that this specialization into narrow branches is the result of centuries of advancements in the sciences. Except for very specific cases, gone are the days of men such as Newton and Einstein who could single-handedly revolutionize an entire field of knowledge. The reason for this is not that there are no more great physicists. Quite the contrary, in fact. The reason is the enormous progress that has been made in physics, and

nuclear physics in particular. There is such a large amount of accumulated information that it is rare to see an experimentalist/theoretician, let alone one who works in other disciplines. However this did not comfort me since it still did not supply me with a purpose, and so the search continued.

It wasn't until I took a step back to look at the bigger picture did my outlook on research change. I now see the importance of research as something which could best be described with the following analogy. Knowledge is like a puzzle. In order to answer the fundamental questions of physics and truly comprehend it, we need to solve this puzzle and look at it as a whole. But it is not that easy. The difficulty is that we have to look for these pieces, compounded by the fact that we do not even know how many pieces there are. An experimentalist helps find these pieces, and a theoretician will help fit them together. Sometimes a huge discovery is made and we find entire new sections to the puzzle. We then must figure out ways to see how this fits in with the larger puzzle. I think this analogy holds true for all branches of physics, as the ultimate goal is to see what this completed puzzle looks like. This search may take years and years, but the finished puzzle is the *why*.

During my time here I have focused my studies on reactions done at the "Centro de Micro-Análisis de Materiales" (CMAM) at the Universidad Autonoma in Madrid. In 2005, we ran a preliminary experiment at CMAM, ^{10}B(^{3}He, p$\alpha\alpha\alpha$). The experiment was intended to study resonances in ^{12}C, but because it was the first experiment performed at the nuclear physics line, it mainly served as a preliminary run. I will not go into the details of the analysis of this experiment since it was repeated in 2008 with much better results. However, it will serve as a demonstration of the benefits gained with good preparation.

I have organized this work in chronological order so as to facilitate the understanding of what goes into an experiment. I will start with a brief introduction of nuclear physics in order to get the reader acquainted with the subject matter. Although a knowledge of nuclear physics is assumed, perhaps this could serve as a starting point for a young student, or at least as a review. Another purpose for the brief outline of nuclear physics is to provide a basis for the motivation of my work. It is very easy in this line of work to lose sight of why we do what we do. One becomes so engrossed in one's work that it is easy to lose sight of the bigger picture. Ultimately the purpose of the introductory chapter is to ask a question. That is, why do we

study ^{12}C? What do we want to learn from this nucleus? What can it teach us? The rest of this thesis is written to answer these questions.

Now that we know what we are after, we must design an experiment to measure this. That is, how do manage to determine the properties of ^{12}C? Chapter 2 discusses what goes into the realization of an experiment. The choice of detectors, the geometry of the detectors, beam energies, electronics setup, etc. Chapter 2 also discusses preliminary analysis of the data, such as calibrating the spectra.

After describing the necessary experimental setup and electronics, we move into the technical details of the analysis procedure in chapter 3. This chapter deals mainly with what we do with the information gathered in the experiment. In other words, how we transform the signals given by the detectors into actual physical events with each particle identified and with a given momentum and energy. We have Gb of data from the experiment which needs to be transformed into something which makes physical sense. This, together with the preliminary analysis, is a very long process, and has proved very tedious at times (calibration of detectors, segmentation faults...), but also fun and enlightening at others (the calibration finally works, the code compiles...).

Finally I will move on to the results of the analysis. That is, what we have learned with this experiment. This will be split up into two separate chapters. The first will discuss results obtained on the observation of γ-decay using charged particle detectors. Chapter 5 is a complete overview on what it is that we learned from ^{12}C, and will serve as a summary of what has been learned about each state. I have also included a short discussion on conclusions and outlook in Chapter 6. Were we able to answer some of the questions proposed in chapter 1? Since there is always more work to be done, I conclude by looking at ways we can improve our understanding of the nucleus in discussion.

You will notice each chapter begins with a quote. I have tried to make the quote in each chapter deal specifically with the content of that chapter. As for the quote utilized to start out this preface, I feel it captures quite well, albeit in a very Feyman-esque manner, the love I have acquired for my work during my years as a PhD student. I do physics not because of any possible practical results which may arise, but, quite simply, because I enjoy it.

We are all star stuff.
Carl Sagan

1 Introduction

One could argue that nuclear physics began with the discovery of radioactivity by Becquerel in 1896 or with the hypothesis of the existence of the nucleus by Rutherford in 1911. It is clear that these events led to an explosion in the development of the field of nuclear physics. Through experimentation we have made huge strides in understanding the fundamental properties of the nucleus, and in the process have introduced the realm of nuclear physics into the general public. This is evidenced by the presence of nuclear physics applications in everything from medicine to energy. Needless to say the field of nuclear physics encompasses many different fields and has slowly been separated into different branches. It is therefore difficult to pinpoint one final 'goal' of research in the field of nuclear physics. Essentially what we want to understand is how the nucleus works, and why does it work this way; i.e. what is it about the interaction between nucleons that causes nuclei to behave differently? Is it possible to provide a general explanation to nuclei which will work for the entire range of nuclei? What are the limits for the existence of nuclei? Figure 1.1 shows the valley of stability of the nuclear chart. There are some patterns which can be observed which have lead to very robust theoretical models. However, there is currently no model that can explain all of the properties of nuclei for the entire range of isotopes. Some models have had great success with regards to predicting properties of heavier nuclei, others for lower mass nuclei, and others for nuclei near the valley of stability.

In order to test these different models physicists have tended to test the behavior of nuclei at the extremes, leading to the development of radioactive nuclear beam facilities throughout the world. These facilities have provided the exotic beams which allow us to study the spectroscopy of drip-line nuclei in detail. The drip-line nuclei refer to those nuclei where adding one more proton (proton drip-line) or adding one more neutron (neutron drip-line) would result in the nucleus no longer being bound. Different technology has been employed to produce radioactive beams in only a handful of facilities

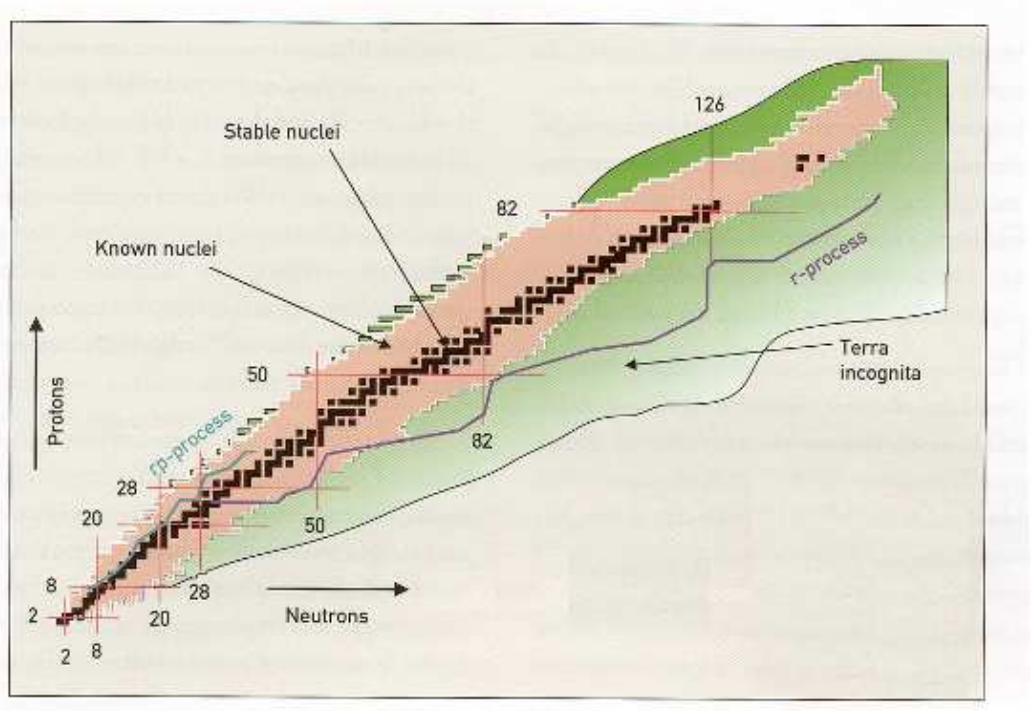

Figure 1.1: Valley of stability in the nuclear chart. In recent years nuclear physics has been testing the nuclei at the extremes of the nuclear chart, and have discovered strange phenomena which occur at both the neutron and proton drip line. The development of radioactive beams has been crucial in pushing the study of nuclei to the drip-lines. Figure taken from [Uni].

around the world. These facilities have played a crucial role in the discovery of many exotic phenomena, such as halo nuclei [Tan85] and two-proton radioactivity [Gio02, Pfu02], and are an essential tool in the field of nuclear astrophysics.

The different RNB facilities throughout the world essentially use one of two techniques to produce radioactive beams: the ISOL technique or in-flight scheme. The ISOL type facilities (isotope separation on-line) have low beam energies (on the order of tens of keV) and usually consist of a high-intensity, light nuclear beam bombarding a thick heavy target, producing all kinds of isotopes, which are then chemically extracted and in continuation sent to the experimental chamber. These beams can be post-accelerated, such as in TRIUMF (Vancouver, Canada), REX-ISOLDE (at CERN in Geneva, Switzerland), SPIRAL (at GANIL in Caen, France), ORNL (Tennessee, USA), or ANL (Illinois, USA), to name a few. The in-flight method generally consists of fragmentation of the beam, and produces RNBs with high kinetic energies (hundreds of MeV/nucleon). Examples of in-flight fragmentation facilities are GSI (Darmstadt, Germany), RIKEN (Tokyo, Japan), NSCL (Michigan, USA), and Dubna (Russia). I hope that I convince the reader that although these RNB facilities are a testament to our advances and play an integral role in pushing the limits of knowledge, stable beam facilities are by no means antiquated and can still produce interesting results.

1.1 Current situation

The development of these radioactive nuclear beam facilities has led to many new interesting physics findings in recent years and has opened up the field of nuclear physics. There are many exciting topics which are currently at the forefront of nuclear physics. These topics range from the study of halo nuclei at the drip-lines to the search for the heaviest elements, or from the understanding of reaction rates for nuclear astrophysics to beta-decay studies beyond the standard model.

Many results which have been obtained in recent years have called for new theoretical models or at least an improvement on current models. In the following section I will briefly discuss some of the most common models used in nuclear physics. Ultimately this will serve as the motivation for the body of this work, since ^{12}C, a very well-studied stable nucleus, has properties which can only be understood using a combination of several models.

1.1.1 Models

Ideally physicists would be able to learn the properties of any nucleus by resolving the Hamiltonian from interactions. Unfortunately, as more and more nucleons are added, this method quickly becomes obsolete even with today's technology due to the amount of processing time needed. As of now there are some calculations available for low excitation energy levels in ^{12}C by using ab-initio models. It is expected that information on higher lying states in ^{12}C will become available for these models in the coming years, thus it is crucial to obtain detailed experimental information on excited states in ^{12}C and to understand their decay modes.

Several nuclear models have been proposed to describe nuclear properties, with varying degrees of success. The shell model, where the nucleons are grouped in specific shells according to the Pauli principle, is successful in reproducing the magic numbers observed in nuclei and the main part of stable nuclei. The cluster model, based on the assumption that the alpha particles is pre-formed inside the nucleus, has played a fundamental role in describing states with pronounced clusters. Perhaps the most ambitious type of model are ab-initio models, which attempt to describe nuclei as systems of nucleons that interact by fundamental interactions, where nucleons are point-like particles which interact by nucleon-nucleon and three-nucleon forces. The calculations are in principle exact, yet they depend on input parameters obtained in experiments (NN and especially NNN forces are not yet well understood and are derived by fits to experimental data). The disadvantage of the ab-initio model is that adding nucleons factorially increases the degrees of freedom, and thus becomes impractical beyond mass 12 with current technology.

At present, the GFMC ab-initio model has so far computed only the ground state of ^{12}C [Pie05], while although the NCSM has calculated excited states in ^{12}C, it has been unable to reproduce the 0^+ Hoyle state [Nav07]. However it is expected that soon these models will be capable of calculating excited states in ^{12}C. If this is the case then clearly those involved in these calculations will need a detailed experimental study of the different excited states in ^{12}C. With the experiment we have carried out we expect that our results obtained on general properties of ^{12}C resonances such as refined values of energies and widths for some cases (see Chapter 5) and also the values obtained on matrix elements (see Chapter 4) will prove useful when testing the accuracy of ab-initio models.

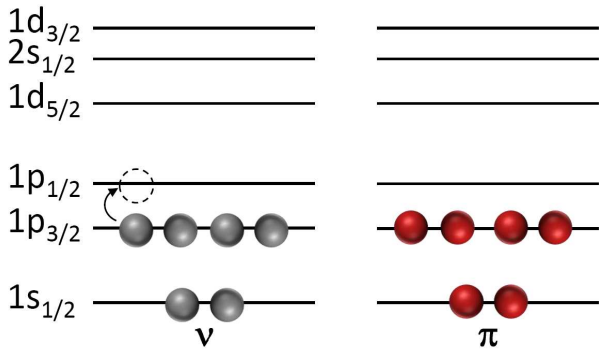

Figure 1.2: Occupied shells of ^{12}C. An example is shown where a neutron from the $1p_{3/2}$ orbital is excited into the $1p_{1/2}$ orbital. This would result in a state with a spin and parity of 1^+ or 2^+.

Shell model

The shell model has proved very successful in describing single-particle states in heavy nuclei. However, it fails at fully describing the structure of ^{12}C. If we look at the single-particle excitations as predicted by the shell model, there are some states in ^{12}C which can not be reproduced. Figure 1.2 shows the filling of shells in ^{12}C for 6 neutrons and 6 protons. If a pair breaks and there is an excitation of a nucleon from the $1p_{3/2}$ orbital to the $1p_{1/2}$ orbital, they combine to give two possible spin and parity assignments: $3/2^- \otimes 1/2^- \rightarrow 1^+$ or 2^+. Similarly, an excitation to the $1d_{5/2}$ will give J^π of $3/2^- \otimes 5/2^+ \rightarrow 1^-$,$2^-$,$3^-$, and 4^- while an excitation to the $2s_{1/2}$ orbital can give 1^- and 2^-. If we look at the level scheme of ^{12}C shown in Fig. 1.3, we see some states which do not fit into any of these possibilities. There is no single-particle coupling which explain the 0^+ state located at 7.65 MeV, or the 4^+ state at 14.08 MeV. The reason for this is that we are treating excitation in ^{12}C in a purely single-particle manner. But this is a simplification, and there are other excitations at play, such as those from the *collective* motion of the nucleons, as described by the cluster model.

Cluster model

The cluster model has successfully reproduced resonance states in ^{12}C using fairly simple methods. The theory behind the cluster model is to treat the ^{12}C nucleus as if it were composed of three alpha particles. The advantage of this model is that the properties of the alpha particle, such as its nuclear radius and Coulomb potential, are very well known. In addition the interactions between alpha particles are well measured and parametrized meaning the ^{8}Be

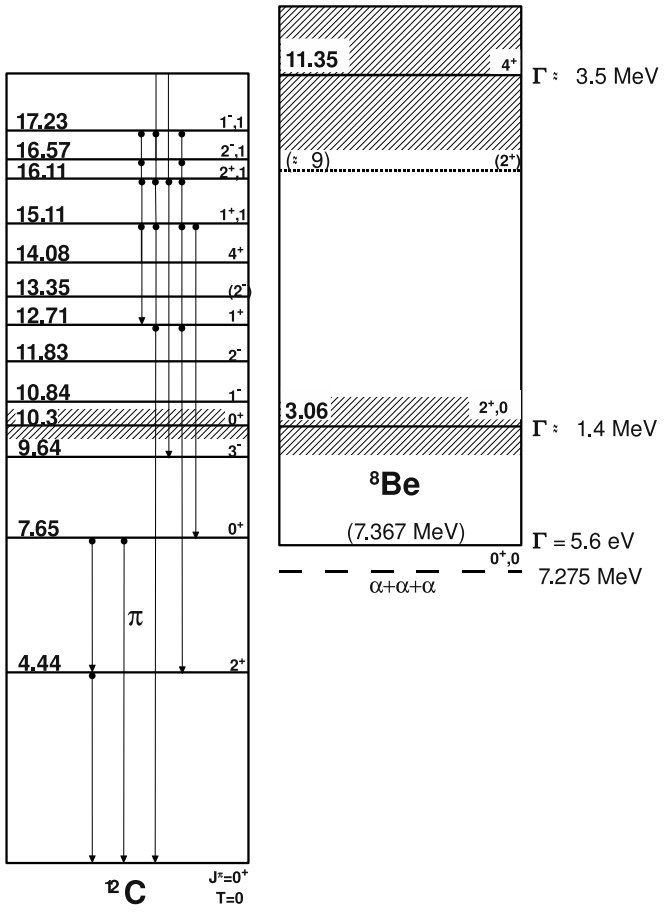

Figure 1.3: Level scheme [TUN] of ^{12}C and the excited states of ^{8}Be are given with respect to the $\alpha + \alpha + \alpha$ break up in ^{12}C to better visualize possible breakup via excited resonances in ^{8}Be.

Table 1.1: States of ^{12}C from experiments. The listed states and their properties are all taken from [Ajz90].

Excitation energy (MeV ± keV)	Width (keV)	J^π
0 (g.s.)	—	0^+
4.44 ± 0.31	$(10.8 \pm 0.6)\times10^{-6}$	2^+
7.65 ± 0.15	$(8.5 \pm 1.0)\times10^{-3}$	0^+
9.64 ± 5	34 ± 5	3^-
10.3 ± 300	3000 ± 700	(0^+)
10.84 ± 16	315 ± 25	1^-
11.83 ± 16	260 ± 25	2^-
12.71 ± 6	$(18.1 \pm 2.8)\times10^{-3}$	1^+
13.35 ± 17	375 ± 40	(2^-)
14.08 ± 15	258 ± 15	4^+
15.11 ± 3	$(43.6 \pm 1.3)\times10^{-3}$	1^+
16.11 ± 0.7	5.3 ± 0.2	2^+

resonances are well understood. For a more detailed look at the application of the cluster model to the triple-alpha decay of ^{12}C, see [DB87]. This type of models are continuously improved, and for a recent example see [Alv07a, Alv07b].

The collective motion associated with a cluster structure will have implications in the properties of excited states and can be used as a predictive tool. For example, the the low-lying 2^+ state situated at 4.44 MeV and the 4^+ state at 14.08 MeV (see Table 1.1 for reference) are known to form part of the rotational band of the ground state of ^{12}C. We would therefore expect the energies of these states to follow the following spectrum [Sat80]

$$E(I) = (\hbar^2/2\mathscr{I})[I(I+1)] \tag{1.1}$$

where $\mathscr{I}$ is the moment of inertia of the nucleus, and I is the spin. We can now interpret the presence of a low-lying 2^+ state as a rotational band based on the ground state.

We can use similar arguments for other states in ^{12}C. Take for example the so-called Hoyle state (the prediction of this state by Fred Hoyle is very interesting and is discussed in greater detail in section 1.2.1) situated at 7.65

MeV with a J^π of 0^+. This state was originally described as a linear chain of alpha particles [Mor56]. If this were the case then it follows that, as in the case above, it would have a rotational band, giving rise to a 2^+ state at around 10 MeV, depending on the structure of the Hoyle state. There was in fact a broad structure around 10 MeV with natural spin and parity (Section 3.5.1) which was therefore assigned as a 2^+ [Mor66]. This lead to many experiments and theoretical calculations attempting to decipher the J^π of this mysterious broad region around 10 MeV with those in support of a 2^+ assignment [Jac73, Ueg79], though there was also those in support of a 0^+ assignment [FSW71]. A 0^+ assignment would raise two important questions. First, what is the structure of the third 0^+ state, and does it have a rotational band built upon it? Secondly, if this broad structure does not have a spin of 2, then where is the elusive 2^+ state? The answer to the latter may lie in the interpretation of the structure of the Hoyle state. Perhaps it does not have such a large deformation associated with a linear chain of alpha particles. Different structures have been proposed for this state [TG70], which would therefore not require the existence of a 2^+ state in that exact energy region. In fact if the Hoyle state is not a linear chain it could have a lower moment of inertia, which would result in a higher expected energy of the 2^+ state, as seen by Equation 1.1. However the resonance in that region was tentatively assigned a spin and parity of 2^+ and experimental probes into the J^π assignment of this resonance was largely abandoned for several decades.

In the past decade the debate on the nature of this excited state has again become active, due in large part to the advances in detectors and in the availability of radioactive beams. β-decay studies using ^{12}N and ^{12}B beams have demonstrated the huge improvements made possible by using highly segmented detectors [Fyn05, Fyn03]. The possibility of multi-particle detection was fundamental in gaining a much better understanding of the 3α breakup of the states in ^{12}C. The ability to detect *all* of the outgoing alpha particles in coincidence was crucial in determining the spin and parity of the resonances and provided much cleaner data, since the ability to impose a three-particle coincidence condition virtually eliminates background (see Section 2.3.3). These β-decay experiments have assigned the resonance originally proposed by Morinaga [Mor66] as a 2^+ to be a 0^+ state in the energy region around 10 MeV [Fyn05, Dig05]. However this did not close the debate since clearly there must be a 2^+ resonance in the vicinity of that region. It is interesting that 50 years later a candidate for the elusive 2^+ excited state of the Hoyle state is still under debate. There has been much recent work on the nature of this 2^+ state [Toh01, Fun03, YS04, von06, Che07], and some evidence for a 2^+ state has been seen [Ito04, Fre06, Fre07, Fre09, Hyl09a,

Hyl09b, Hyl10, Dig09] though there is still no consensus on the issue.

The recent work on the search for the elusive 2^+ state raises many questions. Most importantly, where is it? Is there something about the nature of the 2^+ which makes it so difficult to find? If it is found, what energy does it have, and what does this mean in terms of the nature of the Hoyle state? How high in spin do the rotational bands extend? In Chapter 5 we will look at the ^{12}C spectrum in detail and attempt to find a candidate for this state in the region of interest.

1.2 Other interests in ^{12}C

In the previous section I discussed some reasons of why we wish to study ^{12}C. I hope the importance of determining general properties of this nucleus for ab-initio calculations has become clear. In addition we expect this work to shine some light on some of the open questions regarding the nature of some cluster states. It is clear that there is still a surprisingly great deal of uncertainty regarding the structure of ^{12}C. Yet the importance of ^{12}C extends far beyond these questions. In fact, a better understanding of ^{12}C, one of the most abundant nuclei in the universe, is crucial in the formation of heavy elements in the universe. Understanding the structure of low-lying excited states in ^{12}C provides crucial information on reaction rates in stars and plays a very important role in nuclear astrophysics.

1.2.1 Implications in nuclear astrophysics

Heavy elements above mass 5 were first thought to be produced at the beginning of time in the big bang along with Hydrogen and Helium, yet up until about 1950 this theory could not describe elements above mass 4 [Fow84]. This was because of the bottleneck in mass 5 and mass 8 since there are no stable isotopes with A=5 or A=8. Many physicists tried to give explanations to overcome this "mass gap", and the discussion began about nuclear processes in the stars. Hans Bethe was the first to establish the concept of nucleosynthesis taking place in the stars [Bet39], proposing the CNO cycle and the PP chain, but was unsuccessful in explaining the mechanism of ^{12}C formation in stars.

Yet this discovery brought on another interesting dilemma. It seemed that the reaction rates in stars for producing ^{12}C calculated using the existing model would be too slow to account for the observed abundance of ^{12}C, an element crucial for our existence. This problem stemmed again from the presence of an unbound nucleus, in this case ^{8}Be which rapidly decays into

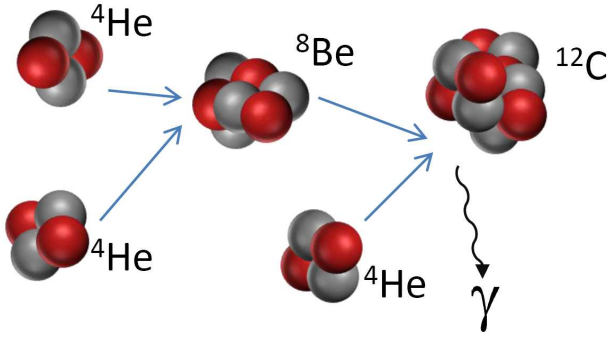

Figure 1.4: Schematic of the triple-α process. Two helium nuclei form an intermediate ^{8}Be resonance which then quickly captures another helium nucleus forming ^{12}C in an excited states. The excited ^{12}C nucleus can then de-excite via the emission of gammas or pions forming a stable carbon nucleus.

two alpha particles, thus the only way to produce ^{12}C would be through what is known as the triple-α process, denoted $\alpha + \alpha + \alpha \rightarrow ^{12}\mathrm{C}+\gamma$. See Fig. 1.3 for the ^{12}C level scheme relative to the states in ^{8}Be. Because of the high-density and strong gravitation in hot stars, the triple alpha process could occur via a two-step process [Sal52]; two alpha particles form a resonance state in ^{8}Be just above the 2α threshold (the 2α threshold is 0.09 MeV below the ^{8}Be ground state) which then traps a third alpha particle to form ^{12}C*, i.e. $\alpha + \alpha \leftrightarrow ^{8}\mathrm{Be}$ (τ=1 $\times 10^{-16}$ s), $^{8}\mathrm{Be}+\alpha \rightarrow ^{12}\mathrm{C}+\gamma$ (see Fig. 1.4). This is a valid alternative to the earlier equation provided the lifetime of the ^{8}Be resonance is longer than the time required for two alpha particles to fuse [Hoy54]. The effect of this resonance in ^{8}Be was to increase the probability for the ^{8}Be to capture a third α particle before decaying back to two alphas, thereby increasing the probability of producing ^{12}C. Yet the likelihood of this process occurring was still not enough to explain the observed abundance of ^{12}C. Finally, in 1953, Fred Hoyle realized that if there were a resonance in ^{12}C just above the triple-α threshold (7.28 MeV), it would greatly increase the reaction rate in the stars thereby reducing the temperature necessary for this process to occur. This predicted resonance was determined at the time to be at an energy of 7.68 MeV [Hoy53, Dun53]. It is known as the Hoyle state, and is now experimentally determined to have an energy of 7.65 MeV. For an interesting history of the triple-alpha process see [Sal07].

In 1966, Waggoner et al. studied the reaction $^{10}\mathrm{B}(^{3}\mathrm{He}, \mathrm{p}\alpha\alpha\alpha)$ [Wag66] to understand the breakup of ^{12}C*. Yet the quest for learning more about the reaction rates in stars by studying the triple-alpha process continues today. In

fact, a recent experiment discussed above which produced excited ^{12}C nuclei from the β-decay of ^{12}B and ^{12}N [Fyn05], suggests that the currently accepted measurements on the reaction rates have errors due to interference effects between states of the same parity (0^+) and because they find no evidence of a 2^+ resonance in this region even though the astrophysical reaction rates of the triple-α process assume the presence of a 2^+ resonance there [Ang99, DB87]. These findings meant that the reaction rates needed to be revised, and indicated that the reaction rate of ^{12}C at temperatures below 5×10^7K are double that of the previously accepted values (the interference of the Hoyle state with the broad 10 MeV state was not taken into account in previous calculations), and that the reaction rate at temperatures above 10^9K must also be modified (due to lack of evidence for the assumed 2^+ state at the proposed energy of 9.1 MeV) [Fyn05]. This has an effect on both the formation of primordial stars and the nucleosynthesis of heavy elements in the explosions of supernovae, which impacts the existing models used to explain the observed element abundances.

Later work by Buchmann and Barnes [BB06] further suggest that other resonances in ^{12}C of natural parity may come into play in determining the triple-α reaction rate at higher temperatures. For example, the 10.84 MeV resonance in ^{12}C with $J^\pi=1^-$ is broad enough ($\Gamma=$ 315 keV [Ajz90]) to influence the triple-α reaction rate at high enough temperatures, and is not yet included in calculations [CF88].

1.2.2 Nuclear structure and theory

The formation of ^{12}C from three alpha particles is very important in understanding the synthesis of elements in the universe. Yet studying the breakup of ^{12}C can also provide information on the decay mechanism involved, such as whether the ^{12}C* decays directly to three alphas or if it decays sequentially, emitting one alpha followed by ^{8}Be*, which in turn decays into two α particles (see Fig. 1.3 for the ^{12}C level scheme relative to the states in ^{8}Be).

Sequential decay and direct decay are the two extreme cases of decay mechanisms which are possible. The sequential decay occurs when an intermediate resonance is narrow. The energy of the first emitted particle depends on the energy available between the initial and intermediate state. Direct decay will occur when no intermediate state is available between the initial and final state. These two cases are illustrated in Fig. 1.5. The interpretation of the data is more difficult when the intermediate state is broad and the energy available for the first particle is of the order of the width of the intermediate state. In one specific case which will be looked at in more detail in Section 5.2.3, the same data obtained from the breakup of the 12.71

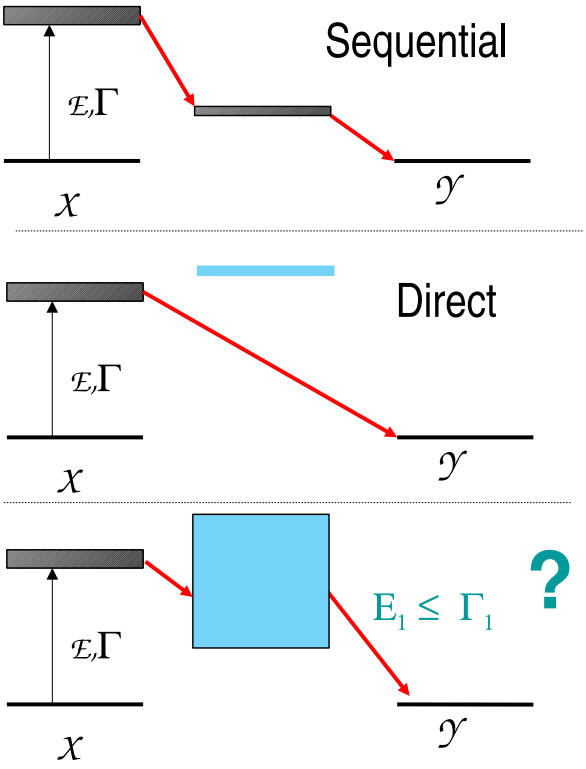

Figure 1.5: Picture illustrating possible mechanisms used to describe the breakup to multi-particle final states. On the top is an example of sequential decay. The breakup will proceed through an intermediate state which has a narrow width. The first emitted particle depends on the difference in energy between the initial and the intermediate state, and the other two of the energy available after the breakup of this intermediate state. In the middle picture is illustrated an example of direct decay. Here, the breakup will proceed democratically because the state of the intermediate nucleus is situated above the initial state, so that in principle no intermediate state is available if the state is narrow. This is also valid if the intermediate state is not accessible due to some nuclear structure feature such as parity violation. In the bottom case, it is not easy to elucidate the decay mechanism and experimental data has been fitted to both approaches. This is because the window (width of the state) of the intermediate nucleus is situated both above and below the initial state, giving both positive and negative transition energies. Similar difficulties arise when the initial resonance is broad.

MeV state and has been fitted equally well using both theoretical approaches [Kor90, BZT74]. Clearly this is not admissible as the physics behind the two mechanisms are very different. Sequential decay is assumed in all of the resonances studied in the reactions, though there exists the possibility of direct decay for some resonances which will be discussed when appropriate. Section 3.5.1 discusses how one can separate the data between different states in the intermediate nucleus (^{8}Be).

1.3 A note on nuclear resonances

I have been referring to resonances and excited states in ^{12}C interchangeably in previous sections and wish to take the time to introduce the concept of a nuclear resonance in more detail. A nuclear resonance is essentially an unstable excited state of a nucleus, and is characterized by its energy and width. The general form of the probability of decay through a resonance centered at E_0 with width Γ is known given by the Breit-Wigner distribution:

$$w(E) \propto \frac{(\Gamma/2)^2}{(E_0 - E)^2 + (\Gamma/2)^2} \tag{1.2}$$

where E_0 is the resonance energy and Γ is the level width

$$\Gamma = 2P_l\gamma^2 \tag{1.3}$$

and γ is the reduced width. The width of the state is inversely proportional to its lifetime, $\tau \propto \hbar/\Gamma$.

One rather simplistic way of viewing a resonance can be provided with an example. Suppose you have an alpha particle and you bombard it with alpha particles. Normally they would not combine because ^{8}Be is unbound. However, when you are at just the right energy (at resonance), a state will be formed when the individual wavefunctions of the two alpha particles overlap with the wavefunction describing the ^{8}Be nucleus. Simplistically, one could visualize this as for a given energy, two alpha particles may be slightly captured by each other and orbit each other. This would correspond to a resonance, and the lifetime of the resonance could be thought of as the number of orbits the alpha particle makes around the other alpha particle. Following with the example of the ^{8}Be nucleus, we can look at the ground state (resonance) in this unbound nucleus and see that the width is ≈ 5 eV [Ajz90] at an energy of 92 keV with respect to two alpha particles. We can estimate the number of orbits an alpha particle will make around the other with this resonance width. For an alpha particle the circumference is about

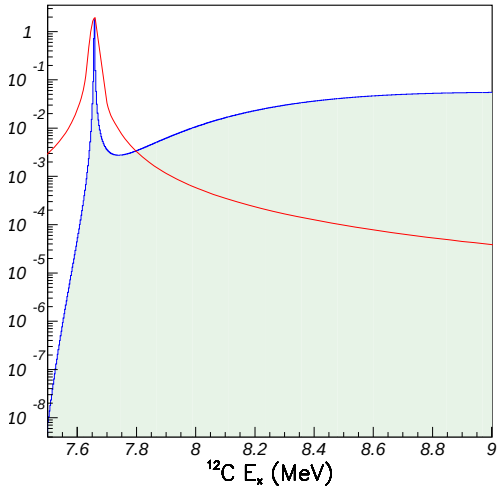

Figure 1.6: The characteristic Breit-Wigner shape for a typical resonance (red) is compared to the shape which arises when penetrability effects are included (blue with solid green). This example is shown for the Hoyle state at 7.65 MeV. Note the appearance of the 'ghost' shape at higher energies when penetrability effects are accounted for. The peaks are not normalized.

1×10^{-14} m, where the radius is calculated from the relation $r = r_0 A^{1/3}$, with $r_0 = 1.25 \times 10^{-15}$ m, to be r=1.7 fm. The velocity of the alpha particle is $\approx$ 2×10^{6} m/s, so that the time for an alpha particle to make a complete orbit around the other alpha particle is roughly 5×10^{-21} s. For Γ=5 eV, this correspond to a lifetime of τ=1.32 $\times10^{-16}$ s. In other words, with a 5 eV width, the alpha particle would make on the order of $\times10^{6}$ orbital revolutions. If, for example, we look at the first excited state of ^{8}Be, which has an excitation energy of 3 MeV and width of 1.5 MeV, we can calculate that this resonance will only live long enough to make just a few orbits.

Before going on to the next section, I want to mention an important point about Equation 1.2. Note that the shape described by a Breit-Wigner resonance is a Lorentzian distribution. This description works well, provided the width of the resonance is small. However, what would happen if the width of the resonance is very large with respect to the energy? If this is the case, then the width of the resonance will be dependent on the energy, and a more complicated expression must be used. This can occur for very broad resonances or for resonances which are close to threshold (for example, the Hoyle state in ^{12}C, which is only 380 keV above the triple-alpha threshold). Using the Hoyle state as an example, the effect on the shape of this resonance is to increase the intensity at high energies, giving rise to a 'ghost' shape, as

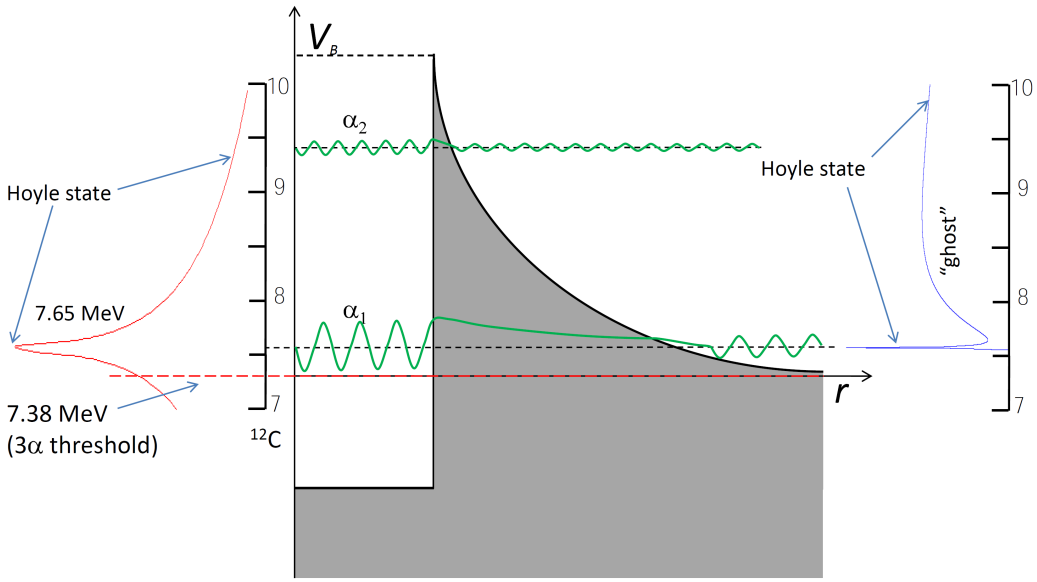

Figure 1.7: Energy of an alpha-particle in the ^{12}C system as a function of their separation energy. The figure illustrates the effect of the penetrability on the shape of the Hoyle state in ^{12}C shown in Fig. 1.6. The Hoyle state as a simple BW is shown to the left in red. α_1 has very little kinetic energy so that its decay probability is hindered by the presence of a large tunneling radius. Although less probable, α_2 has a large kinetic energy, so that the tunneling probability is greatly enhanced. The overall effect this has on the shape of the resonance is to give rise to a ghost shape, where the cross section is enhanced at higher energies

seen in Fig. 1.6. This distortion in the peak-shape means that broad states or states near-threshold can not be fully described by a Lorentzian distribution, introducing the need for a more sophisticated method to fit such peaks (see Section 5.3).

One can understand the distortion of the shape of a resonance near threshold in terms of the lifetime of the resonance. The lifetime (and therefore the width) of the resonance is related to the penetrability of the Coulomb barrier, which in turn is dependent on the energy. The higher the energy, the easier it is to overcome the Coulomb barrier, increasing the probability for the resonance to breakup, giving rise to ghost peaks in the observed spectra. This effect is shown schematically in Fig. 1.7 for the case of the Hoyle state shown in Fig. 1.6. The distortion of the Hoyle state at higher energies will make it difficult to disentangle the properties of other resonances in the region. This is one of the main reasons why it has been so difficult to understand

the nature of the broad structures seen around 10 MeV in ^{12}C discussed in Section 1.1.1. One method which has proved successful when applied to ^{12}C [Fyn09] is the R-matrix method.

The R-matrix method is used primarily to parametrize known experimental quantities, such as cross sections, using a small number of parameters [Des00]. The R-matrix method is based on scattering theory and assumes that the space is divided into two regions: the internal region, where the nuclear force takes place, and the external region, where only the Coulomb force is present. The radius of the internal region is referred to as the R-matrix radius, denoted by a.

In a simple case of a particle scattering off a nucleus, at large distances there is no nuclear interaction and only the Coulomb force arises. As the incoming wave approaches the nucleus (r=a), it will 'feel' the nuclear potential, which will have an effect on the outgoing wave. In the outer region, the wave function can be described analytically using Coulomb wave functions, yet in the internal region, the situation is much more complicated and the wave function must be parametrized in some way. This is where the R-matrix theory comes in. It provides a parametrization using parameters that can be interpreted physically in terms of transition matrix elements.

What the R-matrix theory does is that it essentially connects η_l, the collision matrix which describes the interaction inside the nuclear potential, with the conditions at the nuclear surface. With this, one can determine the cross section, which gives the probability of the resonance decay energies, as will be discussed in Section 5.3.

1.4 Populating excited states in ^{12}C

Before moving on to the next chapter on the experiment used to study ^{12}C, it is worth pointing out that there are different ways of populating states in ^{12}C above the triple-alpha threshold, each with its advantages and disadvantages. Feeding states in ^{12}C through β-decay is one technique which has been applied to the study of ^{12}C with great success by our collaboration [Fyn03, Fyn05, Dig05, Hyl09a, Hyl09b, Hyl10, Dig09]. β-decay studies of either $^{12}_{7}N_5$ ($J^\pi=1^+$) or $^{12}_{5}B_7$ ($J^\pi=1^+$) are ideal for studying positive parity states in ^{12}C since they are virtually background free. However the advantages of the β-decay process are also limiting, since the selection rules will only populate positive parity states below the Q_β value of ^{12}B or ^{12}N.

That is why we have chosen a complementary method to β-decay by studying the resonances in ^{12}C in a reaction experiment. This will populate states of much higher excitation energies and also those with negative par-

ities in ^{12}C. For example, we can study the resonance at 13.35 MeV with a tentatively assigned spin of $J^{\pi}=2^{-}$. Since this resonance has negative parity, it is not populated in β-decay experiments with ^{12}N (1^{+}) and ^{12}B (1^{+}). Another advantage is that because ^{12}C is a stable nucleus, we do not need a large radioactive beam facility to produce ^{12}C since there are several reactions using stable beams with large Q-values which will reach high excitation energies in ^{12}C. We are fortunate to have an excellent accelerator facility near the laboratory, and chose the "Centro de Micro-Análisis de Materiales" (CMAM) at the Universidad Autonoma in Madrid to carry-out the following two reactions to produce ^{12}C resonances:

$$^{10}\mathrm{B} + {}^{3}\mathrm{He} \rightarrow \mathrm{p} + {}^{12}\mathrm{C}^{*} \ @\ 4.9\ \mathrm{MeV}$$

and

$$^{11}\mathrm{B} + {}^{3}\mathrm{He} \rightarrow \mathrm{d} + {}^{12}\mathrm{C}^{*} \ @\ 8.5\ \mathrm{MeV}$$

The purpose of carrying out two similar reactions is to probe states in ^{12}C is to have complementary results which can be compared to each other and which can serve as a cross-check to each other. The advantage of using reactions with light-ions is that the energies in the laboratory frame are similar to center of mass energies. In addition the high Q-values associated with these reactions allows one to populate highly excited states in ^{12}C with very little beam energy. The combined effect is that using low beam energies reduces the kinematical focusing of the reaction, making it easier to detect the outgoing particles.

There have been recent experiments to study the triple alpha continuum in ^{12}C using inelastic scattering. Alpha inelastic scattering of ^{12}C(α,α')^{12}C* was used to probe states of natural parity in ^{12}C. Natural parity refers to states where the spin, j, and the parity, π, satisfy $\pi = (-1)^{j}$. In these experiments only the angular distribution of the outgoing α particle was used to determine spin and parities of resonances in ^{12}C [Ito04, Joh03]. Similar to the studies using β-decay, these alpha inelastic experiments are more selective in that they only populate states of natural parity since both the α particle and the ^{12}C nucleus are 0^{+} nuclei. Therefore alpha inelastic scattering experiments will not populate all states of interest in ^{12}C.

A reaction using inelastic scattering of carbon of the type ^{12}C(^{12}C,3α')^{12}C was recently performed [Fre07] to reexamine properties of all resonances in ^{12}C below 15 MeV in excitation energy. This reaction is similar to the reactions we have chosen in the sense that it indiscriminately populates resonances in ^{12}C. Proton inelastic scattering experiments will similarly populate resonances in ^{12}C discriminately. However, the disadvantage in inelastic scattering is that since there is no Q-value, larger beam energies are needed to

excite states in ^{12}C. This is especially true for proton inelastic scattering since the center of mass energy available to excite ^{12}C is much lower due to the low mass of the proton.

Ultimately, the probe used to study ^{12}C resonances depends on what we want to learn, and the resources available. The goal of this experiment was to understand the properties of resonances in ^{12}C near the triple-alpha threshold. A light-ion reaction is ideal since the high Q-value requires little beam energy so that a local tandem accelerator could be used. The advantage in carrying out an experiment at a local facility is enormous since the lack of time constraints means the equipment can be thoroughly tested and there is time to correct for unforeseen drawbacks. An explanation of the facility and of the experimental setup is detailed in the following chapter.

As an adolescent I aspired to lasting fame, I craved factual certainty, and I thirsted for a meaningful vision of human life - so I became a scientist. This is like becoming an archbishop so you can meet girls.

M. Cartmill

2 Experimental Methods

This chapter focuses on the experimental procedure. There are many factors that go into an experiment, from the accelerator, the target, the setup, all the way into the electronics and the logic of the data acquisition system. I will outline the experimental setup used in the 2008 experiment, though I include a small section on the 2005 setup to serve as a comparison to the 2008 setup. Unless otherwise stated I discuss the experiment of 2008.

Before delving into the specifics of the experiment, such as the accelerator facility, detectors, and electronics, let us look first into the preparation involved. Many questions must be answered before we begin an experiment. For example, what detectors do we use? How many detectors? How long do we measure? These questions depend on the which physics parameters are sought after. Our main goal is to determine the nuclear structure of ^{12}C. Since we have already decided to study ^{12}C by a reaction, we know that our goal then is to detect four particles in coincidence. These will either be a proton or deuteron, depending on the target, and three alpha particles. This immediately tells us we need some form of particle identification in addition to a high segmentation setup to detect many particles in coincidence. Another factor is the energy. By looking at the beam energies and at the Q-value of the different reactions, we can see that we will have a maximum energy of protons of up to 20 MeV, and deuterons up to 18 MeV, so that we must be able to detect particles from hundreds of keV up to 20 MeV.

We now have three important factors we need to design the experiment around. First, we need to be able to separate particles depending on their mass and charge. If we want to be able to separate the light ion from the alpha particles in the reaction, the easiest method is to use a ΔE-E telescope (see Section 2.3.2). This means we will need a thin detector backed by a thick detector to stop the energetic protons. For the thin ΔE detector we used DSSSDs (Double-Sided Silicon Strip Detector) with a thickness of approximately 60 μm. The second factor is we need enough silicon to be able to stop up to 20 MeV protons, so we choose an E detector with sufficient thick-

ness to accomplish this (2.3.3). Finally, we need a setup with enough angular coverage and high granularity to give us significant four-particle coincidence events. A DSSSD provides a highly segmented detector in a small area so that we can detect several particles in coincidence. However one DSSSD will not provide enough angular coverage to detect all of the particles in coincidence. Ideally we could surround the target with DSSSD detectors, but adding DSSSDs to a setup increases the channels of electronics, it also becomes difficult to fit the DSSSDs into a compact setup, and they are also very costly and we do not have too many at our disposal. The number of ΔE-E telescopes was ultimately chosen to be four, as this could provide a good angular coverage (38% of 4π) in a compact setup. In principle the setup could involve six telescopes arranged in a cube so as to maximize the angular coverage. However, in our experiment the detectors were situated on a plane since placing detectors above or below would give shadowing from the target and would not greatly increase the efficiency of detection.

The next question concerns the geometry of the setup. We have four telescope detectors available for the experiment, and we wanted to optimize their position so as to maximize detection of four-particle events. If the reaction occurred at rest in the laboratory frame and proceeded through a direct decay to the available phase space, then the placement of the detectors would be arbitrary since all particles would be emitted isotropically. However, this was not the case, and the best method to determine the angular emission of the particles is by running a Monte Carlo simulation which takes into account the kinematical focusing at low angles, as well as the non-isotropic decay of the ^{12}C states. The simulations used in the preparation of the experiment were also used for the analysis and is discussed in greater detail in Section 3.4. The light ion (either p or d depending on the reaction) was emitted almost isotropically, which is expected given the reaction mechanism. The direction of the alpha particles was largely determined by their available energy, which depended on the state which was populated in ^{12}C. The lower energy alpha particles were seen to be emitted at very low angles, while higher energy alpha particles were more isotropic. The emission of low energy particles at very forward angles is due to the kinematic focusing from the beam. We therefore decided to place two telescopes as close to 0 degrees as possible, while the placement of the other two telescopes was not as important. One obvious problem we ran into in placing the detectors very close to 0 degrees was the bombardment of the detectors by Rutherford scattered beam. This at best gives many triggers and vastly increases dead time, and at worst could damage the detectors. Therefore the final placement of the front detectors was as close to 0 degrees as possible without damaging the detectors.

Table 2.1: The open channels for the reaction ^{3}He on ^{10}B at MeV are listed. The values are taken from http://t2.lanl.gov/data/qtool. The ^{12}C+p channel is the one of interest in this reaction. The channels of interest are highlighted.

Reaction products	**Q-Value (MeV)**
$^{13}\mathrm{N} + \gamma$	21.64
$\mathbf{^{12}C + p}$	19.69
$\mathbf{p} + 3\alpha$	12.42
$\mathbf{^{8}Be + p} + \alpha$	12.33
$^{9}\mathrm{B} + \alpha$	12.14
$^{5}\mathrm{Li} + 2\alpha$	10.45
$^{11}\mathrm{B} + 2\mathrm{p}$	3.74
$^{11}\mathrm{C} + \mathrm{d}$	3.20
$^{12}\mathrm{N} + \mathrm{n}$	1.57
$^{11}\mathrm{C} + \mathrm{p} + \mathrm{n}$	0.97
$^{10}\mathrm{B} + ^{3}\mathrm{He}$	0.00

2.1 Reaction

In 2005 we studied resonances in ^{12}C using the $^{10}\mathrm{B}+^{3}\mathrm{He} \rightarrow \mathrm{p}+^{12}\mathrm{C}^{*}$ reaction at 2.45 MeV. The same reaction was previously studied in 1966 [Wag66] by detecting only two particles in coincidence on an oscilloscope. They determined many new properties of ^{12}C but were limited by the detector technology and electronics at the time. By revisiting this reaction we hoped to extract much more detailed information on these resonances. However the difficulty in extracting information on a nucleus from a reaction is that a reaction indiscriminately populates any energetically possible channel. The open channels from this reaction can be seen in Table 2.1, in which one can see that the p+^{12}C* channel is just one of many open channels. It therefore becomes difficult to select the channel of interest among the many possibilities, though some techniques are discussed in Section 3.3. In any case the preliminary results obtained in 2005 gave us confidence that with a proper setup we could greatly improve upon the current knowledge of ^{12}C resonances.

This is why in 2008, with a new setup with four telescopes, we decided to study the $^{10}\mathrm{B} + ^{3}\mathrm{He} \rightarrow \mathrm{p} + ^{12}\mathrm{C}^{*}$ reaction, yet this time at 4.9 MeV since the p+^{12}C* cross section increases at 4.9 MeV. In addition we studied the

Table 2.2: Some open channels for the reaction ^{3}He on ^{11}B at 8.5 MeV. The values are taken from http://t2.lanl.gov/data/qtool. The $^{12}\mathrm{C} + \mathrm{d}$ channel is the one of interest in this reaction. The channels of interest are highlighted.

Reaction products	**Q-Value (MeV)**
$^{14}\mathrm{N} + \gamma$	20.74
$^{13}\mathrm{C} + \mathrm{p}$	13.19
$\mathbf{^{12}C + d}$	10.46
$^{13}\mathrm{N} + \mathrm{n}$	10.18
$^{10}\mathrm{B} + \alpha$	9.12
$^{12}\mathrm{C} + \mathrm{n} + \mathrm{p}$	8.24
$^{6}\mathrm{Li} + 2\alpha$	4.66
$\mathbf{d} + 3\alpha$	3.19
$\mathbf{^{8}Be + d} + \alpha$	3.10
$^{9}\mathrm{B} + \mathrm{p} + \alpha$	2.53
$^{9}\mathrm{Be} + \mathrm{p} + \alpha$	2.54
$\mathrm{n} + \mathrm{p} + 3\alpha$	0.96
$^{8}\mathrm{Be} + \mathrm{n} + \mathrm{p} + \alpha$	0.87
$^{9}\mathrm{B} + \mathrm{n} + \alpha$	0.69
$^{5}\mathrm{He} + \mathrm{p} + 2\alpha$	0.07
$^{11}\mathrm{B} + ^{3}\mathrm{He}$	0.00
$^{5}\mathrm{Li} + \mathrm{n} + 2\alpha$	-1.00
$^{11}\mathrm{C} + \mathrm{t}$	-2.00
$^{12}\mathrm{B} + 2\mathrm{p}$	-4.35
$^{11}\mathrm{B} + \mathrm{p} + \mathrm{d}$	-5.49

^{11}B + ^{3}He $\rightarrow$ d + ^{12}C* reaction at 8.5 MeV, since this reaction provides complementary results and has less background channels with a deuteron than the former reaction with a proton (Tables 2.2 and 2.1).

In principle increasing the beam energy will increase the probability of populating the channel of interest since there is more energy available to overcome the Coulomb barrier, though the cross section is also determined by other factors. However increasing the beam energy has its negative effect. For example, in the ^{11}B target reaction if the beam energy was increased higher, then the Rutherford scattered ^{3}He ions would have sufficient energy to penetrate the Δ-E detector which would have greatly complicated the particle identification.

2.1.1 Reaction mechanism

The two reactions we are using to populate excited states in ^{12}C are in principle governed by two different mechanisms. The reaction could be the result of a direct reaction or from a compound formation. A direct reaction is a one-step process in which the beam interacts primarily at the surface of the target nucleus, while a compound reaction is a two-step process which occurs when the beam and target form a highly excited compound nucleus which then evaporates off light particles [Kra88, Sat80].

Compound Formation

When two nuclear systems collide, they may coalesce to form a highly excited compound system. This compound nucleus will stay fused together long enough for its excitation energy to be shared by all its constituent nucleons. If sufficient energy is localized on one nucleon, then it can escape. A general compound reaction will take the following form:

$$A + a \rightarrow X^{*} \rightarrow B^{*} + b \tag{2.1}$$

where A is the target, a is the beam, and X* is the highly excited compound nucleus which decays into B* and b. If sufficient excitation energy remains in B*, further particle emissions can occur. One can visualize this as if the nucleus is a liquid drop, in which two colliding droplets combine to form a single compound drop which is excited, or at a high temperature. In order to cool, the compound drop will evaporate particles.

In this particular experiment, a ^{3}He beam was let to impact onto a target composed of ^{10}B. To compare to the above formula, we have

$$^{10}\mathrm{B} + {}^{3}\mathrm{He} \rightarrow {}^{13}\mathrm{N}^{*} \rightarrow {}^{12}\mathrm{C}^{*} + \mathrm{p} \tag{2.2}$$

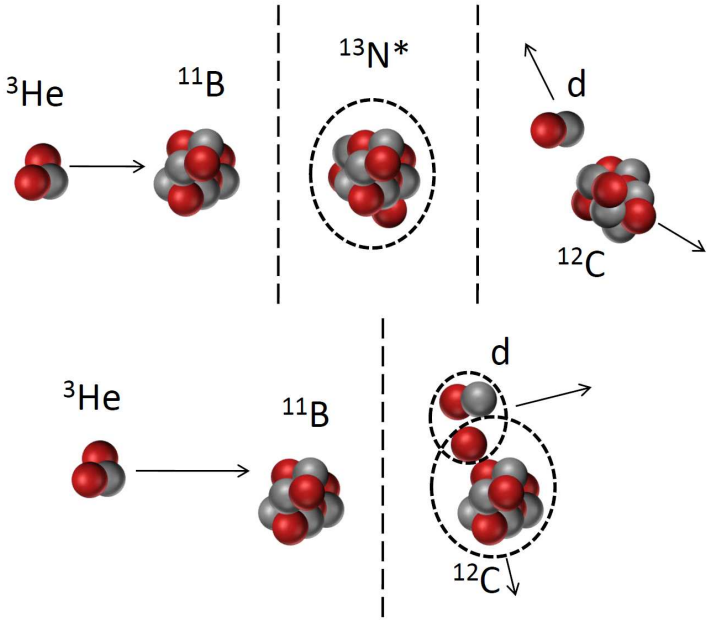

Figure 2.1: Illustration of different reaction mechanisms for the $^{11}\mathrm{B} + {}^{3}\mathrm{He} \rightarrow {}^{12}\mathrm{C}^{*} + \mathrm{d}$, the ^{3}He reaction. The top figure shows the two-step indirect reaction, where a compound nucleus is formed. The bottom shows a direct reaction, where a proton from the beam is transferred to the target.

As mentioned above, the secondary nucleus, ^{12}C*, can further emit particles if it is sufficiently excited. This is what was studied by this experiment: the ^{12}C* breaking up into three alpha particles.

Direct Reaction

Another possibility for the reaction mechanism involved is that the reaction proceeds as a direct reaction. A direct reaction can also be called a transfer reaction, since essentially it involves the transfer of a nucleon (or two) from the projectile to the target. The incoming ^{3}He will interact directly with the surface nucleons of the target. For example, in the case of the $^{10}\mathrm{B} + {}^{3}\mathrm{He} \rightarrow {}^{12}\mathrm{C}^{*} + \mathrm{p}$ reaction, the ^{3}He beam could be seen as transferring a deuteron to the target nucleus. Similarly, in the case of $^{11}\mathrm{B} + {}^{3}\mathrm{He} \rightarrow {}^{12}\mathrm{C}^{*} + \mathrm{d}$, the ^{3}He beam could transfer a proton to the target nucleus. Figure 2.1 shows an example of both a direct and an indirect reaction.

In either case, it is important to determine if there is any difference between a transfer reaction and a compound nucleus formation with respect to the observables. In other words, does the reaction mechanism have an effect

on the particles which we detect? In principle an indirect reaction such as a compound formation loses information on the initial nuclei involved, and the outgoing particles will be emitted isotropically. However, if the reaction were to proceed from a direct reaction, then one would expect the outgoing particles to be emitted in the forward direction since these involve the beam grazing the surface of the target. In reality the situation is more complicated and both types of reactions will occur. However the angular distributions of outgoing particles will be affected by the reaction mechanism and must be taken into account when analyzing the data.

2.2 The projectile accelerator

The accelerator at the Centro de Micro-Análisis de Materiales (CMAM) has been running since November of 2002, yet the experiment discussed in this paper was the first one performed on the nuclear physics line, which our group designed and built (see the work of Adolfo Sabán [Sab03]). The CMAM accelerator was provided by HVEE and is the first Coaxial High Current Tandetron Accelerator of 5 MV using the Cockroft-Walton power supply system [Got02, Eng05]. This 5 MV tandem accelerator feeds several experimental lines at the CMAM, and provides beams with very well-defined energies. See Fig. 2.2 for a layout of the accelerator hall at the CMAM and the different beam lines at CMAM.

2.2.1 Accelerator

An advantage of a Cockroft-Walton high voltage system is that it provides very stable beams, i.e. the beam energy did not fluctuate throughout the experiments. This is because, unlike in Van de Graaff generators, the Cockroft-Walton system is based on solid state circuits and has no moving parts. A well defined beam energy is important not only to keep the beam at a known energy, but also that the beam will stay at the same energy over the full experiment ($<$24 hours). See Fig. 2.3 for a view of the inside of the accelerator tank. Negative ion beams are first accelerated through a vacuum pipe to a positive terminal located in the center to energies of q * V_T, where V_T is the terminal voltage (5 MV maximum) and q is the charge state. The ions then go through a Nitrogen gas stripper in order to remove electrons and thus become positively charged, at which point they are further accelerated to the end of the accelerator by the terminal ground. Therefore when the beam exits the accelerator it will have an energy of V_T(q+1), where q is the charge state obtained by the stripping.

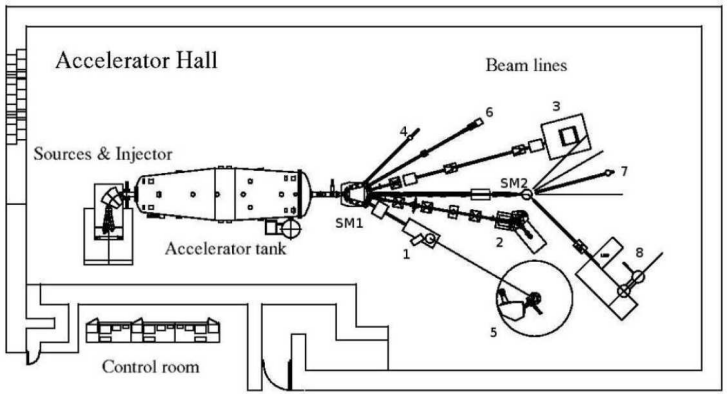

Figure 2.2: General layout of the CMAM accelerator hall (courtesy of [Pas04]). The splitting magnet provides the beam for several different experimental lines. The beam lines with their corresponding numbers are: (1) Multi-Purpose, (2) Time-of-Flight, (3) External micro-beam, (4) Environmental studies, (5) Magnetic spectrograph, 6) Nuclear Physics, (7) Ion-beam Modification of Materials, and (8) Ultra-High Vacuum. The experiment took place in the nuclear physics beam line, which is operated by the CSIC. See [Sab03] for more details on the design of the beam line.

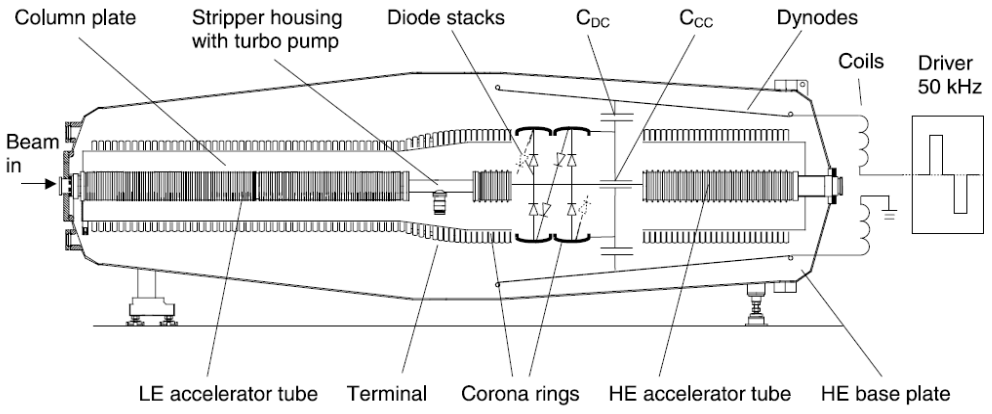

Figure 2.3: Layout of the 5 MV accelerator tank at the CMAM [Got02]

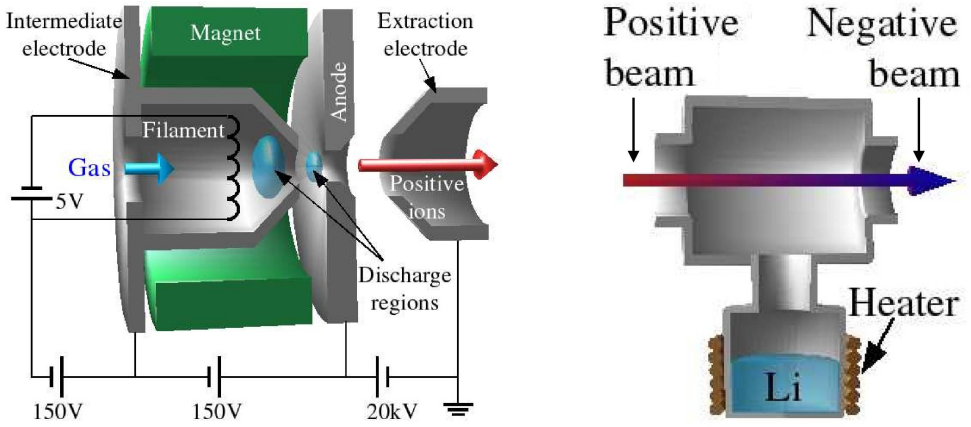

Figure 2.4: Sketch of the (a) Duoplasmatron ion source and (b) Lithium charge exchange canal.

2.2.2 Ion-source

The CMAM facility has two different types of ion sources which together can give almost any element in the periodic table: the Duoplasmatron source and the negative sputtering ion source. The Duoplasmatron source (Fig. 2.4(a)) is used mainly to produce He ions, and thus the source used for this experiment. To get a ^{3}He beam, a ^{3}He gas is injected into the plasma where it is ionized to $^3He^+$. It is then ejected into a Lithium charge exchange channel (Fig. 2.4(b)) to obtain a negative beam, and accelerated towards the accelerator terminal. The sputtering ion source is used for basically any other element in the periodic table.

2.3 Experimental setup

Although I will be focusing on the analysis of the results from the 2008 experiment, I have included some results obtained in the 2005 experiment. The purpose of this is mostly for comparison, and to demonstrate the superiority of the results obtained from the 2008 setup. In this section I will first describe the setup used in the 2005 experiment, followed by the description of the main setup used in 2008. One thing common to both experiments was the reaction chamber, which can be seen in Fig. 2.5.

Figure 2.5: Picture of the nuclear physics line at the CMAM in the foreground. The experimental chamber (measuring 30x40x30 cm^3) is seen on the left-hand side of the picture. A remote controlled slit system [RAM] can also be seen, though Fig. 2.8 shows the slits in better detail.

2.3.1 2005 experimental setup

The beam used was ^{3}He with an energy of 2.45 MeV and a current of 1.22 nA, equivalent to 7.65 x 10^{9} ions/s, . This current is by no means the maximum current achieved by the accelerator. In fact, the current provided by the accelerator was reduced and optimized by the use of collimators and slits mentioned below, since too high a current can damage our detectors. The target of ^{10}B was produced at the Aarhus University. It was enriched to contain 90% of ^{10}B, the other 10% being ^{11}B (^{10}B is only about 20% of the natural abundance of Boron; ^{11}B makes up the rest). The thickness of the target was 17 μg/cm^2 on a ^{12}C support of 3 μg/cm^2.

The setup for the 2005 experiment consisted in two DSSSD telescopes (see Fig. 2.6 for a clearer picture of the detector setup used, and Fig 2.7 to see a general view of the experimental setup); i.e. a DSSSD backed by a thick silicon PAD detector, useful for differentiating between particles of different mass and charge. These two telescopes were placed facing each other and were parallel to the beam, so as to better detect back-to-back coincidences and to avoid Rutherford scattered beam from hitting the detectors.

The different thicknesses of the detectors were not chosen arbitrarily. The reaction leads to α particles in the energy range of 0-10 MeV, and protons in the energy range of 0-22 MeV. Therefore, it was necessary to have a thin enough DSSSD to let protons pass through to the back detector for identification, yet thick enough to stop the alpha particles coming from the break up of ^{12}C. In addition, the back detectors had to be sufficiently thick to stop even the high energy protons produced in the reaction. The additional back telescope (eback3) behind DSSSD2 was included to sufficiently stop the highest energy protons leading to the ground state of ^{12}C.

The slits shown in Fig. 2.7 are located about 70 cm upstream from the chamber and were closed to 0.5 mm $\times$ 0.5 mm in order to collimate the beam as much as possible. These slits also had the advantage that they can be used to optimize the alignment of the beam since they move independently in the x and y direction. There was also a Tungsten collimator ($\phi = 5$ mm) placed at the entrance of the chamber (Figs. 2.6 and 2.7) to cut away the part of the beam which has been scattered on the RAMEM slits. These slits were made especially for the nuclear physics beam line by RAMEM S.A. [RAM]. See Fig. 2.8 for a closer view of the collimating slits. The geometric measurements were done after the experiment was finished with the setup removed from the chamber in order to have a more precise measurement. The purpose of collimating the beam was to avoid scattering of the beam at the entrance of the chamber. If the beam is not well collimated, it can reflect directly into the detectors which would increase the dead time or possibly

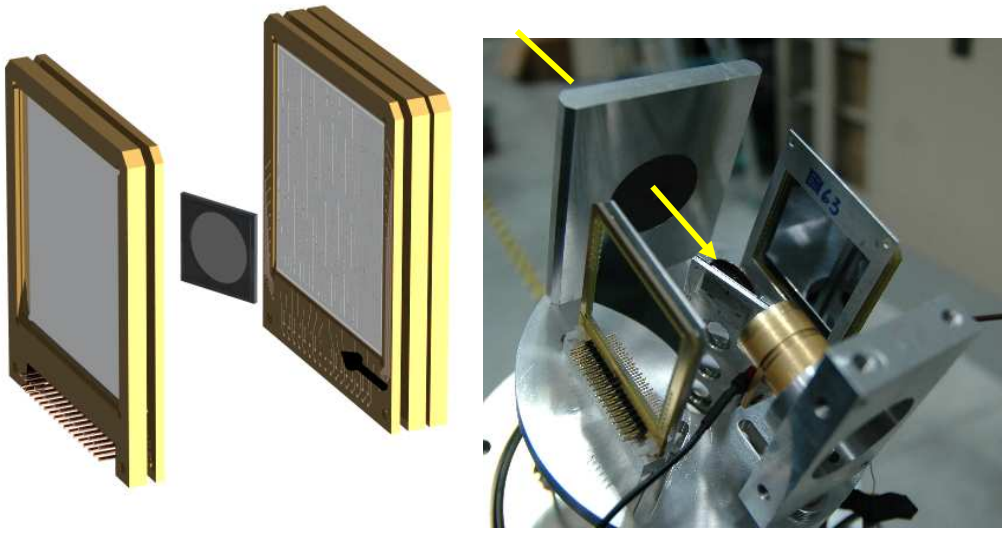

Figure 2.6: View of the 2005 experimental setup, with DSSSD1 (left) backed with one Si-PAD detector, and DSSSD2 (right) backed with two Si-PAD detectors. For reference the distance from one detector to another is only 10 cm. On the left is an illustration of the experimental setup, while on the right-hand-side is a picture from the experimental setup. The picture on the right shows the Tungsten collimator in place to avoid scattered beam from the RAMEM slits, as well as a Faraday cup placed at the end of the beam to monitor the beam intensity. An α source for calibration can be seen attached to the target holder in the picture on the right.

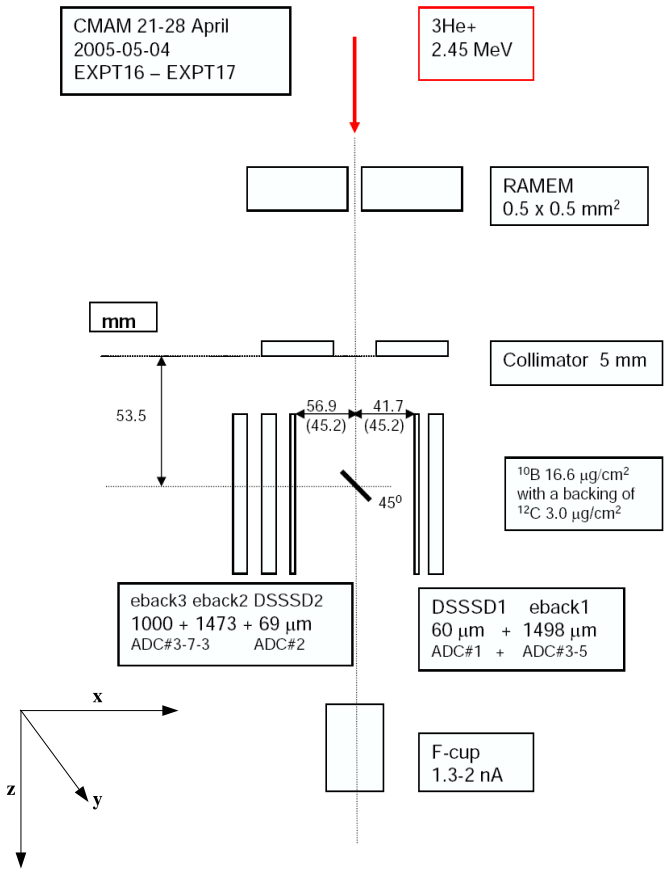

Figure 2.7: Experimental setup. The incoming beam from the accelerator passes through the RAMEM slits, where the diameter is adjusted in the y and z direction. It then passes through the 5 mm Tungsten collimator to avoid scattered beam from the RAMEM slits, before hitting the target, situated at 45° with respect to the beam. The Faraday cup placed after the target was used to optimize the beam and to monitor the beam during the experimental run. In this geometry, the telescopes detect the charged particles produced in the reaction with a subtended angle of $1/9^{th}$ of 4π. The measurements given in parenthesis for the distance from the detector to the target ladder are those used for the experimental data analysis, while the other measurements are the optimized values for the calibrations sources obtained calculated from the calibrations of the DSSSDs.

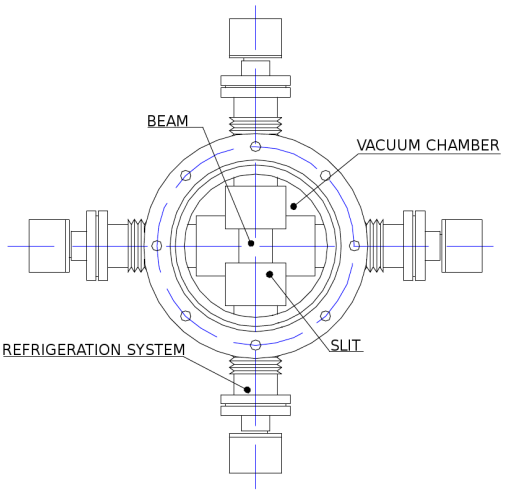

Figure 2.8: Close view of the slits from RAMEM S.A. (on the left-hand-side) used in the nuclear physics beam line. Each of the four slits can be moved independently, providing a better control over the collimation of the beam. The slits can also give a current reading which can be used to determine the position of the beam.

damage the detectors. In addition, the RAMEM slits can be used to attain smaller sizes of the incoming beam. The Faraday cup is used to optimize and to monitor the intensity of the beam.

The angles covered by each DSSSD were from 62°-120° with respect to the target holder, with the distance from each detector to the reaction point being 45.2 mm. Given these angles, one can calculate that the total solid angle covered in this experiment was $\approx \frac{4\pi}{9}$. However, this only refers to detecting one particle per event. In this experiment there was a total of four particles to be detected in one single event. We can calculate the detection efficiency of our setup for n-particle efficiencies by the following:

$$\epsilon_n = \left[\sum_{\substack{i=1,j=1 \\ i \neq j}}^{256} \epsilon_i + \epsilon_j \right]^n \tag{2.3}$$

where ϵ_i is the subtended angle of each pixel in the first detector and ϵ_j the subtended angle of each pixel in the second detector (both are approximated to be about 0.035%). Note that the ϵ_i^n and ϵ_j^n terms do not contribute as they correspond to n-particles hitting the same pixel. In our experiment if two particles were to hit the same pixel it would look as if it was one particle with the sum of the two energies (summing event). The different n-particle

Table 2.3: Comparison of multi-particle detection efficiencies for the setups used in the 2005 and 2008 experiments. Note the large relative improvement in detecting 4-particle coincidences obtained by adding two more telescopes.

Efficiency for n particles (ϵ_n)	2005 setup	2008 setup	Improvement
$n = 1$	11%	38%	$\times 3$
$n = 2$	1.2%	14.5%	$\times 12$
$n = 3$	0.13%	5.5%	$\times 42$
$n = 4$	0.01%	2.1%	$\times 210$

detection efficiencies for the 2005 setup are given in Table 2.3 and compared to the efficiencies of the 2008 setup.

2.3.2 2008 experimental setup

The experimental setup used in the experiment done in 2008 covered 38% of 4π and consisted of four Double Sided Si Strip Detectors (DSSSD) [Ten04], each backed by a non-segmented Si-PAD (Fig. 2.9). All of the DSSSDs have a thickness of 60 μm, and three of them had 16×16 perpendicular strips while the fourth has 32×32 perpendicular strips. The 16×16 DSSSDs have an active area of 50×50 mm^2, giving a pixel size of 3×3 mm^2, while the 32×32 DSSSD has an active area of 67×67 mm^2, giving a pixel size of 2×2 mm^2. The telescopes were arranged to maximize multi-particle detection, placing two DSSSDs as close to 0° as possible. Simulations were done prior to the experiment to test the optimal angular arrangement of the DSSSDs. Because of their higher mass, alpha particles are kinematically focused at small angles in the laboratory frame. However, the high intensity from Rutherford scattered beam becomes a problem at very low angles, giving rise to random coincidences with reaction events, so that the ultimate choice for positioning the detectors was a compromise between increasing multi-particle detection and reducing Rutherford scattered beam particles. The high intensity Rutherford scattered beam can be seen in Fig. 2.11(a).

The choice of highly segmented detectors is advantageous for detecting high multiplicity final states (see Table 2.3). In addition the angular resolution for this geometry of 3° for the 16×16 DSSSDs and 2° for the 32×32 DSSSD reduces the error when reconstructing center of mass energies. The thickness of the front detectors (60 μm) was ideal to separate the alpha particles from the protons and deuterons using ΔE-E plots since the protons

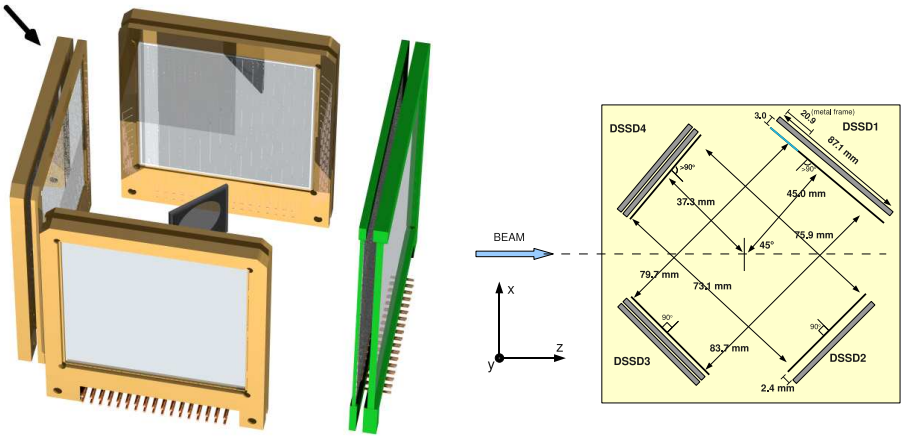

(a) (b)

Figure 2.9: (a) Setup used in the reaction experiments of 2008. The 32×32 strip green detector has a larger active area (67×67 mm^2) than the other three 16×16 strip DSSSDs (50×50 mm^2). This gives a 2 mm strip width and a 3 mm strip width for the 32×32 strip and 16×16 strip DSSSDs, respectively. The detectors are drawn to scale with the target foil. (b) The measurements taken for the setup along with the coordinate system used throughout the chapter.

Table 2.4: Maximum energy which is deposited in Si for different thicknesses calculated using SRIM [Zie03]

Thickness	proton energy	deuteron energy	α energy
69 μm	2.55 MeV	3.25 MeV	10.0 MeV
1000 μm	12.50 MeV	17.0 MeV	50.0 MeV
1500 μm	15.25 MeV	20.0 MeV	50.0 MeV

and deuterons had sufficient energy to go through the DSSSD and deposit energy in the back detector while most of the alpha particles do not have sufficient energy to pass through the DSSSD (this is not true when an alpha particle is the primary ejectile and thus has a higher energy, as in the case of the ^{9}B channel). To make a ΔE detector thin enough in order to allow the alpha particles to reach the E-detector and separate them is not possible so we chose a thickness which was assured to stop the alpha particles of interest. Refer to Table 2.4 for the range of the particles in the different detector thicknesses [Zie03].

In the analysis it is assumed that any particle that comes in coincidence with a proton or deuteron and is stopped in the DSSSD is an alpha particle. However, this is not always the case, e.g. in the case of random coincidences, so further requirements are needed to clean up the spectra. The beam energies for each reaction were chosen to optimize the cross sections while minimizing the focus in the forward direction. The target thickness was minimized to reduce energy losses in the target foil. The targets, depending on the reaction, were 18.9 μg/cm^2 enriched ^{10}B (90%), 22.0 μg/cm^2 ^{11}B and 33.1 μg/cm^2 LiF, all with a 4 μg/cm^2 C backing. Although the energy loss of a 5 MeV alpha particle in e.g. 22.0 μg/cm^2 ^{11}B is only $\approx$ 15 keV, the energy loss of a 500 keV alpha particle is $\approx$ 50 keV, which is not negligible and needs to be taken into account.

The reaction-angles covered by the detectors were from 10°-80° in the forward direction and 100°-170° in the backward direction, where θ is defined in Fig. 2.10. The distances to the target for each detector can be seen in Fig. 2.9(b). Given these angles, one can calculate the total solid angle covered by the setup to be $\approx$ 38% of 4π, three times more with respect to the 2005 setup. As in section 2.3.1, we can calculate the detection efficiencies of different multiplicities n with this setup using the following equation, which is a slightly modified version of Equation 2.3 to account for the 32×32 DSSSD. For a visual representation of the solid angle covered by the 2008 setup refer

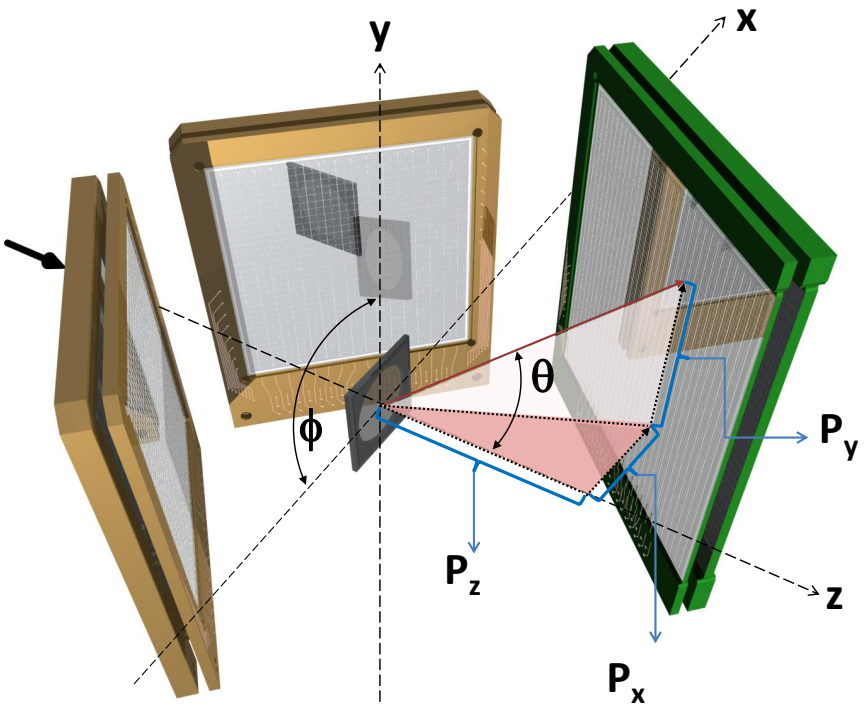

Figure 2.10: The experimental setup with the (x,y,z) and (r,θ,ϕ) coordinate systems illustrated. DSSSD2 has been removed for clarity. The coordinate systems shown were used throughout the analysis.

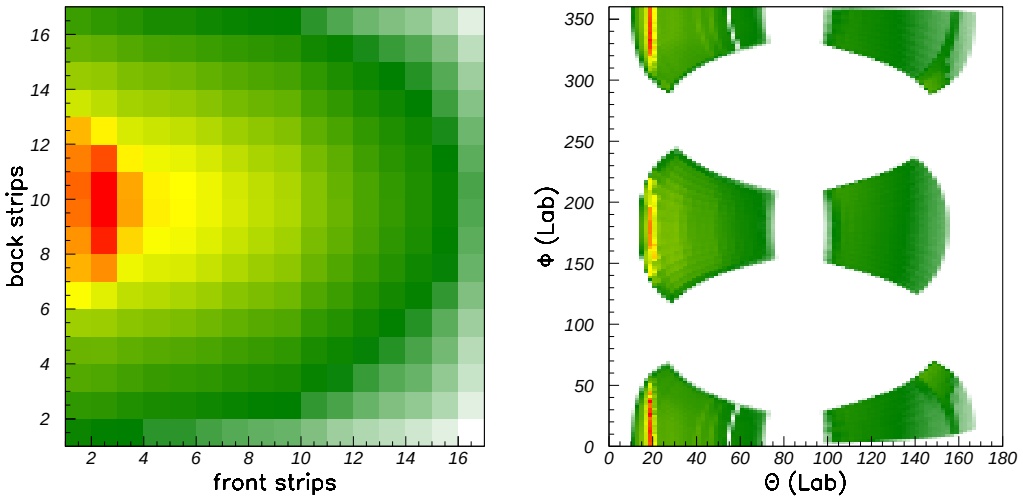

(a) (b)

Figure 2.11: (a) Hitmap of DSSSD2 where the front strips are plotted versus the back strips. The projection of this hitmap onto a sphere is shown in (b), which shows the angular coverage of the experimental setup. This is a projection of a sphere onto a plane, so that 4π coverage would cover the entire plane. Note the bright vertical line at approximately 20^{o} which is due to the high intensity Rutherford scattered beam at forward angles.

to Fig. 2.11.

$$\epsilon_n = \left[\sum_{\substack{i=1 \\ i\neq j\neq k\neq l}}^{256} \sum_{\substack{j=1 \\ i\neq j\neq k\neq l}}^{256} \sum_{\substack{k=1 \\ i\neq j\neq k\neq l}}^{256} \sum_{\substack{l=1 \\ i\neq j\neq k\neq l}}^{512} \epsilon_i + \epsilon_j + \epsilon_k + \epsilon_l \right]^n \tag{2.4}$$

where $\epsilon_i, \epsilon_j, \epsilon_k$ is the subtended angle of each pixel in the 16×16 DSSSDs (all approximated to be about 0.035% of 4π) and ϵ_l the subtended angle of each pixel in the 32×32 DSSSD (approximated to be about 0.027% of 4π due to the smaller pixel size). The average angular resolution in degrees is 3^{o}. The detection efficiencies for different multiplicities for the 2005 and 2008 setup are shown in Table 2.3. Note that by tripling our solid angle coverage, we have increased our 4-particle detection efficiency by over *two orders of magnitude*. The results of the statistics increase between the two experiments will be shown in more detail in the following chapter.

2.3.3 Detectors

There were two different kinds of detectors used in this experiment, DSSSDs and Si-Pad detectors. Both types of detectors function by the same principle. The Si-Pad detectors used were of varying thicknesses, between 1 mm and 1.6 mm, and were doped with the p-donor B to a depth of 500 nm. This 500 nm doped layer depth, along with a layer of 300 nm of Al contact, gives the Si-Pad a dead layer of 800 nm. The DSSSDs are slightly more complicated due to their novel design, but essentially they provide a cost effective way having a highly segmented Si detector. In a DSSSD, the Si layer can either be doped with a p-type or n-type material. The p-type are positive charge carriers (hole) while the n-type are negative charge carriers (electron). A negative voltage is applied to the p-type side so that the positive ions are attracted to it, while the n-side is on a floating ground. When a particle then penetrates the detector, it produces free electrons and holes, which in turn are attracted to their corresponding electrodes. The number of electron-hole pairs depends on the energy of the radiation, so that the pulse measured is directly proportional to the energy of the incoming particle.

The 16 $\times$16 DSSSDs used have 50 mm long strips, each 3 mm wide separated by 0.1 mm, on the front face and 16 orthogonal strips with the same dimensions on the back face. This gives an active area of 50 $\times$ 50 mm^2, thereby creating 256 individual detectors of 3 $\times$ 3 mm^2 each [BFT03]. The 32 $\times$32 DSSSD had an active area of 67 $\times$67 mm^2, with each active strip 2 mm wide separated by 0.1 mm. The front face of the DSSSD is implanted with a p^+-doping depth of only 100 nm on the n-type Si bulk and the Al contact grid covers only 2% of the active surface, so that the deadlayer was reduced to only 100 nm. The back side is implanted with 400 nm of n^+-type, together with an evaporated layer of 200 nm aluminum to act as an electrical contact (see Fig. 2.12). The DSSSDs were developed by the Instituto de Estructura de la Materia in Madrid in cooperation with Micron Semiconductor ltd [Ten04].

2.3.4 Trigger logic

We have so far defined a reaction and a setup, and the next step is to run the experiment. But before we begin taking data, we must first design a system which will be capable of handling the data in such a way that we can process them event-by-event. In the 2008 experiment, there were 165 (32+32+32+64+5) individual channels in the experiment: 32 from each 16$\times$16 DSSSD, 64 from the 32$\times$32 DSSSD, and one for each PAD detector placed behind the DSSSDs (the 32$\times$32 DSSSD was backed by two PAD

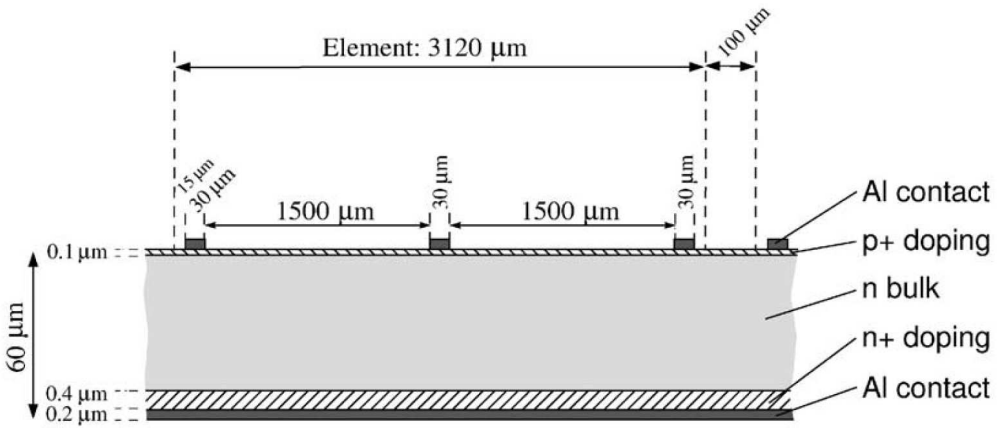

Figure 2.12: Profile view of the newer DSSSDs employed in the 2008 setup. In this design, the deadlayer is only 100 nm [Ten04].

detectors). Therefore we need to design a trigger logic and to run a data acquisition system which is capable of handling 165 channels simultaneously.

In this experiment we ran in listmode, in which every event is recorded individually with a time stamp so we are essentially working on an event-by-event basis. This brings up another important point: how do we define an event? In theory we define an event when a reaction occurs, in which any outgoing particles are in coincidence with each other and are detected nearly instantaneously. However in practice the acquisition system and electronics need time to process the signal so that we must increase the time window accordingly (see section 2.3.5). We also must construct a trigger logic which will tell the acquisition system when a good event occurs and which particles are part of that event. *On a side note, since there are thousands of reactions in the target happening per second, we will inevitably have cases where two reactions enter the same time window, leading to an event having two reactions. How to identify and understand such events is discussed in section 3.1.3.*

To construct the trigger logic one must think of the goals of the experiment since the trigger is specific to the needs and to the experimental setup in use. In this experiment, we wanted to detect a maximum of four particles in coincidence, so ideally all of the DSSSDs are put into the trigger. Since we have independent triggers from both the p-side and n-side of the DSSSD we can put an AND condition between the two to reduce any unwanted noise that may have triggered only one side of the DSSSD. The ΔE and the E detectors are then included in the trigger with an OR condition, since the

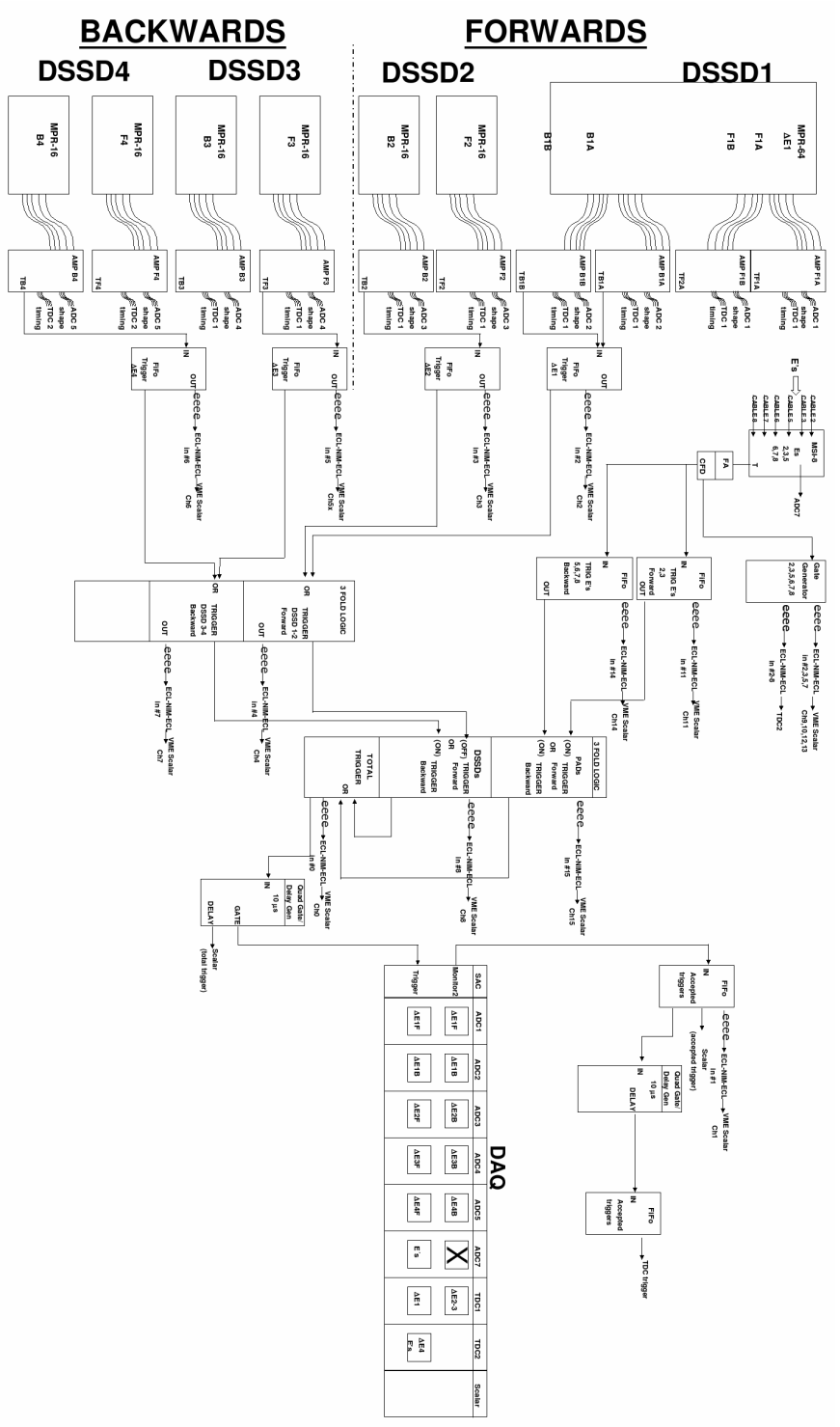

Figure 2.13: Schematic of the logic used in the experiments. To see the figure in more detail refer to Figs. 2.14 and 2.15.

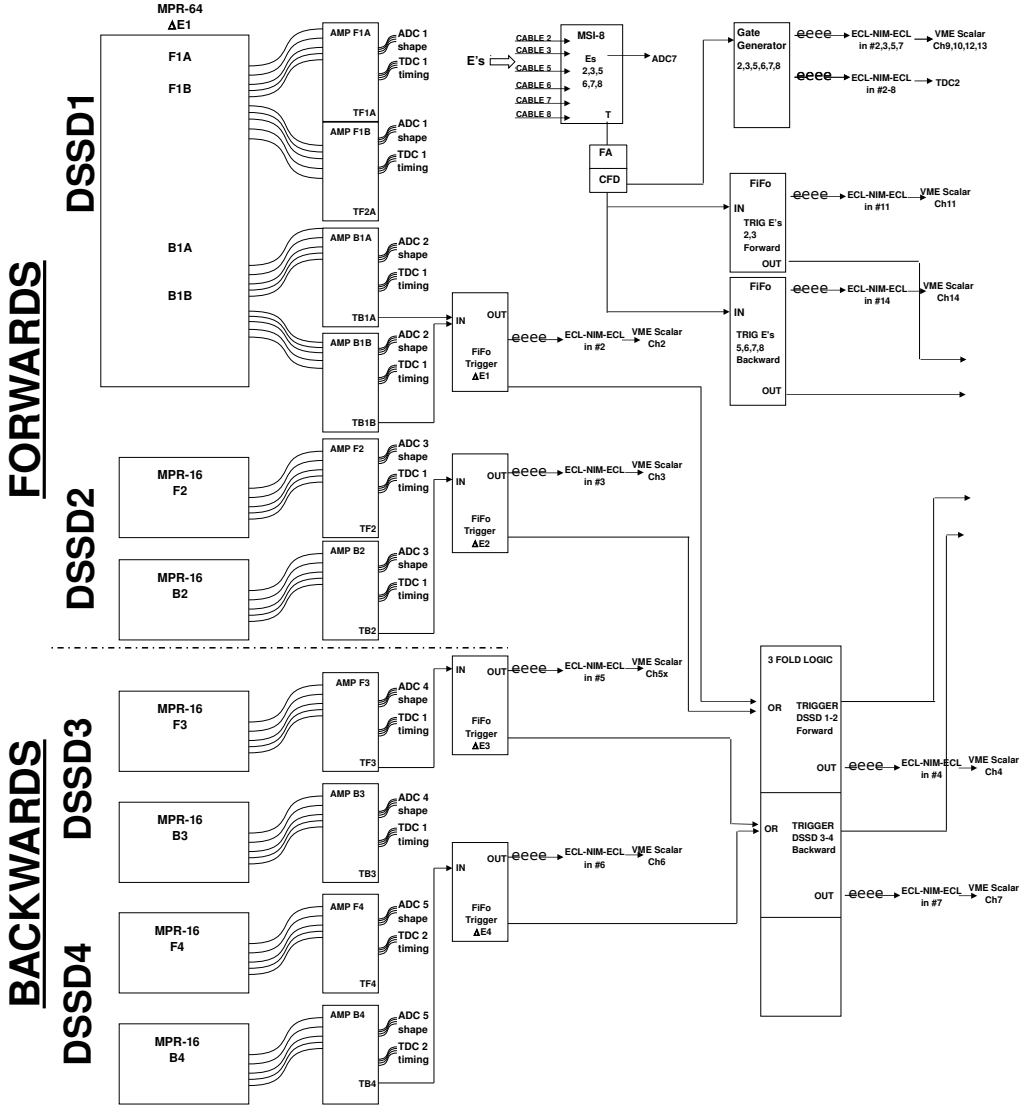

Figure 2.14: Close up of Fig. 2.13 showing the first part of the trigger logic used in the experiments.

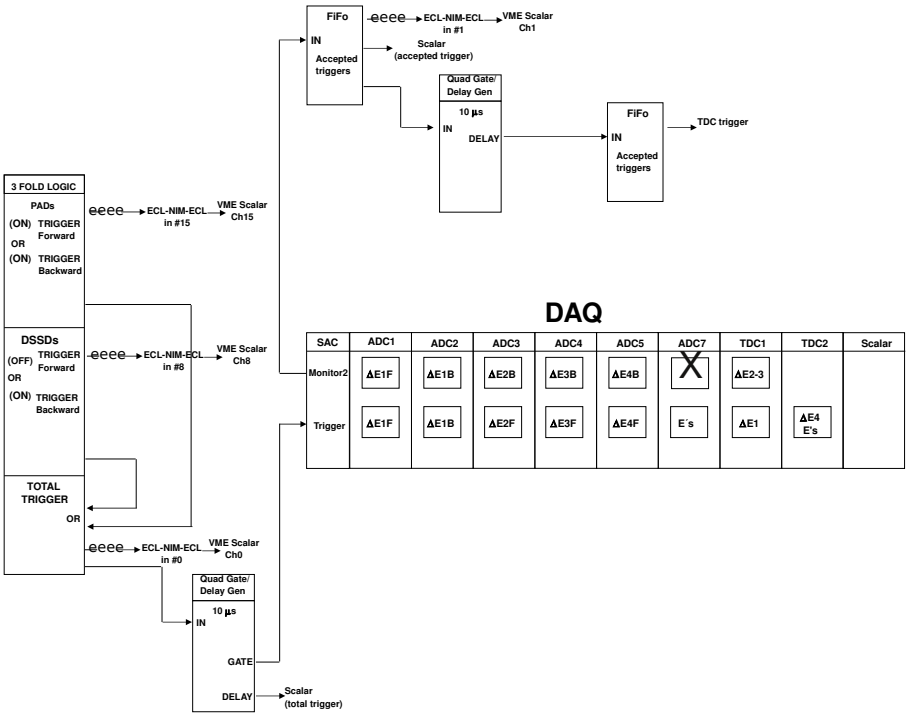

Figure 2.15: Close up of Fig. 2.13 showing the second part of the trigger logic used in the experiments.

alpha particles of interest do not penetrate the ΔE detectors. The forward angle DSSSDs had to be removed from the trigger because the high intensity from Rutherford scattering was giving too much dead time. Thus only the E detectors of the front-facing telescopes were included in the trigger. This did not cause an important loss in data since either the proton or deuteron from the reaction would leave a signal in the E detector. Figure 2.13 shows a detailed schematic of the trigger logic and electronic modules used in the 2008 experimental run (Figs. 2.14 and 2.15 shows the same but split into two pages for easier viewing). The next section will discuss the electronic modules which are used to construct such events and which will translate the voltage signal from the detector into an energy signal of a particle.

2.3.5 Electronics and data acquisition

The previous section discussed the trigger logic needed to handle multi-particle events. In order to process the signals coming from the detectors, very fast electronics is necessary. In addition, since the amplitude of the voltage signal given by the detector provides information on the energy deposited in that detector, we must be able to translate the analog voltage signal into something more useful: an equivalent digital signal. The NIM standard (Nuclear Instrumentation Method) was used for the processing of the signal from the detector to the ADC (Analog to Digital Converter). In order to do this, several different modules were used [Leo87, Kno89]. The electronic modules together with the data acquisition system provide the necessary signal processing and data storage as explained in the following.

Preamplifier

The main purpose of the preamplifier is to make a pulse out of the current that flows through the detector while adding as little noise as possible. The preamplifiers are thus located as close to the detectors as possible, minimizing the length of the cable connecting it to the detector. The preamplifiers used in this experiment were of the charge-sensitive type. In this type of preamplifier, the basic idea is to remove all dependence on the detector capacitance, as variations in the intrinsic capacitance can be caused by the leakage current in the detectors. In this experiment each DSSSD was connected to a Mesytec MPR-16 preamplifier, and further with a 16 pin connection via shielded twisted-pair cable to a Mesytec STM-16 amplification module.

Amplifier

Once the signal passes through the preamplifier, it is sent to the main amplifier for further amplification and to shape the signal to a convenient form for further processing. In this experiment, we needed a fast response time to conserve timing information, as well as a linear amplification in order to conserve the proportion between the input and output signal. Pulse-shaping is important for several reasons. Since the pulse coming from the preamplifier tends to have a long tail on the order of one hundred μs (in our case, we integrate the pulse from the preamplifier over 0.5 μs), a second signal may arrive during this time and will ride on the tail of this first signal, thereby increasing the amplitude of the initial signal (this process is known as pile-up). One should therefore shorten the tail in order to avoid this affect. Pulse-shaping is also used to optimize the signal-to-noise ratio. The amplifiers in this experiment were of the CR-RC pulse shaping type. A CR differentiator transmits frequencies above a cutoff frequency, thereby allowing higher frequencies to pass while filtering low frequencies. The RC integrator does the opposite. The combination of both circuits in sequence significantly reduces the noise.

The STM module used in this experiment housed a timing filter and a discriminator in addition to the amplification module. The discriminator is designed to respond only to input signals with a pulse height greater than a specified threshold value. The threshold value is set so as to reject pulses coming from electronic noise, while accepting valid pulses coming from the detector. The discriminator built-in to the amplifier in this experiment used a leading edge discriminator, meaning the triggering occurs the moment the pulse crosses the threshold level. The module also had delayed timing outputs which went directly to the TDC and were used as a STOP. Finally the modules had a common trigger output, which was used to define the trigger logic.

The common trigger from the different modules were then fed into a gate generator in order to create a coincidence gate. A gate generator is triggered by an input logic signal coming from the detectors, generating a gate pulse with a user-defined time window (in our case roughly 2.5 μs). This gate is then fed to the VME crate to serve as the acquisition window for the DAQ, essentially telling the ADC when to begin taking data and for how long. A delayed trigger is also sent to the TDC as well, since the TDC measures the time between the start of an event and the arrival of each individual detector pulse (STOP).

Analog-to-Digital Converter (ADC)

The amplified energy signal leaving the amplifier goes into the ADC. The purpose of the ADC is to convert the amplitude of an input pulse into a proportional digital number. The ADCs used in this experiment were of peak-sensing type. This means that the maximum of the voltage signal received from the amplifier is digitized, since this maximum voltage is proportional to the energy deposited in the detector. The ADCs used are based on the principle of successive approximation. This technique involves comparing the incoming voltage to a series of reference voltages to determine the height of the pulse. If it is greater than a specified value, the first bit is assigned a one. If it less than, it is assigned a zero. One-half is then added to the reference if it assigned a one, and this type of comparison is done successively until the required number of bits is obtained. The ADCs have a resolution of 12 bits, thereby covering a range of 2^{12} or 4096 channels. The conversion time in the ADCs utilized in the experiment was only 5.7 μs for 32 channels. The width of the ADC window was about 2.5 μs, meaning that when the ADC received a trigger, the acquisition window would stay open for that period of time and any signal that came in during those 2.5 μs was considered to happen in one event.

2.4 Calibrations

The calibrations are one of the most tedious processes when analyzing an experiment, yet also the most important. The purpose of the calibration is to associate a real energy (in keV) to the voltage reading which is fed into the ADC and assigned a channel number. To accomplish this, we use standard alpha sources. The idea is simple. One places different alpha-emitting sources with known energies to impinge on each of our detectors. One then associate the different voltage readings in the ADC to the actually energies of the alpha particles, makes a linear regression, and the detectors are calibrated. This is first done on an oscilloscope in order to set the dynamic range so that the different particle energies will fall within the ADC range and to get a crude estimate of the mV to keV conversion. Once the different amplifications and thresholds have been set using the sources, each strip is individually calibrated. Unfortunately, this is not as easy as it sounds. This is because we are first limited by the energy range of the alpha sources. So, for example, if one is to detect particles with a range of 1 MeV-20 MeV, and there are only sources with an energy of 3 MeV and 5 MeV available, any small error in the calibration will be greatly increased when extrapolated to

Table 2.5: α energies from the triple alpha source and their relative intensities

Source	α-energies (keV)	Weights of the energies (%)
^{239}Pu	$E_{\alpha_1} = 5156$	$W(E_{\alpha_1}) = 73.2$
	$E_{\alpha_2} = 5143$	$W(E_{\alpha_2}) = 15.1$
	$E_{\alpha_3} = 5105$	$W(E_{\alpha_3}) = 10.6$
^{241}Am	$E_{\alpha_1} = 5486$	$W(E_{\alpha_3}) = 85.2$
	$E_{\alpha_2} = 5443$	$W(E_{\alpha_2}) = 12.8$
	$E_{\alpha_3} = 5388$	$W(E_{\alpha_1}) = 1.4$
^{244}Cm	$E_{\alpha_1} = 5805$	$W(E_{\alpha_1}) = 76.4$
	$E_{\alpha_2} = 5763$	$W(E_{\alpha_2}) = 23.6$

higher energies. In addition, when calibrating the detectors, one needs to take into account the energy loss of the alpha particles in the dead-layers of the detector due to the Al contacts and the doped Si that the particles pass through, which will of course depend on the angle of entry, so that the position of the source must also be precisely determined. Similarly there may be dirt or dust on the alpha source which may reduce the outgoing energy of the particle. Other factors are involved which will complicate the calibrations, but these will be discussed when appropriate. I will first discuss here the standard method used to calibrate the detectors by using sources. This method was not sufficient for some of the detectors, and a more precise calibration was done, as will be discussed.

2.4.1 Calibration sources

The sources used for the calibrations were ^{148}Gd with an α energy of 3183 keV, and a triple alpha source which contained ^{239}Pu, ^{241}Am, and ^{244}Cm, with α energies of 5149 keV, 5479 keV, and 5795 keV, respectively. The α-energies from the triple source are the weighted energies since the three sources emit multiple alphas even though they appear as only one peak each(Table 2.5). The resolution of the detectors is approximately 60 keV so that the detector will not be able to differentiate between the alphas of each source of around 50 keV difference.

Source position

The position of the calibration source with respect to the detector must be calculated since each independent strip is to be calibrated and therefore the need to determine the angle of entry of the particle to account for losses due to deadlayers (see Fig. 3.4 and Section 3.1.2 for a detailed explanation on the analysis of deadlayers). The positions of the detectors were calculated by using a program which fits the intensity of the sources with the solid angle they cover. Basically, this program calculated the position of the detectors with respect to the position of the calibration sources on the target ladder. Accurate measurements of the positions were necessary in order to determine the effects of energy losses in the deadlayers of the detectors.

2.4.2 PAD detectors

The calibrations for the back detectors were done with a collimator in place, so that the angle of entry did not vary and therefore the energy loss of the alpha particles in the deadlayer was uniform. In order to calculate the energy loss of an α particle in Si, SRIM tables were used [Zie03]. After taking into account the losses in the deadlayer for the α particles from the ^{148}Gd and triple alpha sources, it turns out that the α particles from the ^{148}Gd source (3183 keV) had an energy of 3017 keV when they entered the sensitive part of the detector, while e.g. the ^{241}Am source had an energy of 5361 keV. These values were then used to perform a linear fit and obtain a relationship between channel number and energy for each back detector.

2.4.3 DSSSDs

The calibration of the DSSSDs was done differently than for the PAD detectors to take into account the strips of the detector. Essentially, a 16×16 DSSSD has 256 pixels which each serve as a detector. However, this does not mean we need to calibrate 256 different detectors. What we will have is 32 different calibrations, one for each strip. It would be very tedious to look at each strip individually, find the two source peaks, determine the centroid, determine the energy lost in the dead-layer, and then calibrate the strip. Instead, this can all be done more or less automatically. The first thing to do is to determine the source position, as explained above. Once we have the source position, we can calculate the dead-layer thickness of each pixel since we know the dimensions of the strips and detector. The calibration itself is straightforward and follows the same method as that for the PAD detector.

By plotting the front strip versus the corresponding back strips of each

DSSSD we can get a good idea of whether the calibrations were done correctly by looking at the difference in energy between the two strips. We can also plot the difference in energy between the front and back strips to determine a good value of this energy difference, since this is used to get rid of unwanted background. Figure 2.16 shows these two types of plots for DSSSD1 taken from the ^{11}B(^{3}He,d$\alpha\alpha\alpha$) reaction data. The events along the diagonal in the E_{front} versus E_{back} plot correspond to similar detected energies in each strip and are taken as valid hits, provided the difference in energy is less than 70 keV. Other features can be identified in this figure which will be explained in more detail in the following chapter as they are pertinent to analysis techniques. The 70 keV signal matching is shown in the $|E_{front} - E_{back}|$ plot of Fig. 2.16.

2.4.4 Internal calibration

As mentioned above, the calibration of the Si detectors was done using standard alpha sources. There is a problem with using this method, however. Recall that the energies of the sources are 3.18 MeV (^{148}Gd) up to 5.80 MeV (^{244}Cm). In the experiment, however, there are a wide range of energies, from hundreds of keV to almost 20 MeV in the PAD detectors. When only using two points separated by a little over 2 MeV for the calibration, when reaching energies at the upper and lower end extremes the calibration may lose precision. To recalibrate the PAD detectors, we first used the alpha source calibration as a rough calibration, and then performed a more precise calibration using the proton (or deuteron) energies which are known to feed well-known excited states in ^{12}C. Only those states in ^{12}C with a very well-known energy were used. In the case of the ^{10}B target, the states at 9.64 MeV, 12.71 MeV, and 16.11 MeV, corresponding to proton energies of 12747 keV, 9916 keV, and 6783 keV CM energies, respectively. For the ^{11}B target, the ground state, 4.44 MeV state, the 9.64 MeV state, and the 12.71 MeV state were used, corresponding to deuteron energies of 14664 keV, 10866 keV, 6402, and 3775 keV CM energies, respectively.

2.5 Geometry

Finally, before moving on to the physics of the analysis, it was critical to precisely determine the geometry of the setup used. The geometry is important to determine the angles of the outgoing particles, used to get information on the momentum of the particles as well as to change to different frames of reference. The easiest way to do this is by physically measuring distances

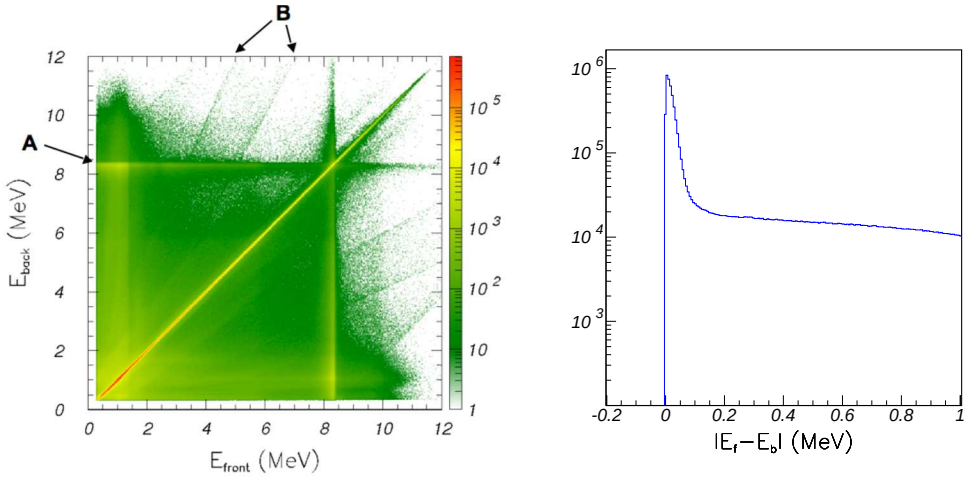

(a) Front Energy vs. Back Energy

(b) $|E_{front}\text{-}E_{back}|$

Figure 2.16: (a) Plot of the raw data, all events, obtained from the ^{11}B(^{3}He, d$\alpha\alpha\alpha$) reaction at 8.9 MeV, where a front strip signal (E_{front}) is matched to any back strip signal (E_{back}) and vice-versa for DSSSD1. The main activity lies on the diagonal of equal front and back energy. Besides this main diagonal, there are two structures, A and B, identified in this figure, which are mirror images along the diagonal. (A) Random coincidence of higher multiplicity events with beam. (B) High intensity on these diagonals correspond to summing events (see Section 3.1) between the emission of alpha particles from the ground state of ^{8}Be. More summing and sharing events will appear on either side of the diagonal. All of these structures are identified and included in the analysis. (b) The one-dimensional plot of (a). A cutoff of 70 keV was used in the analysis.

on the setup itself, which are shown in Fig. 2.9(b). Unfortunately there are some unavoidable errors in doing this, and another method was needed. To calculate the distances between the detectors and the target, we used two basic methods:

- Comparison to theoretical kinematic curves.
- Conservation of momentum requirements.

There are only two free parameters when adjusting the distances of the detectors: the distance from the target to the *center* of the detector (x' in Fig. 2.17), and the distance of the center of each detector itself (defined by the center strip in the detector) with respect to the closest point to the target (Δz' in Fig. 2.17).

2.5.1 Kinematic curves

Let us look at a generic reaction of the form

$$a + X \rightarrow Y + b \tag{2.5}$$

where a is the projectile, X is the (stationary) target, and Y and b are the reaction products. We know that energy and momentum are conserved, and can therefore relate the scattering angle θ of b with the energy of b in the laboratory frame. The relationship between the energy of the outgoing nucleus b (E_b) and θ in the laboratory frame is [Kra88]

$$E_b = \left[\frac{\sqrt{m_a m_b E_a}\cos\theta}{m_Y + m_b} + \frac{\sqrt{m_a m_b E_a \cos^2\theta + (m_Y + m_b)[m_Y Q + (m_Y - m_a)E_a]}}{m_Y + m_b} \right]^2 \tag{2.6}$$

where

$$\begin{aligned} Q &= m_i - m_f = m_X + m_a - m_Y - m_b \\ m_X &= \text{mass of the target } (^{10}\text{B or } ^{11}\text{B}) \\ m_a &= \text{mass of the } ^3\text{He beam} \\ m_b &= \text{mass of p or d} + E_x \\ m_y &= \text{mass of } ^{12}\text{C} \\ E_a &= E_{beam} \end{aligned}$$

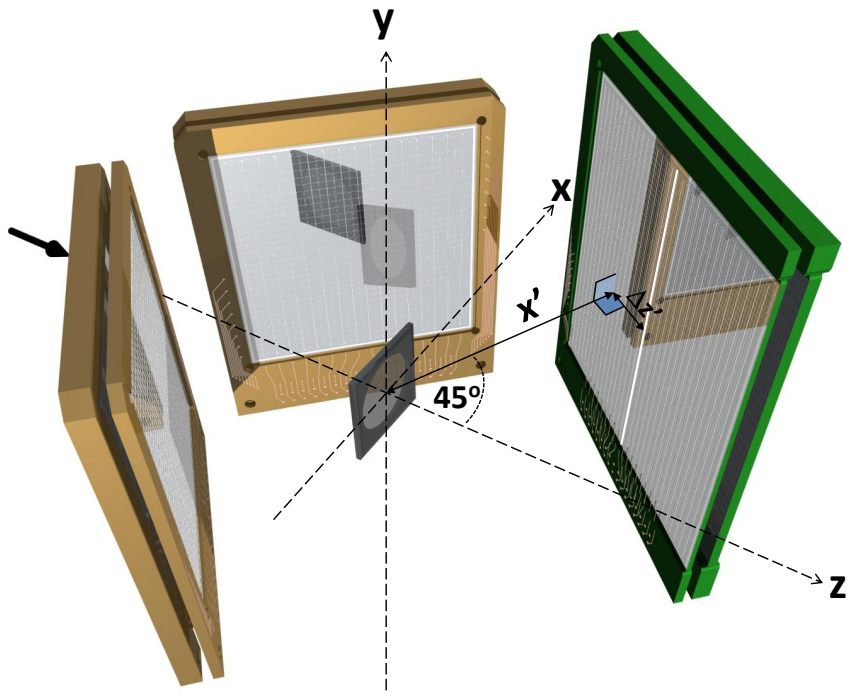

Figure 2.17: The only free parameters when adjusting the position of the detectors are x' and Δz'. x' is the distance to the closest point of the detector in the xz-plane. Δz' is the distance from the center strip of the detector to the closest point to the detector. For reference the center strip of the DSSSD has been highlighted in white.

The masses are given in MeV/c^2 and E_x is the excitation energy in MeV of ^{12}C. What we want to do with these kinematic curves is to exactly determine the geometry of our setup (and therefore, θ), so that a wide range of proton (or deuteron) energies are needed. To obtain this we can use different open channels from our reactions, and also use the different proton energies which depend on the ^{12}C excitation energy populated in the reaction. The excitation energy of the ^{12}C nucleus is added to the rest mass of the proton or deuteron since we are plotting the laboratory energy of the proton or deuteron, in Figs. 2.18 and 2.19.

Since the kinematic curves are very sensitive to the angle of emission of the proton, one can adjust different distances of the detectors relative to the target to get a good overlap with the theoretical kinematic curves calculated from Equation 2.6. Figure 2.18 shows the energy of the proton in the lab frame versus θ for DSSSD1 in the ^{10}B target reaction data with the kinematic curves of the 9.64 MeV state and the 12.71 MeV state from Equation 2.6 superimposed. There are three different pictures shown each with only a slight change of 5 mm on the free parameters in order to demonstrate how sensitive the effect of moving the detector in different directions has on the agreement with the kinematic curves. This is done for each DSSSD and allows us to precisely determine their position with respect to the target.

Figure 2.19 shows kinematic curves for DSSSD1 and DSSSD4 from the ^{3}He+^{10}B and ^{3}He+^{11}B reaction with the theoretical curves in Equation 2.6 superimposed. When the geometry has been adjusted the overlap with the theoretical kinematic curves is quite remarkable. Once there is good agreement with the kinematic curves, we can fine-tune the positions of the detectors using a completely different method which takes advantage of the complete kinematic detection of the experiment.

2.5.2 Fine-tuning the geometry

In order to fine-tune the position of the different detectors we take advantage of the complete kinematics data, and look at the total momentum in the x,y, and z-direction, where the coordinates are defined as in Fig. 2.10. By adjusting different distances of the detector to the target, we look at the effect this has on on the different components of momentum. The details on determining the momentum from the energy and position will be discussed in the next chapter. The components of momentum are very sensitive to any small changes made to the position of the detectors. The different momentum components will of course be affected more or less by different adjustments made to the detector positions. Figure 2.20 shows the total momentum in the x,y, and z component for the ^{11}B(^{3}He,d$\alpha\alpha\alpha$) reaction after making all

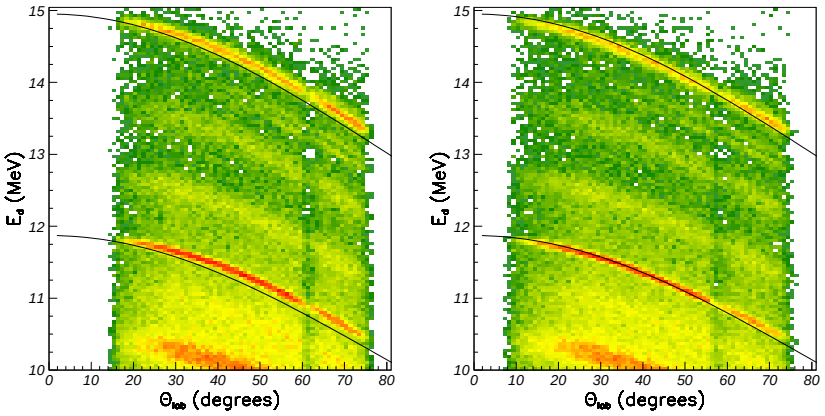

(a)

(b)

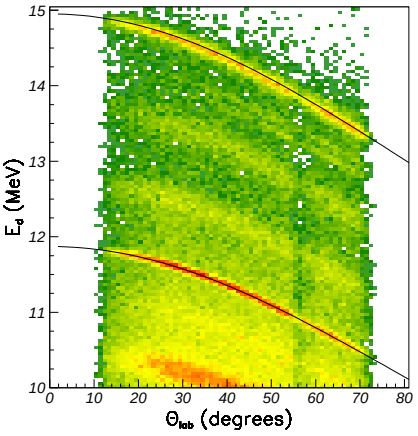

(c)

Figure 2.18: Proton energy vs θ from the ^{10}B target data with the kinematic curves ($E_b = E_p$) in Equation 2.6) corresponding to the Hoyle state (top line) and the 12.71 MeV state (bottom) superimposed. The effect of shifting the position of the detectors is shown for DSSSD1. (a) Effect of shifting the detector 5 mm away from 0 degrees while still keeping the detector perpendicular to the target. (b) Effect of moving the detector 5 mm closer to the target. Note the kinematical curves are stretched out with respect to the calculated lines. This effect, though subtle, can be seen on the edges of edges of the detector: at higher angles the experimental curves lie above the theoretical curves, whereas the lower angles the opposite effect is seen. (c) The geometry measurements included in the final analysis. Note that movement in the vertical direction does not effect the figures, though the position of the y-direction is easily determined from the hitmap in Fig. 2.11(a) since the Rutherford scattering is symmetric in the vertical direction.

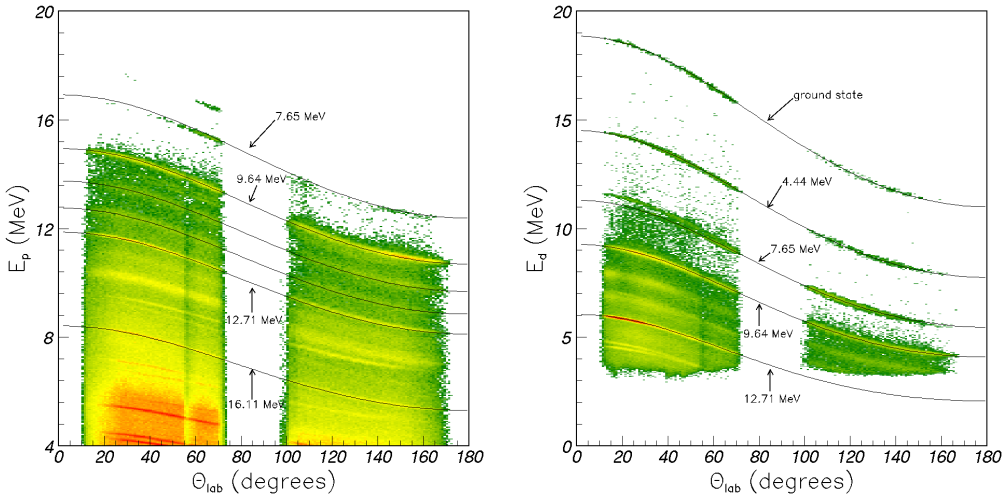

Figure 2.19: (a) Kinematic curves from the ^{3}He+^{10}B reaction with a gate on the protons and (b) kinematic curves from the ^{3}He+^{11}B reaction with a gate on the deuterons. Some calculated kinematic curves from the resonances in ^{12}C are shown superimposed on the figures. The overlap is very good, in part because some of these resonances were used to calibrate the PAD detectors, as discussed in Section 2.4.4. Note that there is less background contamination from different reaction channels in ^{11}B(^{3}He,d) as opposed to ^{10}B(^{3}He,p) . This is simply because there are less open channels with a deuteron as a final product.

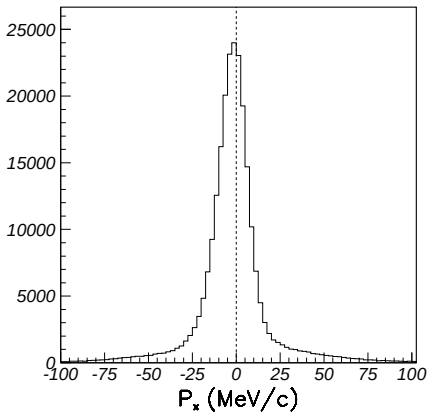

(a)

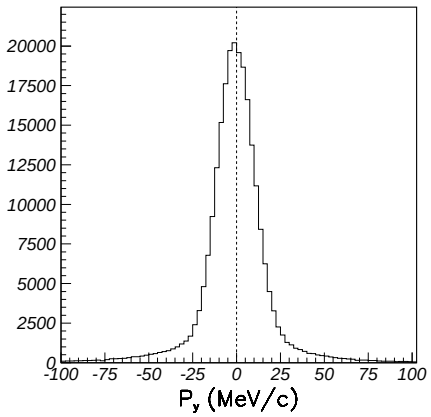

(b)

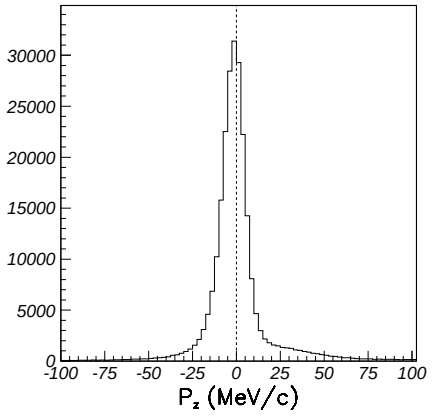

(c)

Figure 2.20: Different components of total momentum for the ^{11}B(^{3}He,d$\alpha\alpha\alpha$) reaction. The total momentum in each case should of course be zero, and the agreement is quite good.

adjustments to the position of the detectors. The peaks are centered near 0 MeV/c, with the largest deviation being ≈ 5 MeV/c, which would correspond to a deviation of ≈ 30 keV in the energy of a proton, within the energy resolution of the detectors. Once we have these established, we can begin to work on more sophisticated analysis techniques to extract the physics of interest in the different experimental reactions, which brings us to Chapter 3.

There's no sense in being precise when you don't even know what you're talking about.

John Von Neumann

3 Analysis Tools

In this chapter I summarize the different analysis techniques necessary to process the raw data. In the previous chapter I discussed preliminary steps which are necessary before analyzing the data, including the energy calibration of the detectors, noise removal, and the determination of the geometry of the experimental setup. This chapter is divided in such a way as to guide the reader through the different step involved in the analysis of this experiment. It is important to keep in mind that the final goal in this type of analysis is to extract results, and to do this we first need to determine several properties. We need to look at each event individually, and for each event we want to determine several properties, including the number of particles in that event, the identity of each particle (proton, deuteron, alpha, etc.), and the energy, momentum, and position of each particle. Finally we must perform simulations in order to take into account any discrimination introduced by the different conditions placed on the data. As the reader shall see, none of the steps involved in the analysis are trivial, and great care must be taken in order to maximize the number of good events in the data. Once we have identified these properties we can begin extracting physics results, discussed in following chapters.

3.1 Techniques

In section 2.4.3 I discussed the importance of imposing a condition on the data where the difference in energy between the front and back strips of a DSSSD be less than 70 keV. This helps reduce background and is an acceptable condition since the individual strips of the DSSSD detector are implanted on the same block of Si, so that they should in principle give equal energy signals. However, if we only take those events for which the difference in energy is less than 70 keV, we may be omitting good events. In fact if the total multiplicity is plotted as in Fig. 3.1, one can notice the large amount

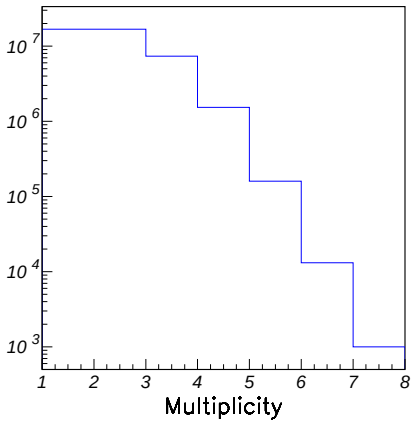

Figure 3.1: Total multiplicity for all detectors.

of events above the expected maximum of multiplicity four. This mainly occurs because there were multiple particles produced in the reaction, and we can get incidences of so-called "summing" and "sharing" events. These events would lie outside of the diagonal in Fig. 2.16 and thus would be removed by the preliminary condition discussed in Section 2.4.3.

To better understand what is meant by summing and sharing events see Fig. 3.2. Summing refers to when two particles hit the same strip on one side and different strips on the other side, so that the energies of the particles are summed together on one side but give individual signals on the other. For example, imagine two alpha particles hitting strip number 3 on the front side, and then one hits strip number 2 on the back strip, while the other hits strip number 4 on the back. Therefore, the energy seen by strip 2 and 4 on the back side would give the correct values for each alpha particle, while the energy seen on the front strip would be the sum of the both alpha particles' energies. To accept these events, conditions were placed so that in cases where, for example, there is one more particle detected in the back strips than in the front strips, if the sum of the energies in the back strips was similar to that of the front strip, then all of the particles were accepted as a multiplicity two event in that detector. Sharing refers to events where a single particle can hit the inter-strip spacing and share its energy between two strips. To recover these events, similar conditions are placed as in the case of summing events, except that when there are adjacent strips, the event multiplicity for that detector is one. In both cases, the allowed energy difference for the energy matching is more relaxed than the 70 keV mentioned

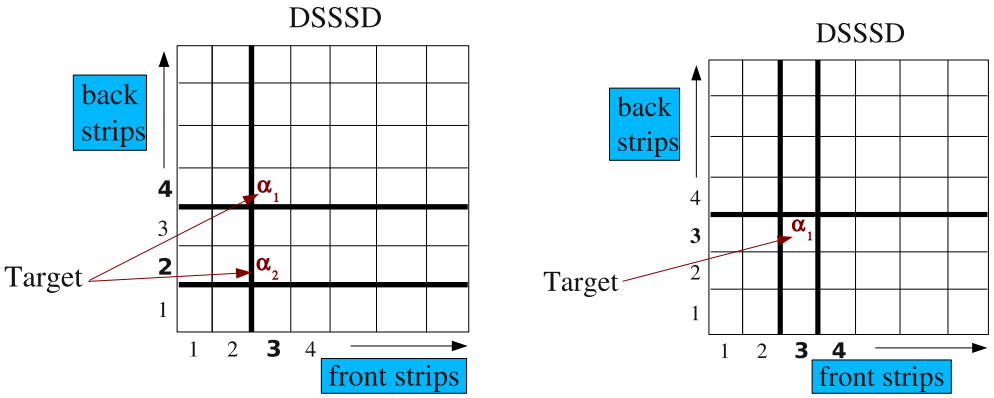

(a) Summing event (b) Sharing event

Figure 3.2: (a) An example of a typical summing event which occurs in a DSSSD. Here two alpha particles hit the same front strip yet two different back strips, so that only strip 3 on the front and strips 2 and 4 on the back have a signal. This is a valid event with multiplicity two if the sum of the energy of the two back strips 2 and 4 equals that of front strip 3. (b) An example of a sharing event which occurs when a particle hits in between two strips and deposits energy in both strips. This event is valid with multiplicity one if the sum of the energy of front strips 3 and 4 equal that of back strip 3. These events are taken into account in the analysis so as to maximize the statistics.

above and was set to 150 keV.

The statistics recovered using these algorithms is quite substantial and can be double-checked with estimates. In the case of sharing events, we recover roughly 5% more events, which is similar to the 6% of sharing events expected from the ratio between an inter-strip spacing of 0.1 mm and a strip width of 3 mm for each detector face. For summing events, we recover about 8% of the total events for the forward facing 16×16 DSSSD. If we assume an equal probability of hitting all the pixels, the probability of summing events where two particles would hit the same back strip or front strip is $\frac{2(n-3)}{n^2-1} \approx 10\%$, where n is the number of strips (n-3 instead of n-1 because summing between neighboring strips is assumed to be a sharing event).

3.1.1 Particle identification

To identify charged particles (alphas, protons, deuterons, etc.) the DSSSD energy signal combined with the possible energy signal in the corresponding PADs gives the total energy of an incident particle. The DSSSDs are thick enough to stop most alpha particles yet thin enough to let protons and deuterons pass so that these lighter ions can easily be differentiated from the higher Z alpha particles when hitting the same DSSSD. In fact the thin character of the DSSSDs (only $\approx 60\mu$m) makes it difficult to detect high energy protons and deuterons since they deposit such little energy in the DSSSD, and may fall below the threshold set just above the noise. Figure 3.3 shows a ΔE-E plot (mass plot) in which the energy loss in the ΔE detector is plotted versus the energy deposited in the E detector. Since the stopping power of a particle in a material is a function of the mass of the incident particle the different particles will show up in different bands, making it easy to distinguish between protons, deuterons, alphas, etc. In this work I use the ΔE vs E convention, as opposed to the ΔE vs E+ΔE plots which are common. The difference is that instead of same-mass particles showing up as straight lines, the particles will have a banana shape.

Figure 3.3 is taken from the ^{11}B(^{3}He,d$\alpha\alpha\alpha$) reaction, and in order to correct for the difference in energy loss as a result of the angle of entry of the particles through the DSSSD, a first-order correction was performed with

$$\Delta E' = \Delta E cos\vartheta \tag{3.1a}$$

$$E' = E + (1 - cos\vartheta)\Delta E, \tag{3.1b}$$

where ΔE is the energy deposited in the DSSSD, E is the total energy, and ϑ is the angle at which the particle enters into the detector [Jep04].

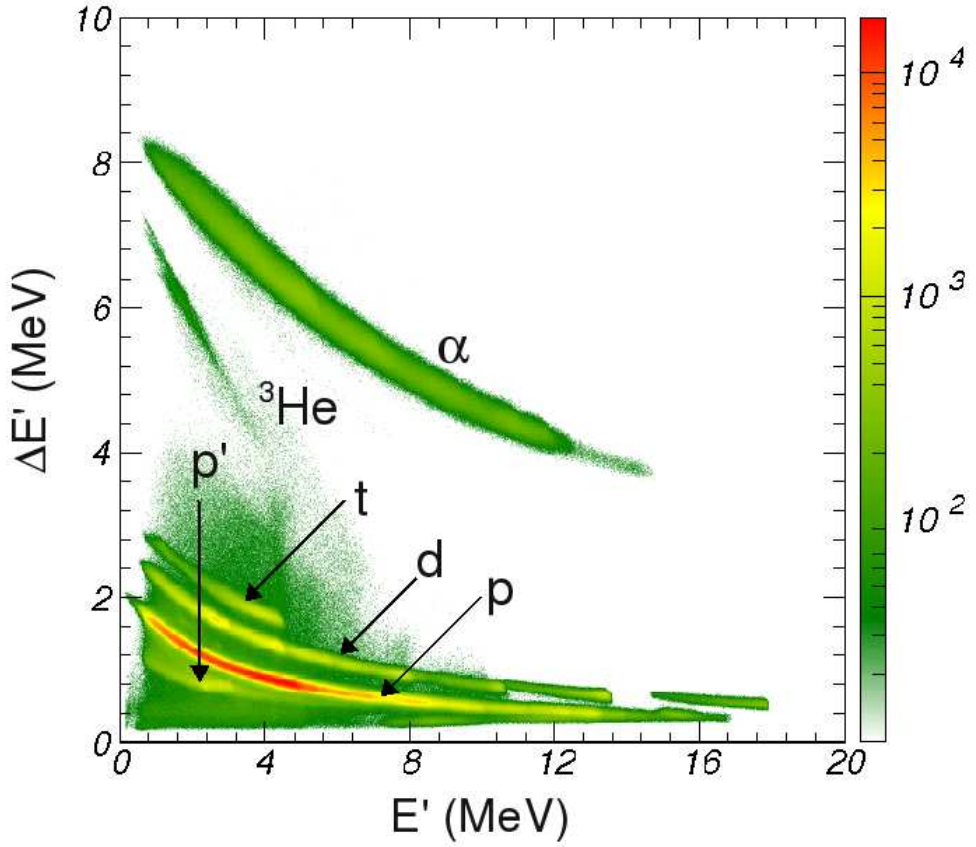

Figure 3.3: ΔE-E$_{back}$ scatter plot from the ^{11}B(^{3}He,d$\alpha\alpha\alpha$) reaction at 8.9 MeV, showing the presence of protons, deuterons, tritons, and alpha particles in the reaction. Also indicated in the figure is a small amount of scattered beam seen as a straight line corresponding to constant total energy. Most of the intensity seen outside of the identified charged particles are lower energy alpha particles (stopped in the DSSSD) in coincidence with protons or deuterons which do penetrate the DSSSD. There is a small area of intensity seen underneath the low intensity proton line (p') which is a result of particles which have lost some of their energy due to edge effects as they are seen in the border of the detector. Additionally, one can see the punch-through effect where high energy protons go through the back detector and begin to extend towards decreasing energy.

The protons were identified through these plots as well as some high-energy alpha particles, since an alpha particle of lower energy does not reach the back detector. Recall that an alpha particle will deposit about 10 MeV in the DSSSDs (60 μm thick) used for this experiment, so that only alpha particles with energies higher than 10 MeV can be identified using this technique. It is important to keep in mind that the alpha particles which are identified in Fig. 3.3 do NOT come from the break-up of $^{12}C^*$. These have too high energy, and they were identified to be coming from a different reaction channel; they are produced in the $^9B^* + \alpha$ channel, and correspond to alpha particles which lead to the ground state in ^9B. Something curious can also be seen in these two plots. Looking closely at the proton line, at about 16 MeV it extends back towards lower energies below the original proton line. This is due to the protons "punching-through" the back detector. The back detectors will only stop protons with an energy of approximately 15 MeV. If ^{12}C is left in its ground state, the proton emerging from the reaction will have an energy of approximately 22 MeV, meaning the proton will not be stopped in the first back detector. Therefore these high-energy protons will leave less energy than they should in these plots and they create this "punch-through" effect.

Note that any particle stopped in the DSSSD in coincidence with a particle with sufficient energy to penetrate the DSSSD will also show up in these plots. Due to the high multiplicity events there can be several particles hitting the same DSSSD which can make it difficult to match the PAD energy with the correct DSSSD energy. That is, the pad energy may be matched with one DSSSD energy to yield a proton, while yielding an deuteron when matched to another DSSSD energy. The result is that there may be a deuteron and a proton inside the gates placed on the ΔE-E plot, or even cases with two deuterons or two protons. Obviously this is due to an alpha particle in coincidence with a proton or deuteron which happens to deposit an energy in the DSSSD which makes it fall in the proton or deuteron gate. Fortunately we can later determine in the analysis the correct identity for each particle by implementing strict cuts using momentum and energy conservation, made possible by the complete kinematic information obtained in this experiment. Although these conditions were discussed in Section 2.1, essentially the procedure for correctly identifying particles in this case is explained below.

Consider the case of a multiplicity four event, where two of the particles impinge on one DSSSD and energy is detected in the PAD detector behind this DSSSD. Assume that the two particles deposit similar energies in the DSSSD, so that they both are inside the deuteron gate. Given that the other two particles are alpha particles, we know that one of these then must be an alpha and the other must be a deuteron. Therefore we temporarily

assign an ID to each of the two particles, and then run momentum and energy conservation checks on the four particles (after including deadlayer loss effects which are dependent on the particle identification). If the conditions are not met, then we go back and choose the other possibility for particle identity and again run the conservation checks. When one combination passes the checks then it is assumed to be a valid four particle coincidence event. This is a somewhat time-consuming process to code, but it significantly helps in recovering events with low alpha particle energies.

Only after the particle has been correctly identified can the energy loss contributions from deadlayers in the detectors be taken into account. Low energy protons or deuterons which do not have sufficient energy to penetrate the DSSSD can also be identified in multiplicity four events. Since, depending on the reaction, we must have three alpha particles and one proton or deuteron, energy and momentum conservation can be applied to each possible particle identity to correctly separate the alpha particles from the proton or deuteron.

3.1.2 Energy reconstruction

Now that we have properly identified the particles we can begin to determine their correct energy. Recall in Section 2.3.3 that the Si detectors used had deadlayers which are inactive yet nevertheless the particles will lose energy when they go through them. This means that the energy we measure in the detector is not the original energy of the particle. Figure 3.4 shows an example of the different inactive regions in which the particle will lose energy. In the figure, the signals from the active part of the detector is just E and ΔE. This gives the energy of active area of the PAD detector and the DSSSD, respectively. The actual energy of the particle must take into account all of the energy losses, so that we have E_{tot} =E+ΔE+E_{dl1}+E_{dl2}+E_{dl3}+E_t, following the naming scheme in the figure. In order to calculate the energy which was lost in each of the unknowns, the reconstruction must be done in reverse order. For example, assume a deuteron deposits energy in both a DSSSD and a PAD detector, so that we have a signal for both E and ΔE. We know the thickness of the non-active layers in the different detectors and we know the angle of entry ϑ from the strips of the DSSSD, so that we can calculate the actual thickness of the inactive layer. Since we know the thickness and the energy of the particle after leaving the inactive region, we can use SRIM tables of stopping powers in Si [Zie03] to determine the energy of the particle before passing through the deadlayer. In other words, since we know E, we can calculate E_{dl3}. We can then calculate E_{dl2}, and this energy added to ΔE lets us calculate E_{dl1}. Finally the sum of these energies can be

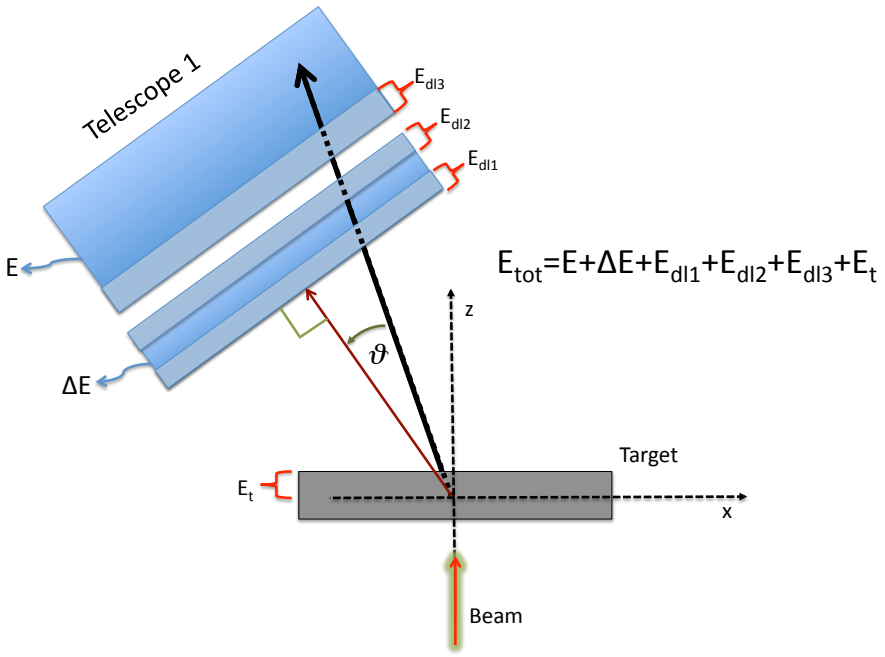

Figure 3.4: Illustration of the different regions where energy losses must be taken into account. The energy detected in the DSSSD (ΔE) and the E detector (E) does not give the total energy of the incoming particle. To obtain the total energy, the energy loss in the different inactive areas must be added. This includes the energy loss which occurs in the target, E_t, as well as the energy loss from the deadlayers of the Si detectors. The angle of entry (ϑ) is used to calculate the effective thickness of the different deadlayers. Once we have the energy of the outgoing particle and the identity, we can calculate the energy lost in a material by using tables of stopping powers from [Zie03].

used to calculate the loss of energy in the target, E_t, which gives us the total energy of the particle. Note the identity of the particle (Z and A) must be known before performing the energy reconstruction since the stopping power of ions in matter depends on charge.

Besides the differences in energy loss for protons and alphas in the dead-layers, an additional correction was made to the energies of the protons and deuterons to take into account the different values of ε, the mean energy required to create an electron-hole pair in Silicon. Since ε is only dependent on Z and since the detectors were calibrated with alpha particle source, the value used for this correction of the pulse height defect was $\varepsilon_\alpha/\varepsilon_p = \varepsilon_\alpha/\varepsilon_d = 0.988$[Len86, Sch93].

3.1.3 Time gates

The event multiplicity for both the ^{11}B(^{3}He,d$\alpha\alpha\alpha$) and ^{10}B(^{3}He, p$\alpha\alpha\alpha$) reactions is a maximum of four. However in Fig. 3.1 it is clear that there are multiplicity events of five or greater. It would be interesting to understand where these higher multiplicity are coming from, and also if there is a possible way to reduce the number of such events. We have already implemented front-back energy matching on the DSSSDs, yet this technique will not reduce random coincidences in the data. By random coincidences we refer to cases in which particles from different reactions are detected in the same time window and are therefore recorded as part of the same event. This is unavoidable since statistically there will always be some mixing of events, and is especially the case for those channels with very high cross sections such as elastic scattering.

To reduce random coincidences the TDC signals obtained in the experiment were used. Recall that the ADC acceptance window was 2.5 μs, which is a relatively large time window. In fact the time resolution of the detectors was about 20 times better than this (FWHM of 100 ns for the DSSSDs and 70 ns for the PAD detectors). Therefore the TDC time window can be fixed to 100 ns, which should significantly reduce the amount of random coincidences, leaving roughly $\frac{0.1\mu s}{2.5\mu s} \approx 4\%$ of them.

The time resolution of the TDC signal comes mainly from two factors. The first is due to the TDC signal coming from any of the particles, if the timing of each strip is not aligned with each other then this causes a widening of the time signal peak. One cause of this is the use of leading edge triggering (LE) instead of constant fraction triggering (CFT). As can be seen in Fig. 3.5, the problem with leading edge timing is that it introduces the problem of walk in the signal, which is dependent on the amplitude of the signal. This will inevitably give a certain minimum resolution which can be avoided if

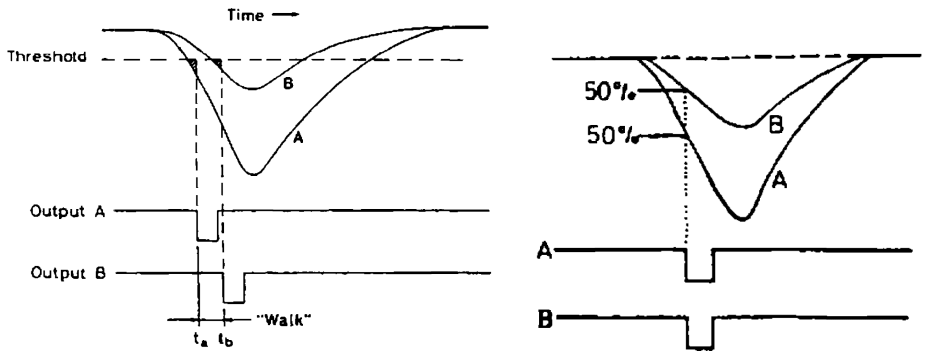

(a) (b)

Figure 3.5: (a) Leading edge timing. Note the introduction of the problem of walk, which inevitably leads to a worse resolution of the timing signal. (b) Constant fraction timing. In this case the problem of walk is virtually eliminated since instead of taking the timing logic value at after crossing a certain threshold, it records the value at a fraction of the signal, which makes it independent of the amplitude of the signal. Both figures are taken from [Leo87].

one is to use the constant fraction triggering method. The effect of this on the TDC logic signals is better seen in Fig. 3.6. Another factor which can widen the resolution of the timing signal is that the different particles will travel through different lengths of wire, depending on the strip of the signal. However this effect is small since the losses in the LEMO cables is only 10 ns/m.

The first step in implementing the time gates is to calibrate the TDC spectra. This is not an absolute calibration in the same sense as the energy calibration. The purpose of this calibration is to place all of the TDC peaks at a predefined position, in this case channel number 2000 (chosen arbitrarily). In order to calibrate the TDC spectra for both the DSSSDs and the back detectors, we need to ensure that the TDC signals are valid particles and not for example a random coincidence. To do this, we gated on protons (^{10}B target) or deuterons (^{11}B target) which left a signal in both a DSSSD and a back detector. We then plotted the resulting TDC spectra for each DSSSD channel as well as the PAD detector. There are of courses instances where the signal will not be the actual trigger and will instead be some random particle in coincidence, or perhaps a trigger on noise. However, the main peak we obtain are from the valid events. What we would then do is to place a gate around this TDC peak at channel 2000 with a width of roughly 100 ns which would be considered accepted events, and rejected particles which

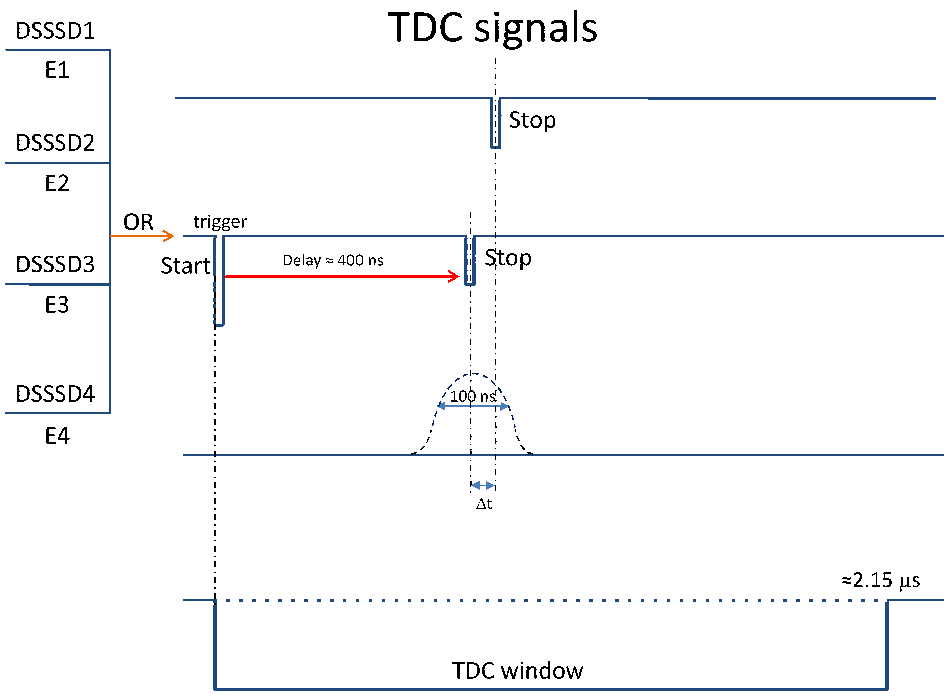

Figure 3.6: Figure demonstrating the cause of the 100 ns time resolution of the TDC signal. The difference Δt between the different timing logic values can arise from the problems of walk introduced by leading edge triggering, as seen in Fig. 3.5, or by differences in the cable length of the setup

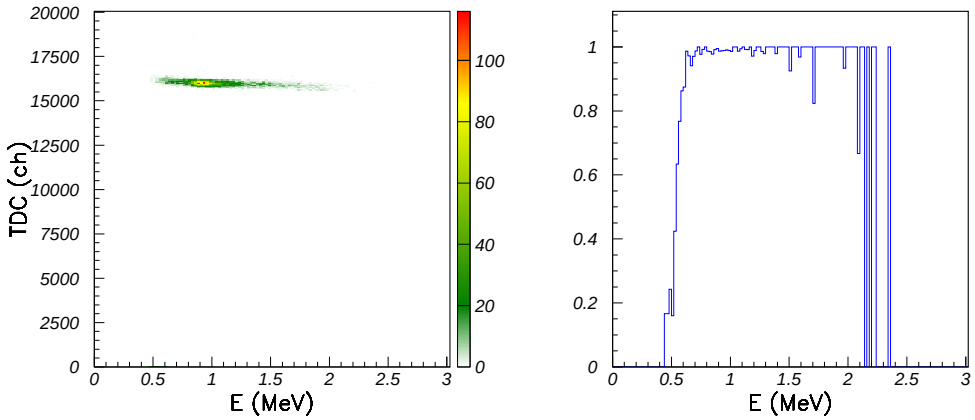

(a) (b)

Figure 3.7: (a) Plot of TDC channel number versus energy in MeV of DSSSD2 strip number 2. The plot is chosen for deuterons from the ^{11}B target of multiplicity one events only. (b) Efficiency of having a non-zero TDC signal in DSSSD2 strip number 2 versus the energy of the detected particle.

did not have a TDC signal within this window. Unfortunately this method of using the TDC signals to remove coincidences will not work for low energy particles, since particles which deposit less than roughly 700 keV fall below the trigger threshold, meaning they do not give a signal, even though they are seen in the ADC. This effect can be seen in Fig. 3.7(a). When this happens we do not impose any requirements on the TDC signal and such an event is accepted. To precisely determine the trigger threshold we plotted the efficiency for having a non-zero TDC signal for each individual channel. This is shown in Fig. 3.7(b). Note this was done individually for each channel in the experimental setup. In order to see the effect of the TDC gates on the total multiplicity of including these TDC requirements can be seen in Fig. 3.8. Though there are still events above multiplicity four, the amount of events with multiplicity larger than four has been greatly reduced with respect to before.

Estimates of random coincidences

Some estimates of expected random coincidences can be made and compared to the data as a consistency check. Let us look at the ^{10}B(^{3}He,p$\alpha\alpha\alpha$) reaction. We estimated the count rate in our detectors from Rutherford scattered ^{3}He^{+}

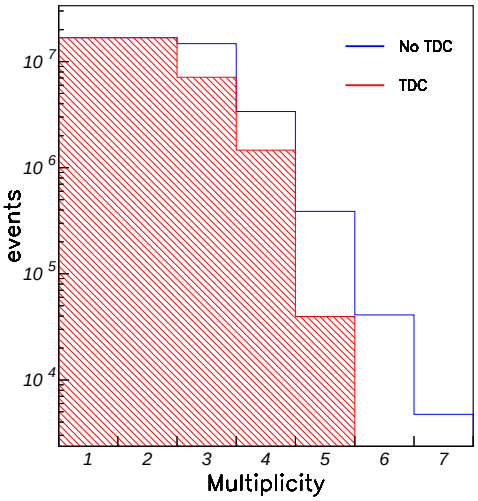

Figure 3.8: Total multiplicity for all detectors. In blue is the multiplicity spectrum without any time requirements as seen in Fig. 3.1. In red is the total multiplicity after implementing stricter time conditions using the TDC. It is inevitable for there to be random coincidences mixed in with the data, but the improvement seen by using the TDC is clear since we see a reduction of a factor 10 in multiplicities > 4.

ions to be $R = 2.3\times10^4$ s^{-1}, based on the beam current measured in the Faraday cup ($\approx 7.5 \times 10^9$ ions/s), target thickness, and Monte Carlo simulations (see Section 3.4) to account for geometric acceptance. The Rutherford count rate could not be directly measured because the forward-facing DSSSDs were not in trigger as described in Section 2.3.4. We observed $Y = 7.1 \times 10^5$ true $p+3\alpha$ coincidences during the ^{10}B experiment. By true coincidences we refer to those events which survive the energy and momentum requirements and the time conditions. With a TDC acceptance window of only 100 ns for the DSSSDs, and R the rate of beam particles impinging on the detectors, one would expect to see $Y \times 100$ ns $\times R = 1.6 \times 10^3$ random coincidence events in the data. The number of random coincidences between a real four-particle coincidence event and a scattered beam particle is determined by looking at the multiplicity five data and imposing momentum and energy requirements on four of the particles. 1.8×10^3 events that fit this description were identified, which is close to the number of total multiplicity five events in the data ($\approx \times10^4$ total multiplicity five events can be observed from Fig. 3.8).

Though Rutherford scattered beam is the major contributor to random coincidences, reaction-reaction coincidences can also contribute to the high multiplicity events. If we follow the method described above, we can look for

random coincidences such as $(p+3\alpha)+(p+3\alpha)$ where we detect two protons and six alphas. To calculate the expected number of such coincidences the rate of scattered beam incident on the detectors (R) is replaced with the rate at which true $p+3\alpha$ coincidences are observed. We took data for 17.6 hours and observed Y $p+3\alpha$ coincidences so the rate is $Y/17.6$ hours $= 11$ s^{-1}. The time window was reduced to a slightly narrower window on the back detectors of 70 ns. Now, the expected number of $(p+3\alpha)+(p+3\alpha)$ coincidences is $Y \times 70\text{ns} \times 11$ s$^{-1} = 0.5$, and we identify 0 in the data. Following the same line of reasoning the expected number of $(p+3\alpha)+(p+2\alpha)$ coincidences would be $2.3 \times 10^6 \times 70\text{ns} \times 11$ s$^{-1} = 1.8$, in reasonable agreement with the 3 such events that is observed in the data.

This random coincidence identification technique can be used to extract true particle coincidences from higher multiplicity events. If there are events with a higher multiplicity than four due to beam-reaction or reaction-reaction coincidences we combine the different particles and match momentum and energy to extract the true four particle coincidences, thereby increasing our multiplicity four event sample. For example, in the case of Rutherford scattered beam in coincidence with four particles, the total sample is increased by about 1%.

3.2 Energy and momentum

The identity and energy of each particle per event is now determined. All that is left is to determine the components of momentum for each particle, which can obtained from the position given by the pixels in the DSSSDs. Once we have the momenta of the particles one can easily switch between different reference frames which will be necessary to determine properties of ^{12}C and its decay products. At this step the light ion in the reaction (either the proton or deuteron depending on if the ^{10}B or ^{11}B target was used) and alpha particles in coincidence have been identified. The light ion will give us information on the ^{12}C nucleus (the resonance energies, widths, etc.), but we first need to convert this energy into a ^{12}C excitation spectrum. In this section the ^{12}C excitation spectrum is computed first, and then the alpha particle energies are converted from the laboratory frame to the ^{12}C center of mass frame. For the sake of simplicity I will be using the ^{10}B+^{3}He reaction to describe the different methods.

3.2.1 3α + p

Calculating the excitation spectrum of ^{12}C was done by selecting the protons in the ΔE-E plots and converting the proton energy into excitation energy in ^{12}C. The DSSSDs provide us with information on the energy as well as the position (x,y,z) of the particles (see Fig. 2.10), so that we can extract the components of momentum in the laboratory frame for each particle (non-relativistic):

$$\begin{aligned} P &= (P_{\mathrm{x}}, P_{\mathrm{y}}, P_{\mathrm{z}}) \\ |P| &= \sqrt{2 \cdot m \cdot E} \\ P_{\mathrm{x}} &= x \cdot |P|/r \\ P_{\mathrm{y}} &= y \cdot |P|/r \\ P_{\mathrm{z}} &= z \cdot |P|/r \end{aligned}$$

where $\vec{r} = \sqrt{x^2 + y^2 + z^2}$, the mass m is in MeV/c^2, the energy E is in MeV, and the momentum P is in MeV/c. Once we have transformed the energy of the particles into momentum, we then proceed to calculate the energy of each particle in the total center of mass frame. To do this we only need to take into account the contribution from the beam, and since the beam is in the z-direction, we can easily do the transformation:

$$\begin{aligned} P_{\mathrm{x}}^{\mathrm{cm}} &= P_{\mathrm{x}} \\ P_{\mathrm{y}}^{\mathrm{cm}} &= P_{\mathrm{y}} \\ P_{\mathrm{z}}^{\mathrm{cm}} &= P_{\mathrm{z}} - P_{\mathrm{beam}} \cdot \left(\frac{m_x}{m_{\mathrm{target}} + m_{\mathrm{beam}}} \right) \\ |P^{\mathrm{cm}}| &= \sqrt{P_{\mathrm{x}}^{\mathrm{cm}} + P_{\mathrm{y}}^{\mathrm{cm}} + P_{\mathrm{z}}^{\mathrm{cm}}} \\ E^{\mathrm{cm}} &= \frac{|P^{\mathrm{cm}}|^2}{2 \cdot m_x} \end{aligned}$$

where m_x is the mass of the particle (either proton,deuteron, or alpha particle).

The excitation energy in ^{12}C, E$_x$, is calculated from the energy of the proton or the deuteron in the center of mass frame $E_{\mathrm{p}}^{\mathrm{cm}}$, depending on if the target is ^{10}B or ^{11}B, respectively:

$$E_x = E_{\rm beam}\left(\frac{m_{\rm target}}{m_{\rm target}+m_{\rm beam}}\right) + Q - E_{\rm p}^{\rm cm}\left(\frac{m_{\rm p}+m_{^{12}{\rm C}}}{m_{^{12}{\rm C}}}\right) \qquad (3.2)$$
$$Q = (m_{\rm beam} + m_{\rm target} - m_{\rm p} - m_{^{12}{\rm C}})$$

where Q is the Q-value of the reaction. With Eq. 3.2, one can now plot the excitation energy of ^{12}C obtained in the experiment. (Note also that we can calculate the excitation energy of ^{9}B in the same way as above, by replacing the proton energies and mass values for those of alpha particles.) Figure 3.9 shows the ^{12}C spectrum obtained in the experiment with no requirements on multiplicity, i.e. the spectrum contains events with one proton, with anywhere from none to three alpha particles in coincidence. The level scheme of ^{12}C is plotted to the left of the figure in order to better identify the different states populated in the reaction. There are a few unidentified peaks in this spectrum which are due to the many reaction channels involving a proton. Most of the background will be removed when we impose different multiplicities.

Once the ^{12}C excitation spectrum has been correctly calculated and the corresponding peaks to different resonances identified, we can follow the break-up of the resonances by placing conditions in the events of different multiplicities. In order to study the break-up into three α particles, we look at events in which a proton was detected in coincidence with at least one other (α) particle. In comparison to Fig. 3.9, which is done without any conditions on α coincidences, Fig. 3.10 shows the effect of placing these conditions. Note, for example, that the 15.11 MeV state virtually disappears when a multiplicity of two or more is required for each event (multiplicity two refers to one proton and one α particle, so that the maximum multiplicity would be of 4, with one proton and 3 α particles in coincidence). This is because the 15.11 MeV has isospin 1 and has a very small alpha branch and decays primarily through γ-decay, as discussed in detail in Chapter 4.

The next step is to focus our attention on the alpha particles which come from the breakup of ^{12}C. Whereas in the case of the proton the conversion is done to the total center of mass reference frame, in the case of the alpha particles the conversion must be made to the center of mass frame of the ^{12}C nucleus in order to learn about the decay mechanism and other important properties of ^{12}C. The transformation is again done using the equations described above. It can be seen in Fig. 3.10 that the four particle coincidence data has the least background. This is why we focused mainly on these four particle coincidence data to study the ^{12}C nucleus and its breakup. In fact the data can be further cleaned by imposing some strict requirements on the data.

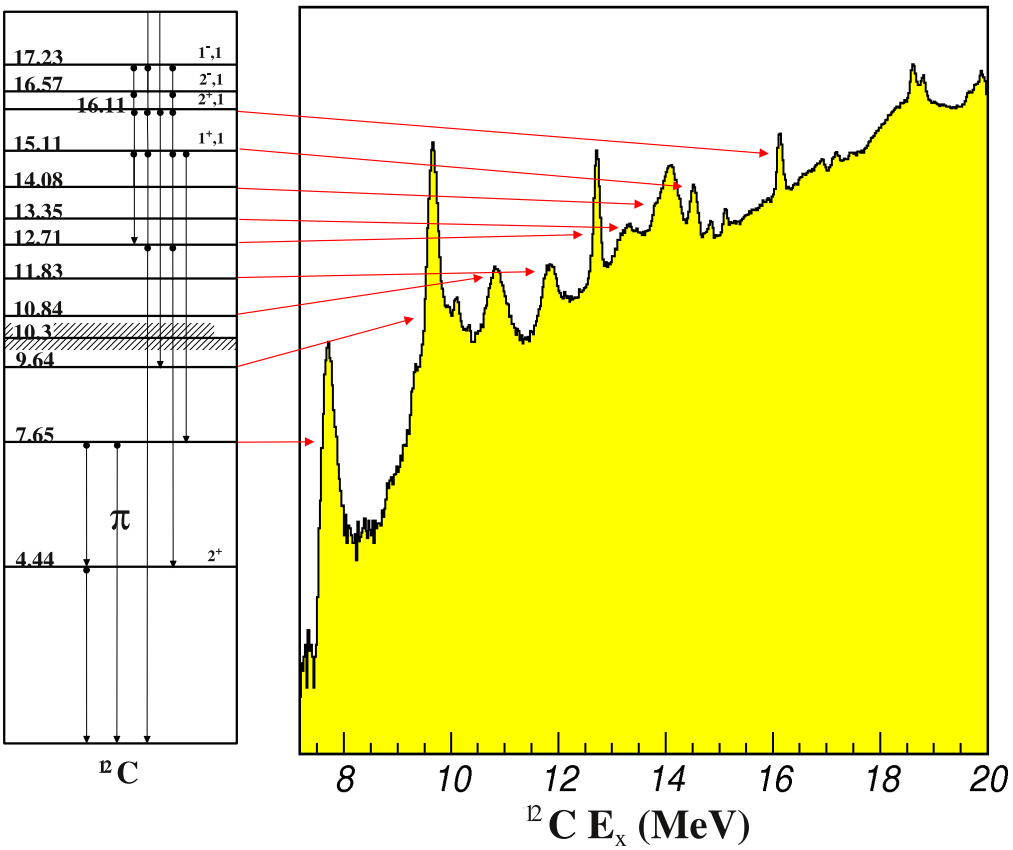

Figure 3.9: Energy (in MeV) of ^{12}C with no conditions on multiplicity. The level scheme [Ajz90] is pictured to the left to identify the different states populated in this reaction. Note the presence of a few more peaks in the spectrum. These peaks correspond to background channels populated in the same reaction (Table 2.1).

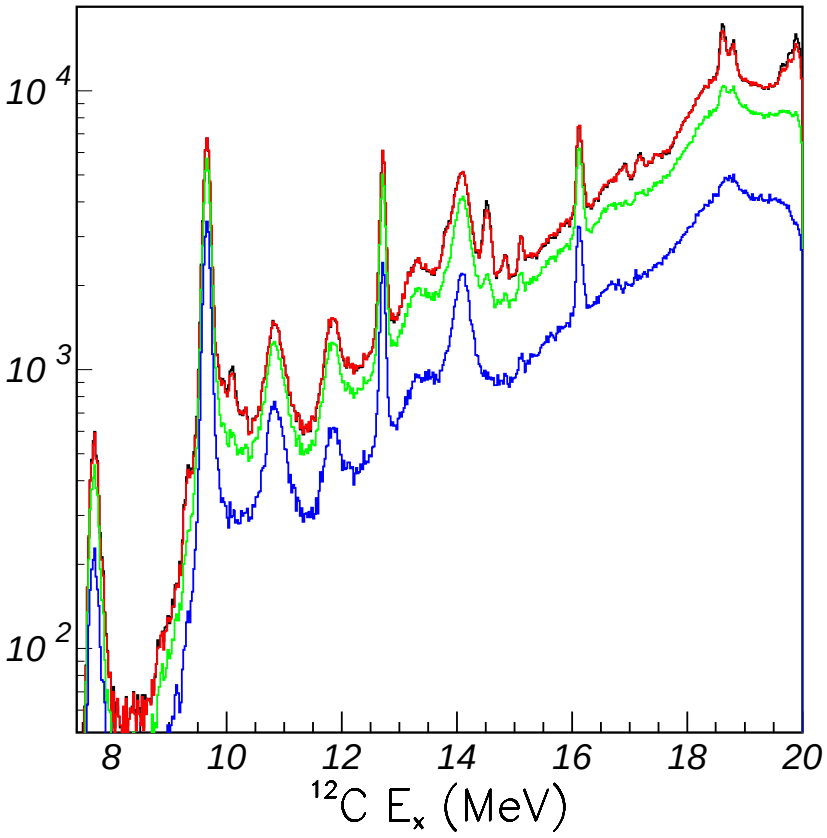

Figure 3.10: Energy (in MeV) of ^{12}C with different multiplicities. The black line is with at least the proton detected (maximum statistics), red is with one proton and one alpha particle, green is with one proton and 2 alphas, while blue is 1 proton and all three alphas. The multiplicity one (black) and two (red) have virtually the same statistics, so that the black line is mostly covered by red. Note how the background peaks mentioned in 3.9 disappear when alpha particles are chosen in coincidence with the proton. Notice also that the 15.11 MeV state, the lowest state of higher isospin (T=1), in ^{12}C also disappears. This is because the 15.11 MeV state decays mainly by γ de-excitation.

3.2.2 Full kinematics

Various techniques to ensure the data is as clean, leaving only the ^{12}C channel, have been outlined. Each step has decreased the total amount of data, yet has greatly increased the purity of the data set. The final step for removing all unwanted data and random coincidences is done by taking advantage of the detection in full kinematics. It is clear that the multiplicity three data can be used to reconstruct the fourth particle, but this always adds some uncertainty. Due to the efficiency of the experimental setup enough four-particle coincidence events were detected that it is possible to restrict the analysis to the four particle events, ensuring a very clean spectra. However there are some cases in which the multiplicity three data (one light-ion and two alphas) served as a comparison to the multiplicity four data. In such cases the energy of the third alpha particle is reconstructed using both energy and momentum conservation, two independent methods which reduce the error in the reconstruction.

The final step in removing random coincidences is by placing gates on both energy and momentum conservation, something possible only with complete kinematics information. This is done by summing the total momentum and total energy in the reaction. The momentum is given by

$$P_{\mathrm{x}}^{\mathrm{tot}} = P_{\mathrm{x}}(p) + P_{\mathrm{x}}(\alpha_1) + P_{\mathrm{x}}(\alpha_2) + P_{\mathrm{x}}(\alpha_3) \tag{3.3}$$

$$P_{\mathrm{y}}^{\mathrm{tot}} = P_{\mathrm{y}}(p) + P_{\mathrm{y}}(\alpha_1) + P_{\mathrm{y}}(\alpha_2) + P_{\mathrm{y}}(\alpha_3) \tag{3.4}$$

$$P_{\mathrm{z}}^{\mathrm{tot}} = P_{\mathrm{z}}(p) + P_{\mathrm{z}}(\alpha_1) + P_{\mathrm{z}}(\alpha_2) + P_{\mathrm{z}}(\alpha_3) - P_{\mathrm{beam}} \tag{3.5}$$

$$|P^{\mathrm{tot}}| = \sqrt{P_{\mathrm{x}}^{\mathrm{tot}} + P_{\mathrm{y}}^{\mathrm{tot}} + P_{\mathrm{z}}^{\mathrm{tot}}} \tag{3.6}$$

and the energy by

$$E_{\mathrm{tot}}^{\mathrm{lab}} = E^{\mathrm{lab}}(p) + E^{\mathrm{lab}}(\alpha_1) + E^{\mathrm{lab}}(\alpha_2) + E^{\mathrm{lab}}(\alpha_3) - E^{\mathrm{lab}}(^3He) - (\mathrm{m}_{^3He} + \mathrm{m}_{^{10}B} - \mathrm{m}_p - 3\mathrm{m}_\alpha)$$

These can be plotted against each other as shown in Fig. 3.11. In this figure it is obvious that although this greatly reduce random coincidences, time gates alone will not suffice. There is still some unwanted reaction channels coming through. Making a narrow gate on energies between -1 MeV and 1 MeV greatly reduces this number and ensures virtually background-free data. While both of these techniques greatly reduce random coincidences, the selectivity of these conditions are independent. Time conditions in the TDC will remove most random coincidences, especially coincidence with scattered

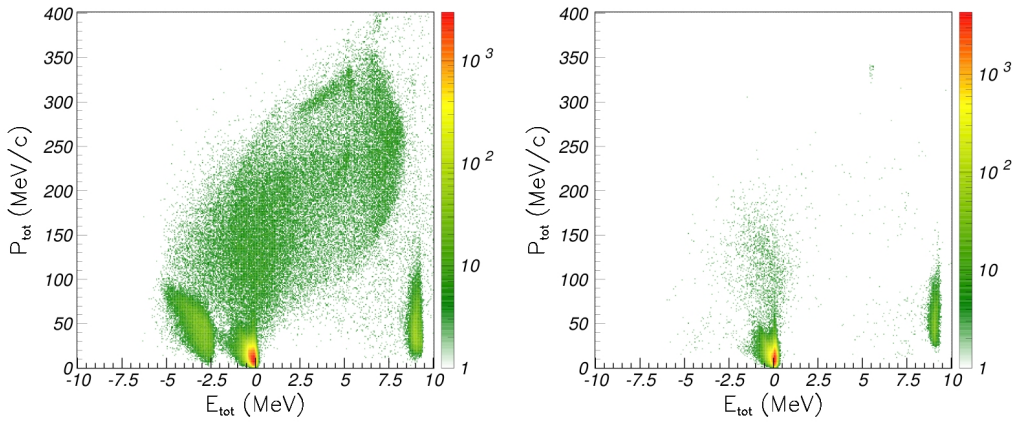

(a) No TDC cuts

(b) With TDC cuts

Figure 3.11: Figure of total momentum $\sum_i \mathrm{P}_i - \mathrm{P}^{beam}$ in the ^{11}B target data set versus $\mathrm{E}^{tot}_{lab} - \mathrm{E}^{beam}$ for four particle coincidence events with and without time conditions in place. It is clear that the TDC cuts greatly reduce the number of random coincidences, yet there are still some left over. However, by gating on energies between -1 MeV and 1 MeV, and on total momenta less than 50 MeV/c, the number of random coincidences present in the data is strongly reduced. In (a), the region of events at E_{tot}=-2.5 MeV with $P_{tot} < 100$ MeV/c is due to incorrectly identifying a proton as a deuteron. Following the method outlined in Section 3.1.1, these events have been removed in (b). There is still an area of intensity in (b) with $P_{tot} < 100$ and E_{tot}=9 MeV. This region of intensity includes multiplicity four data from the ^{11}B(^{3}He,p$\alpha\alpha\alpha$)n reaction where a proton has been incorrectly identified as a deuteron and the neutron has not been detected.

beam. These events could still pass the energy-momentum requirements if we have a true three-coincidence event together with a scattered beam particle. Conversely, as mentioned earlier in Section 3.1.3, though 100 ns is a fairly short time condition, it is inevitable that random coincidences will enter this window. To fully remove these coincidences in the data one must introduce both types of conditions.

Figure 3.12 demonstrates the effects of energy and momentum conservation gates compared to time gates on the data from the ^{10}B(^{3}He,p$\alpha\alpha\alpha$) reaction with event multiplicity four. This figure shows that though time conditions greatly reduce random coincidences, conservation of energy and momentum requirements are needed to fully remove random coincidences. Full removal of contribution from channels with the same multi-particle final states is not possible, but it is possible to gain some insight on their contribution to the overall spectra, as discussed in the following section.

3.3 Separating reaction channels

When dealing with high Q-value reactions there are many open channels leading to the same final state, posing a challenge when extracting results from the analysis. Separating the different open channels is difficult and cannot be done completely, but certain steps can be taken to obtain an acceptable result. The open channels for the ^{3}He + ^{10}B reaction at a beam energy of 4.9 MeV are listed below. Note that they all involve the same final state particles p$\alpha\alpha\alpha$:

$$
\begin{array}{ccc}
\text{Reaction} & \text{Open Channels} & \text{Final State} \\
{}^{10}\mathrm{B} + {}^{3}\mathrm{He} \rightarrow \left\{ \begin{array}{c} p + {}^{12}\mathrm{C}^{*} \rightarrow p + \alpha + {}^{8}\mathrm{Be} \\ \alpha + {}^{9}\mathrm{B}^{*} \rightarrow \alpha + p + {}^{8}\mathrm{Be} \\ \alpha + {}^{9}\mathrm{B}^{*} \rightarrow \alpha + \alpha + {}^{5}\mathrm{Li} \\ {}^{8}\mathrm{Be}^{*} + {}^{5}\mathrm{Li}^{*} \rightarrow {}^{8}\mathrm{Be} + p + \alpha \end{array} \right\} & \rightarrow p + 3\alpha
\end{array}
$$

In the ^{10}B(^{3}He,p$\alpha\alpha\alpha$) reaction, we would expect the p+^{12}C and α+^{9}B channels to be clearly seen in a plot of the proton versus alpha particle CM energies, as illustrated in Fig. 3.13, showing up as horizontal or vertical lines, respectively. The ^{5}Li+^{8}Be channel appears as a diagonal line. If the data in Fig. 3.13 is projected on the E_p axis, then the proton peaks can be seen to correspond to resonances in ^{12}C. If the data is projected onto the E_{α_i} axis, then the peaks from the alphas can be seen to correspond to states in ^{9}B.

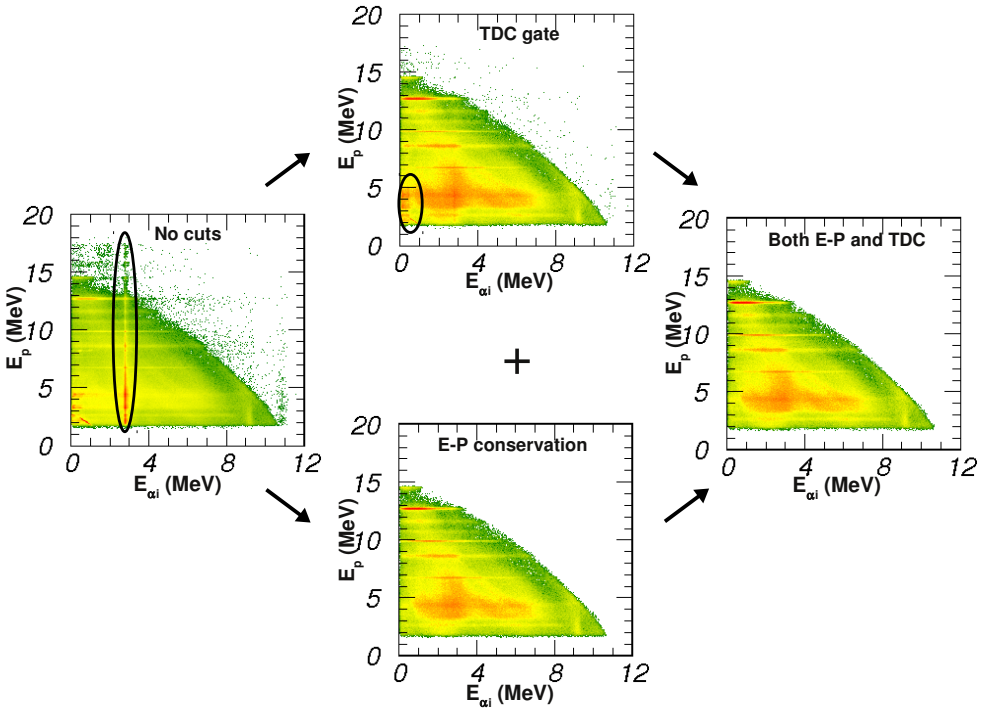

Figure 3.12: Different cuts imposed on the ^{10}B(^{3}He,p$\alpha\alpha\alpha$) multiplicity four events. The spectra of E_{α_i} versus E_p in CM are shown. On the left no conditions have been imposed on the four particle coincidence data. The circled region corresponds to randoms in coincidence with the scattered beam. In the middle, the top figure has only time conditions imposed (TDC gate), while in the bottom figure only conditions on conservation of energy and momentum have been imposed (E-P conservation). Note that in the top figure, although there is a reduction in randoms in coincidence with the beam, low energy random coincidences are still present, indicated in the circled region. On the bottom figure the energy and momentum requirements greatly reduces all random coincidences. Finally, the figure to the right is after imposing both time and energy and moment requirements. Recall that although this figure appears to be virtually indistinguishable from the one to its bottom left, the advantage of using a time condition with the energy and moment conservation requirement is that we recover more multiplicity four events, as discussed in the text.

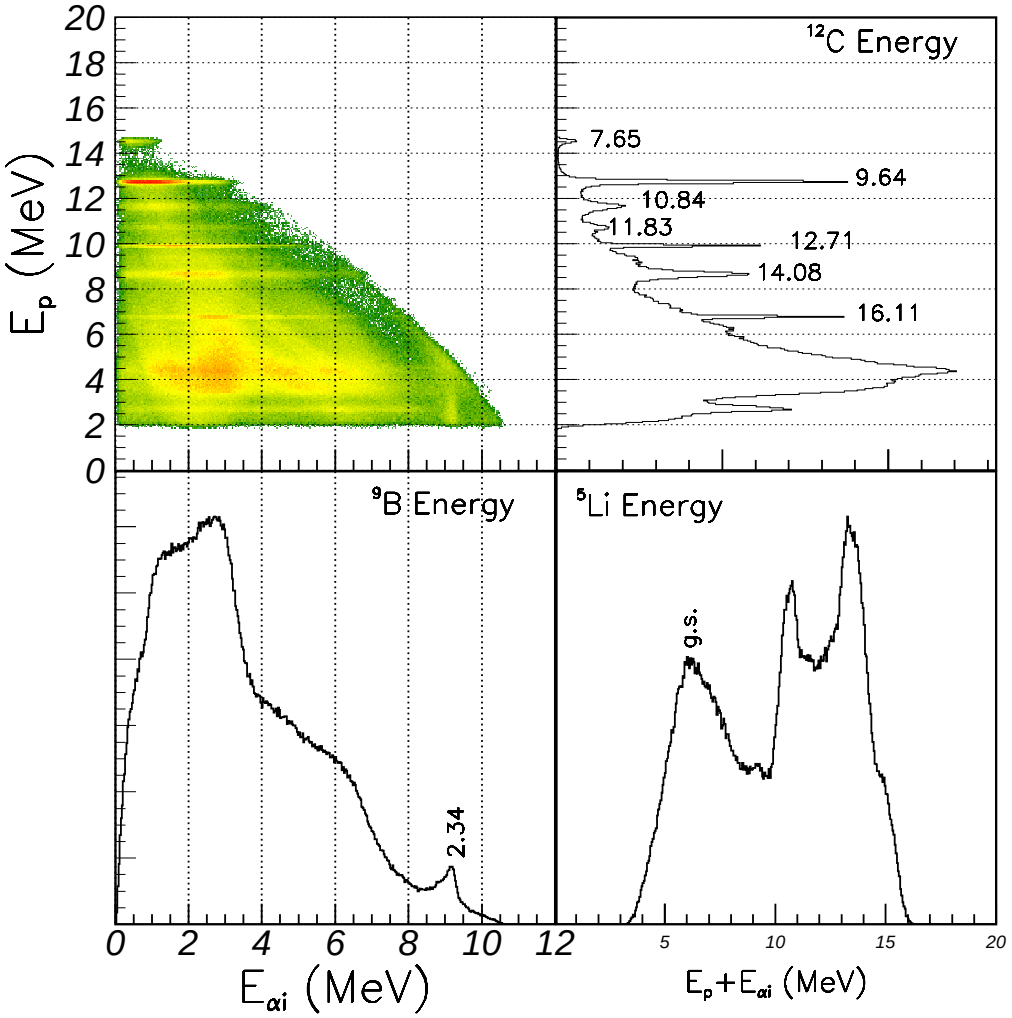

Figure 3.13: Spectra of E_{α_i} versus E_p in CM for the ^{10}B(^{3}He,p$\alpha\alpha\alpha$) multiplicity four reaction data. The projections onto different axes are shown, corresponding to ^{12}C (y-axis) and ^{9}B energy (x-axis). The bottom right corner shows the diagonal projection of the figure, i.e. E_{α_i} + E_p. The ground state in ^{5}Li can be seen though the other two peaks are from background channels.

Similarly, projecting the diagonal of the plot (E_p+ E_{α_i}) shows states which correspond resonances in ^{5}Li.

Figure 3.13 clearly illustrates the fact that the complete removal of intruding reaction channels is not possible. Removing contributions from other channels will always result in a discrimination against certain allowed energies of the reaction channel sought after. To quantify this discrimination the open reaction channels for each different reaction are simulated and then compared to the data.

3.4 Monte Carlo simulations

The importance of simulations has been discussed a few times yet has not been expanded upon. In previous sections the importance of including certain conditions to remove unwanted background was mentioned, as well as the benefits of using momentum and energy conservation cuts to obtain very clean multiplicity four spectra. It is equally important, however, to remove any possible bias introduced by these conditions when extracting results. Furthermore, it is essential to include the detection efficiency of the experimental setup. If we were able to have a 100% efficient 4π detector array then this would not be an issue. However as the detector system does not cover 4π we may favor the detection of some resonances over others due to the kinematic coverage. Monte Carlo simulations are the best tool for dealing with these different issues and are indispensable for a quantitative comparison of experimental results to theory.

The Monte Carlo simulations were structured in three parts: First, the physical description of the reaction process. Second, the simulation of the effects of the detection system. Third, the application of the experimental analysis procedure to the simulated data.

The reaction process is described in terms of a sequential model. The first step is to simulate the primary particles produced in the reaction. The beam, the beam energy, and the target are fixed, whereas the excitation energy of the outgoing ^{12}C nucleus is chosen by the user. The energy of the primary ejectile (proton or deuteron) is determined by kinematics, while the angular distribution of the primary ejectile will depend on the reaction mechanism, and are therefore obtained from fitting the experimental data (see Section 3.4.2). The following step is to simulate the decay of ^{12}C into an alpha particle (α_1) and a ^{8}Be nucleus. Here the ^{8}Be nucleus can be left in its ground state, or it can be in the 2^+ first excited state. In the former case the ^{8}Be is described by the Breit-Wigner formula, but in the latter case the energy of α_1 and ^{8}Be becomes complicated due to the broad width of the ^{8}Be

2^+ state (see Section 1.3), and penetrability effects in the entrance and exit channel should be included [BZT74]. Finally, the breakup of ^{8}Be into two alpha particles is simulated, with the energy and direction again depending on the energy and width of the excited state of the intermediate ^{8}Be nucleus. In the case of decay decay through the 0^+ ground state of ^{8}Be, there is no angular correlation between the first emitted alpha and the other two alpha particles since it has 0 spin. However, if the decay proceeds through the intermediate 2^+ ^{8}Be resonance, then there will exist a correlation between the first emitted alpha particle from ^{12}C and the other alpha particles (see Section 3.4.1).

The second part of the simulation program is concerned with simulating the effects of the detection system. This step essentially takes into account the geometry of the setup (including the finite beam spot size) and the response of the individual detectors to charged particle radiation. The energy resolution is described with a Gaussian function folded with two exponential tails. The effects of summing and sharing, outlined in Section 3.1, are also accounted for in the simulation program. The pulse height defect of the different ions as well as the energy losses in the target and detector dead layers are calculated using the method outlined in 3.1.2. The detection thresholds and trigger logic are also included in the simulations.

The final step in the simulation is to apply the experimental analysis procedure used on the experimental data to the simulated events. To do this the simulated events are saved in identical data structures to the physical events (ntuple). Therefore, the simulated events can be passed through exactly the same analysis program used for the data which is crucial in removing any bias introduced by the various cuts and gates imposed on the data.

As an example, we can look at the 9.64 MeV state (Γ = 34 keV) in the ^{10}B(^{3}He,p$\alpha\alpha\alpha$) reaction, in which the resonance decays into three alpha particles via the ^{8}Be ground state. The simulation is done in three parts:

1. ^{3}He+^{10}B $\rightarrow$p+^{12}C: In the center of mass frame, we have the proton and ^{12}C nucleus emitted in opposite directions. The kinetic energy of the proton and ^{12}C nucleus is calculated from the energy available in the reaction (determined by the Q-value and the excitation energy in^{12}C), which is divided according to the masses of the nuclei. In this case, the proton takes away roughly 12 times more energy than the ^{12}C nucleus. When converted to the laboratory frame, the available energy is easily calculated from the beam energy, and the angular distribution of the proton determined by fits to the data.

2. ^{12}C$\rightarrow$ α_1+^{8}Be(gs): As above, in the center of mass frame the α_1 and ^{8}Be(gs) nucleus will be emitted back-to-back, while here the energy

will be shared in a 1:2 ratio. However, the energy available will depend on the energy of the initial ^{12}C nucleus. The 9.64 MeV state is given by a Breit-Wigner distribution with a width of 34 keV, which is sampled using the pseudo-random number generator RANLUX provided by CERNLIB.

3. ^{8}Be$\rightarrow \alpha_2 + \alpha_3$: This case is the same as above, except the width of the ^{8}Be(gs) is only 5.6 eV. At this stage the direction and energy of each particle emitted in the reaction is known.

The next step is to include the detection system. Here the position and coverage of the detectors used in the experiment are included, along with their characteristics. These include:

- Number of strips and dimensions of strips
- Thickness of the deadlayers in the detectors
- Thickness of the detectors
- Resolution of the detectors
- Detection thresholds

Finally the particles obtained in the simulation are stored in an ntuple to be further processed through the same analysis program as the data. The case of decay through the 2^+ state in ^{8}Be is slightly different since the width of ^{8}Be is very large. The penetrability effects become important and should be taken into account. Another possibility for simulating decay through the broad 2^+ state is to instead assume a decay into 3-body phase space calculated using GENBOD from CERNLIB. The difference in detection efficiencies between a phase-space decay and a sequential decay through a broad resonance with penetrability effects included is only $\approx 5\%$, so that the detection efficiencies were determined assuming a phase-space decay unless otherwise noted. In Chapter 5 the description of the decay of the broad 2^+ state in ^{8}Be is looked at more in detail.

3.4.1 Angular correlations

In the case of a nuclear reaction with successive radiations, the two different radiations will be correlated to each other. This can be understood in the sense that if there is one radiation, barring any polarization effects, it will be emitted isotropically. However, if there is a subsequent radiation, then

Table 3.1: Some values of the Legendre polynomials used for calculating the angular correlations.

n	$P_n(x)$
0	1
1	x
2	$\frac{1}{2}(3x^2-1)$
3	$\frac{1}{2}(5x^3-3x)$
4	$\frac{1}{8}(35x^4-30x^2+3)$
5	$\frac{1}{8}(63x^5-70x^3+15x)$
6	$\frac{1}{16}(231x^6-315x^4+105x^2-5)$

although each of these radiations taken individually will be emitted isotropically, the emission of one *with respect* to the other will not be isotropic.

In [BR53], Biedenharn and Rose discuss a general formalism for understanding these angular correlations. Here we apply this general formalism to the case of decay of a ^{12}C resonance decaying through the 2^+ state in ^{8}Be. The correlation is determined between the first emitted alpha particle from ^{12}C and the second (or third, the choice is arbitrary) emitted alpha particle from the intermediate ^{8}Be nucleus. We then have the following parameters used for notation. j_1 denotes the spin of the initial resonance, in this case the spin of the ^{12}C resonance. j_2 denotes the spin of the final state, which in our case will always be 0 since our final state is an alpha particle. j corresponds to the spin of the intermediate state, in our case that of the ^{8}Be nucleus.

The general formalism introduced by Biedenharn and Rose for the angular correlation where β is the angle defined by the trajectory of the first emitted alpha particle and the second emitted alpha particle is

$$W_{\alpha-\alpha}(\beta) = \sum_{\nu} b_\nu(l_1 l_1; \alpha_1) b_\nu(l_2 l_2; \alpha_2) A_\nu P_\nu(cos\beta) \tag{3.7}$$

where

$$b_\nu = \frac{2l(l+1)}{2l(l+1)-\nu(\nu+1)}; A_\nu = F_\nu(l_1 j_1 j) F_\nu(l_2 j_2 j) \tag{3.8}$$

and the sum is over ν, which is an even integer in the range of 0 to the smallest integer of the set $2(l_1)_{max}$, $2(l_2)_{max}$, or $2j$. $P_\nu(cos\beta)$ are the Legendre Polynomials, some of which are listed in Table 3.1, and F_ν is found in [BR53].

Let us determine the angular distribution W_β expected for a 1^+ state in ^{12}C which decays through the 2^+ state in ^{8}Be (decay through the 0^+ ground state in ^{8}Be is forbidden by parity conservation). In this case we have $j_1 = 1$, $j_2 = 0$, and $j = 2$. The angular momentum of the first alpha particle is restricted to $l_1 = 2$, as is the angular momentum of the second emitted alpha particle so that $l_2 = 2$ (refer to Table 3.3).

The values of A_ν, where $F_\nu(l_1 j_1 j) = F_\nu(212)$ and $F_\nu(l_2 j_2 j) = F_\nu(202)$, are $A_0 = 1$ $A_2 = 0.1786$, and $A_4 = -0.7619$. In addition, $b_\nu(l_1) = b_\nu(l_2)$, where $b_0 = 1$, $b_2 = 2$, and $b_4 = -3/2$. Using the tabulated values for the Legendre polynomials, we have

$$\begin{aligned} W(\beta) &= \sum_\nu W_\nu = W_0 + W_2 + W_4 \\ &\approx 1 + 0.1786 \cdot 2 \cdot (3\cos^2\beta - 1) \\ &\quad -0.7619 \cdot \frac{9}{32} \cdot (35\cos^4\beta - 30\cos^2\beta + 3) \\ &\approx 1 + 1.0716\cos^2\beta - .3572 - 7.5\cos^4\beta + 6.43\cos^2\beta - 0.643 \\ &\approx 7.5\cos^2\beta - 7.5\cos^4\beta \\ &\approx 7.5\cos^2\beta\sin^2\beta \\ &\propto \sin^2 2\beta \end{aligned} \tag{3.9}$$

Therefore in the case of decay of the 1^+ resonance in ^{12}C, the angular correlation will be proportional to $\sin^2\beta$ where β is the angle between the first emitted alpha and one of the other two emitted alphas. The determination of the angular correlation between the alphas of the 12.71 MeV 1^+ resonance will prove useful in Section 5.2.3.

3.4.2 Angular distributions

The angular distribution of the light-ion affects the detection efficiency so that a detailed understanding of the distribution for each resonance was necessary. Therefore the angular distribution of the light ion needs to be fit for each resonance. Figure 3.14(a) shows the angular distribution of the deuteron in CM angles for the 9.64 MeV resonance of ^{12}C populated in the ^{11}B(^{3}He,d$\alpha\alpha\alpha$) reaction in arbitrary units. However this distribution does not take into account any detection efficiencies due to the placement of the detectors. In order to remove any effects caused by detector bias, the same reaction is simulated assuming an isotropic distribution of the deuteron through the experimental setup. This is shown in Fig. 3.14(b) and provides a very illustrative example of the effect of detection efficiency. At low, middle, and

high angles there are no deuterons as expected. However one can see a dip in the distribution at roughly 60°. This dip is due to a broken strip in DSSSD1. Finally the experimental distribution was divided by the distribution from the simulation to give Fig. 3.14(c). This figure shows the deviation of the angular distribution of the deuteron from an isotropic distribution.

There are several interesting features which can be learned from Fig. 3.14(c). In Section 2.1.1 it was described that an indirect reaction results in an isotropic distribution of the deuteron, while a direct reaction would give a forward-focused distribution. There is a peak in forward angles suggesting a direct reaction, though in reality there is a mix of the two reaction mechanisms. Note the presence of a strong peak at $\approx 30°$. This is a strong indication that a transfer reaction was the dominant mechanism for the 9.64 MeV channel.

3.4.3 Detection efficiencies

The simulations can be compared to the data for a given reaction channel in order to determine detection efficiencies. Table 3.2 shows the efficiency of the experimental setup for detecting a few $^{12}C^*$ states in the $^3He+^{10}B$ reaction. The multiplicity ratios from the simulations and from the data give a very good agreement, with deviations being less than 10%. This tells us that our simulation is getting the relative efficiencies correct.

One can see from Table 3.2 that the detection efficiencies are very dependent on the reaction channel. Figure 3.15 illustrates the dependency of the detection efficiency for the $^{10}B(^3He,p\alpha\alpha\alpha)$ reaction on the intermediate resonance of ^8Be. Figure 3.15(a) shows a typical event in which the decay proceeded via the ground state of ^8Be. The ground state of ^8Be is very narrow and has a very low excitation energy, so that the two alphas from its decay will have little kinetic energy and be focused in the direction of the beam. In the case of an intermediate decay via the broad 2^+ state of ^8Be, the alpha particles are much less correlated so that the emission of the two alpha particles from ^8Be is essentially isotropic.

3.5 The $^{12}C \rightarrow 3\alpha$ breakup

The question of how the ^{12}C nucleus will breakup into three alpha particles was touched upon in the introduction, and is a very difficult one to answer. There are essentially two possibilities. One is for ^{12}C to break up directly and the other for the decay to be sequential. In this case the sequential decay would first involve the decay via a resonance in ^8Be. Direct decay does not

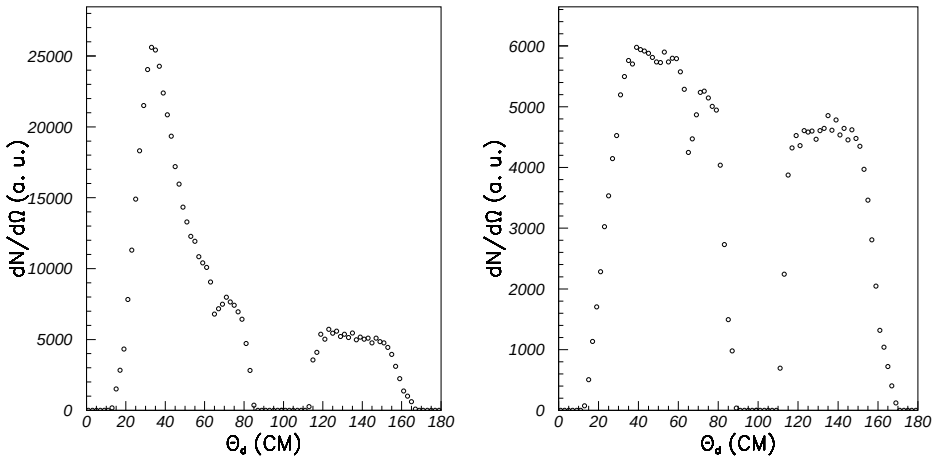

(a) Data (b) Simulation

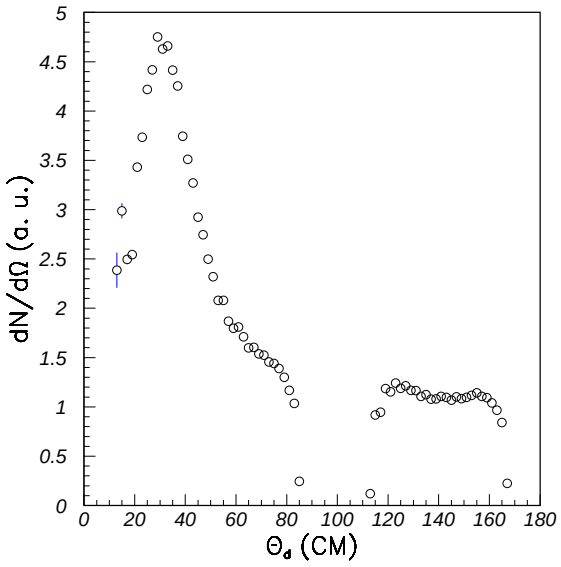

(c) Data/simulation

Figure 3.14: Angular distribution of deuteron from the 3^- 9.64 MeV resonance populated in the ^{11}B(^{3}He,d$\alpha\alpha\alpha$) reaction given in a linear scale in arbitrary units. (a) shows the angular distribution taken from the data, (b) shows the distribution from the simulation, and (c) shows the data/simulation so that any detection bias has been removed. The non-isotropic distribution seen in (b) comes purely from kinematics and the placement of this particular DSSSD. The dip seen at 60° is the result of a dead strip in the DSSSD, though this is corrected when the detection efficiency is taken into account in (c).

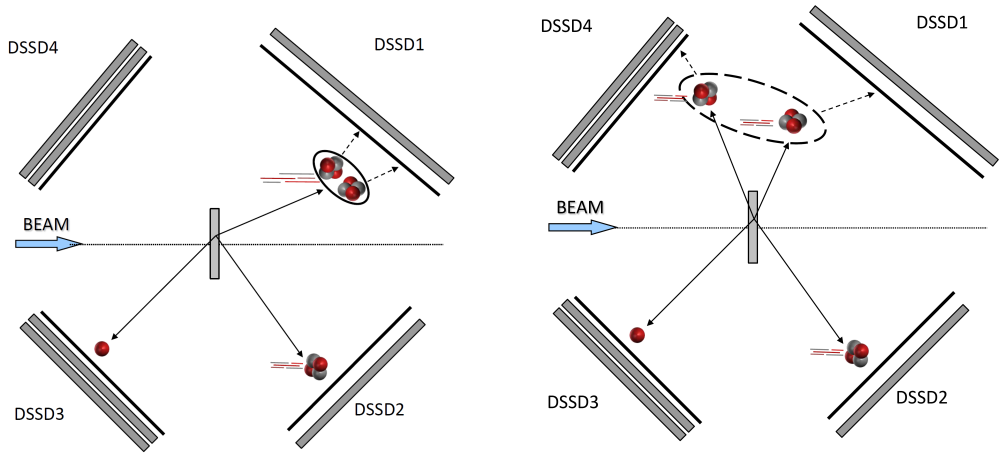

(a) ^{12}C(9.64), ^{8}Be(g.s.) channel (b) ^{12}C(12.71), ^{8}Be(2^+) channel

Figure 3.15: Figure showing two possible channels in the ^{3}He+^{10}B reaction in order to demonstrate the dependence of the detection efficiency on different channels. In (a), the ^{8}Be nucleus is in its ground state and also has little kinetic energy, so that it is forward-focused from the beam energy. This will cause the two alphas from the ^{8}Be nucleus to be forward-peaked and thus be detected by our detectors at low angles. Similarly the third alpha particle also has little energy and is peaked at forward angles where it is more likely to be detected by the front DSSSDs. In (b), the ^{8}Be nucleus is in a the broad 2^+ state so that its constituent alpha particles are much less correlated. In this case the emission of the alpha particles is essentially isotropic so that there is no favoring of forward angles. Therefore are detection efficiency is reduced with respect to case (a). The placement of the detectors at low angles was not by accident, since the kinematical focusing of the alpha particles at low energies was known during simulations leading up to the experiment and the telescopes were placed accordingly.

Table 3.2: Efficiency of the experimental setup for detecting selected $^{12}C^*$ decay channels in the $^3He+^{10}B$ reaction, taking into account geometry, reaction kinematics, and detector response. The different columns show the efficiency of detecting different multiplicity events. Listed first is multiplicity ≥ 1 events (i.e., the probability of detecting a proton), then multiplicity 3 events ($p + 2\alpha$), and finally multiplicity 4 events ($p + 3\alpha$). In the case of isotropic 4-particle decay, the efficiency would be the solid angle coverage to the fourth power; in our case, $(38\%)^4$=2.08% (from Equation 2.4)

$$^3He + ^{10}B \rightarrow p + ^{12}C^* \rightarrow p + \alpha + ^8Be^* \rightarrow p + 3\alpha$$

	mult. ≥ 1 p	mult. 3 $p + 2\alpha$	mult. 4 $p + 3\alpha$
Resonances	[%]	[%]	[%]
$^{12}C(9.64)$, $^8Be(g.s.)$	20.5	4.98	1.43
$^{12}C(12.71)$, $^8Be(2^+)$	18.7	4.27	0.69
$^{12}C(16.11)$, $^8Be(2^+)$	19.8	4.14	0.71

involve any intermediate resonance, and the alpha particles would decay to the available phase space.

3.5.1 Sequential decay through ^{8}Be

We can try to determine the decay mechanism by transforming the α particle energies into the ^{12}C center of mass frame. This can give us information on the decay mode of each resonance in ^{12}C, such as whether a particular resonance will decay through the 0^+ ground state in ^{8}Be or through the 2^+ state in ^{8}Be, or both. A powerful method to visualize this is to make a "Fynbo plot"[Fyn00], in which the ^{12}C excitation energy is plotted versus the individual α particle energies in the ^{12}C center of mass frame, as seen in Fig. 3.16. In this particular figure, the vertical axis is the sum of the three α particles. This is equivalent to the ^{12}C excitation energy minus the 3α breakup threshold of 7.275 MeV. This figure is produced from the $^{11}B(^3He,d\alpha\alpha\alpha)$ reaction data in which the ^{12}C excitation calculated from the deuteron energy is plotted onto the ordinate and each of the three different alpha particle energies are plotted onto the abscissa.

In Fig. 3.16 features which show evidence for a sequential decay through ^{8}Be are shown. The diagonal bands indicate breakup through the narrow

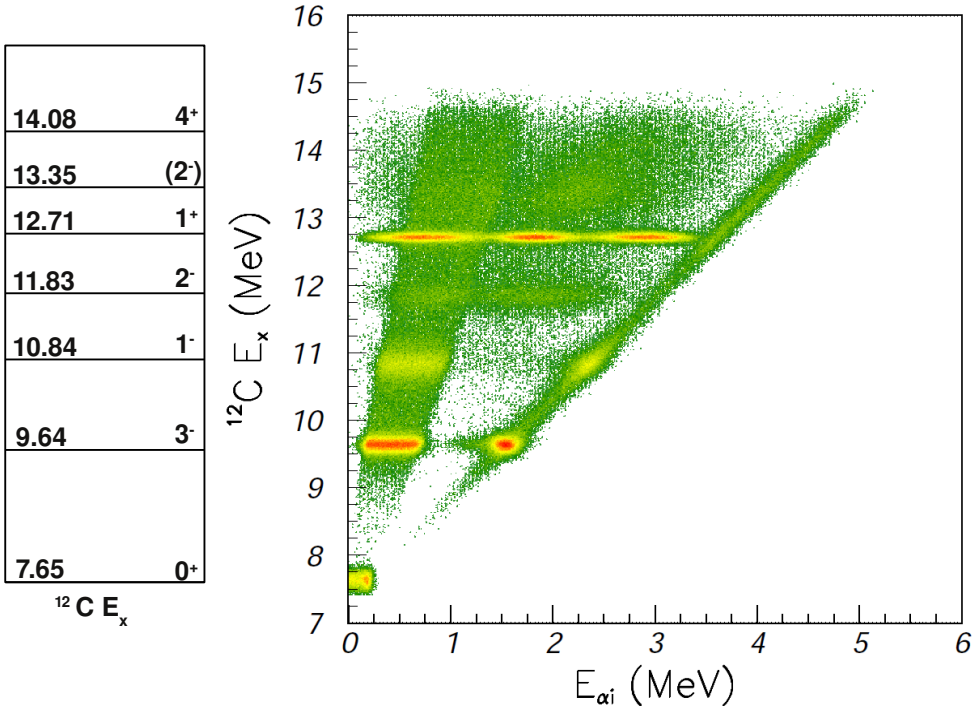

Figure 3.16: Excitation energy of ^{12}C versus the individual α particle energies taken from the multiplicity four events of the ^{11}B(^{3}He,d$\alpha\alpha\alpha$) reaction data. The excitation energy is equal to the sum of the three α particle energies plus the triple-alpha threshold (7.275 MeV). A partial level scheme of ^{12}C is included alongside the figure.

Table 3.3: Spin and parity, J^π, assignments for resonances in ^{12}C which break-up sequentially via α-decay through the 0^+ and/or 2^+ states in ^8Be. The possible orbital angular momentum l values of the first emitted alpha particle which decays to ^8Be is provided.

^{12}C E_x	J^π	l_{α_1} ($^8Be_{0^+}$)	l_{α_1} of α_1 ($^8Be_{2^+}$)
7.65	0^+	0	2
12.71	1^+	-	2
16.11	2^+	2	0,2
	3^+	-	2,4
14.08	4^+	4	2,4,6
10.84	1^-	1	1,3
11.83	2^-	-	1,3
9.64	3^-	3	1,3,5
13.34[a]	(4^-)	-	3,5

[a] The J^π of the 13.34 MeV state is debated and is discussed in detail in Section 5.2.4.

ground state of ^8Be. The diagonal to the right corresponds to the first and most energetic alpha particle, while the diagonal band to the left corresponds to the two alpha particles which decay from the ground state of ^8Be.

The sequential decay mechanism is clear when the decay proceeds through the ground state of ^8Be. However, it becomes quite complicated to differentiate between decay through the broad 2^+ resonance in ^8Be and direct decay into three alpha particles [Alv08]. Section 5.2.3 looks at the question of interpretation of the decay mechanism in more detail, though a sequential picture fits well with data and will be assumed here. Whether the break-up of the alphas passes through the 0^+ or 2^+ intermediate state in ^8Be depends on several factors, most importantly the selection rules from the conservation of angular momentum.

Selection rules

Only the natural parity states can decay via the 0^+ ground state in ^8Be without violating parity (it would necessitate an odd l but no change in parity, or vice-versa, which is forbidden). Natural parity refers to states which satisfy $\pi = (-1)^l$, where l is the spin and and π the parity.

Table 3.3 is included to provide information on possible angular momen-

tum values for the decay of some ^{12}C resonances through the ^{8}Be 0^+ ground state and/or 2^+ first excited state at 3.06 MeV. The possible l values for the first alpha particle ($J^{\pi}=0^+$) are limited by $|J_{^{12}C} - J_{^{8}Be}| \leq l \leq J_{^{12}C} + J_{^{8}Be}$ and by parity conservation, with $\pi_{^{12}\mathrm{C}^*} = (-1)^l * \pi_{^{8}\mathrm{Be}^*} * \pi_{^{4}\mathrm{He}} \Longrightarrow \pi_{^{12}\mathrm{C}^*} = (-1)^l$ where l is the orbital angular momentum of the α particle, and both parities $\pi_{^{8}\mathrm{Be}^*}$ and $\pi_{^{4}\mathrm{He}}$ are positive. The penetrability of the alpha particle will decrease with increasing l_α due to the presence of the centrifugal barrier.

Separating the breakup via ^{8}Be

We can try to separate out the decay which proceeds via the ground state of ^{8}Be. To do this we calculate the invariant mass of ^{8}Be with the momentum of a pair of α particles using the following [Ohl65]

$$E(^{8}Be) = \frac{\vec{P_{1-2}}^{\,2}}{2\mu} = \frac{(\frac{\mu}{m_\alpha}\vec{P_1} - \frac{\mu}{m_\alpha}\vec{P_2})^2}{2\mu} = \frac{(\vec{P_1} - \vec{P_2})^2}{4m_\alpha}$$
$$= \frac{|P_1|^2 + |P_2|^2 - 2 \cdot |P_1| \cdot |P2| \cdot cos\theta}{4m_\alpha} \tag{3.10}$$

$$cos\theta = \frac{P_{x_1}^2 \cdot P_{x_2}^2 + P_{y_1}^2 \cdot P_{y_2}^2 + P_{z_1}^2 \cdot P_{z_2}^2}{|P_1| \cdot |P_2|} \tag{3.11}$$

where $\mu = m_\alpha/2$ is the reduced mass of the ^{8}Be system This formula assumes we know which pair of α particles make up the short-lived ^{8}Be resonances. However since we cannot always differentiate between the first α particle emitted in the break-up of ^{12}C resonances and the α-pair that would make up the intermediate ^{8}Be resonance, Equations 3.10 and 3.11 were applied for all three possible α pairs.

Figure 3.17 displays an example of the ^{8}Be energy spectrum obtained from the multiplicity four ^{11}B(^{3}He,d$\alpha\alpha\alpha$) reaction data in which the three possible α pairs are summed together. The ground state peak of ^{8}Be located at 0.09 MeV is clearly visible and highlighted in red. The broad 2^+ state (3.06 MeV, Γ= 1.37 MeV) cannot be easily distinguished since the cases in which the incorrect alpha pair was chosen gives background. Interference between the alpha particles (alpha particles are identical bosons so that the final state wavefunction must be made symmetric) may arise since the broad 2^+ state is very short-lived. If this is the case then the question of which alpha particle is emitted first is impossible to answer, and the different alpha-pair choices will appear as background. Therefore the data was split into data which proceeds through the ground state and that which does not.

We can then make a similar plot as Fig. 3.16 with the data separated depending on the intermediate resonance through which it proceeds. Figure

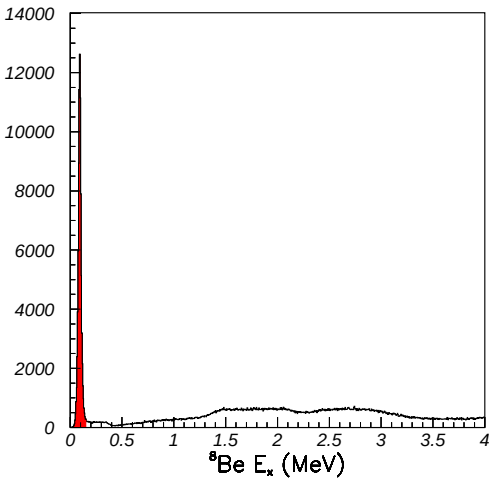

Figure 3.17: ^{8}Be invariant mass calculated using the three possible alpha pairs from the ^{11}B(^{3}He,d$\alpha\alpha\alpha$) multiplicity four reaction data. The area shaded in red corresponds to the narrow ^{8}Be ground state peak at 0.092 MeV (Γ=6.8 eV) with respect to the 2α-threshold. Any data outside this peak is considered to decay through the broad 2^+ resonance in ^{8}Be. The reason why there is no shape typical of a characteristic broad peak at the 2^+ resonance of 3.06 MeV is that this part of the spectrum also includes the choice of wrong α pairs.

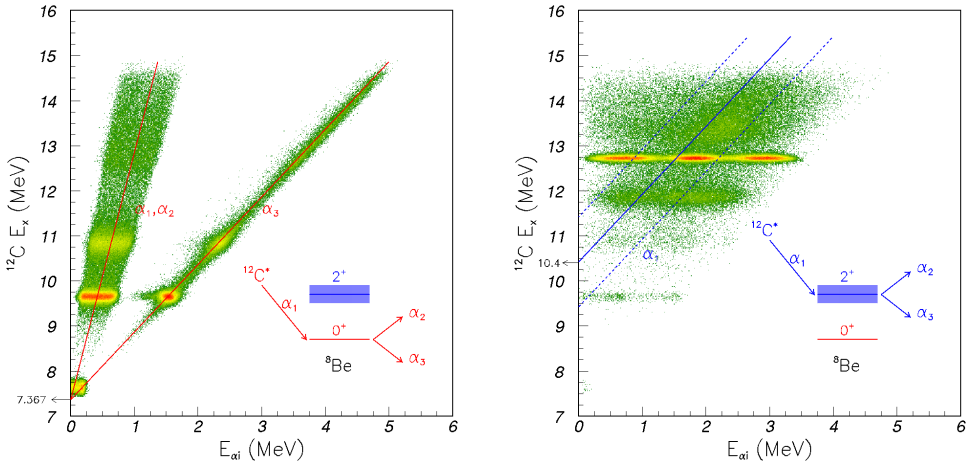

(a) (b)

Figure 3.18: (a) ^{12}C Excitation energy versus the individual alpha energies. This plot corresponds to those states in ^{12}C which decay through the 0^+ state in ^{8}Be, as indicated in the lower right-hand corner. Note the red line going through α_1 corresponding to the first emitted α particle. (b) Excitation energy in ^{12}C versus the individual alpha energies showing decay through the 2^+ state in ^{8}Be. Note the blue line going through α_1 corresponding to the first emitted α particle. This is just to guide the eye, as we are assuming that there is no interference between the alphas.

3.18(a) shows data which proceeds through the ground state of ^{8}Be, where there is a gate on ^{8}Be in Fig. 3.17 between 40 keV and 150 keV. Figure 3.18(b) shows the rest of the data. Figures 3.18(a) and 3.18(b) contain a lot of information. For convenience, I have denoted here α_1 as the first emitted particle, while α_2 and α_3 refer to the pair that makes up the ^{8}Be resonance. Refer first to Fig. 3.18(a), corresponding to the states which decay through the ground state of ^{8}Be. The red line cutting through α_1 has a slope of 3/2. This comes from the following: in the case of decay through the ground state of ^{8}Be, the first particle would carry an energy [Pre03]

$$E_1 = \frac{2}{3} * (E_{sum} - 0.092)MeV, \tag{3.12}$$

where 0.092 MeV is the separation energy of the ground state of ^{8}Be into two α particles. Therefore, the line corresponding to α_1 would be the following:

$$E_{sum} = \frac{3}{2} * E_1 + 0.092MeV. \tag{3.13}$$

One striking feature of Fig. 3.18(a) is that the data which proceeds through the ^{8}Be 0^+ ground state is continuous through all states in ^{12}C, including those with unnatural parity (*e.g.* 12.7 MeV 1^+) seen in Table 3.3. This is due to the fact that in this type of reaction experiments, we populate all states with no discrimination, so that we are seeing contribution of ^{12}C $\rightarrow^8$Be (0^+) transitions from the tails of other broad resonances in ^{12}C. In addition, there is also some background present due to contamination from other reaction channels. For example, the ^{3}He + ^{11}B $\rightarrow^6$Li* + ^{8}Be(0^+) channel has very broad resonances which will appear as background in the figure.

Figure 3.18(b) represents those states which decay via the ^{8}Be 2^+ state. This plot is not as clean as the one shown in Fig. 3.18(a) because it is difficult to avoid unwanted data since the 2^+ state is broad and therefore the energies are not so well-defined. This difficulty can be seen in Fig. 3.17 which was used as a reference. The red peak is clearly defined, making it much easier to separate the 0^+ ^{8}Be data. It is still possible to discern the broad line corresponding to the decay of the first emitted α particle shown in blue in Fig. 3.18(b). This line intercepts the y-axis at about 10.4 MeV, which is simply the 7.367 MeV seen in Fig. 3.18(a) added to the energy of the broad 2^+ state in ^{8}Be at 3.06 MeV. However, this line is drawn to guide the eye and has no real meaning since there may be interference between alpha particles.

We can plot the projection of the data in Fig. 3.18 to get the ^{12}C excitation separated into decay through the 0^+ and 2^+ states in ^{8}Be. Figure 3.19 makes it easier to visualize the states that decay through the 0^+ (red)

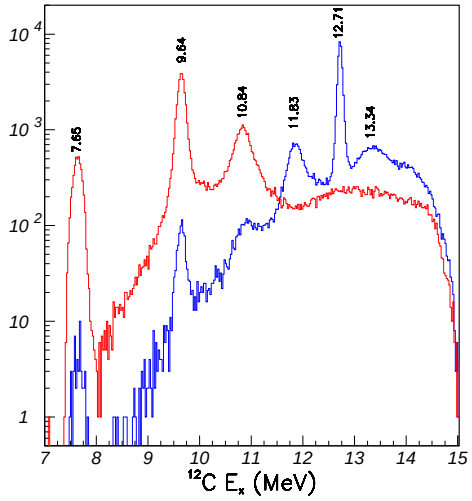

Figure 3.19: This ^{12}C spectrum corresponds to the projection on the y-axis of Figs. 3.18(a) (red) and 3.18(b) (blue). In red are the states that decay through the 0^+ ground state in ^8Be. In blue are the states which decay via the 2^+ state in ^8Be. It is interesting to observe that states such as the 9.64 MeV (3^-), the 10.84 (1^-), and the 14.08 (4^+) decay through both the 0^+ and 2^+ states in ^8Be, while others, such as 11.83 (2^-), 12.71 (1^+), and 13.35 (2^-) states only decay through ^8Be (2^+), as expected from Table 3.3. The 7.65 (0^+) decays only through ^8Be (0^+), and the small number of counts present in blue are due to decays through the tail of the ^8Be (0^+) which fall outside of the gate placed on ground state of ^8Be.

and/or the 2^+ state (blue) in ^{8}Be, and can be compared with those states shown in Table 3.3. By comparing the intensity of the peaks in Fig. 3.19, we can determine partial branching ratios in cases in which the resonance is of natural parity. This calls for a more detailed analysis and will be discussed in Section 5.1.

This one's tricky. You have to use imaginary numbers, like eleventeen...

Calvin & Hobbes

4

Indirect Observation of γ-decay

In this chapter we now have the ^{12}C channel well identified and we can proceed to extract some physics results from the data. This chapter focuses on the analysis and results obtained following the observation of γ-decay using Si detectors in this experiment [Kir09]. In the next chapter we will take a detailed look at each of the individual resonances in order to determine spin and parities of individual resonances, the branching ratios of the intermediate decay through ^{8}Be, and also search for proposed resonances in ^{12}C. The work involved in doing this deserves it's own chapter, so I chose to separate this from the current chapter highlighting some results.

4.1 γ-branch of the 15.11 MeV and 12.71 MeV resonances in ^{12}C

Recall in Section 3.2.1 the presence of resonances in ^{12}C above the triple-alpha threshold which with a very small α-decay width. For example, in Fig. 3.10, the T=1 15.11 MeV state disappears when the multiplicity four condition is imposed, since this state decays primarily by γ-decay. However, while performing different gates on the momentum and energy conservation it became apparent that it was perhaps possible to search for indirect evidence of γ-decay. So far I have mostly been using the energy of the light ion to calculate the excitation energy of ^{12}C. However the ^{12}C excitation energy can also be calculated by the invariant mass of the three alpha particles. Once we have the individual energy of each alpha particle in the center of mass frame of the ^{12}C nucleus, then simply the sum of the three alpha particles will give us the excitation energy of ^{12}C above the triple-alpha threshold. Therefore we can calculate the excitation energy from the three alpha particles as

$$^{12}\mathrm{C}\ \mathrm{E}_x^{3\alpha} = \sum \alpha_i + (3m_\alpha - m_{^{12}C})$$

where $3m_\alpha - m_{^{12}C} = 7.275$ MeV is the triple alpha threshold. Now we have two methods to calculate the ^{12}C energy. The first involves the primary ejectile (proton in the case of the ^{10}B target reaction and deuteron in the case of the ^{11}B target reaction), and the second involves the alpha particles. Up until now we have assumed that these two quantities would be more or else equal. In fact, when we look at energy conservation, if they are not within a certain energy we discard the event. But, what would happen if a higher lying state in ^{12}C were to decay via γ emission into a lower excited state which is still above the triple-alpha threshold?

If this were to occur, we would have two different values for the excitation energy, depending on if it was calculated from the ejectile or from the products. Let us look at the ^{10}B(^{3}He,p$\alpha\alpha\alpha$) reaction as an example. In this case, the excitation energy calculated from the proton would differ from that calculated from the three alpha particles. The former would give us information on the initial state populated in ^{12}C (the state which would subsequently emit a γ), while the latter would give the final excitation energy. Therefore the difference of ^{12}C excitation energy obtained between the ejectile and the three alpha particles gives the energy of the undetected γ. This seems like a very nice method in theory, but the quality of the data must be very clean to unambiguously claim the presence of γ-decay.

To visualize the difference in energy expected from the emission of a γ-ray we can plot the excitation energy in ^{12}C calculated from the primary projectile versus that calculated from the invariant mass of the alpha particles. Figure 4.1 shows such a plot, with no conditions on energy or momentum requirements. Along the diagonal are events where the excitation energy calculated from the primary projectile is the same as that calculated from the alpha particles. Note that it is virtually impossible to discern any features below the diagonal, which is where we would expect events to appear if there was any γ-decay. The reason for this is that we have not implemented any conditions on momentum or energy conservation.

Clearly if we were to include a condition on the conservation of energy, we would be selecting only events along the diagonal and would remove any events which came from a γ-decay. However, it is possible to implement momentum conservation requirements since the momentum carried away by the γ-ray is very small compared to the other momenta involved in the reaction, and is within the experimental resolution (refer to Fig. 3.11, where the condition on the momentum requirements was less than 50 MeV/c, much smaller than E_γ/c).

If the momentum conservation requirements are implemented we obtain what is shown in Fig. 4.2(a), where we can begin to see evidence for missing energy from a possible γ-decay, highlighted by vertical bands for the 15.11

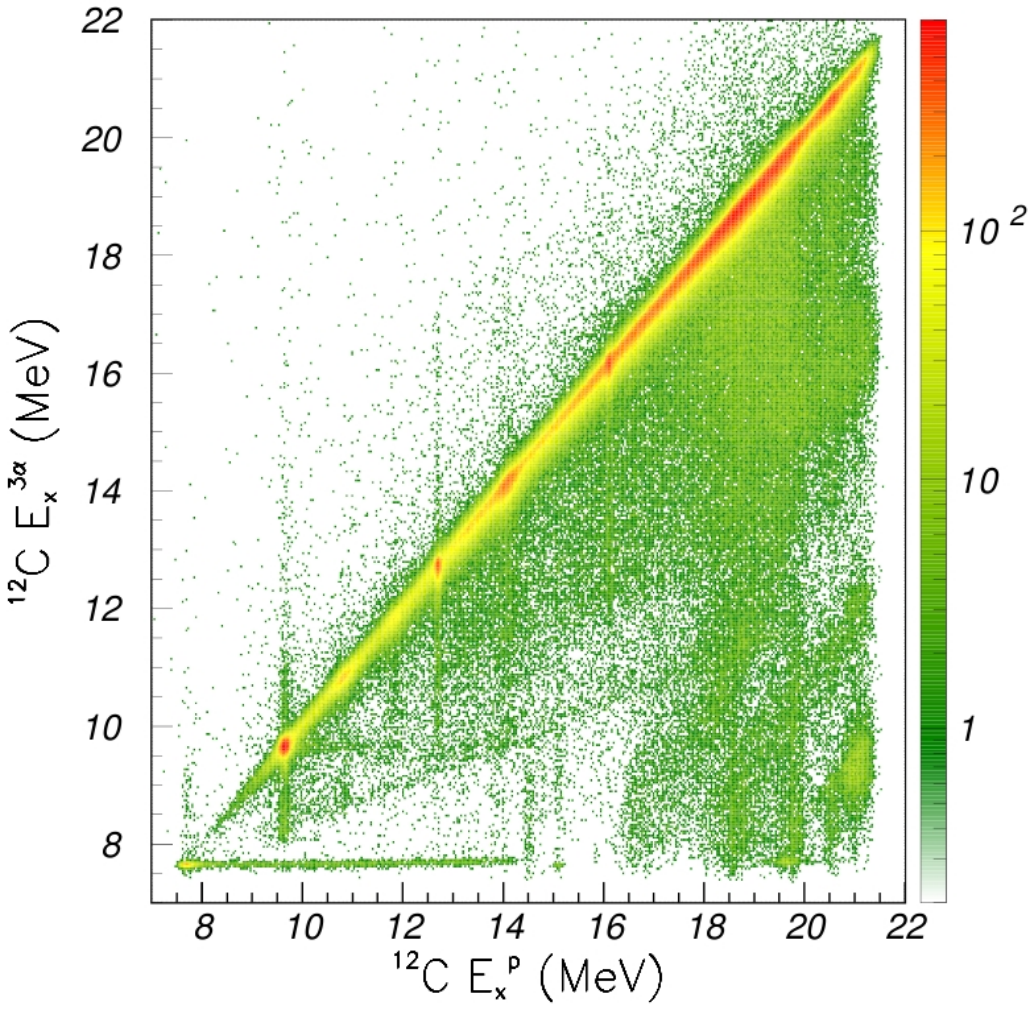

Figure 4.1: Complete kinematics data from the ^{10}B(^{3}He,p$\alpha\alpha\alpha$) reaction. The ^{12}C excitation energy calculated from the energy of the proton is along the abscissa while the ^{12}C excitation energy calculated from the invariant mass of the three α particles is along the ordinate. In this figure there is no condition on the conservation of momentum.

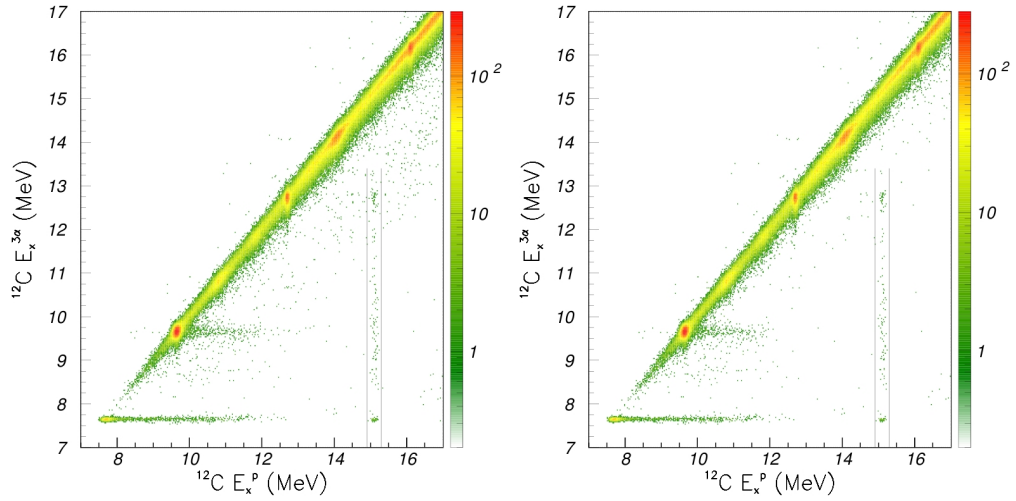

Figure 4.2: (a) Implementing momentum conservation to the date displayed in Fig. 4.1. The horizontal bands extending from the diagonal with constant $E_x^{3\alpha}$ of 7.65 MeV and 9.64 MeV and increasing E_x^p corresponds to events where the proton did not fully deposit its energy in the E detector. A gate with vertical lines has been placed around the 15.11 MeV region showing γ-decay to other resonances in ^{12}C. There are still scattered events which can be seen below the diagonal and which will contribute as background to the gate around 15.11 MeV. This was found to be mostly due to protons hitting the border of the DSSSD ($\approx$ 2% of events). The result of removing these events as shown in (b).

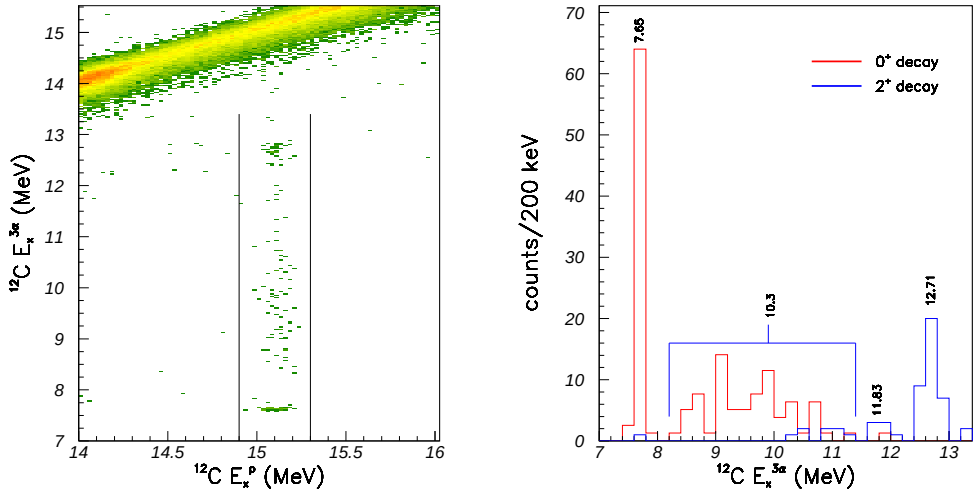

(a) (b)

Figure 4.3: (a) Close-up of the region of interest in Fig. 4.2. (b) The projection of (a), separating the contribution which goes through the 0^+ ^{8}Be ground state and that which does not. The condition placed on the ground state decay is the same as that outlined in Section 3.5.

MeV state. Though there are a number of events within the gate, there still seems to be several scattered events below the diagonal which have made it through the momentum requirements, as well bands extending towards the right of the 7.65 MeV and the 9.64 MeV state. These bands are simply caused by protons which punch through the PAD detectors, leaving less energy deposited in the PAD detector, and thereby appearing as increasing energy in E_x^p. The events which are seen below the diagonal were identified as protons which hit the outside strips of the DSSSD detectors. The problem was that the proton would be hitting the outside strips of the DSSSD, but would then hit the border of the PAD detector, thereby not fully depositing its energy in the PAD detector. These events were thus removed, and as can be seen in Fig. 4.2(b) the area below the diagonal is much cleaner. The remaining events which do appear are a result of random coincidences which pass the momentum cut. We now have clear evidence of γ-decay of the 15.11 MeV resonance and by gating on the area shown in Fig. 4.2(b) we can try to deduce γ-branches of the 15.11 MeV state to lower states above the triple-alpha threshold.

Figure 4.3(a) shows a closer look at the region of interest in Fig. 4.2(b). If we now place a gate on the 15.11 MeV of constant E_x^p below the diagonal and plot the ^{12}C excitation energy calculated from the invariant mass of the

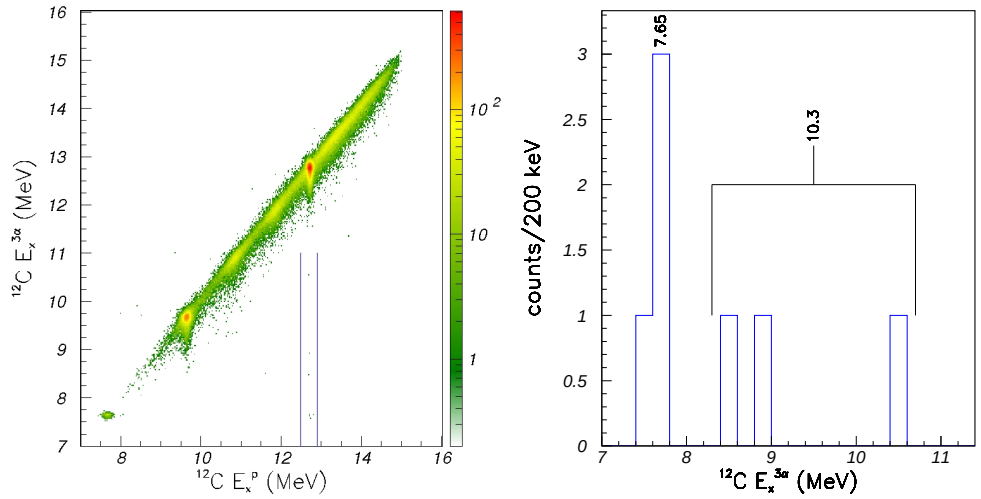

(a) (b)

Figure 4.4: (a) Same figure as Fig. 4.2 but from the ^{11}B(^{3}He,d$\alpha\alpha\alpha$) reaction data. A gate has been placed on the region where the γ-decay of the 12.71 MeV has occurred, the result of which is shown in (b). Figure (b) also shows indicates the different resonances in ^{12}C populated from the γ de-excitation of the 12.71 MeV state.

alpha particles, we obtain a spectrum of the γ-delayed 3α breakup of the 15.11 MeV state. This spectrum can be further divided into states which decay via the 0^+ ^{8}Be ground state and the rest (Fig. 4.3(b)).

In a similar way as with the 15.11 MeV state, the γ branches of the 12.71 MeV state can also be extracted. Figure 4.4 shows a plot of the ^{12}C spectrum populated in the γ-decay of the 12.71 MeV state. In this case, however, the ^{11}B(^{3}He,d$\alpha\alpha\alpha$) reaction was used since it is cleaner in the region underneath the 12.71 MeV state due to the absence of punch-through deuterons. In this case the statistics are very low compared with the 15.11 MeV branches, so that the background must be treated more carefully, as outlined in [Kir09].

Though we can now see how to extract γ branches to states above the triple alpha threshold, another method must be used to determine the γ branches to bound states (0 and 4.44 MeV) in ^{12}C. In this case, a similar method is used, except we look for coincidences between a proton (or deuteron) and a ^{12}C nucleus. Again, the light-ion will give the energy of the initially populated resonance. If there is a γ-decay to a bound state, there will be a deficit in energy in the same way as before, except here the total energy is given by $E_p + E_{^{12}C} - (Q + E_{^3He})$, and the missing energy will be given by the initially populated resonance. Unfortunately this makes it impossible

to distinguish between transitions to the ground state and to the 4.44 MeV state.

4.1.1 Detection efficiency

In order to extract the branching ratios for both the 15.11 MeV and the 12.71 MeV states we must include the detection efficiency of the different channels. To do this Monte Carlo simulations were carried out, as described in Section 3.4, to determine the probability of detecting four particles in the case of γ-delayed 3α breakup of the 15.11 MeV state and the 12.71 MeV state. In both cases, the efficiencies are heavily influenced by the decay path (i.e. through the 0^+ or 2^+ intermediate ^{8}Be state).

To determine the effect of the choice of break-up model for the unnatural parity states at 12.71 and 11.83 MeV excitation energy that breakup through the excited state of ^{8}Be, we used both a direct decay model phase-space simulation and a sequential decay model through the 2^+ ^{8}Be state [Fyn03]. The differences in detection efficiency between the two was less than 5%. However, in the case of decays through the narrow ground state of ^{8}Be (7.65 MeV, 10.3 MeV, and 10.84 MeV), the choice of a sequential model makes a large difference and increases the detection efficiency. This effect can be seen schematically in Fig. 3.15, where the ground state occupy a very limited region of phase space so that the four-particle detection efficiency is larger compared to that of a direct decay.

The decay of the 10.3 MeV state (Table 1.1) is a special case due to the broad nature of the resonance. This state was discussed in detail in the opening chapter where a conclusive description of the state is still under debate. However, we can use the β-decay spectrum measured by [Hyl09a] to describe the shape of the 10.3 MeV state. This is possible due to the parallels between M1 γ-decays and Gamow-Teller β decays outlined in Section 4.2, as long as we correct for detection efficiency and scale the spectrum by E_γ^3 to account for the phase space factor of M1 γ transitions. If the state were a 2^+, though other multipoles are possible (see Table 4.2), M1 would dominate over higher multipoles (Equation 4.3).

We can compare the detection efficiencies given by the simulations with our experimental data to determine errors of the efficiency estimation. It turns out that the simulated efficiencies are correct within 10% accuracy. However, in the case of the transition from the γ-decay of the 12.71 MeV state to the 7.65 MeV state, we assume an error of 20%. The reason for this increase in uncertainty is due to the fact that the alphas in the decay have very low energies in the laboratory frame and are therefore much more sensitive to the experimental detection thresholds.

Table 4.1: Branching ratios of the 1^+, T=1 15.11 and the 1^+, T=0 12.71 MeV states in ^{12}C from this work

Transition	Events	Det. eff.	γ branch[AW72]	γ branch
15.11 $\rightarrow$ 12.71	39	0.74 %	1.4±0.4 %	1.2±0.2 %
11.83	8	0.57 %	...	0.32±0.12 %
10.84	<7.3[a]	1.30 %	...	<0.13 %
10.3	65	1.09 %	(1.6)[b] %	1.4±0.2 %
7.65	70	0.36 %	2.6±0.7 %	4.4±0.8 %
0.00 and 4.44	40344	9.9 %	94±2 %	92.7±1.0 %
12.71 $\rightarrow$ 10.3	3	0.40 %	...	$0.9^{+0.6}_{-0.5}$ %
7.65	4	0.18 %	...	$2.6^{+1.6}_{-1.2}$ %
0 and 4.44	11660	13.9 %	100 %	$96.6^{+1.7}_{-1.3}$ %

[a] Upper limit valid at the 90% confidence limit.
[b] The 15.11 $\rightarrow$ 10.3 was not observed by [AW72] and was estimated from the measured β-decay branch.

We can correct the number of events for each resonance in Table 4.1 with the detection efficiencies. This corrected number of events can then be used to determine the partial alpha branches of the 15.11 MeV resonance and the 12.71 MeV resonance shown in Table 4.1. The results are compared with known literature values in cases where they are available. For a detailed look at these results refer to [Kir09].

4.2 Comparison to β-decay

The 15.11 MeV state forms an isospin triplet together with the ground states of ^{12}B and ^{12}N, making it ideal for comparing M1 γ decays with Gamow-Teller β decays [AW72]. This means that the results obtained for the γ branches can be compared to the GT β decays branches of ^{12}B and ^{12}N measured by our collaboration [Hyl09a]. Essentially this parallel makes it possible to separate the spin and orbital contributions of the M1 γ-transition strength, where the M1 γ width is given by the square of the sum of the spin and orbital amplitudes as

$$\Gamma_\gamma = (\gamma_\sigma + \gamma_l)^2, \tag{4.1}$$

Table 4.2: Allowed multipoles for γ decay of the 1^+ 15.11 MeV state. Recall that I_i=1 and π=positive

Final State (MeV)	J_f^π	Possible L values	$\Delta\pi$	Multipole
12.71	1^+	1,2	no	M1,E2
11.83	2^-	1,2,3	yes	E1,M2,E3
10.3	0^+	1	no	M1
7.65	0^+	1	no	M1
4.44	2^+	1,2,3	no	M1,E2,M3
0.00	0^+	1	no	M1

We want to isolate the orbital contribution to the M1 matrix element, and to do this we can compare γ_σ to the ft value of the GT β decay. Before proceeding, however, we need to make sure the that M1 transitions dominate the decays from the 15.11 MeV state.

4.2.1 Background on γ-decay

Let us look at the possible γ transitions of the 15.11 MeV resonance. The selection rules of angular momentum for γ-decay are as follows, with the exception that L$\neq$0 since there are no monopole transitions:

$$|I_i - I_f| \leqslant L \leqslant I_i + I_f$$

The parity selection rules determine whether the transition is magnetic or electric. If there is no change in parity, $\Delta\pi$=no, then it is electric if L is even, and magnetic if L is odd. If there is a change in parity, $\Delta\pi$=yes, then it is electric if L is odd, and magnetic if L is even. With these selection rules we can determine the possible multipole transitions for γ decay from the 15.11 MeV state in Table 4.2.

Not including the negative parity state at 11.83 MeV, we would like to determine which multipole will dominate in cases where more than one are possible. We can use Weisskopf estimates [BW52] to estimate the transition probabilities assuming a single nucleon is responsible for the transition. For M1 and E2 we have

$$\begin{aligned} \lambda(M1) &= 5.6 \times 10^{13} E^3 \\ \lambda(E2) &= 7.3 \times 10^{7} A^{4/3} E^5 \end{aligned} \tag{4.2}$$

where E the is the gamma energy in MeV and A is the mass number (A=12 in this case). One can see that lower multipoles are dominant. We can compare the relative intensity of M1 transitions to E2 transitions

$$\frac{\lambda(M1)}{\lambda(E2)} = \frac{5.6 \times 10^{13} E^3}{7.3 \times 10^7 A^{4/3} E^5} = 2.8 \times 10^4 E_\gamma^{-2} \tag{4.3}$$

It is clear from the above equation that increasing the gamma energy will decrease the dominance of the M1 transition. If we take the highest energy gamma transition of 15.11→7.65 MeV of E_γ =7.46 MeV, then we see that M1 will still dominate over E2 by a factor of about 3750:1. We can therefore assume that all γ decays will be dominated by M1 decay, except for the 11.83 MeV state, in which E1 will dominate. Now that we see that these γ decays to positive parity states in ^{12}C are essentially M1 transitions, we can explore the parallels between these transitions and Gamow-Teller decays.

4.2.2 β-decays and γ-decays

Alburger and Wilkinson [AW72] show that the expected parallel between Gamow-Teller β decay and M1 γ decay arises because the β-decay matrix element has the same form as the part of the M1 matrix element that depends on the nucleon spin. This was written in Equation 4.1 as

$$\Gamma_\gamma = (\gamma_\sigma + \gamma_l)^2,$$

where γ_σ and γ_l are the spin and orbital amplitudes, respectively. Therefore

$$\frac{\gamma_l}{\gamma_\sigma} = \frac{1}{\mu_p - \mu_n} \frac{\langle f \mid\mid \tau_l \mid\mid i \rangle}{\langle f \mid\mid \tau_\sigma \mid\mid i \rangle}$$

and since $\mu_p - \mu_n \approx 5$, we can see that the γ_σ will dominate. In order to compare experimental values of ft values and γ decay branching ratios Alburger and Wilkinson derive the following relation:

$$\Gamma_\gamma(ft) = \frac{1}{3} E_\gamma^3 \frac{e^2}{M^2 \hbar c^5} C (\mu_p - \mu_n)^2 (1 + \frac{\gamma_l}{\gamma_\sigma})^2 \xi^{-1} (ft)_F (1 + \delta^R)^{-1} \text{eV} \cdot \text{sec} \tag{4.4}$$

where C takes into account the isospin couplings

$$C = \left| \begin{pmatrix} T_f & 1 & T_i \\ T_z^\gamma & 0 & -T_z^\gamma \end{pmatrix} \Big/ \begin{pmatrix} T_f & 1 & T_i \\ T_{fz}^\beta & 1 & -T_{iz}^\beta \end{pmatrix} \right|^2 \tag{4.5}$$

Table 4.3: B(M1) values for the different final states populated in a γ-transition from the 15.11 MeV state. The γ_l^2 obtained from the comparison to the β decay of ^{12}N and ^{12}B are also shown

Final state (MeV)	J^π	ft value[a] ($\times 10^4$ s)	Γ_γ (eV)	γ_l^2 [b] (eV)	B(M1) (μ_N^2)	B(M1) (theory) [AW72][c]	[Kan07]
12.71	1^+	0.81(3)	0.49(10)	0.06(4)	3.0(6)	2.9	2.5
10.3	(0^+)	2.18(5)	0.55(10)	0.002(7)	0.43(8)	—	—
7.65	0^+	3.88(7)	1.8(3)	0.04(5)	0.37(7)	—	0.014
4.44	2^+	14(2)	0.9(4)	0.01(3)	0.07(3)	0.0931	0.09
0.00	0^+	1.222(5)	36.9(8)	0.03(2)	0.92(2)	0.768	0.17

[a] The β-decay ft values are taken from [Hyl09a].
[b] The smaller value of the two possibilities.
[c] These value are shell model calculations from Cohen and Kurath

T_f and T_i is the final and initial isospin value for the γ-decay (numerator) and β-decay (denominator). In both cases we have $T_f = 0$ since the isospin of the states in ^{12}C below the 15.11 MeV state is T=0. As for the isospin of the initial state, we will always have $T_i = 1$ because in the 15.11 MeV resonance is T=1 and the ground states of both ^{12}B and ^{12}N are also T=1. Since ^{12}C contains the same number of neutrons and protons, the projection of isospin is $T_z^\gamma = 0$ and also $T_{fz}^\beta = 0$. $T_{iz}^\beta = 1$ for ^{12}N and $T_{iz}^\beta = -1$ for ^{12}B. So for example in the case of coupling of γ-decay in ^{12}C with β-decay in ^{12}N we have:

$$C = \left| \begin{pmatrix} 0 & 1 & 1 \\ 0 & 0 & 0 \end{pmatrix} \Big/ \begin{pmatrix} 0 & 1 & 1 \\ 0 & 1 & -1 \end{pmatrix} \right|^2 = \left| -\sqrt{\frac{1}{3}} \Big/ \sqrt{\frac{1}{3}} \right|^2 = 1 \qquad (4.6)$$

Now, with $C = 1$, and taking the following values from [AW72]; $\xi^{-1} = (G_A/G_V)^2 = 1.503$, $(ft)_F = 3073$ s, and the "outer" radiative correction $\delta^R \approx 0$, we get

$$\gamma_\sigma^2 ft = 123\, E_\gamma^3 \text{ eV} \cdot \text{s}$$

We now have a formula where we can determine the spin part of the M1 matrix element from the ft value of the GT β decay. This allows us to isolate the orbital part γ_l in Equation 4.1, which can then be compared to theory in the future. Table 4.3 lists calculated values of γ_l and B(M1) values for different resonances in ^{12}C. Assuming M1 transitions dominate, the B(M1)

values are calculated from the partial widths given in Table 4.1 using the following [BM75]:

$$\Gamma_\gamma = 1.76 \times 10^{13} \hbar E_\gamma^3 B(M1)$$

where the partial width, Γ_γ is calculated from the branching ratios in Table 4.1. This calculation assumes a transition to the ground state of Γ_{γ_0} = (36.9±0.8) eV (the weighted average of [Ajz90, Che73, von00]), and a relative branching ratio to the 4.44 MeV state of (2.3 ± 0.9)% [AW72]. Knowing the branching ratio to the ground state is 92.7%-2.3%=90.4%, and that Γ_{γ_0} = (36.9 ± 0.8), we can obtain the partial widths for the other states as shown in Table 4.3.

The calculated B(M1) values are compared to theoretical calculations. The B(M1) predictions of Cohen and Kurath in [AW72] are based on shell model calculations, while the predictions from [Kan07] are based on the ab-initio antisymmetrized molecular dynamics (AMD) approach. This is a clear case where our experimental results can be directly compared to theory in order to make more robust theoretical models.

4.3 α-branch of the 15.11 MeV and 12.71 MeV resonance

4.3.1 α-branch of the 15.11 MeV resonance

Having extracted the γ branch of the 15.11 MeV state, it would be interesting to determine the α branch as well. We know that it must be very small, since the 15.11 MeV peak virtually disappears when the multiplicity four condition is imposed on the data (Fig. 3.10). Determining the α branch of the 15.11 MeV is especially difficult due to the large background present in the ^{10}B(^{3}He,p$\alpha\alpha\alpha$) reaction data. There are two different methods we used to try to determine the α branch, or at least provide an upper limit.

The first method was to look at the p+α multiplicity two coincidences. In order to remove any contribution from p+^{12}C coincidences we restricted our search of the α particle to greater than 60° in the laboratory frame (the heavy ^{12}C nucleus is kinematically focused in the forward direction). The p+α coincidence spectrum gives a clear signal of 500±100 events on top of a background of about 4000 events, shown in Fig. 4.5. Simulations were used to take into account the possible contribution from the γ-delayed 3α breakup of the 15.11 MeV state, which gave 280±30 events. Therefore the leftover

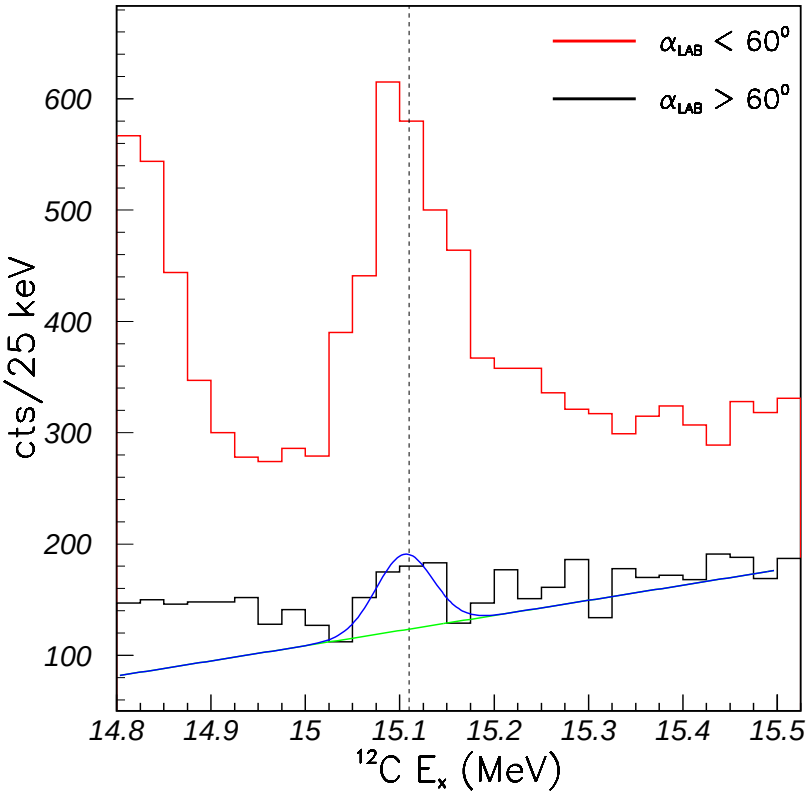

Figure 4.5: Excitation energy in ^{12}C of p+α multiplicity two data from the ^{10}B(^{3}He,p$\alpha\alpha\alpha$) reaction showing evidence for a signal of α of the 15.11 MeV state. The data is split into two regions in order to remove possible contribution from p+^{12}C coincidences. Red shows data where $\theta_\alpha^{lab} < 60°$ (forward angles) and in black is data with $\theta_\alpha^{lab} > 60°$ with contribution since. The red data shows a clear peak at 15.11 MeV due to the contribution from p+^{12}C coincidences. However, the black data, where any possible contribution from p+^{12}C coincidences has been removed with the condition that the α particles is restricted to laboratory angles greater than 60°, also shows a peak at 15.11 MeV, indicating the presence of a non-zero α-branch of the 15.11 MeV state. The peak has been fitted with a Gaussian on a linear background.

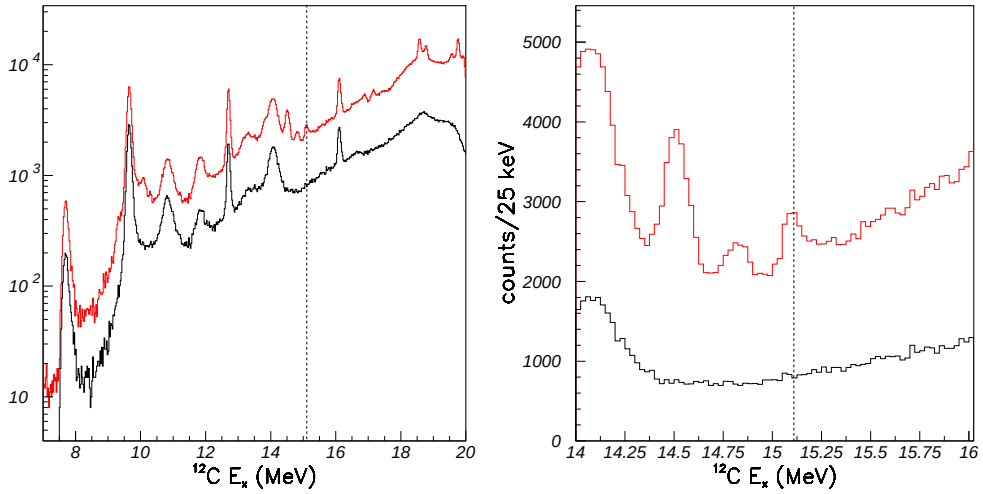

(a) (b)

Figure 4.6: (a) ^{12}C excitation energy obtained from the ^{10}B(^{3}He,p$\alpha\alpha\alpha$) reaction. In red is data with no condition on multiplicity, and in black is data of multiplicity four with requirements on energy and momentum conservation. The dashed line represents the position of the 15.11 MeV, visible only in the data with no conditions on multiplicity. (b) A blown-up part of the part (a) from the region between 14 MeV and 16 MeV to better see the region of the expected signal.

signal was 220±100, corresponding to a branching ratio of Γ_α/Γ=(2.8±1.2)% (error is given for 1σ).

We can compare this value to the one given by [BZT74] and adopted in the literature [Ajz90] of Γ_α/Γ=(4.1±0.9)%. Clearly this value is larger than ours, but it is important to mention that [BZT74] did not account for the 0.32% γ branch to the 11.83 MeV state and the 1.4% γ branch to the broad 10.3 MeV state. Therefore if we remove the contribution of these branches from their value, we arrive at Γ_α/Γ=(2.4±0.9)%, which is in good agreement with our value.

The second method was to search for a signal in the multiplicity four data. Figure 4.6(a) shows the ^{12}C excitation energy spectrum from this data with energy and momentum conservation requirements imposed in order to eliminate contribution from γ-delayed 3α decays. Even if we focus in on the region where we would expect to see a peak if the 15.11 MeV state decays via alphas, as in Fig. 4.6(b), there is still no clear signal. However, if we again assume a linear background as in Fig. 4.5, we can establish an upper bound of a signal hiding in the background. Once we correct for the detection

efficiencies, we get an upper limit of 3.3% which is in agreement with our estimate of the α-branch using the previous method.

4.3.2 α-branch of the 12.71 MeV resonance

Determining the branching ratio of the 12.71 MeV resonance is much easier than in the case of the 15.11 MeV resonance. The branching ratios of the 12.71 MeV can be extracted directly from the observed ratio of α to γ decays and from the detection efficiencies derived from simulations. From table 4.1 we obtain the efficiency corrected number of events for all γ-decays of the 12.71 MeV state to be $3/0.0040 + 4/0.0018 + 11660/0.139 = 86856$ efficiency corrected events for γ-decays.

For the alpha decays, we continue the projection in Fig. 4.4(a) to include the alpha decays of the 12.71 MeV state and obtain 22560 events. Using the detection efficiency obtained in Table 3.2 of 0.69%, we obtain a value of $\Gamma_\alpha/\Gamma = (97.4\pm0.3)\%$ and $\Gamma_\gamma/\Gamma = (2.6 \pm 0.4)\%$ [Kir09], in agreement with $\Gamma_\gamma/\Gamma = (2.22 \pm 0.14)\%$ in [Ajz90].

4.4 A note on isospin mixing

Alpha-decay of the T=1, 1^+ 15.11 MeV state would, in principle, violate the conservation of isospin. However it was shown above that there exists a small alpha-branch of the 15.11 MeV state which must be due to isospin mixing with another state. It turns out that there is a T=0, 1^+ state at 12.71 MeV which must be mixing with the 15.11 MeV state. Perhaps the small alpha branch in the 15.11 MeV state comes directly from the presence of a small isospin 0 contribution due to mixing with the 12.71 MeV state. It would then be interesting if we could somehow deduce the amount of mixing from the alpha branch in the 15.11 MeV state. Similarly, if the Γ_α/Γ of the 15.11 MeV state is a result of mixing with the 12.71 MeV state, then perhaps we can relate Γ_α/Γ of the 15.11 MeV state directly with that of the 12.71 MeV state, so that $\Gamma_\alpha/\Gamma(15.11) = 1 - \Gamma_\alpha/\Gamma(12.71)$. These assumptions hold since there are no other 1^+ states in ^{12}C in the energy range of these two.

In [Rei70] they consider the question of isospin mixing in these two 1^+ states in ^{12}C and write the following equations:

$$
\begin{aligned}
\mid 12.71\rangle &= \alpha \mid T=0\rangle + \beta \mid T=1\rangle \\
\mid 15.11\rangle &= \beta \mid T=0\rangle - \alpha \mid T=1\rangle
\end{aligned}
$$

where $\alpha^2 + \beta^2 = 1$. We can then compare the alpha branches of the 15.11 MeV and 12.71 MeV states to the isospin mixing

$$\frac{\theta_\alpha^2(15.11)}{\theta_\alpha^2(12.71)} = \frac{\beta^2}{\alpha^2} \tag{4.7}$$

where the θ_α^2 is the dimensionless reduced width and can be obtained from the absolute particle widths Γ_α. The absolute α-particle widths Γ_α of the 15.11 MeV and the 12.71 MeV states are calculated from the relative widths obtained in Section 4.3 and the tabulated widths of $\Gamma(12.71) = 18.1$ eV and $\Gamma(15.11) = 43.6$ eV [Ajz90]. This gives us absolute widths of

$$\Gamma_\alpha(12.71) = 17.6\text{eV}$$
$$\Gamma_\alpha(15.11) = 1.2\text{eV}$$

To calculate the dimensionless reduced width, we have [Rei70]

$$\theta_\alpha^2 = \Gamma_\alpha/(2kRP_c \cdot \frac{3}{2}\hbar^2/\mu R^2)$$

where P_c is the Coulomb penetrability, k is the relative momentum of the α-particle and ^{8}Be nucleus, and $\frac{3}{2}\hbar^2/\mu R^2$ is the single-particle reduced width. Since we are taking a ratio of these two values, all of the elements are the same except for the penetrability which depends on the energy available to the alpha particle. This comes to $\frac{15.11-7.275-3.06}{12.71-7.275-3.06} = 4.775/2.375 \approx 2$, so Equation 4.7 becomes

$$\frac{\theta_\alpha^2(15.11)}{\theta_\alpha^2(12.71)} = \frac{\beta^2}{\alpha^2} = \frac{\Gamma_\alpha(15.11)}{2 \cdot \Gamma_\alpha(12.71)} = 0.0341 \tag{4.8}$$

We can now determine α and β to be

$$\alpha = 0.983, \beta = 0.182$$

resulting in an isospin impurity of $\beta^2 \approx 3.3\%$, similar to the value of 3.5% obtained in [Rei70]. Using this value for isospin mixing one could derive the γ-branches for the 12.71 MeV and 15.11 MeV states. It is important to point out that the isospin mixing numbers are based on many assumptions and so the values must not be taken too seriously. However the idea behind the

isospin mixing could in principle be applied to the 2^+, T=1 state at 16.11 MeV in a similar manner. Since this state has a clear α-branch there must be isospin mixing with a lower-lying 2^+ state in ^{12}C. The only known state is a bound state at 4.44 MeV. However perhaps this could be used to confirm the presence of a lower-lying 2^+ in the energy region of the 16.11 MeV state and its properties. This would be something interesting to investigate and can perhaps become another tool to search for the elusive 2^+ rotational state based on the Hoyle state discussed at length in Chapter 1.

As a math atheist, I should be excused from this.

Calvin & Hobbes

5

Overview of ^{12}C Resonances

The main goal of this work is to search for possible new states in ^{12}C and to gain a better understanding of known states. It is clear that in order to fully understand the ^{12}C spectrum and to disentangle the different resonances, it is important to use a more sophisticated method such as the R-matrix formalism. The R-matrix formalism plays a crucial role in understanding the broad structures underlying the ^{12}C excitation spectrum, and a very detailed analysis is necessary in order to fully disentangle the spins and parities of the broad structures near the triple-alpha threshold in ^{12}C as discussed in [Hyl10]. The tools necessary for such an analysis are discussed in Section 5.3. However, we can still use a more simple approach if we wish to focus on determining properties of non-interfering, narrow resonances.

Section 5.1 describes the procedure used to determine the properties of such resonances, and a justification is first given to ensure that using a Breit-Wigner function to fit the resonances is valid. In Section 5.2 two particular resonances of interest will be looked at in more detail using Dalitz plot, a method that will also be introduced. Finally, as discussed above, Section 5.3 introduces R-matrix theory and describes a preliminary analysis where the resonances in ^{12}C were fit using the R-matrix formalism.

5.1 Determining the properties of ^{12}C resonances

I will start by describing how to better determine the J^{π} and the energy and widths of resonances where possible, as well as to determine the partial branching of natural parity states. Table 5.1 shows a list of the different resonances examined in detail in this work and gives which properties we seek to improve upon. There are some cases in which our data will not be able to improve over the literature values, e.g. widths for very narrow resonances, energies for well-studied resonances, or states which were used in the calibration. In fact resonances with well-defined energies were used to

Table 5.1: Literature values [Ajz90] for energy, width, and J^π of resonances in ^{12}C are given in the first part of the table. Possible improvements on the properties of these states are listed on the right hand part of the table, as well as which reaction data is used to study the particular resonance. The Hoyle state at 7.65 MeV, the 12.71 MeV state, and the 16.11 MeV state have assigned values for energy and width which could not be improved upon in this analysis. The 9.64 MeV state and the 12.71 MeV state were used to re-calibrate the level energies for the ^{11}B target data, and the 16.11 MeV state was also used to recalibrate the level energies for the ^{10}B data. The broad 10.3 MeV state needs to be studied with a more sophisticated approach [Hyl10] than the one applied here. Partial branches of states of natural parity (shown in **bold**) are also determined.

E_x (keV)	Γ (keV)	J^π	Energy	Γ	Target(s)
7654(0.12)	$8.5(1)\times10^{-3}$	$\mathbf{0^+}$	—	—	^{11}B,^{10}B
9641(5)	34(5)	$\mathbf{3^-}$	—	yes	^{11}B,^{10}B
10300(300)	3000(700)	(0^+)	—	—	^{11}B,^{10}B
10844(16)	315(25)	$\mathbf{1^-}$	yes	yes	^{11}B,^{10}B
11828(16)	260(25)	2^-	yes	yes	^{11}B,^{10}B
12710(6)	$18.1(2.8)\times10^{-3}$	1^+	—	—	^{11}B,^{10}B
13352(17)	375(40)	(2^-)	yes	yes	^{11}B
14083(15)	258(15)	$\mathbf{4^+}$	yes	yes	^{10}B
16106(0.7)	5.2(0.2)	$\mathbf{2^+}$	—	—	^{10}B
20500(100)	300(50)	(3^+)	yes	yes	^{10}B

re-calibrate the spectra.

The excitation spectra of ^{12}C determined from the energy of the light-ion (Eq. 3.2) from both the reactions with the ^{11}B and ^{10}B targets are reproduced in Fig. 5.1. The spectra are analyzed by fitting the corresponding peaks to a Breit-Wigner function. This approach is justified since the known levels are relatively narrow ($\Gamma < 500$ keV) and do not have any known interfering states (states with the same J^π) which could deform their peak shapes. However there are broad resonances in ^{12}C which may have the same spin-parities as states we want to fit. There are several criteria which must be looked at before continuing with this approach:

- **No states nearby with the same spin-parity**. There are no known states in ^{12}C with the same spin-parity as the states to be fitted us-

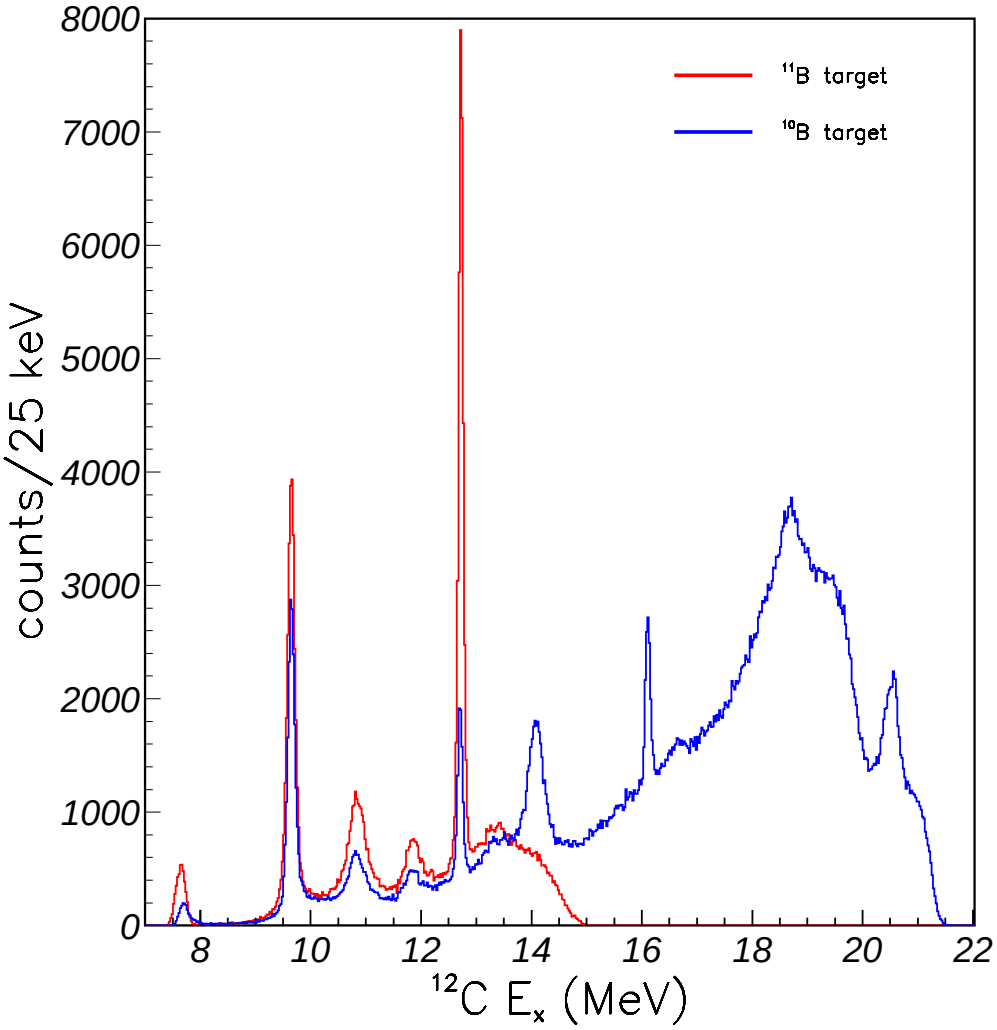

Figure 5.1: Excitation energy of ^{12}C from multiplicity four data for both the ^{11}B and ^{10}B target reactions. As previously discussed the ^{11}B target reaction data has a smaller Q-value so it only populates states in ^{12}C up to 15 MeV in excitation energy, while the ^{10}B target reaction data populates much higher excitation energies.

ing this method. However there exists a possibility that broad states with unknown spin-parity assignments may interfere with one of these resonances. If this were true then the peaks we seek to fit would have asymmetric peaks. This is not the case as seen in Fig. 5.5.

- **Contributions from background**. Background contribution could be from different reaction channels with the same multi-particle final states or from very broad resonances in ^{12}C. The issue of background contribution from different channels is discussed in Section 5.1.1. Background contribution from a very broad resonance would be slow-varying so that the inclusion of a linear background is sufficient.

The energy and width of each resonance was determined first before extracting partial branches of the natural parity states. The fitting procedures were similar yet in the case of extracting widths great care was taken to take into account the different resolutions of the detectors. The states in ^{12}C which are sufficiently narrow and which do not have interfering states were treated as a simple Breit-Wigner (Eq. 1.2) with a linear background. The Breit-Wigner function was folded with a Gaussian distribution to simulate the experimental resolution which was especially important for narrow states. In order to get independent determinations of properties, the data was separated by reaction and by multiplicity, and the excitation energy was determined by the primary ejectile. To extract widths and energies, the data was also separated depending on where the primary ejectile was detected since the resolution of the detectors vary depending on the detector. However, when determining the branching ratios of decay via the ground state of ^{8}Be the data was not subdivided into detector or angle in order to maximize statistics.

5.1.1 Determination of energy and width

Accurate values for the resolution were very important in fitting the ^{12}C spectra, especially for states with a width similar to the resolution (roughly 40 keV), and were therefore calculated for each state and at the different angular bins. The data was divided up into angular bins of 10° for each DSSSD, where the angle is determined by the primary ejectile (proton or deuteron, depending on the choice of target). This is significantly larger than the experimental angular resolution of $\approx 3°$, and the choice of 10° was made so as to have a significant number of statistics while also taking into account the dependence of the resolution on the angle.

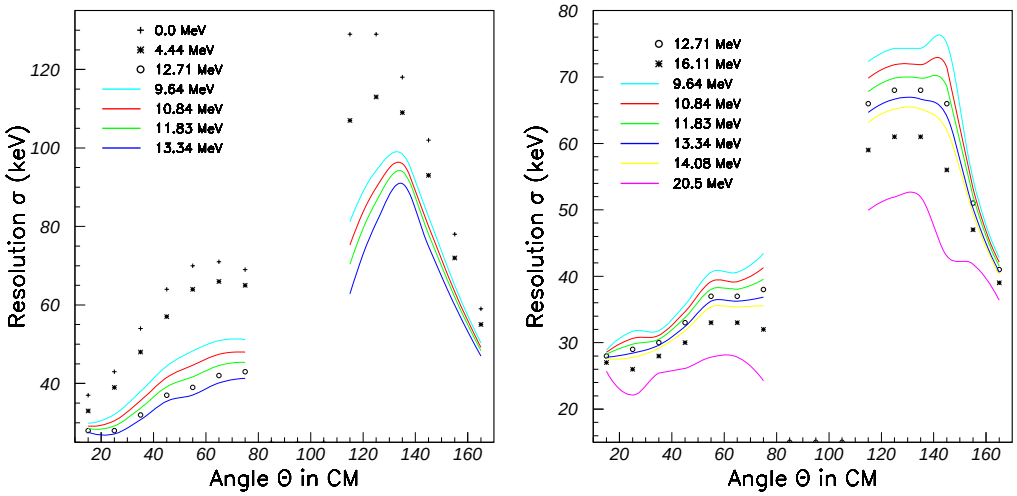

(a) (b)

Figure 5.2: Detection resolution in keV as a function of energy and θ_{CM}. (a) Data from the ^{11}B(^{3}He, d$\alpha\alpha\alpha$) reaction. The resolutions for DSSSD1 (forward angles) and DSSSD4 (backward angles) are shown. (b) Data from the ^{10}B(^{3}He, p$\alpha\alpha\alpha$) reaction, showing resolutions for DSSD1 and DSSD4. The 32×32 DSSSD1 has better resolution than the 16×16 DSSSD4 since DSSSD1 has 2 mm strips compared to the 3 mm wide strips of DSSSD4. The superior angular resolution gained by having more narrow strips is reflected in the figures.

Experimental resolution

The experimental resolution is determined by the intrinsic detector resolution, the angular resolution, and energy losses from the angle of entry, so there is a dependency on the energy and angle of the primary ejectile, and on the detector. The total detection resolution for each resonance was calculated for states with very narrow widths relative to the resolution ($\Gamma <$ 1 keV), and then extrapolated to the peak energies. To determine the resolution in the case of the ^{11}B target, the ground state, 4.4 MeV state, and the 12.71 MeV state were used for DSSSD1 and DSSSD2, while only the first two were used for DSSSD3 and DSSSD4 since the 12.71 MeV peak is not seen at backwards angles. In the analysis of the ^{10}B(^{3}He, p$\alpha\alpha\alpha$) data, only the 12.71 MeV and the 16.11 MeV states were used. The detection resolutions applied to the ^{10}B and ^{11}B targets are shown in Fig. 5.2.

Background contribution

When extracting the widths of states from the experimental spectra it is very important that one has a good understanding of the background. The complete kinematics allows us to remove most unwanted background and random coincidences, yet it is not possible to completely remove contribution from background channels with the same multi-particle final states (Sec. 3.3). Both reactions have contributing background channels. The ^{10}B target data has the following channels

$$^{10}\mathrm{B} + {}^{3}\mathrm{He} \rightarrow \left\{ \begin{array}{rl} p + {}^{12}\mathrm{C} & \rightarrow p + \alpha + {}^{8}\mathrm{Be} \\ \alpha + {}^{9}\mathrm{B} & \rightarrow \alpha + p + {}^{8}\mathrm{Be} \\ \alpha + {}^{9}\mathrm{B} & \rightarrow \alpha + \alpha + {}^{5}\mathrm{Li} \\ {}^{8}\mathrm{Be} + {}^{5}\mathrm{Li} & \rightarrow {}^{8}\mathrm{Be} + p + \alpha \end{array} \right\} \rightarrow p + 3\alpha \qquad (5.1)$$

while for the ^{11}B target the contributing channels are

$$^{3}\mathrm{He} + {}^{11}\mathrm{B} \rightarrow \left\{ \begin{array}{rl} d + {}^{12}\mathrm{C} & \rightarrow d + \alpha + {}^{8}\mathrm{Be} \\ \alpha + {}^{10}\mathrm{B} & \rightarrow \alpha + d + {}^{8}\mathrm{Be} \\ {}^{8}\mathrm{Be} + {}^{6}\mathrm{Li} & \rightarrow {}^{8}\mathrm{Be} + d + \alpha \end{array} \right\} \rightarrow d + 3\alpha \qquad (5.2)$$

Fortunately, it is possible to remove some contribution from different channels. In the case of the ^{11}B target data, we do not see the α+^{10}B channel since the emitted deuterons are not energetic enough to be seen in the ΔE-E plot. Additionally, contribution from narrow states in ^{5}Li and ^{6}Li can be removed by selecting on the regions shown in the E_{α_i} versus $E_{p/d}$ plots in Figs. 5.3 and 5.4 for the ^{10}B target and ^{11}B target data, respectively. Since the broad background states give a constant background for a constant $E_{p/d}$, their contribution to the fits are taken into account by assuming a linear background.

Results on energy and width of the ^{12}C resonances

The fits for each data set are done individually for each detector over angular bins of ten degrees. As an example, Fig. 5.5 shows some fits to the ^{12}C resonances made to certain angles for the DSSSD1 from multiplicity three data in the ^{11}B(^{3}He, d$\alpha\alpha\alpha$) reaction. Although the detector was divided into angular bins of ten degrees ranging from 10°-80° only four regions are displayed in the figure. The energy from the fit of the 9.64 and the 12.71 MeV resonance was used to adjust the individual calibrations for each angular bin. The results of the values obtained for excitation energies are shown in Fig. 5.6 for this same data set, while the results of the widths obtained for the DSSSD1

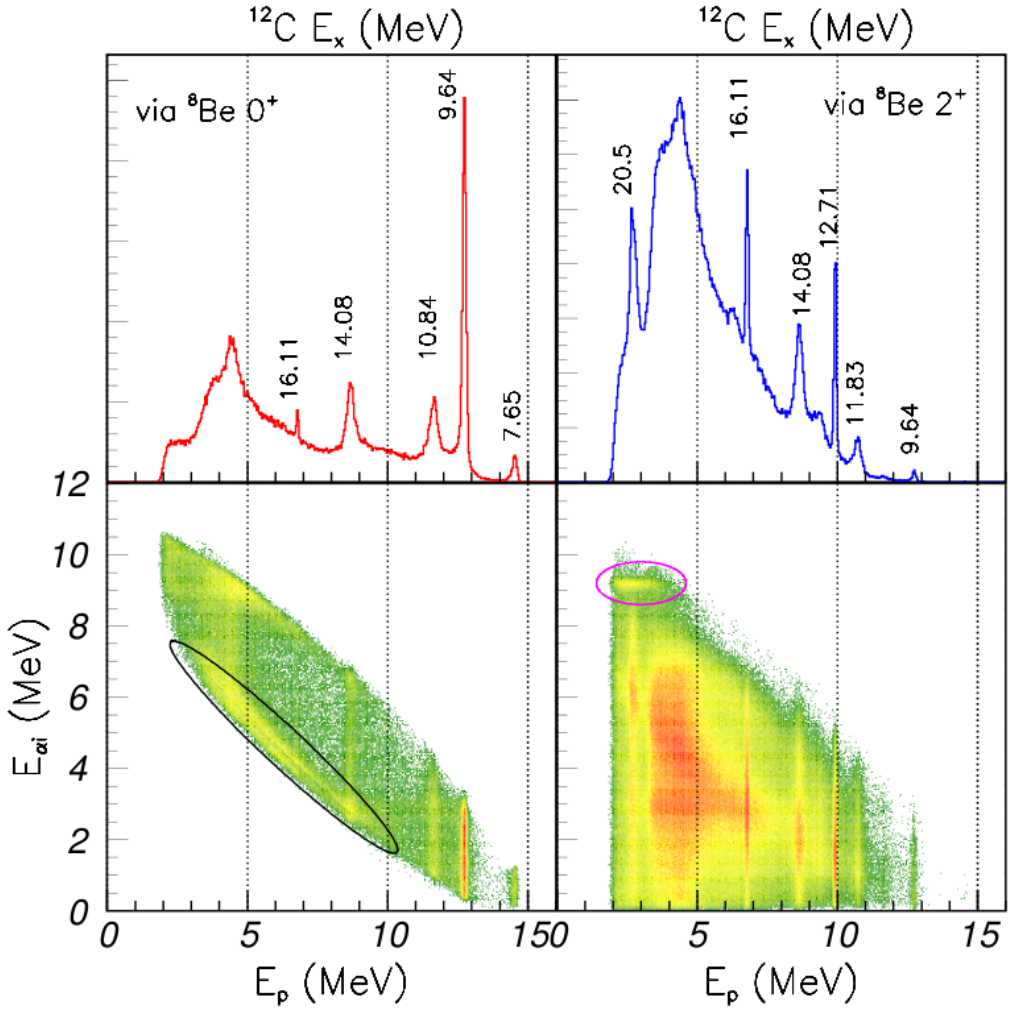

Figure 5.3: Multiplicity four data from the ^{10}B(^{3}He,p$\alpha\alpha\alpha$) reaction. The data has been split into decay which proceeds via the ground state in ^{8}Be (left) and the rest (right), as explained in the text. Levels in ^{12}C can be seen as constant proton energies, and are seen in the projections in the top of the E_{α_i} versus E_p plot figure. The contribution from the narrow ground state of ^{5}Li is circled in black in the ^{8}Be ground state branch. Similarly, in the plot of decay via the 2^+ of ^{8}Be, the narrow 2.36 MeV state in ^{9}B is circled in pink. Both of these contributions have been removed when doing the fits. There are clearly structures from broader states visible in both plots which cannot be fully removed.

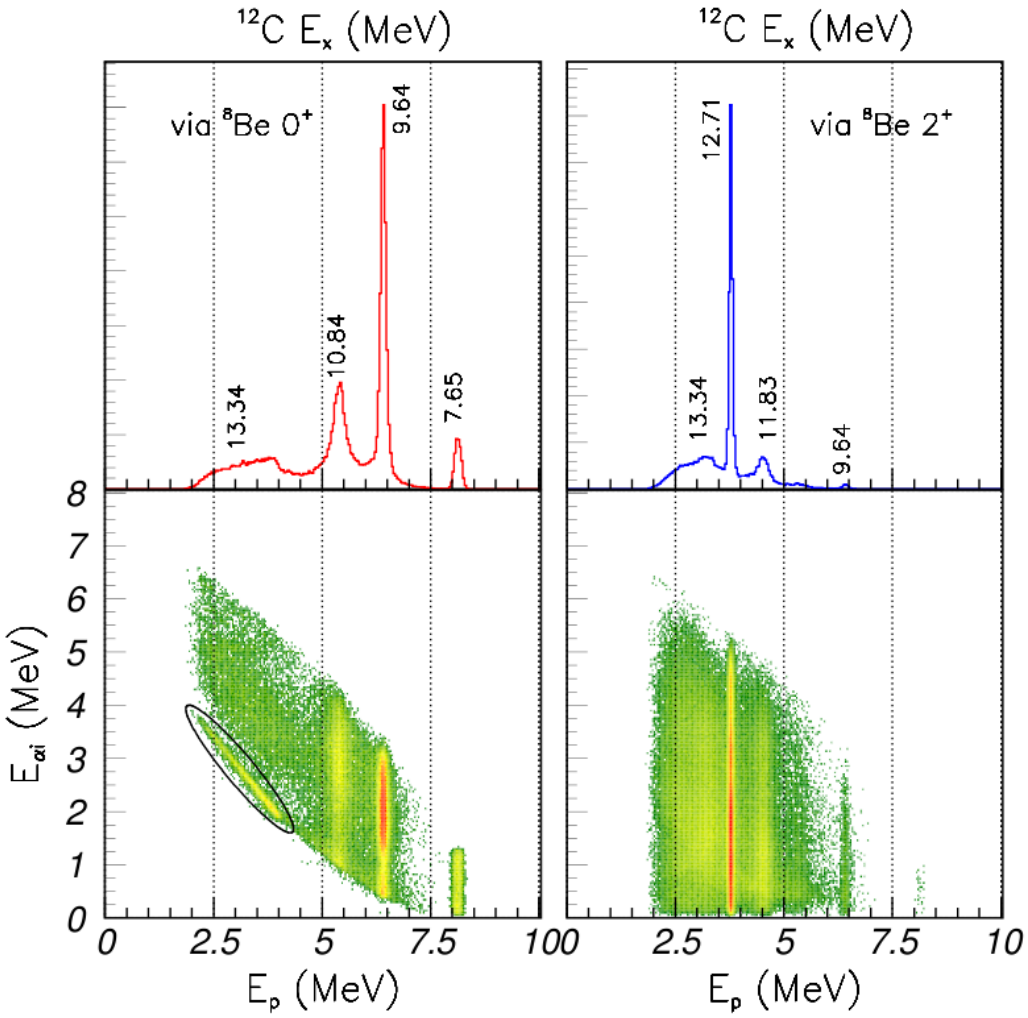

Figure 5.4: Multiplicity four data from the ^{11}B(^{3}He,d$\alpha\alpha\alpha$) reaction. As in Fig. 5.3, the data has been split into decay which proceeds via the ground state in ^{8}Be (left) and the rest (right). It is clear from the projections of the deuteron energies that the ^{12}C excitation energy spectrum is cleaner than that obtained in the reaction with the ^{10}B target. The narrow 2.19 MeV state in ^{6}Li is circled in black on the left, and was removed when performing fits on the data.

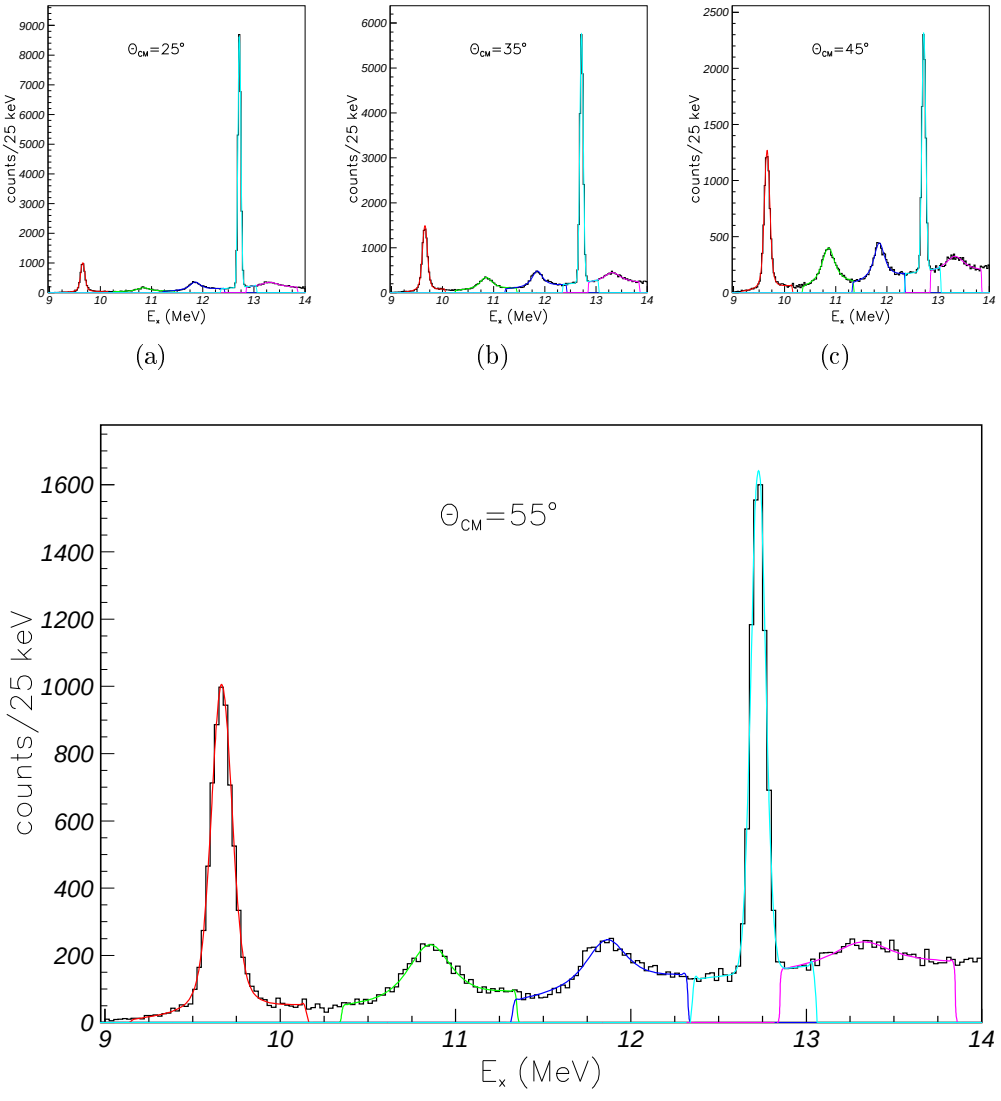

(a) (b) (c)

(d)

Figure 5.5: Excitation energy in ^{12}C for different CM angles of the deuteron in the ^{11}B(^{3}He,d$\alpha\alpha\alpha$) multiplicity 3 reaction data. The Breit-Wigner function folded with a Gaussian distribution fits are shown for the 9.64, 10.84, 11.83, and 13.35 MeV states.

^{10}B(^{3}He, p$\alpha\alpha\alpha$) data set are shown in Fig. 5.7. The weighted average of the values and the statistical errors are displayed in the figures. However, the errors do not take into account systematic errors due to possible background fits and to errors in the experimental resolution. A systematic error of 5 keV was assigned to the excitation energies as determined by the adjustments made when re-calibrating the spectra. The systematic errors of the widths was determined individually for each state by varying the background models (e.g. one degree versus two degree polynomial).

The average values for excitation energy and widths of the resonances in ^{12}C for each target are given in Table 5.2 along with both the systematic and statistical errors. Only DSSSD1 was used to determine the width of the 9.64 resonance since it had the best experimental resolution of the four detectors. This is a result of the superior angular resolution and can be seen in Fig. 5.2.

The final values for excitation energies and widths resulting from averaging over the two targets are given in Table 5.3. To determine the errors, first the total error σ was assigned for each target value from the relation $\sigma = \sqrt{\sigma_{stat}^2 + \sigma_{syst}^2}$. The weighted error was corrected for overdispersion where necessary as follows:

$$\sigma_{\bar{x}} = \sqrt{\frac{1}{\sum(1/{\sigma_i}^2)} \frac{1}{(n-1)} \sum_n \frac{(x_i - \bar{x})^2}{\sigma_i^2}} \tag{5.3}$$

The values for the excitation energy of the different ^{12}C resonances given in Table 5.3 are within error of the literature values, with the exception of the 13.35 MeV state. However there are cases where the width of the resonances have substantial deviations from literature values. The width of the 3^- 9.64 MeV state is larger than that given in the compilation of [Ajz90], although the value we obtain agrees very well with the value of $\Gamma = 42(3)$ keV in [Fre09]. The very large deviation between for the width of 13.35 MeV state 375(40) keV in [Ajz90] versus our value of 427(18) keV could be accounted for by the fact that the literature value [Ajz90] is averaged over many different values: 500±80 keV [RRP71], 290±70 keV [Wag66], 430±100 keV [BDE62], 355±50 keV [SB65], 700±100 keV [HM61].

5.1.2 Partial branches

The advantage of having the individual alpha energies is that it allows us to separate the decay path of the alpha particles through ^{8}Be by using the invariant mass technique (Sec. 3.5.1). The gate imposed on the $\alpha - \alpha$ relative energy was from 0-230 keV in the case of the multiplicity three data,

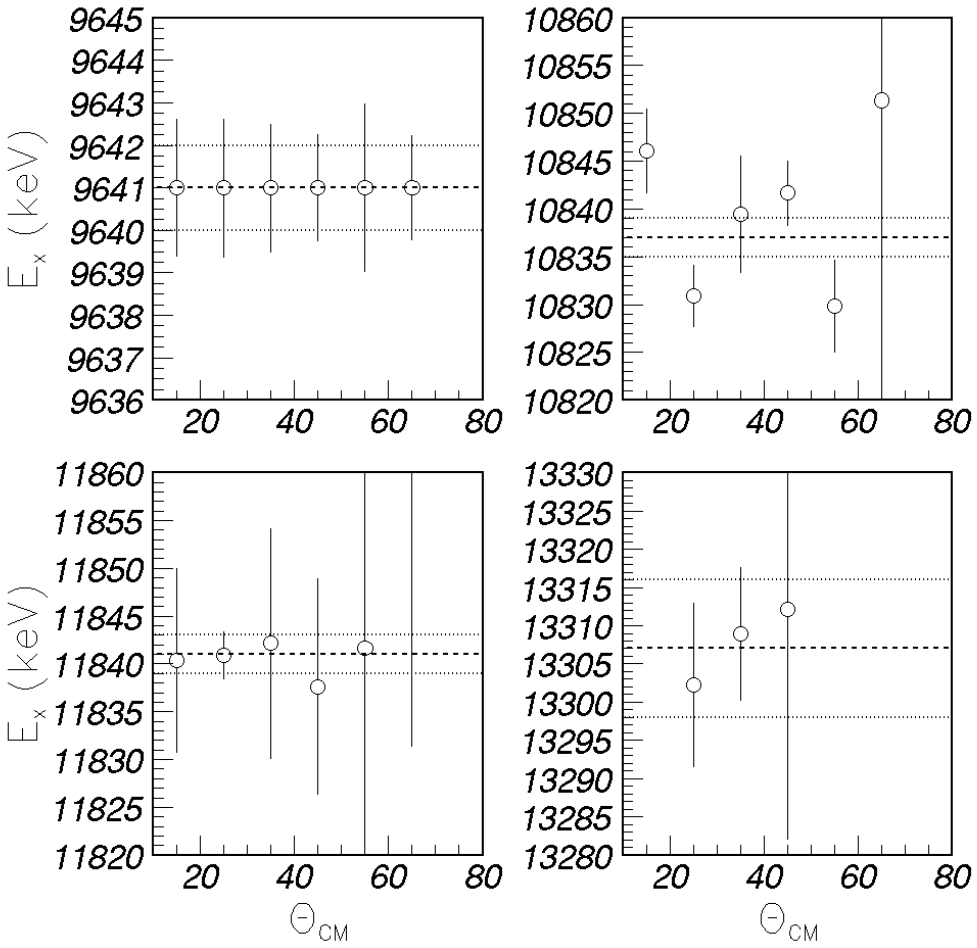

Figure 5.6: Experimental values of the excitation energy in ^{12}C versus θ_{CM} for DSSSD1 in the multiplicity three ^{11}B(^{3}He,d$\alpha\alpha\alpha$) reaction data. The average value over the different angles and the associated error are shown for each resonance. The 9.64 MeV state was used to re-calibrate the spectra at each angular bin. Only three angular bins are used to determine the excitation energy of the 13.35 MeV resonance since at higher angles the intensity decreases.

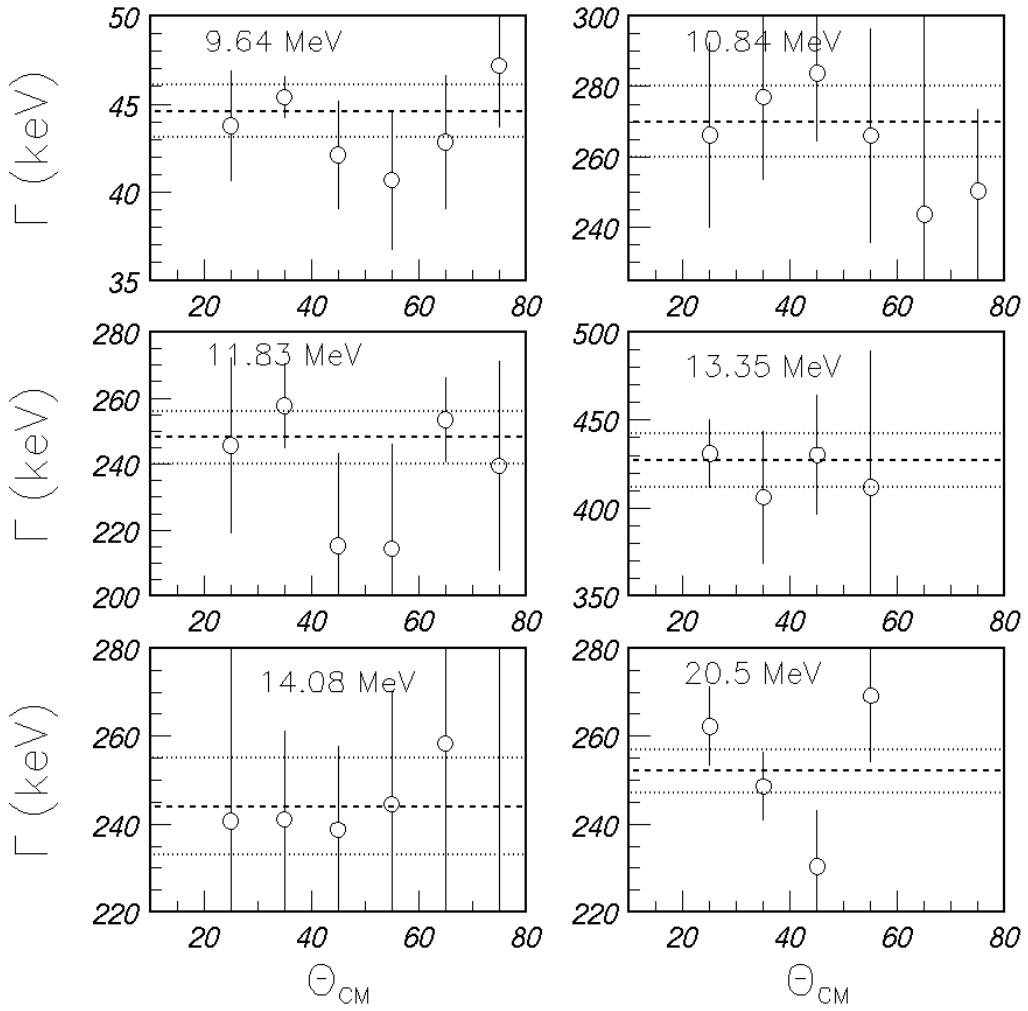

Figure 5.7: Widths and errors of the 9.64, 10.84, 11.83, 13.35, 14.08, and 20.5 MeV resonances in ^{12}C versus θ_{CM} for DSSSD1 in the multiplicity three ^{10}B(^{3}He,p$\alpha\alpha\alpha$) reaction data (the widths for the 13.35 MeV resonance are taken from the multiplicity three ^{11}B(^{3}He,d$\alpha\alpha\alpha$) data set). The values are averaged over the angular bins for each DSSSD, and then averaged over the different DSSSDs.

Table 5.2: Both statistical errors and systematic errors are given. The systematic errors in the energy determination is determined by the calibration error in the determination of the resonances at 9.64 MeV, 12.71 MeV, and 16.11 MeV. The systematic error for the width is determined by the uncertainty in the experimental resolution for the 9.64 MeV state, and by differences attributed to the effect of the background for the other states.

E_x ^{12}C (MeV)	target	E_x (keV)	σ_{stat} (keV)	σ_{syst} (keV)	Γ (keV)	σ_{stat} (keV)	σ_{syst} (keV)
9.64	^{10}B	—	—	—	44.6[a]	0.9	5[b]
9.64	^{11}B	—	—	—	43.2[a]	1.4	5[b]
10.84	^{10}B	10826	2	5	272	10	5
10.84	^{11}B	10838	1	5	276	5	10
11.83	^{10}B	11821	2	5	246	7	10
11.83	^{11}B	11839	1	5	242	5	6
13.35	^{11}B	13307	7	5	427	15	10
14.08	^{10}B	14074	1	5	250	7	9
20.5	^{10}B	20559	1	5	252	5	14

[a] Only DSSSD1 was used to determine the width due to the better experimental resolution (see Fig. 5.2).

[b] The assigned systematic error of 5 keV is determined exclusively from the error in the experimental resolution of 2 keV, which accounts for an uncertainty of 5 keV.

Table 5.3: New values obtained for the energy and width of resonances in ^{12}C. Unless otherwise noted, the literature values of J^π, Γ, and E_x are taken from [Ajz90]. The energy of the 16.11 MeV state and the 9.64 MeV state were fixed. The results are preliminary, and the final results will be published in [Alc10].

E_x ^{12}C (keV)	J^π	Γ (keV)	E_x (keV) this work	Γ (keV) this work
9641(5)	3^-	34(5)	—	44(4)
10844(16)	1^-	315(25)	10833(9)	274(7)
11828(16)	2^-	260(25)	11830(13)	243(6)
13352(17)	(2^-)	375(40)	13307(8)	427(18)
14083(15)	4^+	258(15)	14074(5)	249(11)
20500(100)	(3^+)	300(50)	20559(5)	252(15)

and between 40-150 keV in the multiplicity four data set (recall the ground state is situated 92 keV above the 2α threshold).

The method used above to determine widths and energies of the peaks was similarly used to determine the partial branches of the states of natural parity. However in this case the data was not divided into different angular bins so as to accumulate more statistics. In addition, the branching ratios need to be corrected for the detection efficiency of the setup. Including the sequential breakup of the resonances both through the ground state and through the broad 2^+ state was done through the use of Monte Carlo simulations (Section 3.4) in a similar manner as in Section 4.1.1. In the case of breakup through the 2^+ state in ^{8}Be, the particles were assumed to breakup into the available phase space.

Efficiency correction

To correct the branching ratios for the detection efficiency, the first step was to use the simulations to determine the efficiency for detecting decay through the 0^+ and 2^+ state in ^{8}Be. The angular distribution expected for the alpha particles depends on the intermediate decay state, here ^{8}Be(0^+) and ^{8}Be(2^+), so the detection efficiency will be different for each case. This was taken into account by simulating a 100% decay through the ground state for a given resonance, and then calculating the branching ratio to the ground state, eff_0. The same was done to determine the efficiency of the branching ratio to decay

via the 2^+ state in ^{8}Be, eff_2. This will take into account all factors associated with the determination of decay through the different states in ^{8}Be, such as detection efficiency and the effect of the size of the gate on the ^{8}Be ground state.

To correct for efficiency one needs to correct the number of counts obtained in the data for decay via the 0^+ state (N_0) and the decay via the 2^+ state (N_2). To determine the number of counts corrected for efficiency going through the 0^+ state (N_0') and 2^+ state (N_2'), we have the following expressions

$$N_0' \cdot \text{eff}_0 + N_2' \cdot (1 - \text{eff}_2) = N_0 \tag{5.4}$$

$$N_0' \cdot (1 - \text{eff}_0) + N_2' \cdot \text{eff}_2 = N_2 \tag{5.5}$$

$$N_0' + N_2' = N_0 + N_2 \tag{5.6}$$

Therefore the final efficiency corrected ratio for decay via the 0^+ state in ^{8}Be is $\frac{N_0'}{N_0'+N_2'}$

Correction for penetrability

The branching ratios also were corrected for the presence of the ghost of the ground state in ^{8}Be (the blown-up tail at high energy). As in the case of the Hoyle state (Section 1.3), the ground state of ^{8}Be is near threshold and its shape will be deformed in a similar manner as the Hoyle state (Fig. 1.6). If a gate is placed on the ground state peak at 92 keV, then a decay through the blown-up tail of the ground state will be regarded in the analysis as decaying via the 2^+ state in ^{8}Be and the branching ratio determined for decay through the ground state in ^{8}Be will be lower. However when making these corrections the assumed nuclear radius of the ^{8}Be+α system will have an effect on the shape of the ghost peak.

The radius of the system is defined as the channel radius, $a_c = r_0(A_1^{1/3} + A_2^{1/3})$ where A_1 is the the number of nucleons in the alpha particle and A_2 is the the number of nucleons in ^{8}Be. The choice of r_0 can vary the shape of the ghost and therefore affect the extracted branching ratios. This can be better understood schematically in Fig. 1.7, where increasing the value of the nuclear radius, r_0, will reduce the Coulomb radius so that the tunneling probability will increase, which will increase the penetrability. Increasing the penetrability, as seen in Eq. 1.2, will increase the probability of decay and hence the intensity of the peak. This increase in intensity will affect the decay to both the ground state peak at 92 keV in ^{8}Be as well as the higher energy tail, but will have a larger effect on the decay to the 92 keV peak. A

Table 5.4: Branching ratios of natural parity resonances in ^{12}C to the ground state of ^{8}Be. The branching ratios are shown with and without correcting for the decay via the ghost of the ^{8}Be ground state (with $r_0 = 2$ fm for ^{8}Be). The alpha-decay width to the ground state of ^{8}Be is calculated from the new values for the widths given in Table 5.3 and from the branching ratios. Note that the effect of including the ghost significantly increases the efficiency corrected branching ratios of the lower-energy excited states.

E_x ^{12}C (MeV)	J^π	B.R. % (no corr.)[a]	B.R. % (corr.)[b]	B.R. % (literature)	$\Gamma_{\alpha 0}$ (keV)
9.64	3^-	96.3(1)	99.5(6)	97.2[Fre07]	32(2)
10.84	1^-	94.7(5)	99.4(6)	—	249(2)
14.08	4^+	22.8(2.0)	24.2(2.0)	17(4)[c]	50(11)
16.11	2^+	5.6(1)	6.4(1)	4.4[d]	0.3(1.0)[e]

[a] Branching ratios are to the ground state of ^{8}Be. This does not include the effects of decay through the ghost.

[b] Branching ratio to the ground state of ^{8}Be, with the effect of the ghost peak included.

[c] Ref. [Fre07] gives the branching ratio of 17% and [Cau91] gives a value of $\Gamma_{\alpha 1}/\Gamma$=0.83 ± 0.04, corresponding to 17(4)% as well.

[d] Ref. [Ajz90] gives $\Gamma_{\alpha 0} = 0.29$ keV and $\Gamma_{\alpha 1} = 6.3$ keV

[e] Using the tabulated value of Γ=5.3 ± 0.2 keV from [Ajz90]. This value doesn't include the small proton and gamma widths ($\Gamma_p = 0.02$ keV and $\Gamma_\gamma = 13$ eV).

choice of a smaller radius will have the opposite effect. Clearly the choice of too small a radius will overestimate the branching ratio, while too large of a radius will underestimate the correction. Therefore the choice of radius was to use the recent value of [Hyl10], with $a_c = 4.5$ fm (corresponding to a value of $r_0 \approx 1.25$ fm.

We can deduce the reduced width to the ^{8}Be ground state, $\Gamma_{\alpha 0}$, from the partial branches and widths shown in Table 5.3, and the obtained branching ratios of decay to the ^{8}Be ground state. Table 5.4 shows the branching ratios, corrected for the effect of the ghost peak of the ^{8}Be ground state, and the extracted partial branches to the ground state $\Gamma_{\alpha 0}$ of natural parity resonances in ^{12}C. To calculate $\Gamma_{\alpha 0}$ for the narrow 16.11 MeV state the width of Γ=5.3 keV was taken from [Ajz90]. These values can then be compared

to spectroscopic factors from shell model calculations. More detailed results will be given in [Alc10].

5.2 Closer look at some of the ^{12}C resonances

The previous section looked at known resonances in ^{12}C and assigned values obtained in this work for widths and excitation energies where possible. There are some particular states which deserve a closer look. For example, there are cases where some properties of a resonance, such as the J^π, are not well understood or have been recently called into question. Dalitz plots are an excellent tool to understand and determine the J^π of resonances in a three-body breakup.

5.2.1 Dalitz plots

Dalitz plots provide a very useful method for representing the phase space of a 3-body breakup. It was originally developed by R.H. Dalitz [Dal53] in 1953 as a means to represent the decay of the K-meson (formerly known as the τ meson) into three pions. It provides a way to represent 3-body decay onto a scatter plot by exploiting the fact that the decay can be described using only two variables.

Let us take a nucleus X with mass M_X which decays into 3 identical particles (in our case it is ^{12}C decaying into three alpha particles). The decay amplitude M is limited only by the spin, isospin, and parity of the final state, and is governed by Bose statistics since alpha particles are identical bosons. It can be thought of as a sum of the products of these properties, namely

$$M = \sum M_I M_F M_{J\pi}$$

where M_I carries the isospin dependence, $M_{J\pi}$ carries the spin and parity dependence, and M_F carries the energy-momentum dependence. The momenta and energy of the three alpha particles must obey the following conservation laws

$$\begin{aligned} E_1 &= \sqrt{m_\alpha^2 c^4 + p_1^2 c^2} \\ \overrightarrow{p_1} + \overrightarrow{p_2} + \overrightarrow{p_3} &= 0 \\ E_1 + E_2 + E_3 &= m_{^{12}C} c^2 \end{aligned}$$

where the energies of the three alpha particles is the rest mass of ^{12}C since this is calculated in the CM frame of the ^{12}C breakup. Because we are

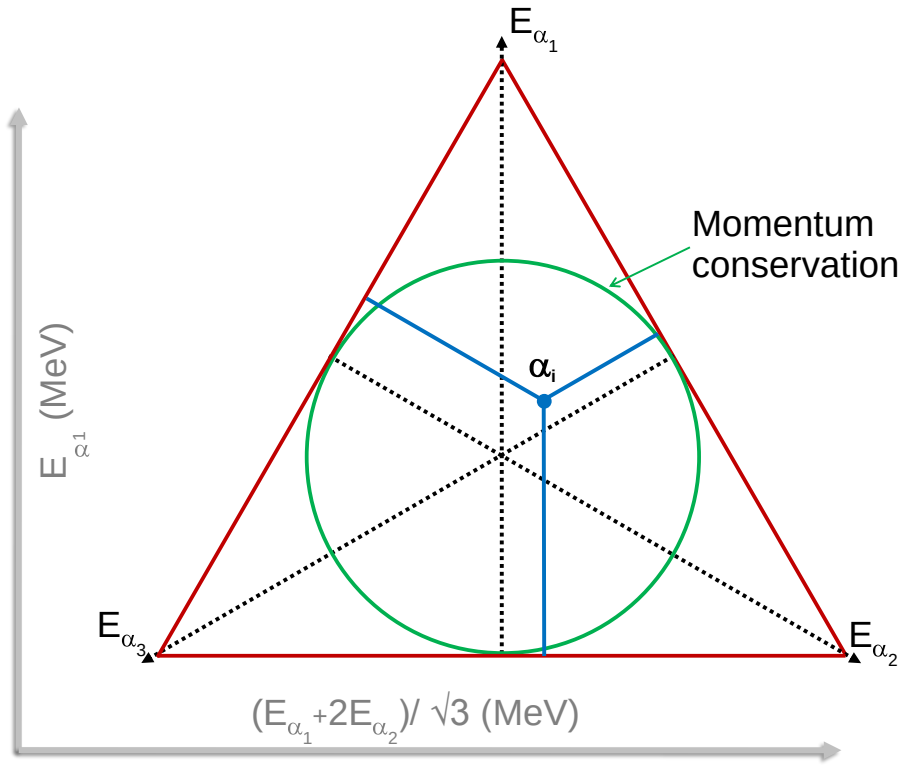

Figure 5.8: Dalitz plot showing available phasespace due to momentum and energy conservation. The triangle in red shows the kinematically allowed region due to energy conservation, while the green circle shows the available region due to momentum conservation. In blue is shown an example of a possible event.

dealing with three identical particles in the final state, we can take advantage of the symmetry so that the momentum and energy variables of the three alpha particles can be expressed in terms of the variables of any two particles. Therefore M_F can be expressed only as a function of the energy, so that the density of the Dalitz plot is proportional to

$$D = \sum |M|^2$$

which gives the key as to why Dalitz plots are so powerful. We can plot our experimental data in such a way that we fit the individual alpha particles energies in an equilateral triangle as shown in Fig. 5.8. The intensity is constrained inside the triangle due to energy conservation, and inside the circle due to momentum conservation. The final state is thus defined by only one point on the circle. A pure phase space distribution would give a uniform

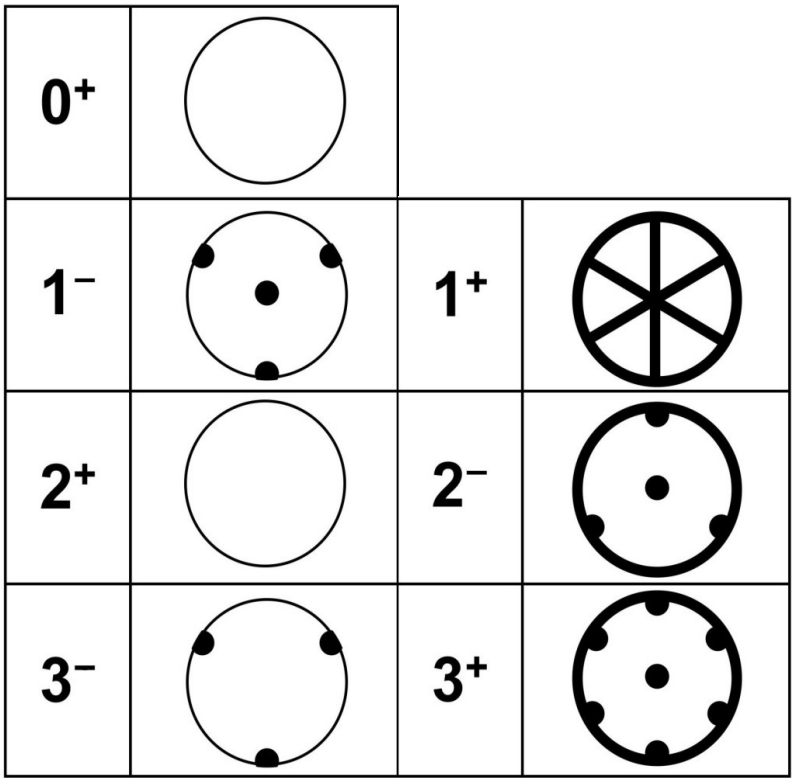

Figure 5.9: Regions of vanishing density shown in black in a Dalitz plot for several J^{π} states in ^{12}C due to conservation of spin and parity. The figure has been adapted from [Zem64].

Dalitz plot. Any deviance from a uniform distribution could be due to one of two occurrences:

- Angular momentum and parity conservation, as well as boson symmetry.
- Interactions between the particles determined by the decay mechanism.

Both structures are independent of each other, and are discussed in more detail below.

Role of symmetries

Zemach [Zem64] explored the role of symmetries in a three-pion decays and found that using Bose statistics and constraints from spin, parity, and isospin conservation forces regions of the Dalitz plots to vanish. The formulation

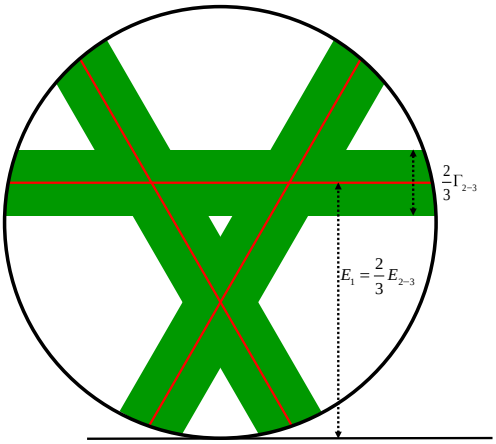

Figure 5.10: Dalitz plot illustrating the regions of *expected* intensity if the decay proceeds sequentially through the broad 2^+ state in ^{8}Be.

used by Zemach and the conclusions he made on the Dalitz plot can be applied to the breakup of ^{12}C into three alpha particles provided the difference in parity between the pion and the alpha particle are taken into account. Figure 5.9 is taken from [Zem64] and adapted to fit the case of three-particle alpha decay. It shows the regions of vanishing density for different J^π states in ^{12}C.

Sequential model

The vanishing regions of a Dalitz plot are independent of decay mechanism, meaning they will be present in a decay following the sequential mechanism or the direct mechanism. A direct decay will give no additional features in a Dalitz plot. However, if the decay proceeds sequentially, then new features will arise simply from kinematics. If $E_{\alpha 1}$ gives the energy of the first alpha particle and E_{2-3} the energy of the intermediate nucleus (in this case ^{8}Be) then this will show up as a horizontal band of constant energy as in Fig. 5.10. There are three bands due to the three-fold symmetry. Similarly, the width of this band is determined by the width of the intermediate state. These figures will vary depending on the ^{12}C state investigated since the energy of the ^{8}Be will depend on the Q-value of the reaction.

5.2.2 Dalitz plots for ^{12}C resonances

The Dalitz plots are obtained experimentally by first removing the contribution to the states which decay through the ground state of ^{8}Be. A narrow

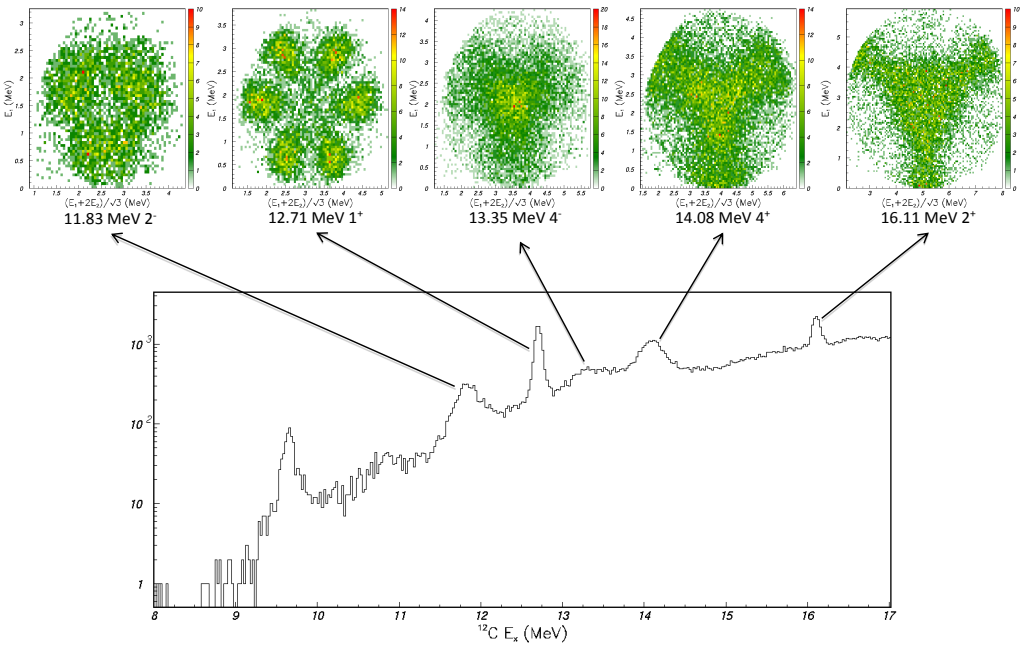

Figure 5.11: Dalitz plots for several states from the ^{10}B(^{3}He,p$\alpha\alpha\alpha$) reaction data. The Dalitz plot for the 9.64 MeV states and the 10.84 MeV states are not shown due to their low statistics (these are natural parity states which decay primarily through the ground state of ^{8}Be). The plots for the different states can be compared to the expected regions of vanishing density due to symmetry constraints shown in Fig. 5.9.

gate is then placed for each resonance and the alpha energies are transformed to construct the Dalitz plot. Fig. 5.11 shows Dalitz plots for several resonances in ^{12}C from the ^{10}B(^{3}He,p$\alpha\alpha\alpha$) reaction data. The plots shown have features which are a result of both the symmetry constraints and the reaction mechanism. There are some specific resonances which deserve a more detailed look, and are discussed below.

5.2.3 12.71 MeV State, $J^\pi = 1^+$

The breakup of the 1^+ 12.71 MeV resonance provides an ideal case for determining the reaction mechanism. The question of whether the decay proceeds sequentially through the first excited state of ^{8}Be or if it decays directly into

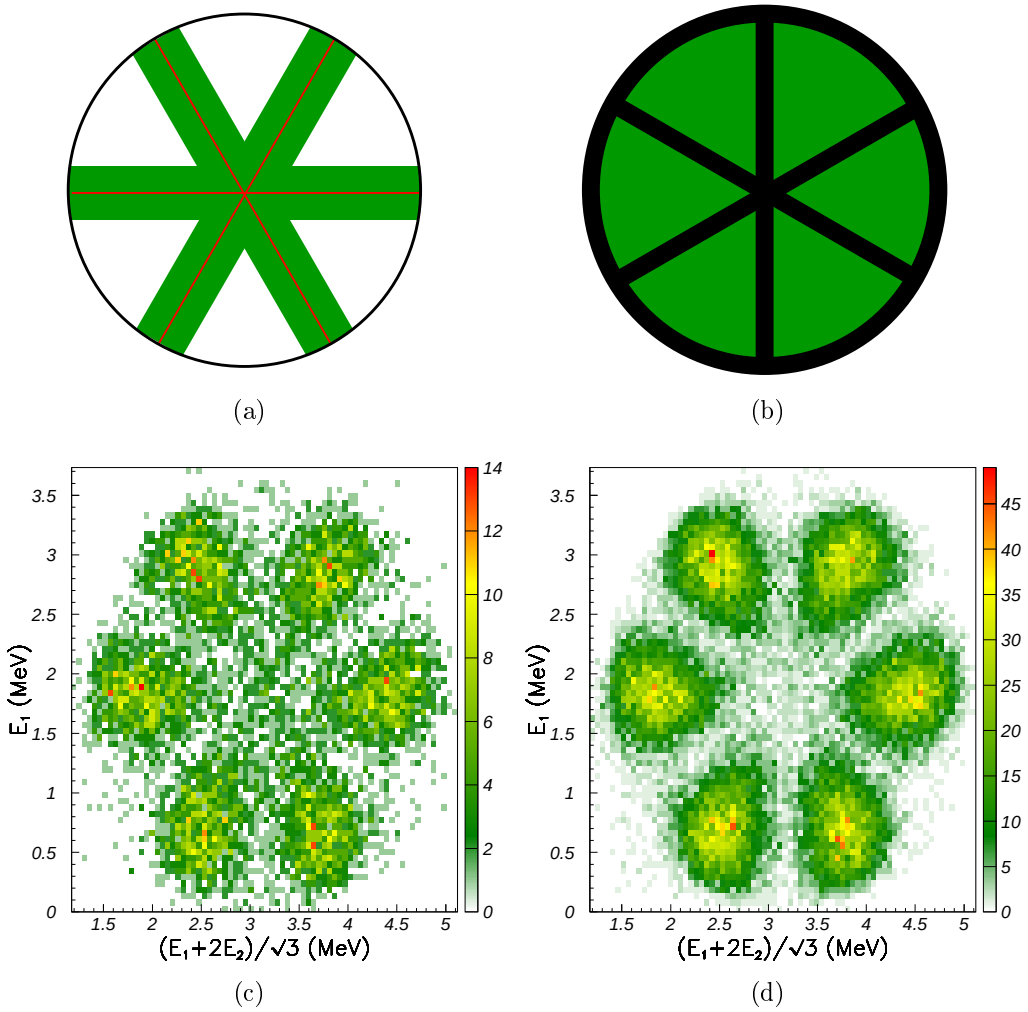

Figure 5.12: (a) Region of expected intensity assuming a sequential decay in the Dalitz plot of the 12.71 MeV state, and (b) regions of vanishing density in the Dalitz plot of the 12.71 MeV state due to symmetry constraints. (c) Dalitz plot of the 12.71 MeV state for the ^{10}B(^{3}He,p$\alpha\alpha\alpha$) reaction data and (d) the ^{11}B(^{3}He,d$\alpha\alpha\alpha$) reaction data. Note the greater presence of background in (c) than in (d).

three alpha particles have surprisingly similar consequences on the shape of the individual alpha spectrum. The alpha spectrum of the breakup of the 12.71 MeV resonance measured in the reaction ^{13}C(^{3}He,α)^{12}C* [BZT74] was analyzed assuming both direct decay [Kor90] and sequential decay taking into account Bose symmetry effects [BZT74] with moderate success. The case of the breakup of the 12.71 MeV resonance is still under debate, as it has recently been cited as an example of direct decay [Gri00, Gri01] and determined experimentally as an example of a sequential decay [Fyn03]. The latter measured the breakup of the 12.71 MeV resonance in complete kinematics from the β-decay of ^{12}N in order to better understand the decay mechanism. Fynbo et al. [Fyn03] compared their data to Monte Carlo simulations based on three models: direct breakup following the formulation of Ref. [Kor90], and sequential with and without Bose symmetry interference effects, following the work of Ref. [BZT74]. The model of sequential decay including the interference effects was determined to best reproduce their data. However some recent work based on direct breakup in a cluster model picture of three alpha particles was similarly successful in reproducing their experimental data [Alv07a]. Therefore the question of whether the 1^{+} 12.71 MeV still remains unanswered and is difficult to answer [Fyn09].

Dalitz plots provide a very useful manner to see the differences in these models and how they fit with the data. In fact symmetry constraints in the breakup of the 12.71 MeV give rise to very unique features in the Dalitz plot as seen in Fig. 5.12. In this figure the Dalitz plot from the ^{11}B(^{3}He,d$\alpha\alpha\alpha$) reaction data provides the cleanest spectrum due to the lower background in this data set. This plot was used to compare to two different models discussed below: two descriptions of democratic decay, based on the work of Ref. [Kor90] and the newer work on the cluster model in Ref. [Alv07a], and sequential decay based on the work of Ref. [BZT74]. The calculations of the different models were processed through the simulations to account for detection efficiencies.

Democratic decay

The democratic decay model proposed in [Kor90] and used in [Fyn03] has a probability of decay defined by:

$$\frac{d^3P}{dE_\alpha d\Omega_\alpha d\Omega_{\alpha-\alpha}} = \frac{2^{15}}{3^3 7\pi Q} 0.1429 x^{1/2}(1-x)^{1/2}\times \left\{ \begin{array}{r} 2.449^2 x^2(1-x)^2(36x^2-36x+\frac{63}{8})^2 K_1^{2222}(\theta) \\ -2.449\cdot 12x^3(1-x)^3(36x^2-36x+\frac{63}{8})K_1^{2244}(\theta) \\ +36x^4(1-x)^4 K_1^{4444}(\theta) \end{array} \right\} \quad (5.7)$$

where:

- $Q = E_1 + E_2 + E_3$= the available energy
- $x = \frac{E_1 M}{Q(m_2+m_3)} = \frac{3E_1}{2(E_1+E_2+E_3)}$, with $M = m_1 + m_2 + m_3$
- $x^{1/2}(1-x)^{1/2}$ is the phase-space factor
- The first term in the brackets corresponds to decays with $l_{\alpha-\alpha} = l_{\alpha-\alpha\alpha} = 2$, the third term to decays with $l_{\alpha-\alpha} = l_{\alpha-\alpha\alpha} = 4$, and the middle term corresponds to the interference of the two.
- The angular correlation functions, where θ is the angle between one particle and the relative momentum of the other two, are

$$K_1^{2222}(\theta) = (\tfrac{15}{32}\pi^2)\sin^2(\theta)\cos^2(\theta)$$
$$K_1^{2244}(\theta) = (\tfrac{15}{64}\pi^2)\sqrt{3/2}\sin^2(\theta)\cos^2(\theta)(7\cos^2(\theta)-3)$$
$$K_1^{4444}(\theta) = (\tfrac{45}{16^2}\pi^2)\sin^2(\theta)\cos^2(\theta)(7\cos^2(\theta)-3)^2$$

Equation 5.7 is then put through the simulation program to take into account the detection efficiencies of the setup. The interference term between the two lower order terms of l arises since alpha particles are identical bosons. This is also taken into account in the modelling of the sequential decay.

The model used in Ref. [Alv07a] uses the hyperspherical adiabatic expansion method with complex scaling [Nie01, Fed03]. It is similar to that used above except that it incorporates Coulomb repulsion. This inclusion of Coulomb effects has a large effect on the distribution of the alpha particles.

Sequential decay

The sequential decay model proposed in [BZT74] and used in [Fyn03] uses a sequential R-matrix model (see Section 5.3 for a detailed explanation of the R-matrix model) with interference effects taken into account in the order of emission of the three alpha particles since it is not possible to distinguish which particle is emitted first. The amplitude of emission of one of the alpha particles α_1 with angles (Θ_1, Φ_1) in the ^{12}C center of mass frame, and a second alpha particle α_2 with angles (θ_2, ϕ_2) in the ^{8}Be center of mass frame, is defines as:

$$f = \sum_{m_b} (l m_a - m_b j_b m_b | j_a m_a) Y_l^{m_a - m_b}(\Theta_1, \Phi_1) Y_{l'}^{m_b}(\theta_2, \phi_2) \frac{[(\Gamma_1/\sqrt{E_1})(\Gamma_2/\sqrt{E_{23}})]^{1/2} e^{i(w_l - \varphi_l)} e^{i(w_{l'} - \varphi_{l'})}}{E_0 - \gamma_2^2 [S_{l'}(E_{23}) - S_{l'}(E_0)] - E_{23} - \frac{1}{2} i \Gamma_2} \tag{5.8}$$

where:
j_a= spin of the state in ^{12}C
j_b= spin of the state in ^{8}Be
l= orbital angular momentum in the decay $^{12}\mathrm{C} \rightarrow \alpha + {}^8\mathrm{Be}$
l'= orbital angular momentum in the decay $^8\mathrm{Be} \rightarrow 2\alpha$
Γ_1= partial width for the decay $^{12}\mathrm{C} \rightarrow \alpha + {}^8\mathrm{Be}$
Γ_2= partial width for the decay $^8\mathrm{Be} \rightarrow 2\alpha$
E_1= energy of the first emitted alpha particle in the ^{12}C center of mass system.
E_{23}= relative energy of α_2 and α_3
E_0= resonance energy of the 2^+ of ^{8}Be
$w_l - \varphi_l$= Coulomb minus the hard sphere phase shift corresponding to the two particles scattering
$S_{l'}$= R-matrix shift function which depends on the choice of r_0. It is found from the Coulomb wave functions.

The correlation between α_1 and α_2 is given by Eq. 3.9. Since the three alpha particles are identical bosons, the final decay amplitude is obtained by symmetrizing in the coordinates of the three alpha particles, then squaring, and finally averaging over the projections of spin of the initial state, $m_a = -1, 0, 1$, giving:

$$W = \sum_{m_a} (f_1 + f_2 + f_3)^2 \tag{5.9}$$

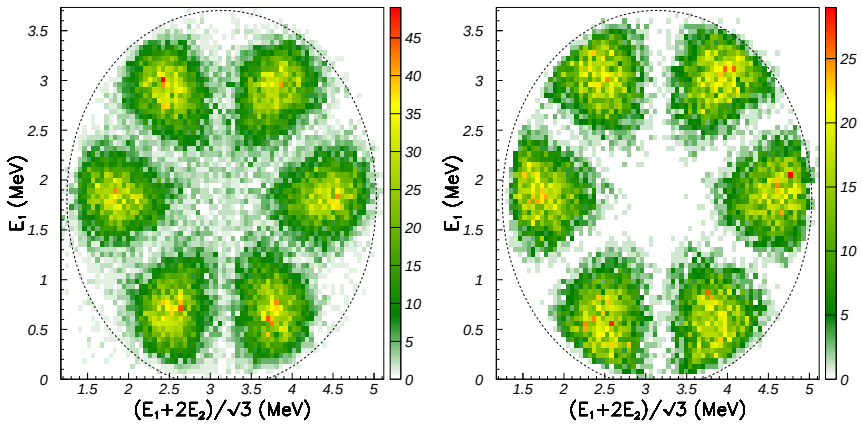

(a) Data (b) Cluster model

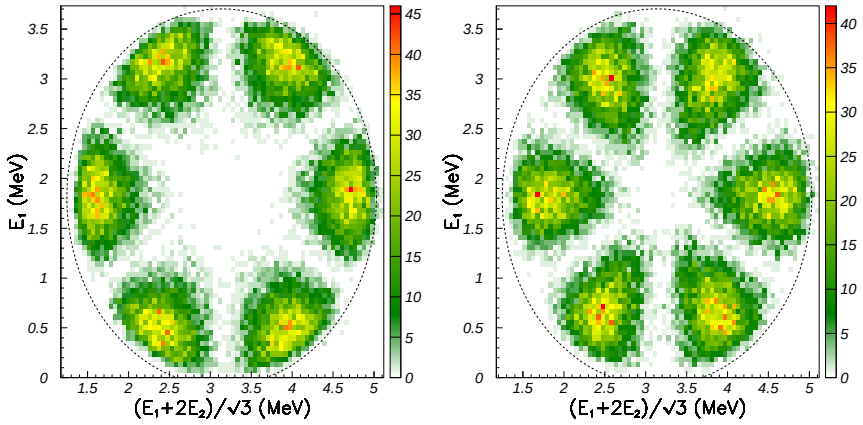

(c) Democratic (d) R-matrix

Figure 5.13: (a) Dalitz plot of the 12.71 MeV resonance taken from the ^{11}B(^{3}He,d$\alpha\alpha\alpha$) reaction data. (b) The Dalitz plot using the alpha spectrum from cluster model calculations [Alv07a]. (c) Dalitz plot where the alpha particles are simulated assuming a democratic decay using Equation 5.7. (d) Dalitz plot in which the alpha particle energies are calculated assuming a sequential decay given by Equation 5.8. Both the democratic decay model and to a lesser extent the cluster model have the density more spread out at the outer regions. Referring to Fig. 5.12(a) sequential decay confines the data in this region, as seen in (d), while the regions in (b) and (c) tend to only be governed by symmetry constraints as in Fig. 5.12(b). The more spread out density seen in the cluster model (b) is consistent with the inclusion of Coulomb effects in their calculations and results in a better fit to the data. The data most closely resembles the sequential model with Bose symmetry effects included (d).

The results of the simulations of both the sequential model and direct decay model are given in Fig. 5.13 along with the Dalitz plot of cluster model calculations. The sequential model most closely resembles the data. However, by changing the parameters of the $\alpha - \alpha$ interactions the direct decay model [Fyn09] is also able to reproduce the experimental results. The conclusion given in Ref. [Fyn09] is that the alpha particle distribution of the breakup of the 1^+ 12.71 MeV resonance is mostly determined by symmetry effects, meaning the decay mechanism has little effect on the final distribution of the alpha particles. In addition, the picture of direct decay versus sequential decay becomes muddled when the intermediate resonance is very short-lived, as in the case of the 2^+ ^{8}Be resonance.

5.2.4 13.35 MeV State, $J^\pi = (2^-)$

The 13.35 MeV state has a debated J^π assignment. Ref. [Ajz90] lists it tentatively as a 2^-, though a footnote listed as private communication gives a most likely assignment of 4^-, and a recent article using angular correlations in the ^{12}C(^{12}C, 3α)^{12}C reaction [Fre07] lists possible values as 2^-, 3^+, and 4^-. Clearly this resonance is of unnatural parity since it has no decay width through the ground state in ^{8}Be (see Fig. 3.19). To gain insight into the spin-parity of this resonance Dalitz plots are very useful. Figure 5.14 shows the Dalitz plots obtained in our data compared to expected regions of vanishing density in black for the case of a 2^- and a 4^- state. The comparison unambiguously supports a spin-parity assignment of 4^-, in agreement with calculations performed using the cluster model [Alv08] described above.

5.3 R-matrix analysis

In Section 5.1 the resonances in ^{12}C were fit using a Breit-Wigner distribution. This simplification was justified for the states studied there since they were sufficiently narrow and they had no known interfering states (states with the same J^π) with similar energy. However one goal of this analysis was to search for possible new states and to gain a better understanding of the broad resonance(s) in the region $\sim$10 MeV. To fully understand the broad resonance(s) in that region it is absolutely necessary to use a more sophisticated technique such as the R-matrix formalism [Hyl10]. This section will focus on using the R-matrix formalism to attempt to disentangle the broad resonances in ^{12}C. However before performing fits using the R-matrix method it is important to gain a full understanding of possible background contributions to the spectra. This is essential, as without a good understanding

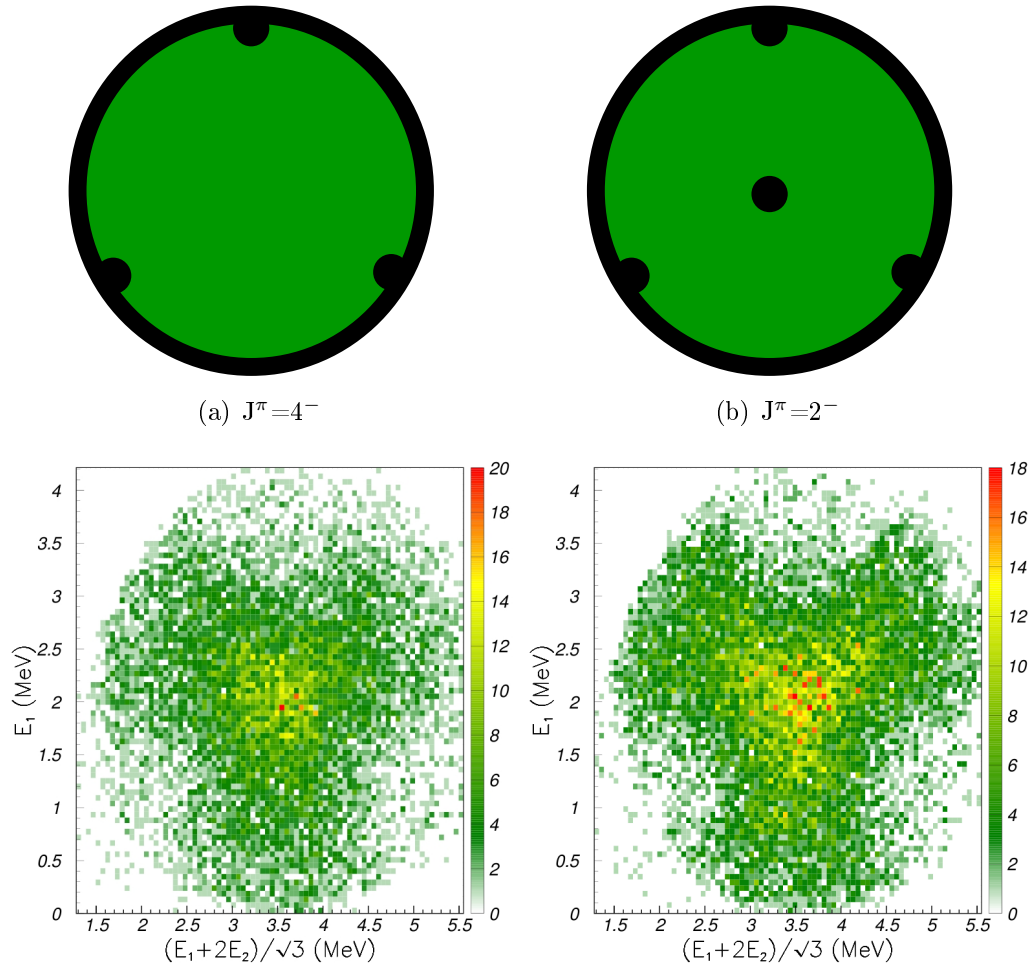

(a) $J^{\pi}=4^{-}$ (b) $J^{\pi}=2^{-}$

(c) ^{10}B(^{3}He,p$\alpha\alpha\alpha$) reaction data (d) ^{11}B(^{3}He,d$\alpha\alpha\alpha$) reaction data

Figure 5.14: Dalitz plot of the 13.35 MeV state for (c) ^{10}B(^{3}He,p$\alpha\alpha\alpha$) reaction data and (d) ^{11}B(^{3}He,d$\alpha\alpha\alpha$) reaction data. The top two figures show the expected regions of vanishing density due to symmetry constraints for a 4^{-} (a) and 2^{-} (b) state. In the case of the 2^{-} (as well as the 3^{+} in Fig. 5.9) there should be no intensity in the center of the Dalitz plot. Only a $J^{\pi}=4^{-}$ fits with the presence of intensity in the center of the Dalitz plot of the obtained data.

on the background present in the data, we cannot conclude anything substantial about possible new resonances. The first step is then to reduce the background as much as possible, as discussed in Chapter 3. However we still have contributing reactions with the same final state particles which cannot be easily removed. To this effect, the ^{11}B(^{3}He,d$\alpha\alpha\alpha$) reaction has less contributing background than the ^{10}B(^{3}He, p$\alpha\alpha\alpha$) reaction. The following analysis will therefore concentrate on the former reaction.

5.3.1 Understanding the background contribution

There are several possible channels which will contribute to the background of the ^{12}C excitation spectrum in the ^{11}B(^{3}He,d$\alpha\alpha\alpha$) reactions listed in Eq. 5.2. The Q-value for the α+^{10}B channel is 9.12 MeV, and the threshold for deuteron emission is 6.03 MeV. The highest state populated in ^{10}B which can emit a deuteron is the 8.07 MeV state. Therefore the available energy for the deuteron is only ≈1.7 MeV in the center of mass. A deuteron with this energy will be completely stopped in the DSSSDs, and will not be selected in the ΔE-E plot. Therefore the α+^{10}B channel does not contribute to background.

The ^{8}Be+^{6}Li channel is a different matter. In this case there are several contributing states in ^{6}Li which can emit a deuteron:

$$
\begin{aligned}
^8\mathrm{Be(gs)} + {}^6\mathrm{Li}(3^+)\\
^8\mathrm{Be(gs)} + {}^6\mathrm{Li}(2^+)\\
^8\mathrm{Be(gs)} + {}^6\mathrm{Li}(1^+)\\
^8\mathrm{Be(exc)} + {}^6\mathrm{Li}(3^+)\\
^8\mathrm{Be(exc)} + {}^6\mathrm{Li}(2^+)\\
^8\mathrm{Be(exc)} + {}^6\mathrm{Li}(1^+)
\end{aligned}
$$

The 3^+ state is a narrow resonance (Γ=24 keV) situated at 2.19 MeV. This state can easily be identified in Fig. 5.4, so that its contribution can be removed. Unfortunately, the 2^+ 4.31 MeV state and the 1^+ 5.65 MeV resonances in ^{6}Li are much broader (Γ=1.3 MeV and 1.5 MeV, respectively) and cannot be easily removed. Since the contribution to the ^{12}C excitation spectrum from these states cannot be removed, the channels are simulated and the resulting spectra are fit using a 6 degree polynomial which is then included in the final fit of the ^{12}C spectra with only the intensity as a free parameter. However in order to include the contributions from the broad ^{6}Li states as a constant background which only varies in intensity, a critical assumption must be made. If the contribution of any of these states to the

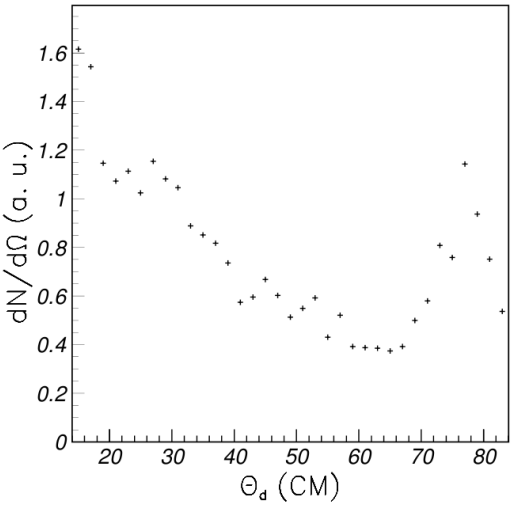

Figure 5.15: Normalized angular distribution of the deuteron in the CM system with respect to an isotropic distribution. This distribution is from the ^{8}Be(gs)+^{6}Li(3^{+}) channel. The distribution varies at most by a factor of two from an isotropic distribution. Given that the 3^{+} state in ^{6}Li has a large angular momentum value we deduce that this is formed in a compound reaction, which gives us confidence that the deuterons from ^{6}Li are emitted isotropically.

^{12}C spectrum varies with the angle of the emitted deuteron, then this method will not work because the contribution would no longer be constant. In other words, since the angular distributions of the deuterons cannot be determined by fitting the broad ^{6}Li states, if the deuterons emitted from this channel are non-isotropic, then the contribution to ^{12}C cannot be fit as just a background.

In order to treat the ^{6}Li background as a constant in the final fit of the ^{12}C spectrum, it is necessary to prove the assumption that the angular distribution of the emitted deuteron is isotropic. This is first done by studying the possible reaction mechanism for the ^{8}Be+^{6}Li channel. As discussed in Section 2.1.1, a direct reaction and a compound reaction give very different angular distributions. In fact, while a direct reaction would give a non-isotropic angular distribution, a compound reaction would give more or less an isotropic distribution of the emitted particles. If this were a direct reaction, then it would involve the transfer of a triton from the ^{11}B target to the incoming ^{3}He beam. This seems very unlikely, although if ^{11}B is seen

as a cluster of two alpha particles and a triton this could increase the cross section for this reaction. We can look for an indication of either of these reaction mechanisms by looking at the angular distribution of the narrow ^{6}Li(3^+) channel.

Figure 5.15 shows the normalized angular distribution of the deuteron in the center of mass system gated on the narrow ^{6}Li(3^+) state and the ground state of ^{8}Be. Normalized means that the experimental angular distribution has been divided by a Monte Carlo simulation which assumes an isotropic angular distribution. In the figure one can see that the deuteron is emitted almost isotropically, with a much smaller variation in angle than seen for the ^{12}C channel as shown in Fig. 3.14. Considering also that the 3^+ state would be expected to deviate more from an isotropic distribution than the 2^+ and 1^+ states due to the higher angular momentum transfer, we can safely assume that the contribution from the ^{6}Li in the ^{12}C spectra does not vary with angle.

5.3.2 Fitting procedure

The first step in the fitting procedure is that only the data of the ^{12}C excitation spectra which decays through the ground state of ^{8}Be is selected. Similar to the procedure outline in Section 5.1, the ^{12}C excitation energy spectra is then separated into four angular bins of the deuteron in the center of mass, with θ_d(CM) from 0°-60°, 60°-100°, 100°-140°, and 140°-180°. The next step is to perform Monte Carlo simulations of the ^{8}Be(gs)+^{6}Li(1^+) and ^{8}Be(gs)+^{6}Li(2^+) channels. The contribution which these channels give to the excitation energy spectra of ^{12}C is then quantified by fitting the curve to a 6 degree polynomial in the four different angular bins, giving two polynomial functions in each angular bin (one for each state in ^{6}Li). The two obtained 6 degree polynomial functions are then included in the final fit of the ^{12}C spectra where the only varying parameter is the intensity of each polynomial function. An upper limit on the intensity of the ^{6}Li contribution from the 1^+ and 2^+ states can be established as shown in Fig. 5.16. In this figure the data is shown in black, and the contribution to the ^{12}C excitation energy spectra from the ^{6}Li(1^+) channel and the ^{6}Li(2^+) channel is shown in blue and red, respectively. The red and blue curve are each fit to a 6 degree polynomial function to be included in the final R-matrix fit. The contribution of the ^{6}Li channels shown in Fig. 5.16 is the maximum possible contribution, so that in the final R-matrix fit performed at each angular range this upper limit is placed on the intensity of both the polynomial functions corresponding to the ^{6}Li(1^+) channel and the ^{6}Li(2^+) channel. The ^{12}C excitation energy spectra shown in black is still the final spectra to be fitted, however. Corrections for

detection efficiency have not yet been included.

Detection efficiency

The normal procedure to account for the difference in detection efficiency would be to put the reaction through the Monte Carlo simulations as described in Section 3.4. Unfortunately this will not work when we want to perform an R-Matrix fit with e.g. interfering states. Therefore the detection efficiency must be taken into account in the ^{12}C spectra prior to the final fits.

The detection efficiencies are determined by simulating many narrow states for different energies and angles, and then extracting the efficiency as a function of angle and energy. This is then multiplied by the spectrum before performing the final fit. To determine the detection efficiency, the simulated energies were done in steps of 125 keV, from 7.5 MeV up to 15.375 MeV, but were separated into two different regions at 9 MeV. Energies above 9 MeV are divided into angular bins of 5°, while energies below 9 MeV are divided into angular bins of 2°. The reason for this very fine angular binning at low energies is the large dependence of the efficiency on the angle for low energies.

In Appendix A, Figs. A.1 and A.3 show the detection efficiency of ^{12}C for different angles and energies above 9 MeV (starting at 9.25 MeV). Here the angular binning was of 5°. Figures A.5, A.7 and A.9 show the efficiency for 9.25 MeV and below. In this case the angular binning is of 2°. Note the large changes in efficiency for very small changes in angle as compared with Figs. A.1 and A.3.

The efficiency corrected plots are then extracted from the detection efficiencies, the effect of which is shown in Fig. 5.17. One can see that the effect on the spectra of including the detection efficiency is most pronounced at low energies. To obtain the final spectra to be fitted, the spectra have been added together into four angular regions described above to give more statistics and cover a larger angular range. This can only be done because because the expected background from ^{6}Li is assumed isotropic. In addition, separating the data to be fitted into four angular regions will help in separating contribution from states since it will favor certain spins over others, and can become an excellent tool in searching for states hidden in the background.

5.3.3 R-Matrix fit

We now have finally incorporated all the corrections so that we can begin to fit the spectra using the R-Matrix formalism. The formalism has been introduced in Section 1.3, and the details are applied here to the d+^{12}C →

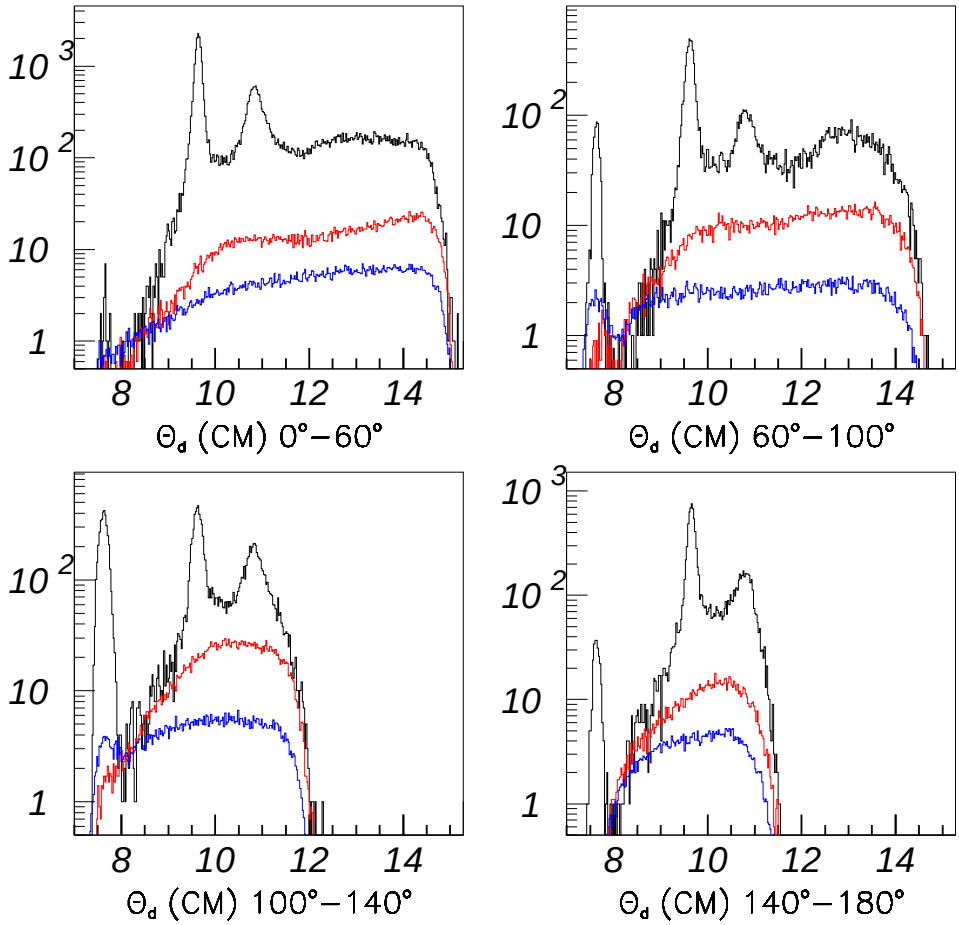

Figure 5.16: The ^{12}C excitation energy spectrum for different angular ranges, gated on the decay through the ground state of ^{8}Be. The black line shows the data, while the red and the blue lines show the contribution from the 2^+ (red) and 1^+ (blue) states in ^{6}Li. The ^{6}Li contribution has been scaled to get an upper limit for this contribution, so that each figure has the same normalization. The contribution from the ^{6}Li states at each angular range is fit using a 6 degree polynomial, which is then included in the fitting routine as background contribution, with only the intensity as a free parameter. Note that the figures are in a logarithmic scale, and that the ^{6}Li contribution is therefore very small compared to the ^{12}C contribution.

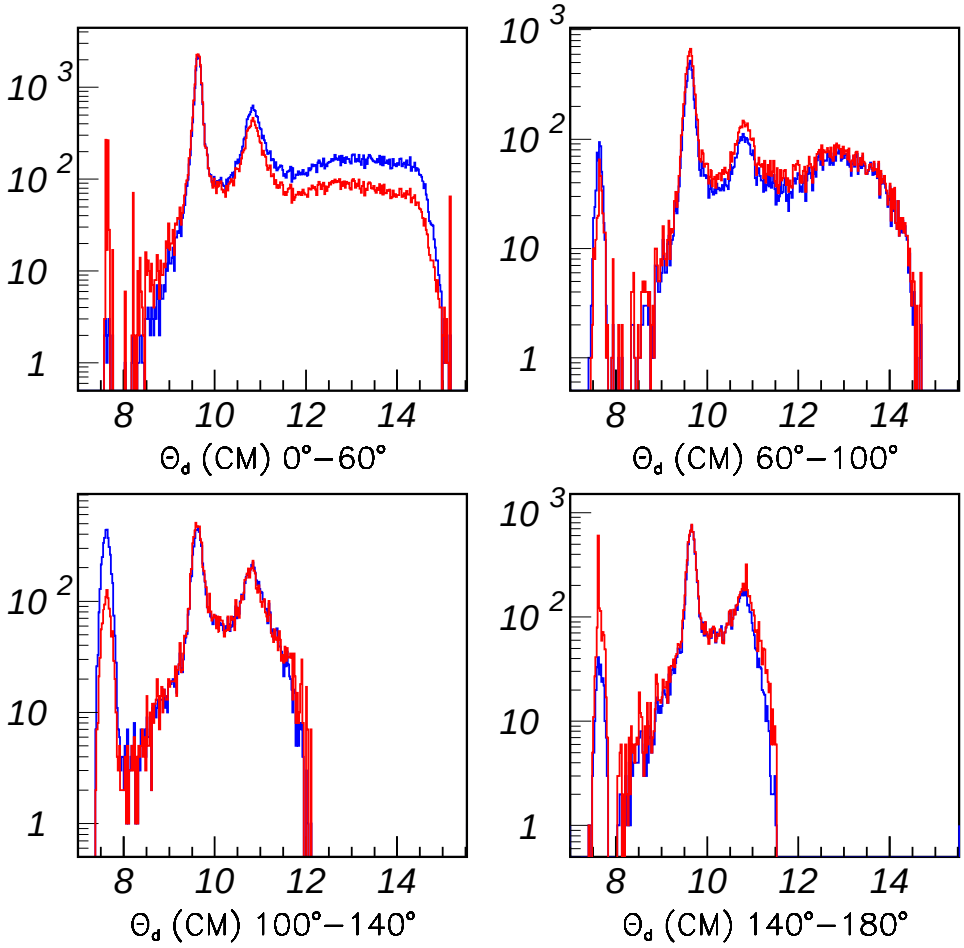

Figure 5.17: ^{12}C excitation energy for different angular ranges, gated on the ground state of ^{8}Be. The data is in blue, and the efficiency corrected data, which will be fitted using R-matrix theory, is shown in red. In both the ranges from 0°-60° and 140°-180° the efficiency corrected plots at low energies is greater than the observed spectrum. This is a result of the very low efficiencies at low energies in these angular regions observed in Figs. A.5, A.7, and A.9.

$\alpha + {}^8$Be(gs) reaction channel. In this case only a single-channel formula should be necessary since the data is separated to include only ^{12}C decay through the ^{8}Be(gs) channel. The decay through the 2^+ state in ^{8}Be calls for a more complicated approach due to the broad nature of the state and will not be discussed.

The first step is to determine if the single-channel approach is valid in this case. It is clear that in cases where a natural parity resonance decays through the ^{8}Be(gs) and ^{8}Be(2^+) states with similar intensities then this assumption may run into problems, since the α decay width will be shared by both decays and a fit to one of them individually will not give a complete result for the decay width. However, if the natural parity states decay primarily through the ^{8}Be(gs) then this approach is valid. It is sufficient to look at Table 5.3 to observe that this is the case. The formalism follows that given in [Bar88], with the exception that this will not include the steps pertinent to β-decay.

The transition probability is defined as

$$w = \int w(E)dE \tag{5.10}$$

where $w(E) = \sum w_c(E)$. The subscript c refers to summing over the different channels which can contribute. For example, as previously discussed, the decay through the ^{8}Be(gs) and ^{8}Be(2^+) state are separate channels and need to be looked at independently. For the moment we are dealing only with a single channel approach, i.e. $^{12}\mathrm{C} \rightarrow \alpha + {}^8$ Be(gs). $w_c(E)$ is defined as

$$w_c(E) = fP_c\left|\sum_{\lambda\mu} g_{\lambda x}\gamma_{\mu c}A_{\lambda\mu}\right|^2 \tag{5.11}$$

where $g_{\lambda x}$ is the feeding amplitude, $\gamma_{\mu c}$ is the reduced with, P_c is the penetration factor, and f is the phase-space factor. Essentially this is the feeding to the different states in ^{12}C in our reaction, which is important to include due to the very broad states in ^{12}C. Consider, for example, the broad 10 MeV state. If the feeding at 9 MeV is different from that at 10 MeV, then this would distort the shape of the broad 10 MeV state and would give incorrect R-matrix parameters. The difficulty comes when trying to describe this factor. The feeding to the different states depends on the reaction mechanism involved. However, whether ^{12}C was populated in a compound reaction or a direct reaction, the feeding to the different states will only depend on the penetrability of the d+^{12}C system.

The inverse of the matrix $A_{\lambda\mu}$ is given by

$$(A^{-1})_{\lambda\mu} = (E_\lambda - E)\delta_{\lambda\mu} - \sum_c (S_c - B_c + iP_c)\gamma_{\lambda c}\gamma_{\mu c} \tag{5.12}$$

The λ and μ are necessary if there are interfering levels (same J^π). However, if the levels do not interfere, then they can be summed incoherently and Equation 5.12 is reduced to

$$(A^{-1})_\lambda = (E_\lambda - E) - \sum_c (S_c - B_c + iP_c)\gamma_{\lambda c}^2 \tag{5.13}$$

so that in the very simple case of decay of non-interfering states in the one channel approach, Eq. 5.11 becomes

$$w(E) = fP_l \left| \frac{g_\lambda \gamma_\lambda}{(E_\lambda - E) - \sum_c (S_c - B_c + iP)\gamma_\lambda^2} \right|^2 \tag{5.14}$$

Recall that in Equation 1.3 we defined the level width as $\Gamma = 2P_l\gamma^2$, so that Equation 5.14 becomes

$$\begin{aligned} w(E) &= f g_\lambda^2 \frac{\Gamma/2}{|(E_\lambda - E) - (S_c - B_c + iP)\gamma_\lambda^2|^2} \\ &= f g_\lambda^2 \frac{\Gamma/2}{(E_\lambda - E + \Delta)^2 + (\Gamma/2)^2} \end{aligned} \tag{5.15}$$

where $\Delta(E) = -\sum_c \gamma_\lambda^2 (S_c - B_c)$ is a correction from the energy dependence of Γ. Eq. 5.15 is the familiar Breit-Wigner distribution in Eq. 1.2 when there are no interfering channels. However, in this particular case we are looking at a single-channel approach with interfering states, so that we will have to use Eq. 5.11.

Example for a non-interfering state

Equation 5.14 is used to fit the ^{12}C excitation spectrum. However to get a clear idea of how this is used in the fitting routine it is important to describe the procedure in detail. Let us look at the different components of Equation 5.14. The first variable is f, the feeding of the different ^{12}C resonances analogous to the β feeding. This is determined by calculating the penetrability of the d+^{12}C system. The P_l factor included above is the penetrability of the α+^{8}Be system. The penetrability factor is defined by

$$P_l = \frac{\rho}{F_l^2(\eta, \rho) + G_l^2(\eta, \rho)} \tag{5.16}$$

where F_l and G_l are the regular and irregular Coulomb wave functions, respectively, which are calculated using the CERNLIB routine WCLBES. In addition,

$$\rho = kR = R\sqrt{2\mu E/\hbar^2} \tag{5.17}$$

and

$$\eta = \frac{Z_1 Z_2 e^2}{\hbar} \cdot \sqrt{\frac{\mu}{2E}} \tag{5.18}$$

with $R = R_0(A_1^{1/3} + A_2^{1/3})$ and $\mu = m\frac{A_1 A_2}{A_1 + A_2}$ is the reduced mass (m=931.5 MeV/c^2)

Similarly, we can obtain the shift function

$$S_l = \frac{F_l(dF_l/dr) + G_l(dG_l/dr)}{F_l^2 + G_l^2} \tag{5.19}$$

We can see that both the shift factor and the penetrability only depend on the Coulomb wave functions. This is because R_0 is chosen such that only the Coulomb potential influences the wavefunctions.

Recall that the penetrability P_l appears in the expression for the width of the resonance, $\Gamma_\lambda = 2P_l(E - E_f)\gamma_\lambda^2$. Conversely, the shift function S_l appears in the expression for the resonance energy, as $E_r = E_\lambda - S_l(E)\gamma_\lambda^2$. This makes sense, because the level width is also a measure of the lifetime of the resonance, and this depends on the penetrability. The more probable for the particle to escape, the shorter the lifetime, and the broader the width. Similarly, it is expected for the shift function to appear in the expression of observed resonance energy since it represents a shift in the observed resonance energy E_r. It is worth mentioning that both the shift in energy and the level width have a dependence on the interior of the nucleus (r<R) through the reduced width γ_λ. The final parameter to be discussed is the boundary condition parameter B_c, which is chosen so that $B_c = S_c(E_r)$.

Looking back at Equation 5.14 we now know how to calculate several parameters. The other factors are variables in our fit or constants. The three variables which go into the fit are g_λ, the intensity of the peak, E_λ, the energy of the resonance, and γ_λ, the reduced width of the resonance. Note that E_λ also goes into the boundary condition parameter B_c. In other words the shift function and penetrability only depend on the energy and various properties of the resonance, such as the Z and A of the involved nuclei.

Analytical Hoyle state fit

The R-matrix fits must be convoluted with a Gaussian distribution so as to take into account the experimental resolution. This is especially important for very narrow states. However [Bar88] gives an analytical expression for the

area under the Hoyle state peak, so that it is not necessary to fold the peak with the resolution. The area under the Hoyle state peak is then compared directly with w as defined in Equation 5.11 provided we derive an analytical expression for w:

$$w_\lambda = ((\ln 2)/Nt_{1/2}) \sum_x |B_{\lambda x}|^2 f_\lambda J_\lambda \tag{5.20}$$

where

$$J_\lambda = \sum_c \int dE P_c \left| \sum_\mu \gamma_{\mu c} A_{\lambda\mu} \right|^2 \tag{5.21}$$

and

$$B_{\lambda x} = C(Nt_{1/2}/\ln 2)^{1/2} g_{\lambda x} \tag{5.22}$$

and for a narrow level (in this case, the Hoyle state)

$$J_\lambda = \pi \Big/ \left[1 + \sum_c \gamma_{\lambda c}^2 \frac{dS_c}{dE} \right]_{E_\lambda} \tag{5.23}$$

which is valid as long as $B_c = S_c(E_\lambda)$. We can now clean up Equation 5.20 by removing the pieces relevant to β-decay as we have done above, so that we can now have an analytical expression for w_λ

$$w_\lambda = \frac{f \cdot g_\lambda^2 \pi}{\left[1 + \sum_c \gamma_{\lambda c}^2 \frac{dS_c}{dE} \right]_{E_\lambda}} = \frac{f \cdot g_\lambda^2 \pi}{1 + \gamma_\lambda^2 \frac{dS}{dE}} \tag{5.24}$$

which is evaluated at a fixed energy E_λ, in this case the Hoyle state. We now have an expression which we can compare to the area under the Hoyle state peak, and then extract g_λ, one of the R-matrix fit parameters. All that goes into this expression is the reduced width γ_λ^2 and $\frac{dS}{dE}$, the derivative of the shift function.

Fitting parameters

The fitting routine is performed using states which decay through the ^{8}Be ground state in the energy region of interest. In our case then we have included the following levels:

Level λ (MeV)	Reduced width (MeV$^{1/2}$)	J$^\pi$
7.654	0.6	0^+
11.0	0.45	0^+
9.64	0.1	3^-
10.84	0.2	1^-
11.0	0.44	2^+

In addition to the level energies, the radius (chosen to be r_0=1.87 fm) and the fit to the different ^{6}Li spectra are included as well. The fit includes both the broad 0^+ state and a 2^+ state in the region of 11 MeV. Figure 5.18 shows a preliminary fit of the spectra with the following parameters obtained in the fit:

J$^\pi$	Energy (MeV)	Reduced width (MeV$^{1/2}$)	Observed width (keV)
0^+	7.654	-0.400	4.61×10^{-3}
0^+	11.100	0.446	1360
3^-	9.654	0.100	41
1^-	10.844	0.200	259
2^+	11.19	0.443	1374

The fit gives a χ^2 value of 226 with 121 degrees of freedom. The magenta color in Fig. 5.18 is the small contribution from the 4 MeV ^{6}Li state. There is no significant contribution from the 5 MeV ^{6}Li state. The widths and excitation energies obtained for the 3^- and the 1^- resonance agrees well with the values given in Table 5.3. The width and energy of the Hoyle state was fixed to the literature value given in Ref. [Ajz90]. The energy and the width of the broad 11.1 MeV 0^+ resonance and the broad 11.2 MeV 2^+ resonance are in good agreement with the values of 11.2 MeV ($\Gamma = 1.5$MeV) for the 0^+ resonance and 11.1 MeV ($\Gamma = 1.4$MeV) for the 2^+ resonance given in [Hyl10]. A discussion of the results and their relevance to previous values is discussed below.

Remarks on the 9-12 MeV region in ^{12}C

The excitation energy region of 9-12 MeV in ^{12}C was discussed in detail in Chapter 1. The understanding of the broad features in that region has served as motivation for many recent experiments, including this one. The motivation for studying this region in ^{12}C was to search for the collective 2^+ excitation of the Hoyle state in order to gain understanding on the structure

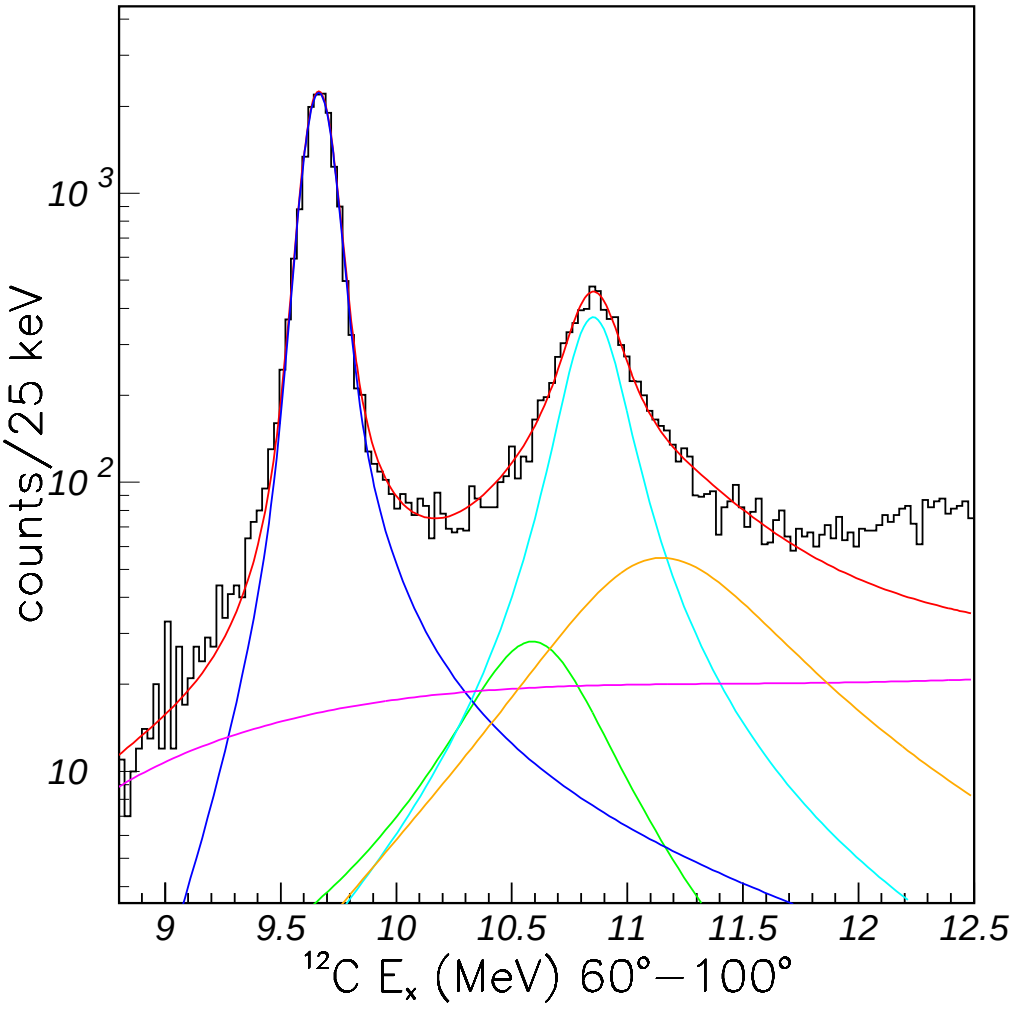

Figure 5.18: Result of the fit of the ^{12}C excitation energy spectrum in the region from 60°-100°. The efficiency corrected data which decays through the ground state of ^{8}Be is shown in black. In red is the total fit for the spectrum, while green shows the contribution from two 0^+ states (7.65 MeV and 10.5 MeV), dark blue shows the contribution from the 3^- state (9.64 MeV), light blue shows the contribution from the 1^- state (10.84 MeV), orange shows the contribution from the 2^+ state (11.2 MeV), and magenta shows the contribution from the 2^+ 4 MeV state in ^{5}Li. The fit is only for below 12 MeV in excitation energy since above the spectrum becomes difficult to fit due to the cut-off in energy.

of the Hoyle state. In addition the presence or absence of a 2^+ resonance in this region may contribute to the triple-alpha reaction rate at high temperatures (Section 1.2.1).

Recent work using β-decay [Hyl10] and a sophisticated R-matrix analysis has found evidence for a 2^+ resonance at 11.1 MeV ($\Gamma = 1.4$MeV), overlapping with a 0^+ resonance at 11.2 MeV ($\Gamma = 1.5$MeV). However they do not find evidence for a 2^+ in the vicinity of 9 MeV, which would seem to contradict the work on ^{12}C(p,p$'$) [Fre09] which finds evidence for a 2^+ resonance at 9.6 MeV ($\Gamma = 600$keV) and the work on ^{12}C(α, α') [Ito04] which finds evidence for a 2^+ resonance at 9.9 MeV ($\Gamma = 1.0$MeV).

Possible reasons for the discrepancy between the two experiments could be due to the different probing mechanism or to the different analysis techniques. In principle both β-decay and inelastic scattering studies are good probes for finding a 2^+ resonance. As discussed in Section 1.4, β-decay studies provide a clean probe of the region above the triple-alpha threshold, populating only 0^+, 1^+, and 2^+ resonances. In the experiments by Hyldegaard et al. [Hyl10], the resonances in ^{12}C were studied by two different methods: by detecting the sum of the alpha particle energies from the decay of ^{12}C and by detecting the individual alpha energies from the decay of ^{12}C. The latter allows the data to be separated depending on if the decay proceeds through the ground state or the 2^+ state in ^{8}Be while the former is able to detect very low-energy alpha particles. The data in each case was analyzed using a sophisticated R-matrix formalism to take into account interference between the 0^+ resonances and to understand the broad nature of the states.

The different inelastic scattering experiments do not detect the breakup alpha particles, but the advantage of these experiments is that in the case of [Fre09] the outgoing protons were measured at different angles. The data was then analyzed by comparing the cross section of the region at 9-12 MeV for different angles with coupled-channels calculations. However, the region at 9-12 MeV was not fitted using a very sophisticated R-matrix technique which means that the observed energy corresponding to a 2^+ state at 9.6 MeV may in fact be different from 9.6 MeV.

Our preliminary results on the region from 9-12 MeV indicate that the data can be explained by both a broad 0^+ contribution and a broad 2^+ contribution. These results are in agreement with those obtained in Ref. [Hyl10], and there is no clear evidence of a 2^+ resonance in the vicinity of 9-10 MeV as found by Refs. [Fre09, Ito04]. However, the fit is preliminary as the region at 12 MeV and above does not have the energy cut-off seen in Fig. 5.16 taken into account. Therefore one should not completely rule out the possibility of a broad 2^+ resonance with a different energy than that obtained above.

A witty saying proves nothing.

Voltaire

6 Conclusion

The goal of this work was to study the structure of excited states in ^{12}C from light-ion reactions in complete kinematics. A significant part of this thesis was dedicated to analysis techniques used to extract physics results from the data, and the different results obtained in the analysis were presented in detail. In this concluding chapter some final observations and remarks are given.

6.1 Summary

The work outlined in this thesis can be summarized as follows:

- The motivation for this work involves many fields, from nuclear astrophysics to theoretical ab initio calculations. Previous experiments by our collaboration studied excited states in ^{12}C from the β-decay of ^{12}N and ^{12}B. However, the states populated in ^{12}C from β-decay are limited to positive parity states with J$\leq$ 2. A reaction experiment was carried out to determine properties of resonances in ^{12}C using a complementary method.

- The ^{3}He + ^{11}B $\rightarrow$ d+^{12}C* reaction was carried out at an energy of 8.5 MeV and the ^{3}He + ^{10}B $\rightarrow$ p+^{12}C* reaction was carried out at an energy of 4.9 MeV in the CMAM accelerator facility in Madrid. The outgoing particles in the reaction, the light ion and three alpha particles from the breakup of ^{12}C*, were detected in complete kinematics using a setup with four telescope detectors. The multi-segmentation of the detectors allowed for the detection of both the energy and the position of the particles.

- There were many open channels in the two studied reactions which needed to be removed as best as possible from the data. This was

done through various analysis techniques outlined in great detail. The steps of removing unwanted contribution from background channels and random coincidences were described. This included the use of time gates imposed on the data to remove random contributions, and the use of energy and momentum conservation requirements. Nevertheless channels with the same multi-particle final states are impossible to completely remove from the data.

- The use of Monte Carlo simulations was presented as an essential tool in the data analysis. Simulations were performed to take into account the detection efficiency of the setup, and were also important in removing any possible bias introduced by the various gates and conditions placed on the data.

- New results on γ-branches of the 15.11 MeV state to the 7.65, 10.84, 11.83, and 12.71 MeV states were determine using a novel technique to indirectly measure γ-rays from charged-particle detectors. This method is ideal when looking for γ-decay to broad states. The results from the γ-branches were compared to literature values when such information was available. The γ-branches of the 15.11 MeV state to the 11.83, 10.84, and broad 10 MeV state were previously unmeasured. Similarly, γ-branches of the 12.71 MeV state to the 7.65 MeV and the broad 10 MeV states were measured. Absolute γ-branches were determined from the relative branching ratios.

- The γ-branches were compared with Gamow-Teller β-decays, which allowed for the separation of the orbital contribution to the M1 matrix element. These values of γ_l were calculated for M1 decays from the 15.11 MeV state and can be directly compared with shell model calculations. The B(M1) values were determined from the data and compared to theoretical calculations, which can prove useful for further work on theoretical models.

- The isospin-forbidden α-decay of the T=1, $J^\pi = 1^+$ 15.11 MeV resonance in ^{12}C was observed. This decay must be the result of isospin mixing with the T=0, $J^\pi = 1^+$ 12.71 MeV resonance and some preliminary estimates on the amount of isospin mixing were made.

- Energy and widths of several known states in ^{12}C were determined. These values were obtained by fitting known resonances to Breit-Wigner distributions folded with a Gaussian to take into account the experimental resolution. In addition the J^π of the 13.35 MeV resonance was determined to be 4^- through the use of Dalitz plots.

- For states of natural parity in ^{12}C, the data could be separated into states which decay via the ground state in ^{8}Be and those which do not. The partial branching ratios of natural parity states to decay through the ^{8}Be(gs) were determined for the 9.64, 10.84, 14.08, and the 16.11 MeV resonances. The partial branches $\Gamma_{\alpha 0}$ were then extracted from the total alpha widths.

- The R-matrix formalism was introduced as a tool to search for new resonances in ^{12}C, especially in the region from 9-12 MeV. The results obtained from this analysis do not find evidence for contribution of a 2^+ resonance in this region.

6.2 Outlook

The data obtained in the ^{3}He + ^{11}B $\rightarrow$ d+^{12}C* and^{3}He + ^{10}B $\rightarrow$ p+^{12}C* reactions contain many different channels besides the ^{12}C channel. Future work can be done to study excited states in both ^{9}B and ^{9}Be in great detail. In addition, further work on R-matrix fits of ^{12}C is needed to give conclusive results as to the existence of 0^+ and 2^+ states in the broad region from 9-12 MeV.

There are other experiments which could give insight into the presence of the 2^+ state in that region. A recent experiment by Fynbo et al. impinges a proton beam at low energies (less than 400 keV) on a ^{11}B target. The purpose of the experiment is to probe the $J^+ = 2^+$ 16.11 MeV state in ^{12}C and search for γ-delayed 3α-breakup (similar to the method of detecting gammas described in Chapter 4). By searching for γ-decays to the broad region at 10 MeV, it may be possible to determine the J^π of the populated resonance by exploiting the larger probability of M1 transitions to a 2^+ resonance over E2 transitions to a 0^+ resonance (Eq. 4.2).

6.2.1 Fusion reactor

There is an unexpected application of the results which can be further investigated as well, related to data for a fusion reactor. Clean fusion energy is highly sought after and its discovery would greatly impact the world. Many different fusion reactions have been proposed, though these reactions release most of their energy in the form of neutrons. Aneutronic fusion has been proposed to reduce the problems of neutron production. One example of aneutronic fusion which has been proposed is p+^{11}B$\rightarrow 3\alpha + 8.7$ MeV. This reaction is an ideal candidate since the large amount of energy released is in

the form of alpha particles and the competing channels with neutrons have lower cross sections and there has been much activity in making this feasible [Vol06]. Measurements of the energy distributions of the outgoing alpha particles are important, but are made difficult by the fact that this reaction proceeds sequentially mostly through the 2^+ state in ^{8}Be. Attempts have been made to measure the distribution of the alpha energies [Lin98] though there are discrepancies between data. There is still work underway to understand the angular and energy distribution of the emitted alpha particles in the p+^{11}B reaction for an aneutronic fusion reactor [Pri09]. It is possible that with the data obtained in this experiment we could give insight into this problem.

6.3 Remarks

I hope that with this work I have at least convinced the reader that there is still interesting physics to be done in the valley of stability and at small accelerator facilities. It was a wonderful learning experience to work on an experiment at a small facility where it is easier to see the bigger picture of things. I also feel very lucky to have been a part of this experiment from the early preparations all the way until the publication of results. Hopefully, these results will add one more additional piece to the puzzle that is nuclear physics.

7
Resumen en Castellano

7.1 Introducción

El núcleo es un sistema de muchos cuerpos cuya cohesión y comportamiento depende de tres de las cuatro interacciones fundamentales: fuerte, débil y electromagnética. A grandes rasgos, podemos decir que en su investigación se pretende describir como funciona el núcleo, por qué funciona de esa manera y como se modifica su comportamiento cuando variamos la energía de excitación, el momento angular o el balance de neutrones y protones. Es decir, ¿qué ocurre en las interacciones entre nucleones que causa que no todos los núcleos se comporten de la misma forma? ¿Es posible obtener un modelo teórico que pueda describir las propiedades de todos los núcleos?

Para responder a estas preguntas, los físicos han llevado los núcleos a los límites de su existencia, lo que ha generado la construcción de numerosas instalaciones de haces radioactivos en todo el mundo. El desarrollo de instalaciones de haces de núcleos radioactivos ha dado lugar a fenómenos muy interesantes en los últimos años. Actualmente, las investigaciones en física nuclear son muy variadas, desde estudios de núcleos con halo hasta la búsqueda de elementos superpesados, desde la astrofísica nuclear hasta la desintegración doble β sin emisión de neutrino cuya descripción va más allá del modelo estándar. Muchos resultados obtenidos en estos años han mejorado los modelos teóricos existentes o han ayudado a crear modelos nuevos para mejorar la comprensión del funcionamiento del núcleo.

7.1.1 Motivación

El objetivo final de la física nuclear sería resolver el Hamiltoniano de cualquier núcleo a partir de las interacciones entre nucleones. Debido a que los núcleos se componen de numerosos nucleones y sólo se ha podido aplicar a sistemas de unos pocos nucleones, este método es poco eficaz. Existen cálculos basados en primeros principios capaces de describir los primeros niveles excitados

de los núcleos ligeros hasta A=12. En el caso del ^{12}C aún no llegan a los niveles excitados por encima del umbral de tres partículas alfa, que es la región de interés de este trabajo. Por ejemplo, el modelo de Green's Function Monte Carlo (GFMC) tiene calculado el nivel fundamental del ^{12}C [Pie05], mientras que el No-Core Shell Model (NCSM) ha llegado a calcular niveles excitados del ^{12}C, aunque no el segundo estado 0^+, llamado el estado de Hoyle [Nav07]. Llegado a este punto de sofisticación en los cálculos es necesario revisar los datos experimentales y comprobar que el conocimiento de los estados excitados a nivel de valores de energía, anchuras, espín-paridad y elementos de matriz sea suficientemente preciso para poder comprobar la veracidad de los logros teóricos.

De gran interés y, por tanto, una motivación importante para realizar el experimento objeto de este trabajo es poder entender mejor la región de energía de excitación del ^{12}C entre 9-12 MeV. El estado de Hoyle a 7.65 MeV fue explicado como una cadena lineal de tres partículas alfa hace más de cincuenta años [Mor56]. Si esto fuera cierto, debería de tener una banda rotacional acoplada con un primer estado excitado 2^+ a una energía de excitación entre 9-10 MeV, dependiendo de la estructura del estado de Hoyle. Por ello, se asignó originalmente un estado ancho descubierto en estudios de reacción a 10 MeV como el estado 2^+ buscado [Mor56]. Sin embargo, dicho estado se estudió en detalle en años posteriores y se estableció como un 0^+ [FSW71, Ueg79].

En la ultima década, el debate sobre la existencia de un estado con espín-paridad 0^+ en esa región se ha reabierto, impulsado por una parte por el avance de los cálculos teóricos y, por la otra, por los avances tecnológicos tanto en haces radiactivos como en desarrollos de detectores multibandas de partículas cargadas y en la electrónica integral asociada. Estudios sobre la desintegración β empleando haces de ^{12}N y ^{12}B han sido claves para entender los estados en la región de 9-12 MeV del ^{12}C. En la ultima década se han encontrado indicios de un estado de 2^+ en esta región [Ito04, Fre06, Fre07, Fre09, Hyl09a, Hyl09b, Hyl10, Dig09], pero aún no hay consenso sobre este tema.

El estudio de la ruptura del ^{12}C en tres partículas alfa puede dar información sobre la tasa de reacción de elementos pesados en el universo. El proceso de fusión triple-alfa (cuando tres partículas alfa se fusionan y forman un núcleo del ^{12}C) depende mayoritariamente del estado de Hoyle a 7.65 MeV del ^{12}C, a tan solo 380 keV del umbral de tres partículas alfa [Hoy54], aunque otros estados influyen a temperaturas más extremas [BB06]. Un mejor conocimiento de los estados alrededor del umbral de tres alfas puede ayudar a calcular la tasa de formación del ^{12}C en los medios estelares con más precisión. Incluso un experimento reciente [Fyn05], en el que se demues-

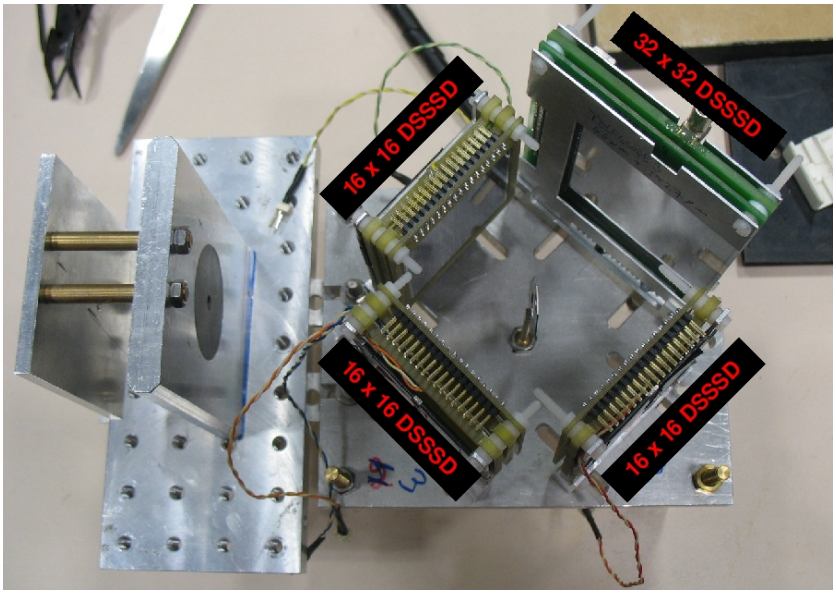

Figure 7.1: Foto del dispositivo experimental utilizado en los experimentos objeto de este trabajo realizados en la línea de física nuclear del CMAM (UAM). Se puede observar los cuatro telescopios de partículas cargadas: tres de ellos formados por un DSSSD de 16 ×16 bandas y el otro por un DSSSD de 32 × 32 bandas. A la izquierda se puede observar el colimador del haz entrante y en el medio de los detectores el blanco.

tra las interferencias entre los dos estados 0^+ (Hoyle y estado a 10 MeV), ha deducido que las tasas de la reacción de triple-alfa existentes [Ang99, DB87] tienen errores en el cálculo de dicha tasa de reacción a temperaturas extremas.

7.2 Experimento y análisis

Con el objetivo de revisar y determinar los estados excitados conocidos del ^{12}C hasta energías de unos 17 MeV se realizó una serie de experimentos en los que se estudiaron dos reacciones diferentes: ^{3}He + ^{11}B → d+^{12}C* con una energía de haz incidente de 8.5 MeV y ^{3}He + ^{10}B → p+^{12}C* con una energía de 4.9 MeV. Este experimento se llevó a cabo en la línea de física nuclear en el Centro de Micro Análisis de Materiales (CMAM) [Got02], ubicado en la Universidad Autónoma de Madrid. El dispositivo experimental utilizado en las dos reacciones disponía de cuatro telescopios que cubrían ≈ 38% de 4π, y contaba con un colimador de wolframio ($\phi = 5$ mm) (ver Fig. 7.1).

Un telescopio para la detección de partículas cargadas está formado por dos detectores. Si la partícula atraviesa el detector frontal y se detiene en el

segundo detector, el estudio de la energía perdida en el primer detector más la depositada en el segundo nos permitirá determinar no solo la energía de la partícula incidente si no también su carga y masa. En el caso en estudio, los dos detectores son un DSSSD de 256 pixeles (Double-Sided Silicon Strip Detector) de 60 μm junto a un detector grueso de 1000 μm. Con estos telescopios se obtiene información de la energía y de la posición de la partícula entrante, así como de su tipo.

Con la información de energía de las partículas detectadas y con la información obtenida de la posición de la partícula a través del pixel del DSSSD (x,y,z), se pueden determinar los componentes de los momentos de todas las partículas

$$\begin{aligned} P &= (P_{\mathrm{x}}, P_{\mathrm{y}}, P_{\mathrm{z}}) \\ |P| &= \sqrt{2 \cdot m \cdot E} \\ P_{\mathrm{x}} &= x \cdot |P|/r \\ P_{\mathrm{y}} &= y \cdot |P|/r \\ P_{\mathrm{z}} &= z \cdot |P|/r \end{aligned}$$

donde $\vec{r} = \sqrt{x^2 + y^2 + z^2}$, la masa m en MeV/c^2 y la energía E en MeV. Esto permite depurar notablemente los datos no deseados de otros canales de reacción, aunque no se puedan eliminar por completo los canales que contienen las mismas partículas salientes. En el caso de la reacción estudiado utilizando el blanco de ^{10}B, los diferentes canales de reacción concurrentes, cuyos productos finales son idénticos, se indican a continuación:

$$^{10}\mathrm{B} + {}^{3}\mathrm{He} \rightarrow \left\{ \begin{array}{rl} p + {}^{12}\mathrm{C}^{*} & \rightarrow p + \alpha + {}^{8}\mathrm{Be} \\ \alpha + {}^{9}\mathrm{B}^{*} & \rightarrow \alpha + p + {}^{8}\mathrm{Be} \\ \alpha + {}^{9}\mathrm{B}^{*} & \rightarrow \alpha + \alpha + {}^{5}\mathrm{Li} \\ {}^{8}\mathrm{Be} + {}^{5}\mathrm{Li}^{*} & \rightarrow {}^{8}\mathrm{Be} + p + \alpha \end{array} \right\} \rightarrow p + 3\alpha$$

lo mismo para la reacción con el blanco de ^{11}B:

$$^{3}\mathrm{He} + {}^{11}\mathrm{B} \rightarrow \left\{ \begin{array}{rl} d + {}^{12}\mathrm{C}^{*} & \rightarrow d + \alpha + {}^{8}\mathrm{Be} \\ \alpha + {}^{10}\mathrm{B}^{*} & \rightarrow \alpha + d + {}^{8}\mathrm{Be} \\ {}^{8}\mathrm{Be} + {}^{6}\mathrm{Li}^{*} & \rightarrow {}^{8}\mathrm{Be} + d + \alpha \end{array} \right\} \rightarrow d + 3\alpha$$

Esto significa que, por ejemplo, para el caso de la reacción de ^{10}B + ^{3}He y considerando el caso de la detección de cuatro partículas, p+3α, no se puede identificar qué proporción de los fragmentos finales provienen del canal que alimentan los estados excitados del ^{12}C. No obstante, en el caso

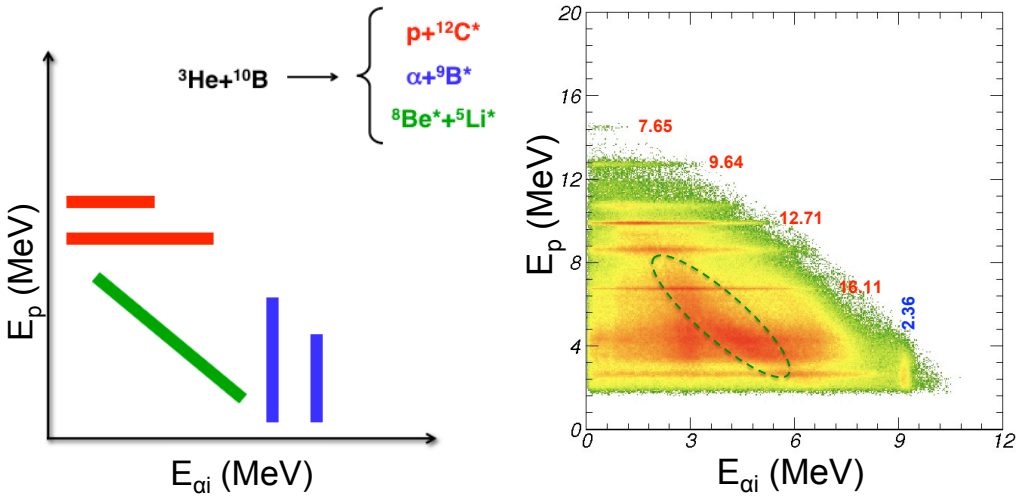

(a) (b)

Figure 7.2: A la izquierda se muestra un esquema de $E_{\alpha i}$ frente a E_p en CM donde se pueden ver esquematicamente los diferentes canales de la reacción de $^{10}\mathrm{B} + {}^{3}\mathrm{He}$, cuyos productos finales son p+3α. A la derecha se muestra un espectro bidimensional equivalente a (a) de los datos de la reacción de $^{10}\mathrm{B} + {}^{3}\mathrm{He}$, donde están indicados diferentes estados excitados del ^{12}C en rojo y un estado excitado del ^{9}B en azul. En verde se indica un estado ancho del ^{5}Li.

de que un canal de fondo vaya a un estado excitado intermedio estrecho será posible eliminar la contribución de dicho fondo [Alc09]. Cuando un canal de fondo corresponde a un estado intermedio excitado bastante ancho es difícil eliminar dicho fondo mediante las condiciones de conservación de energía y de momento exigidos a los datos de la coincidencia cuádruple. En este caso, se emplean simulaciones Monte Carlo para conocer la contribución al canal del ^{12}C. En la Fig. 7.2 se observa un esquema de la energía del protón en el centro de masas frente a la energía individual de los alfas en el centro de masas para la reacción de $^{10}\mathrm{B} + {}^{3}\mathrm{He}$.

La ruptura de estados del ^{12}C suele ocurrir por un proceso secuencial, es decir:

$$\begin{aligned} {}^{12}\mathrm{C} &\rightarrow \alpha + {}^{8}\mathrm{Be} \\ {}^{8}\mathrm{Be} &\rightarrow \alpha + \alpha \end{aligned}$$

El paso intermedio en este proceso puede ocurrir a través del estado fundamental del ^{8}Be ($J^{\pi}=0^{+}$, Γ=5.6 eV) o a través del primer estado excitado del ^{8}Be ($J^{\pi}=2^{+}$, Γ=1.4 MeV) o de ambos. Se puede calcular la energía de excitación del ^{8}Be con la información de las energías individuales de las partículas alfa. Con este método se pueden separar las contribuciones de la ruptura del ^{12}C dependiendo de su mecanismo de ruptura y determinar las razones de ramificación parciales a través del ^{8}Be(gs) o ^{8}Be(exc).

7.3 Resultados

7.3.1 Detección indirecta de transiciones γ

En este experimento se utilizaron exclusivamente detectores de partículas cargadas (DSSSD). A pesar de esto, ha sido posible desarrollar una técnica que nos ha permitido determinar la contribución de desexcitación parcial o total de los niveles a través de radiación electromagnética, midiendo el defecto de energía entre la obtenida a partir del protón o deuterón que puebla un estado excitado en ^{12}C y la obtenida en la reconstrucción de las tres partículas alfas asociadas al mismo suceso. Esto se debe a que se puede calcular la energía de excitación del ^{12}C con dos métodos distintos. En primer lugar, se puede calcular la energía de excitación del ^{12}C a partir de la energía del fragmento ligero (protón o deuterón dependiendo de la reacción). Segundo, se puede reconstruir la energía del ^{12}C a partir de las energías de las tres partículas alfa que provienen de su ruptura. La energía de excitación calculada con el primer método nos da directamente la energía inicial del estado poblado

Table 7.1: Razones de ramificación de transiciones electromagnéticas γ del estado 1^+, T=1 a 15.11 MeV y el estado 1^+, T=0 a 12.71 MeV del ^{12}C

Transición	Sucesos	Eff.	BR-γ	BR-γ [AW72]
15.11 → 12.71	39	0.74 %	1.2±0.2 %	1.4±0.4 %
11.83	8	0.57 %	0.32±0.12 %	...
10.84	<7.3	1.30 %	<0.13 %	...
10.3	65	1.09 %	1.4±0.2 %	(1.6) %
7.65	70	0.36 %	2.6±0.7 %	4.4±0.8 %
0.00 and 4.44	40344	9.9 %	92.7±1.0 %	94±2 %
12.71 → 10.3	3	0.40 %	$0.9^{+0.6}_{-0.5}$ %	...
7.65	4	0.18 %	$2.6^{+1.6}_{-1.2}$ %	...
0 and 4.44	11660	13.9 %	$96.6^{+1.7}_{-1.3}$ %	100 %

del ^{12}C. Normalmente, el estado inicial del ^{12}C se rompe en tres partículas alfa con lo que la energía reconstruida por el segundo método coincide con la energía de excitación calculada a partir de la energía del ión ligero. Sin embargo, si el estado poblado inicialmente del ^{12}C emite un γ y el estado final se rompe en tres partículas alfa, los valores de energía de excitación del ^{12}C obtenidos a través de los dos métodos no coincidirán, y la diferencia entre ellas será la energía de la transición γ. Esto se muestra en la Fig. 7.3 para la reacción de ^{10}B(^{3}He,p$\alpha\alpha\alpha$).

Con este método se han determinado las transiciones γ que desexcitan el estado de 15.11 MeV y de 12.71 MeV a estados por encima del umbral triple-alfa. También se han deducido las desexcitaciones a estados por debajo de este umbral mediante el estudio de coincidencias del ión ligero y del ^{12}C. A raíz de estas medidas se pueden calcular las razones de ramificación de transiciones γ para el estado de 15.11 MeV y 12.71 MeV (Tabla 7.1 y Fig. 7.3).

El estado de T=1 a 15.11 MeV de excitación se desexcita en ^{12}C fundamentalmente por emisión electromagnética. Esto se debe a que la desintegración α está prohibida por conservación de isospín. Sin embargo, a partir de la mezcla de isospín con el estado de 12.71 MeV, el estado de 15.11 MeV tendrá una pequeña anchura del canal de emisión α. En este trabajo se han podido asignar sucesos a una ruptura en tres partículas alfa del estado de 15.11 MeV y se ha determinado la anchura del canal α, Γ_α/Γ=(2.8±1.2)% [Kir09].

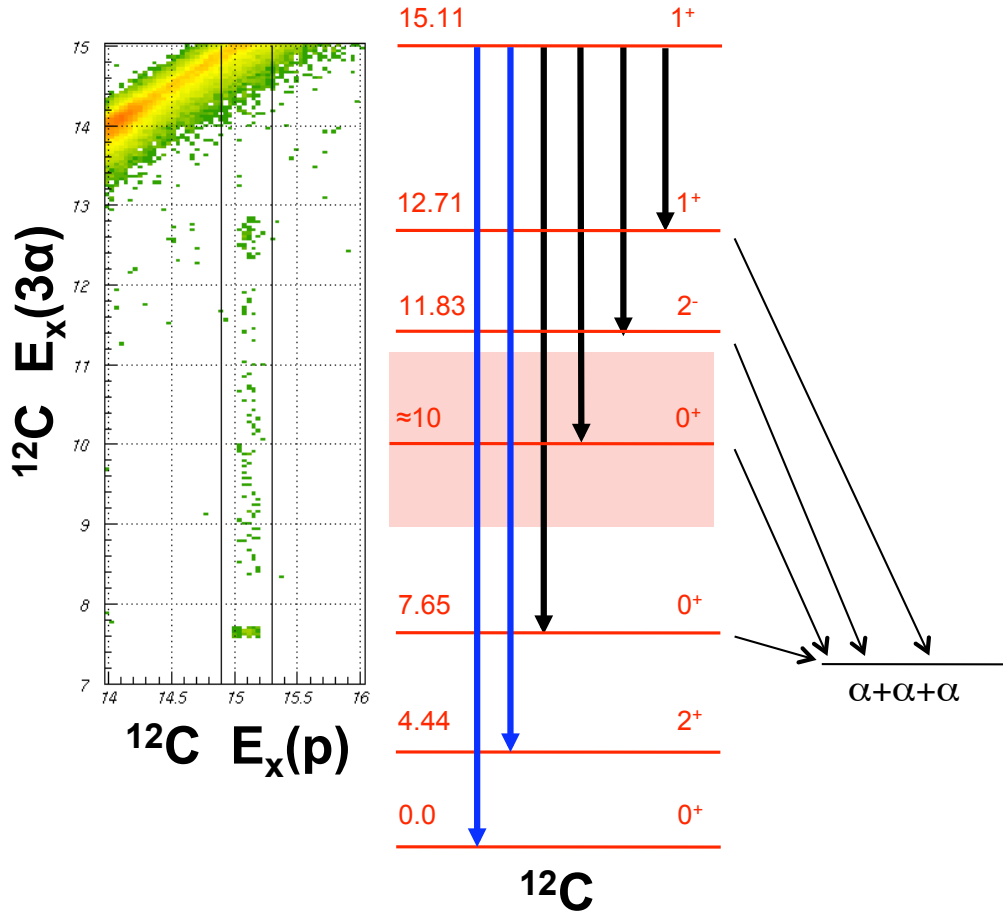

Figure 7.3: A la izquierda, esquema bidimensional de excitación del ^{12}C calculada a partir de la energía del protón frente a la energía de excitación del ^{12}C calculado a partir de las tres partículas alfa. Los sucesos en la diagonal corresponden a la desexcitación del estado en cuestion mediante la ruptura en 3α. Los seleccionados en la línea vertical corresponden a sucesos con una clara diferencia de energía entre la suma de 3α y la energía del protón. A la derecha se muestra el método de deducción de las transiciones γ ejemplarizado para el caso del nivel de 15.11 MeV (T=1) del ^{12}C. Se muestran las vías de desexcitación γ a estados no ligados que rompen en 3α y el resto de intensidad para este estado se atribuye a desexcitación a los estados ligados fundamental y primer excitado. Las razones de ramificación se muestran en la tabla 7.1.

Table 7.2: Valores de energía y Γ obtenidos para estados del ^{12}C. Los valores conocidos de J^{π}, Γ y E_x son de [Ajz90]. La energía del estado de 9.64 MeV fue utilizado para recalibrar el espectro.

E_x ^{12}C (keV)	J^{π}	Γ (keV)	E_x (keV) (present)	Γ (keV) (present)
9641(5)	3^-	34(5)	—	43(5)
10844(16)	1^-	315(25)	10847(5)	272(5)
11828(16)	2^-	260(25)	11838(5)	229(7)
13352(17)	(2^-)	375(40)	13305(9)	510(40)
14083(15)	4^+	258(15)	14078(5)	273(5)
20500(100)	(3^+)	300(50)	20553(5)	245(7)

7.3.2 Energía y anchura de niveles del ^{12}C

Para calcular las propiedades de los estados del ^{12}C es necesario tener un conocimiento preciso sobre los posibles canales que contribuyen al fondo de los espectros. De estos, los que tienen estados intermedios estrechos se pueden eliminar directamente de los datos. En cambio, aquellos con estados intermedios anchos son difícilmente separables. Sin embargo, las contribuciones de estos canales varían poco respecto a los estados del ^{12}C con lo que se han tenido en cuenta ajustando el espectro con un fondo lineal.

Los estados excitados del ^{12}C, cuyos valores de energía y de anchura no están bien definidos, se han ajustado con la convolución de una distribución Breit-Wigner y una distribución Gaussiana. La convolución se ha realizado para diferentes ángulos, ya que la energía varía en función del ángulo de entrada del ión ligero. Para obtener los resultados finales se ha calculado una media ponderada de los diferentes rangos del ángulo y de las dos reacciones. La Tabla 7.2 muestra los valores de energía y anchura calculados en este trabajo y su comparación con el trabajo de compilación [Ajz90].

7.3.3 Razones de ramificación parciales de niveles excitados del ^{12}C

Los estados de espín-paridad naturales que se desintegran por un proceso secuencial a través del ^{8}Be se pueden separar dependiendo del estado que pueblan en ^{8}Be. Estados de espín-paridad natural son estados con $\pi = (-1)^l$, donde l es el espín y π es la paridad. Una vez se seleccionan los datos, se pueden emplear los ajustes explicados anteriormente para conocer las ra-

Table 7.3: Razones de ramificación de estados de espín-paridad natural del ^{12}C que se desintegran a través del estado fundamental de ^{8}Be. Se muestra el efecto de incluir la corrección del pico fantasma del ^{8}Be(gs). La anchura del canal α al estado fundamental de ^{8}Be ($\Gamma_{\alpha 0}$) se ha calculado utilizando los valores obtenidos en este trabajo de las anchuras de los estados.

E_x ^{12}C (MeV)	J^π	B.R. % (sin corr.)[a]	B.R. % (corr.)[b]	B.R. % (literature)	$\Gamma_{\alpha 0}$ (keV)
9.64	3^-	96.3(1)	99.5(6)	97.2[Fre07]	32(2)
10.84	1^-	94.7(5)	99.4(6)	—	249(2)
14.08	4^+	22.8(2.0)	24.2(2.0)	17(4)	50(11)
16.11	2^+	5.6(1)	6.4(1)	4.4[Ajz90]	0.3(1.0)

[a] Las razones de ramificación al estado fundamental de ^{8}Be no incluyen la corrección del pico fantasma.
[b] Las razones de ramificación al estado fundamental de ^{8}Be incluyen la corrección del pico fantasma.

zones de ramificación parciales, es decir, la proporción de población de los diferentes estados de ^{8}Be (estado fundamental o el primer estado excitado). Es importante tener en cuenta la eficiencia de detección de los diferentes canales de reacción. Esto se hace mediante simulaciones Monte Carlo y una vez obtenidas las eficiencias se pueden calcular, de una manera absoluta, las razones de ramificación parciales.

Existe otra corrección a considerar en el cálculo de las razones de ramificaciones parciales debido al llamado pico fantasma (ghost-peak) del estado fundamental del ^{8}Be. El pico fantasma es un aumento de intensidad a energías altas del estado fundamental, debido a la cercanía del estado fundamental al umbral de dos alfas. El hecho de que el estado fundamental del ^{8}Be esté muy cerca del umbral de dos alfas (92 keV) distorsiona la forma del pico. A altas energías, la probabilidad de penetrar la barrera de Coulomb aumenta debido al menor radio de la barrera, incrementando la probabilidad de desintegración a esas energías. Hay que tener en cuenta esta corrección porque si no se puede sobrestimar la contribución al primer estado excitado. Los valores de las razones de ramificación se muestran en la Tabla 7.3 donde se puede apreciar el efecto de incluir la corrección por el pico fantasma del estado fundamental del ^{8}Be.

7.3.4 Determinación de J^{π} del estado 13.35 MeV del ^{12}C

Los diagramas de Dalitz [Dal53] consisten en la representación bidimensional de las energías de las tres partículas α en la que en el eje y se representa la energía de una partícula (E_1) y en el eje x una combinación lineal de dos partículas ($\frac{E_1+2E_2}{\sqrt{3}}$). Es un método muy útil para obtener información acerca del espín y de la paridad de un estado que se desintegra dando lugar a tres partículas. El método se basa en el análisis del espín y de la paridad del estado final y en las leyes de conservación. Representar los datos experimentales en un diagrama de Dalitz puede dar información sobre el mecanismo de ruptura y sobre el espín-paridad del estado inicial. Una ruptura directa en tres cuerpos no deja ninguna forma característica, mientras que una ruptura secuencial sí. Independientemente del mecanismo de ruptura, la estadística de Bose y las restricciones debidas a la conservación de espín, paridad e isospín obligan a que ciertas zonas en un diagrama de Dalitz estén vacías [Zem64].

Esta metodología se ha aplicado para determinar el espín-paridad, J^{π} del estado de 13.35 MeV del ^{12}C que aunque ha sido descrito en la literatura [Ajz90] como un 2^- muestra indicios de poder ser un 4^- [Fre06] según resultados de estudios de reacción. Para averiguar el J^{π} de este estado se ha hecho un diagrama de Dalitz con los datos experimentales. La Fig. 7.4 muestra un diagrama de Dalitz del estado de 13.35 MeV junto a un diagrama de Dalitz para la ruptura de un estado del ^{12}C en tres partículas alfa. Estas figuras muestran en negro las zonas donde la densidad desaparece, debido a la conservación del espín-paridad para un estado inicial del ^{12}C con $J^{\pi}=2^-$ y para un estado inicial del ^{12}C con $J^{\pi}=4^-$. En la figura se puede observar que la distribución bidimensional de los datos excluye la posibilidad de que el estado de 13.35 MeV del ^{12}C sea un 2^-, ya que la figura experimental contiene sucesos en el centro, algo prohibido por la conservación de espín-paridad. Por eso, el J^{π} del estado de 13.35 MeV del ^{12}C se ha asignado como un 4^-.

7.3.5 Ajuste de matriz-R del espectro del ^{12}C

El espectro del ^{12}C obtenido a partir de la selección de protones o deuterones se ha ajustado utilizando la teoría de matriz-R para conocer los estados que contribuyen a la región del ^{12}C entre 9-12 MeV de energía de excitación. Se han empleado simulaciones Monte Carlo para conocer la contribución de los canales de fondo al espectro del ^{12}C y los resultados se han incluido en el ajuste como un parámetro libre. El ajuste se ha centrado en la reacción de $^{11}B(^3He,d\alpha\alpha\alpha)$, ya que la contribución de fondo es menor. Los resultados de los ajustes preliminares no encuentran contribución de un estado 2^+ en la

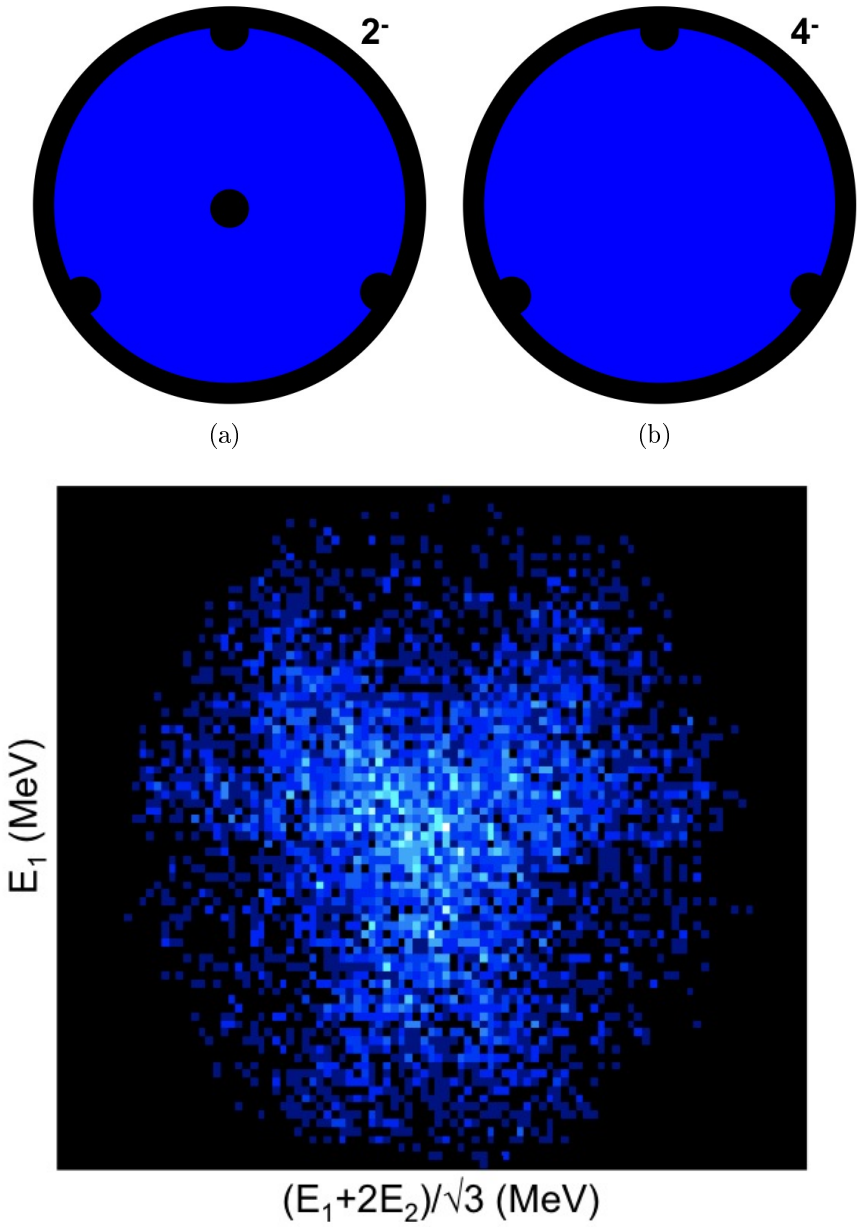

(a) (b)

(c)

Figure 7.4: Diagrama de Dalitz para el estado de 13.35 MeV del ^{12}C. Se representa la energía de una partícula emitida (E_1) frente a una combinación lineal de dos de ellas ($\frac{E_1+2E_2}{\sqrt{3}}$). Los datos experimentales obtenidos a partir de la reacción ^{3}He + ^{11}B se muestran en (c), mientras que en la parte superior de la figura se ven las zonas donde se espera que no haya datos para un estado de 2^- (a) y uno de 4^- (b) debido a las restricciones por simetrías.

región de 9-12 MeV del ^{12}C.

7.4 Conclusiones

7.4.1 Resumen

El trabajo de esta tesis se resume en:

- La motivación de este trabajo engloba varias ramas de la física, desde la astrofísica nuclear hasta los cálculos recientes de primeros principios. Experimentos previos de nuestra colaboración han estudiado los estados excitados del ^{12}C a partir de la desintegración β del ^{12}N y ^{12}B. Sin embargo, los estados del ^{12}C poblados a partir de la desintegración β están limitados a estados de paridad positiva y con J$\leq$ 2. Por ello, se ha hecho un experimento de reacciones para determinar mejor las propiedades de las resonancias del ^{12}C y poder estudiar estados de mayor energía de excitación y espín-paridad.

- Hemos estudiado las reacciones ^{3}He+^{11}B $\rightarrow$ d+^{12}C* a una energía de 8.5 MeV y ^{3}He + ^{10}B $\rightarrow$ p+^{12}C* a una energía de 4.9 MeV en el CMAM de Madrid. Los productos de la reacción: un ión ligero, protón o deuterón y tres partículas alfa procedentes de la desintegración del ^{12}C* han sido detectados en cinemática completa utilizando un dispositivo experimental de cuatro telescopios que cubrían un ángulo solido de 38% de 4π. La multisegmentación de los detectores ha permitido obtener información sobre la energía y el momento de las partículas detectadas.

- En las dos reacciones estudiadas hay muchos canales abiertos que se deben eliminar de los datos de la mejor manera posible. Esto se llevó a cabo utilizando varias técnicas de análisis. El procedimiento para eliminar contribuciones no deseadas tanto de otros canales como de coincidencias aleatorias ha sido explicado en detalle en este texto. Las técnicas utilizadas incluyen tanto las condiciones en la señal de coincidencia temporal como el uso de algoritmos que exijan conservación de momento y de energía. Sin embargo, se ha visto que canales con los mismos estados finales no se pueden limpiar totalmente.

- El uso de simulaciones Monte Carlo ha constituido una herramienta esencial en este análisis. Se hicieron simulaciones para determinar la eficiencia de detección del dispositivo experimental, ya que depende de

cada canal en estudio. Las correlaciones angulares de las partículas alfa dependen del canal intermedio de desintegración, es decir, a través de qué nivel del ^{8}Be ocurre el proceso.

- Se ha desarrollado un nuevo método que utiliza detectores de partículas cargadas para determinar las emisiones de radiación electromagnética. Se han identificado nuevas transiciones γ del estado de 15.11 MeV a los estados 7.65, 10, 10.84, 11.83 y 12.71 MeV y se han determinado sus razones de ramificación. Este método es ideal para identificar emisiones de radiación γ a estados anchos. Los resultados de las razones de ramificación de emisión γ han sido comparados con valores ya publicados. Se observa un acuerdo razonable teniendo en cuenta que se han observado nuevas ramas de desexcitación. Las transiciones γ del estado de 15.11 MeV a los estados de 11.83, 10.84 y al estado ancho a 10 MeV no se conocían previamente. Las transiciones γ del estado de 12.71 MeV a los estados de 7.65 MeV y el estado ancho de 10 MeV han sido medidas con este mismo método. Las razones de ramificación absolutas se han obtenido a partir de los valores relativos.

- Las transiciones γ de tipo M1 fueron comparadas con la probabilidad de transición β de tipo Gamow-Teller. Esto ha permitido separar la contribución orbital (γ_l), de la contribución de espín (γ_σ), del elemento de matriz M1. Los valores de γ_l han sido calculados para las transiciones M1 del estado 15.11 MeV y pueden compararse directamente con cálculos del modelo de capas. Existe un acuerdo razonable entre los valores B(M1) obtenidos de los datos experimentales y los cálculos teóricos del modelo de capas [CK65] para el estado a 12.71 MeV.

- Se observó la emisión α del nivel de 15.11 MeV, (T=1, $J^\pi = 1^+$) que está prohibido por conservación de isospín y se ha determinado su razón de ramificación de valor de 2.8%. Esta emisión se debe a la mezcla de isospín con el estado de T=0, $J^\pi = 1^+$ 12.71 MeV. A partir de esta razón de ramificación parcial se ha obtenido además una estimación sobre la mezcla del nivel 15.11 MeV con el nivel 12.71 MeV en ^{12}C de $\beta^2 = 3.3\%$.

- Las energías y las anchuras de los estados conocidos del ^{12}C se han obtenido a través del ajuste a una función que resulta de la convolución de una distribución Breit-Wigner con una distribución Gaussiana que tiene en cuenta la resolución del sistema experimental. El J^π del estado a 13.35 MeV se ha asignado como 4^- de una manera definitiva a partir de los diagramas de Dalitz.

- Para los estados de paridad natural del ^{12}C, los datos se han clasificado en función de su canal de desintegración intermedia. Se han obtenido las razones de ramificación parciales a través del estado fundamental del ^{8}Be de los estados de paridad natural de 9.64, 10.84, 14.08 y 16.11 MeV. Los $\Gamma_{\alpha 0}$, la anchura parcial de desintegración al estado fundamental del ^{8}Be, han sido extraídos a partir de las anchuras alfa totales.

- Se ha introducido el formalismo de matriz-R como herramienta para buscar nuevas resonancias del ^{12}C, con especial interés en la región de 9-12 MeV. Los resultados del análisis indican que se puede explicar el espectro sin considerar la contribución de un nivel 2^+ en esta región. Sin embargo, estos son resultados preliminares y aún no se han obtenido datos más concluyentes.

7.4.2 Perspectivas futuras

Los datos obtenidos en las reacciones ^{3}He + ^{11}B $\rightarrow$ d+^{12}C* y ^{3}He + ^{10}B $\rightarrow$ p+^{12}C* contienen más canales de reacción a parte del canal del ^{12}C. Estudios sobre estos canales pueden servir para futuros trabajos como, por ejemplo, el estudio de estados excitados de ^{9}B y ^{9}Be. Futuros trabajos en los ajustes de los espectros con matriz-R del ^{12}C podrán ser utilizados para obtener resultados concluyentes sobre la existencia de estados anchos de 0^+ y 2^+ en la región de 9-12 MeV.

Se han llevado a cabo nuevos experimentos con el objetivo de aportar nuevas evidencias sobre la existencia de un estado 2^+ en esta región. Un ejemplo es el reciente experimento por Fynbo et al. que consiste en el impacto de un protón de baja energía contra un blanco de ^{11}B. Este experimento fue realizado para poblar el estado de $J^+ = 2^+$ a 16.11 MeV del ^{12}C y buscar las emisiones de 3α después de la emisión de un γ, utilizando el mismo método indirecto que en este trabajo. Es posible determinar el J^π del estado poblado buscando emisiones γ al estado ancho de 10 MeV y haciendo uso de las transiciones M1 a estados 2^+ que son más probables que las transiciones E2 a estados 0^+.

Reactor de fusión

Los resultados obtenidos tienen el valor añadido de poder ser de aplicación en reactores de fusión, lo que deberá ser investigado en el futuro. La obtención de energía limpia de fusión tendrá gran impacto sobre la humanidad. Se han propuesto muchas reacciones distintas para realizar dicha fusión, pero la mayoría de ellas emiten su energía en forma de neutrones. La fusión aneutrónica

fue propuesta para reducir los problemas de producción de neutrones. Un ejemplo de fusión aneutrónica es la siguiente reacción: p+^{11}B$\rightarrow$ 3α+8.7 MeV. Está reacción es ideal por la gran cantidad de energía liberada y gran sección eficaz frente a los canales con neutrones que tienen secciones eficaces más bajas. Las medidas de distribución de energía en las partículas alfa salientes son muy importantes para modelar esta reacción, pero presentan muchas dificultades, ya que esta reacción discurre mayoritariamente a través del estado 2^+ en ^{8}Be. Ha habido varios intentos de medir la distribución de energía en las alfas [Lin98], pero existen discrepancias entre los datos obtenidos. Aún queda un largo camino por recorrer para entender la distribución en ángulo y en energía de las partículas alfa emitidas en la reacción p+^{11}B para un reactor aneutrónico de fusión [Pri09]. Es posible que se puedan deducir estas distribuciones a partir los datos obtenidos en el experimento que se ha analizado y presentado en este trabajo de tesis.

7.4.3 Discusión

Espero que con este trabajo de tesis haya quedado claro que aún queda física interesante por hacer en el valle de la estabilidad. Ha sido una experiencia enriquecedora haber podido trabajar en un experimento con un acelerador pequeño donde uno puede tener una visión más amplia del experimento. Tuve la oportunidad de participar desde el principio en el primer experimento que se realizó en la línea de física nuclear del CMAM. En este experimento pude descubrir, a través del análisis de los datos, las dificultades técnicas y las posibles mejoras del sistema experimental. Teniendo en cuenta esta nueva situación, diseñé un sistema mejorado y desarrollé las técnicas de análisis que he presentado en este trabajo de tesis. Espero que con estos resultados se pueda añadir una pieza más al puzle que es la física nuclear.

A

Detection efficiencies for R-Matrix fits

Figures A.1 and A.3 show the detection efficiency of ^{12}C for different angles and energies above 9 MeV (starting at 9.25 MeV) for states which decay through the ^{8}Be(gs) while Figs. A.2 and A.4 show the same but for decay through the ^{8}Be(exc). Here the angular binning was of 5°. Figures A.5, A.7 and A.9 show the efficiency below for 9.25 MeV for states which decay through the ^{8}Be(gs) while Figs. A.6, A.8 and A.10 are for decays through the ^{8}Be(exc). In this case the angular binning is of 2°. Note the large changes in efficiency for very small changes in angle as compared with Figs. A.1 and A.3.

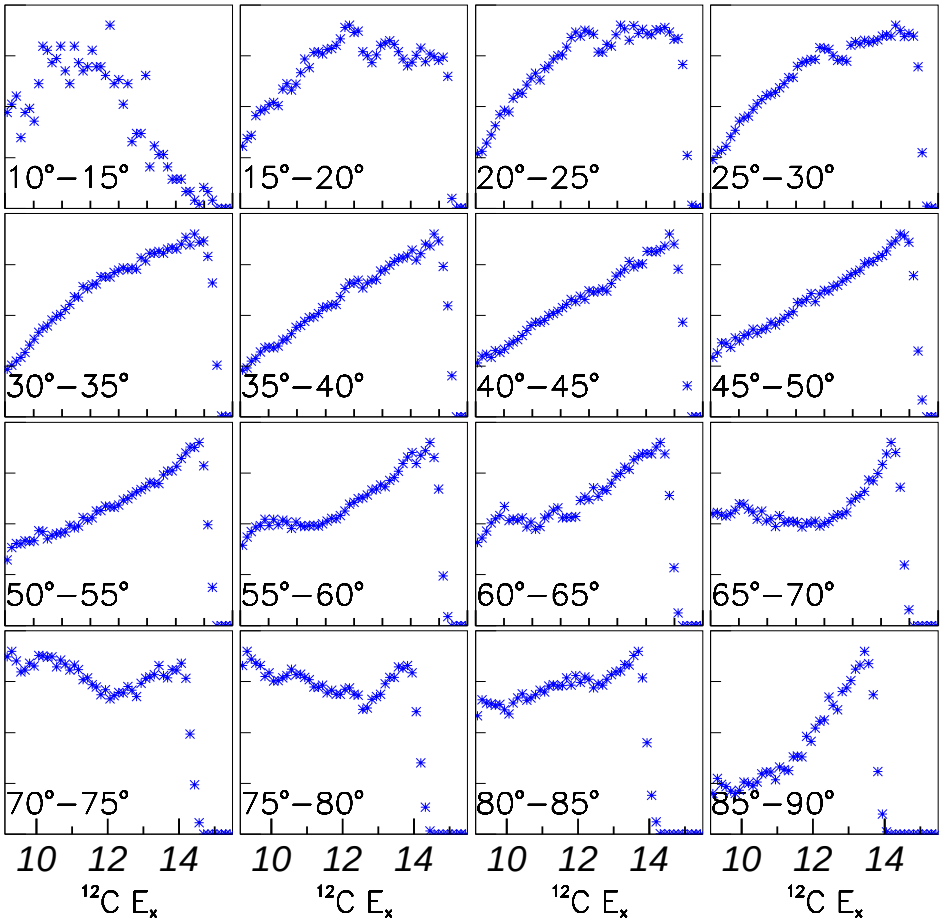

Figure A.1: Detection efficiency as a function of energy and angle of the deuteron in the CM system for decays through the ^{8}Be(gs), for energies above 9.25 MeV. The deuteron CM angles are between 10° and 90°. In this case the energy simulations have been done in steps of 125 keV. For each angular bin, the distribution has been fitted and then multiplied by the data to correct for efficiency.

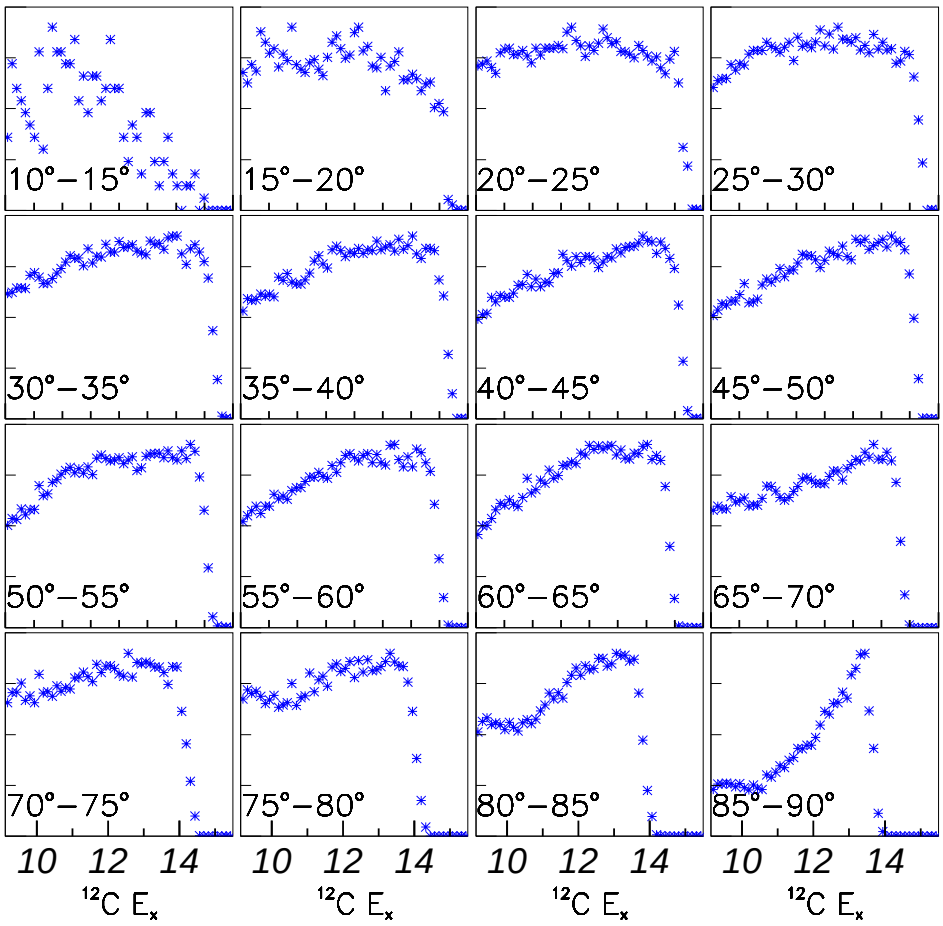

Figure A.2: Detection efficiency as a function of energy and angle of the deuteron in the CM system for decays through the ^{8}Be(exc), for energies above 9.25 MeV. The deuteron CM angles are between 10° and 90°. In this case the energy simulations have been done in steps of 125 keV. For each angular bin, the distribution has been fitted and then multiplied by the data to correct for efficiency.

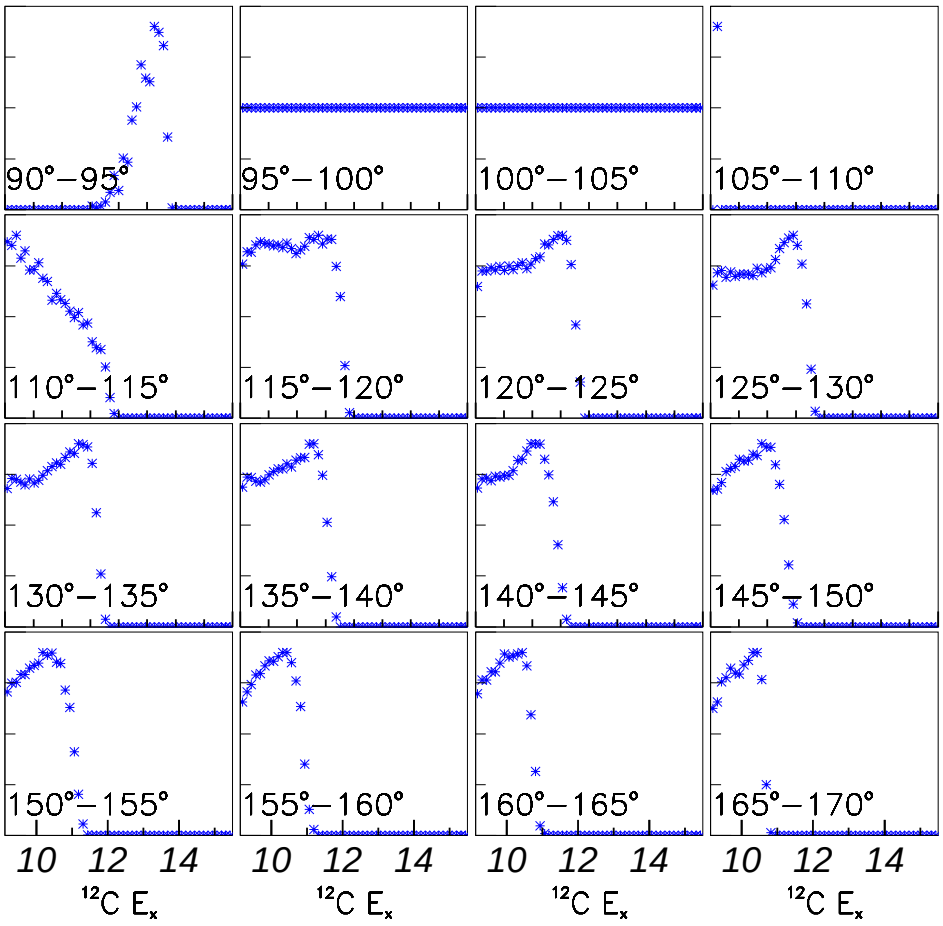

Figure A.3: Detection efficiency as a function of energy and angle of the deuteron in the CM system for decays through the ^{8}Be(gs), for energies above 9.25 MeV. The deuteron CM angles are between 90° and 170°. For each angular bin, the distribution has been fitted and then multiplied by the data for that angular bin to correct for efficiency.

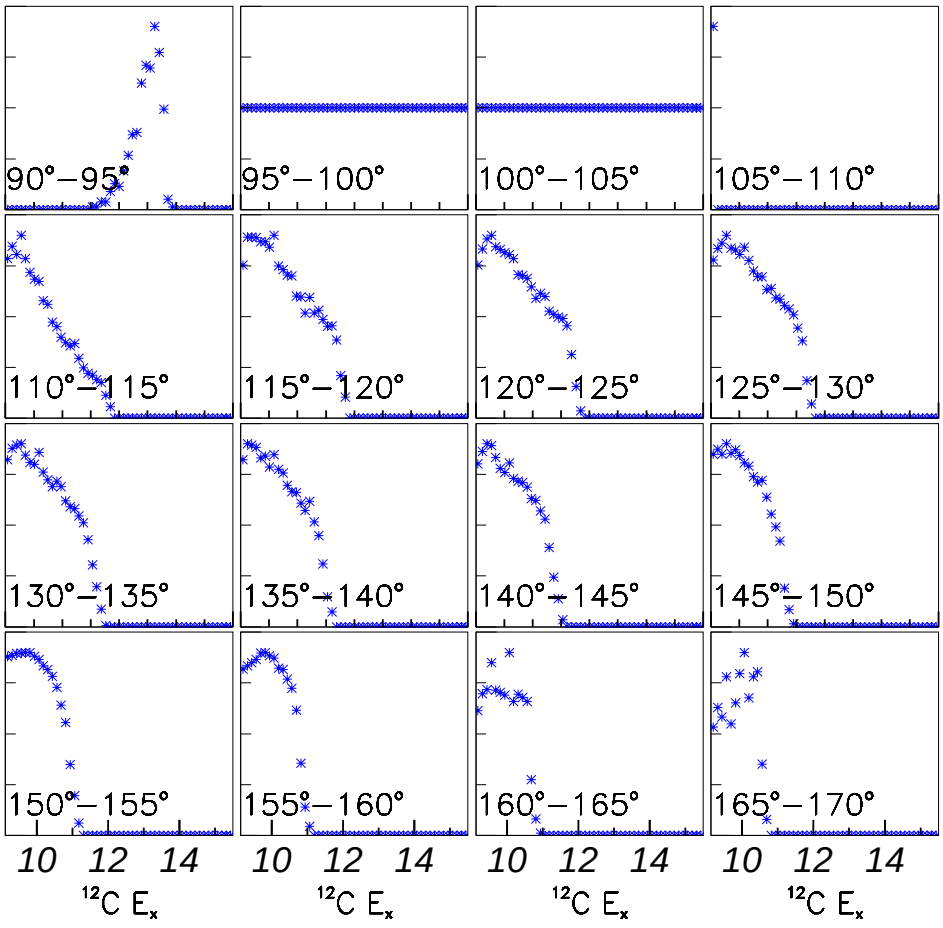

Figure A.4: Detection efficiency as a function of energy and angle of the deuteron in the CM system for decays through the ^{8}Be(exc), for energies above 9.25 MeV. The deuteron CM angles are between 90° and 170°. For each angular bin, the distribution has been fitted and then multiplied by the data for that angular bin to correct for efficiency.

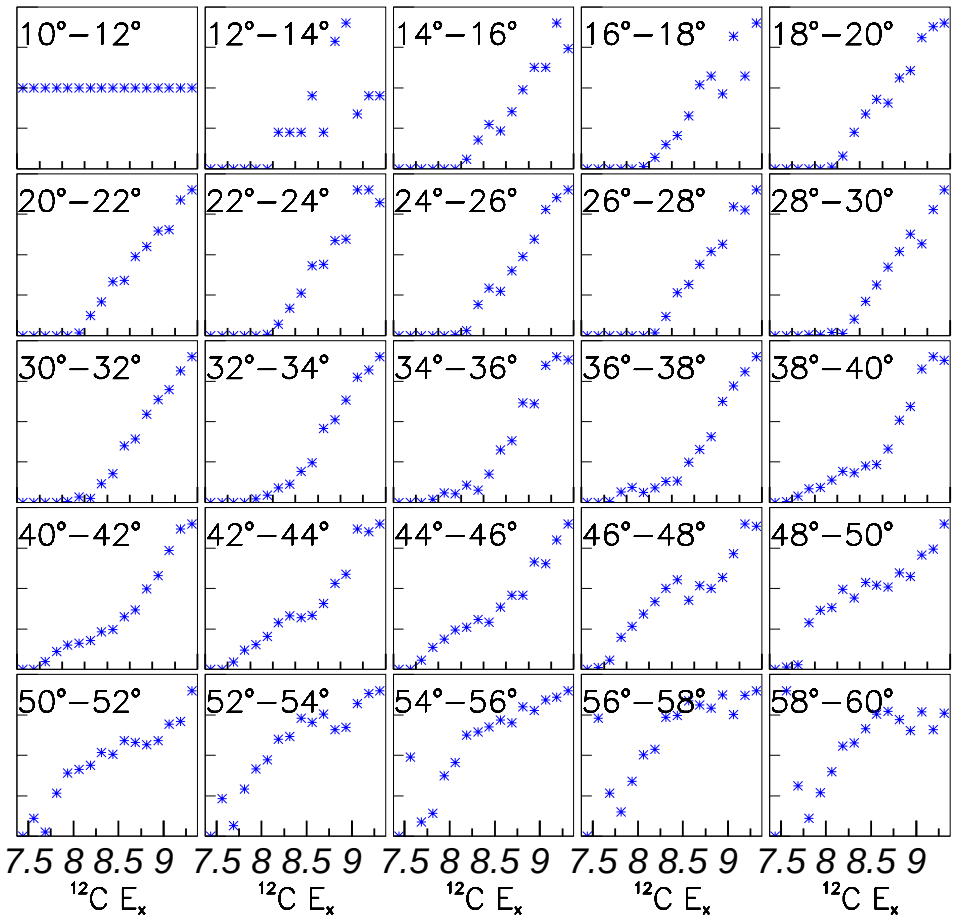

Figure A.5: Detection efficiency as a function of energy and angle of the deuteron in the CM system for decays through the ^{8}Be(gs), for energies below 9.25 MeV. The deuteron CM angles are between 10° and 60°. In this case the energy simulations have been done in steps of 125 keV. For each angular bin, the distribution has been fitted and then multiplied by the data to correct for efficiency.

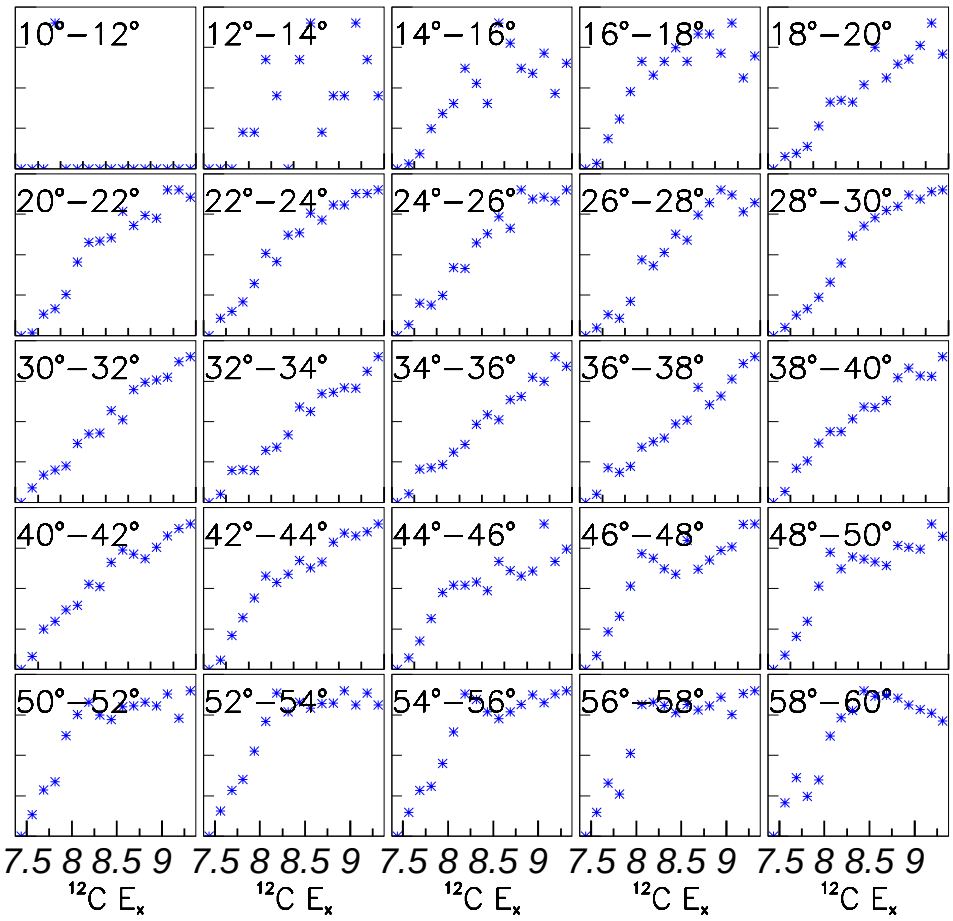

Figure A.6: Detection efficiency as a function of energy and angle of the deuteron in the CM system for decays through the ^{8}Be(exc), for energies below 9.25 MeV. The deuteron CM angles are between 10° and 60°. In this case the energy simulations have been done in steps of 125 keV. For each angular bin, the distribution has been fitted and then multiplied by the data to correct for efficiency.

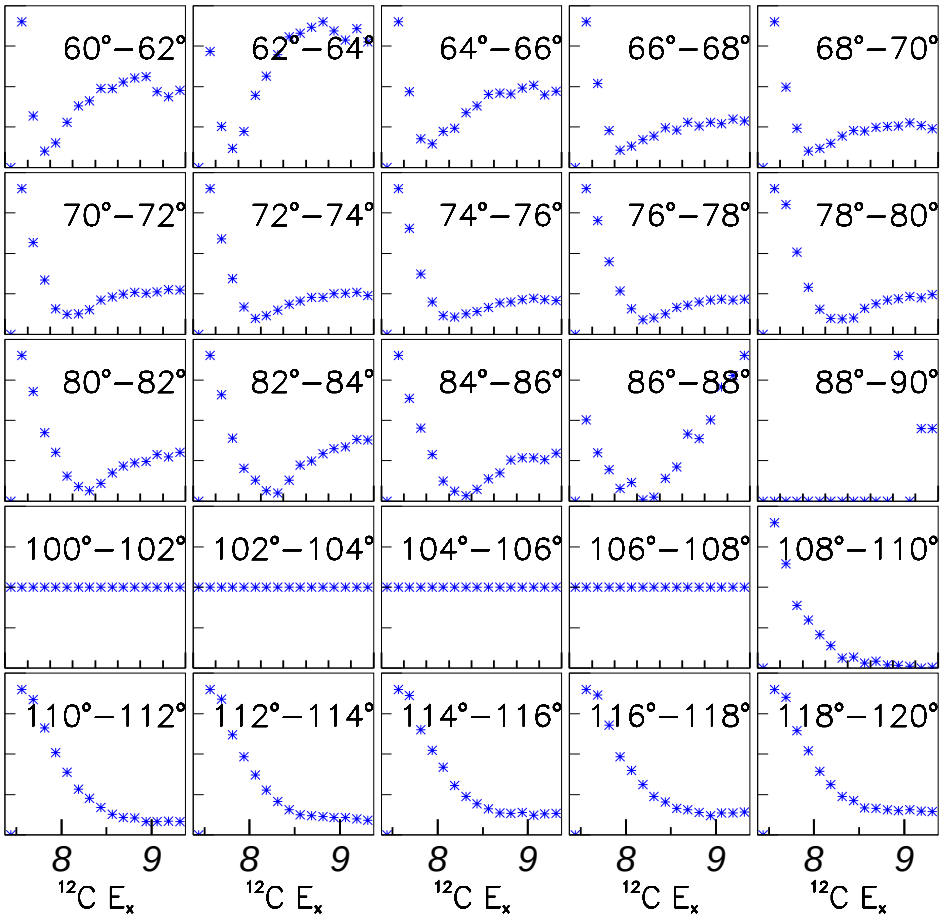

Figure A.7: Detection efficiency as a function of energy and angle of the deuteron in the CM system for decays through the ^{8}Be(gs), for energies below 9.25 MeV. The deuteron CM angles are between 60° and 120°. Note that angles between 90°-100° are not displayed because they are empty. In this case the energy simulations have been done in steps of 125 keV. For each angular bin, the distribution has been fitted and then multiplied by the data to correct for efficiency.

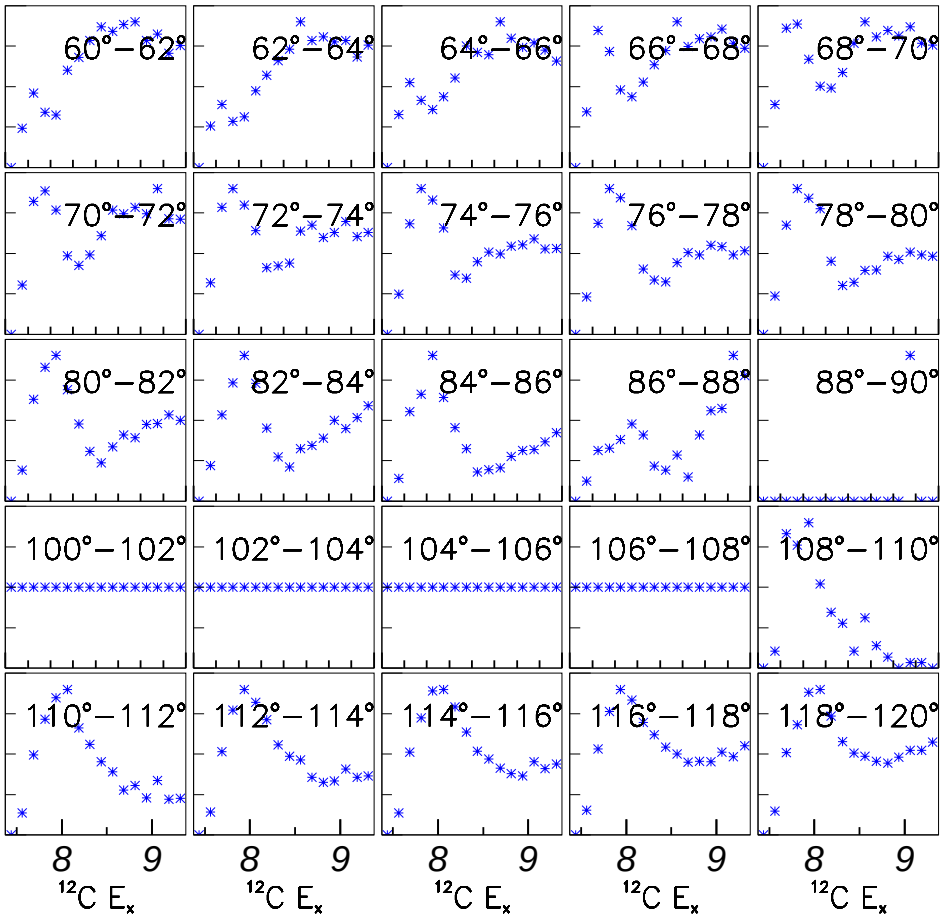

Figure A.8: Detection efficiency as a function of energy and angle of the deuteron in the CM system for decays through the ^{8}Be(exc), for energies below 9.25 MeV. The deuteron CM angles are between 60° and 120°. Note that angles between 90°-100° are not displayed because they are empty. In this case the energy simulations have been done in steps of 125 keV. For each angular bin, the distribution has been fitted and then multiplied by the data to correct for efficiency.

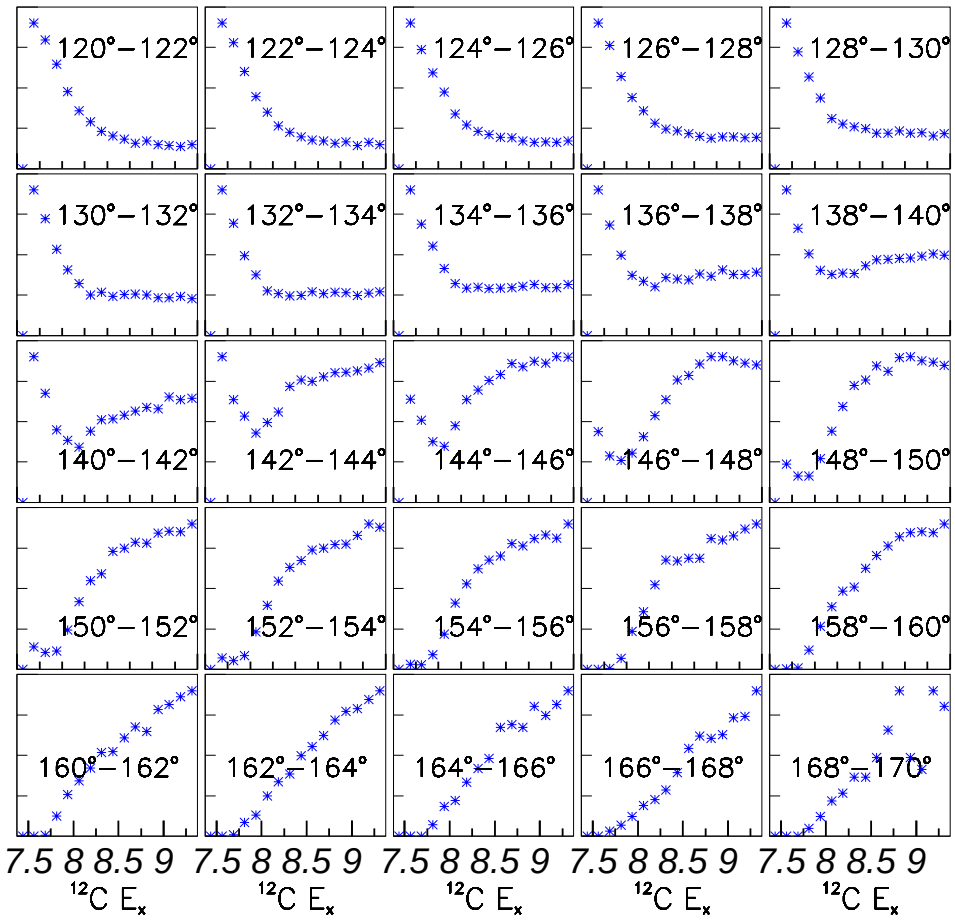

Figure A.9: Detection efficiency as a function of energy and angle of the deuteron in the CM system for decays through the ^{8}Be(gs), for energies below 9.25 MeV. The deuteron CM angles are between 120° and 170°. In this case the energy simulations have been done in steps of 125 keV. For each angular bin, the distribution has been fitted and then multiplied by the data to correct for efficiency.

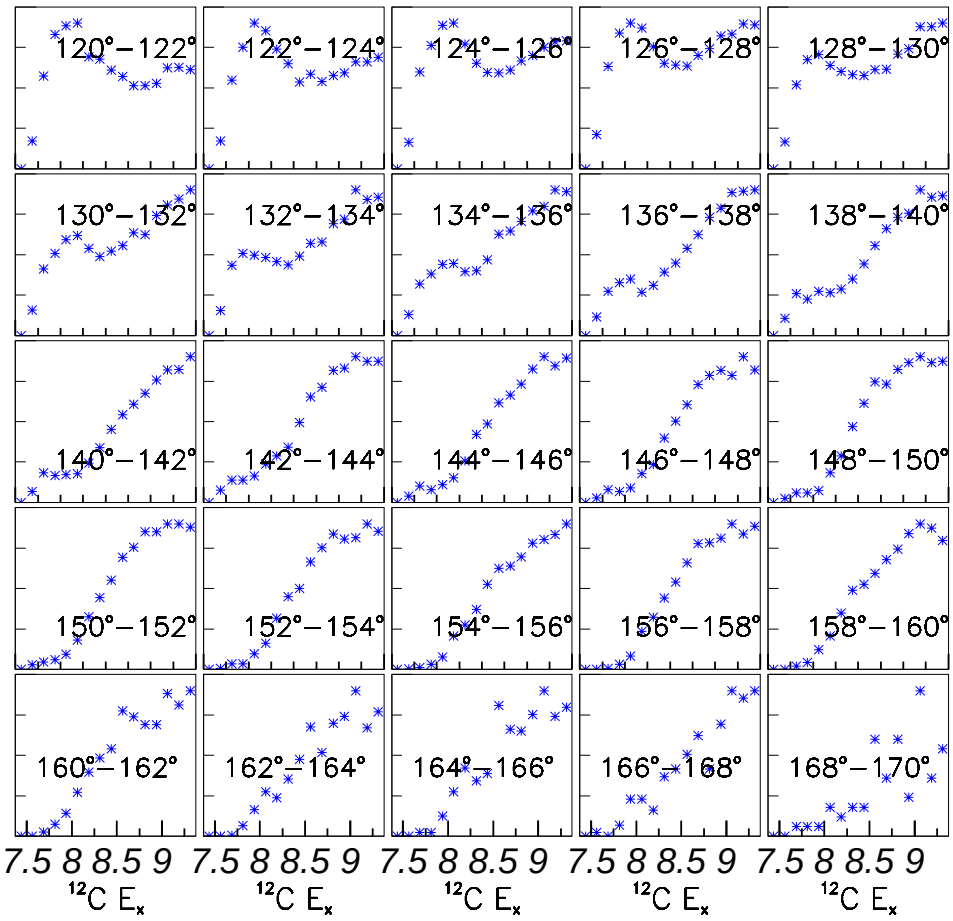

Figure A.10: Detection efficiency as a function of energy and angle of the deuteron in the CM system for decays through the ^{8}Be(exc), for energies below 9.25 MeV. The deuteron CM angles are between 120° and 170°. In this case the energy simulations have been done in steps of 125 keV. For each angular bin, the distribution has been fitted and then multiplied by the data to correct for efficiency.

Bibliography

[Ajz90] F. Ajzenberg-Selove, Nucl. Phys. A **506**, 1 (1990).

[Alc09] M. Alcorta et al., Nucl. Inst. and Methods A **605**, 318 (2009).

[Alc10] M. Alcorta et al., to be published.

[Alv07a] R. Alvarez-Rodríguez et al., Phys. Rev. Lett. **99**, 072503 (2007).

[Alv07b] R. Alvarez-Rodríguez et al., Eur. Phys. J. A **31**, 303 (2007).

[Alv08] R. Alvarez-Rodríguez et al., Phys. Rev. Lett. **100**, 192501 (2008).

[Ang99] C. Angulo et al., Nucl. Phys. A **656**, 3 (1999).

[AW72] D.E. Alburger and D.H. Wilkinson, Phys. Rev. C **5**, 384 (1972).

[Bar88] F.C. Barker, Nucl. Phys. A **487**, 269 (1988).

[BB06] L.R. Buchmann and C.A. Barnes, Nucl. Phys. A **777**, 254 (2006).

[BDE62] C.P. Browne, W.E. Dorenbusch, and J.R. Erskine, Phys. Rev. **125**, 992 (1962).

[Bet39] H.A. Bethe, Phys. Rev. **55**, 434 (1939).

[BFT03] U.C. Bergmann, H.O.U. Fynbo, and O. Tengblad, Nucl. Inst. and Methods A **515**, 657 (2003).

[BM75] A. Bohr and B.R. Mottelson, *Nuclear Structure, vol. I*, Benjamin Inc., (1975).

[BR53] L.C. Biedenharn and M.E. Rose, Rev. Mod. Phys. **25**, 729 (1953).

[BW52] J.M. Blatt and V.F. Weisskopf, *Theoretical Nuclear Physics*, John Wiley & Sons, Inc., (1952).

[BZT74] D.P. Balamuth, R.W. Zurmühle, and S.L. Tabor, Phys. Rev. C **10**, 975 (1974).

[Cau91] D.D. Caussyn et al., Phys. Rev. C **43**, 205 (1991).

[CF88] G.R. Caughlan and W.A. Fowler, At. Data Nucl. Data Tables **40**, 283 (1988).

[Che73] B.T. Chertok et al., Phys. Rev. C **8**, 23 (1973).

[Che07] M. Chernykh et al., Phys. Rev. Lett. **98**, 032501 (2007).

[CK65] S. Cohen and D. Kurath, Nucl. Phys. A **73**, 1 (1965).

[Dal53] R.H. Dalitz, Philos. Mag. **44**, 1068 (1953).

[DB87] P. Descouvemont and D. Baye, Phys. Rev. C **36**, 54 (1987).

[Des00] P. Descouvemont, *manual presented at school*, 2000.

[Dig05] C.Aa. Diget et al., Nucl. Phys. A **760**, 3 (2005).

[Dig09] C.Aa. Diget et al., Phys. Rev. C **80**, 034316 (2009).

[Dun53] D.N.F. Dunbar et al., Phys. Rev. **92**, 649 (1953).

[Eng05] O. Enguita et al., SNEAP Laboratory report in: Symposium of North Eastern Acc. Pers., (2005).

[Fed03] D.V. Federov et al., Few-Body Syst. **33**, 153 (2003).

[Fow84] W.A. Fowler, Rev. Mod. Phys. **46**, 149 (1984).

[Fre06] M. Freer et al., Phys. Rev. Lett. **96**, 042501 (2006).

[Fre07] M. Freer et al., Phys. Rev. C **76**, 034320 (2007).

[Fre09] M. Freer et al., Phys. Rev. C **80**, 041303(R) (2009).

[FSW71] H. Friedrich, L. Satpathy, and A. Weiguny, Phys. Lett. B **36**, 189 (1971).

[Fun03] Y. Funaki et al., Phys. Rev. C **67**, 051306(R) (2003).

[Fyn00] H.O.U. Fynbo et al., Nucl. Phys. A **677**, 38 (2000).

[Fyn03] H.O.U. Fynbo et al., Phys. Rev. Lett. **91**, 82502 (2003).

[Fyn05] H.O.U. Fynbo et al., Nature **433**, 137 (2005).

[Fyn09] H.O.U. Fynbo et al., Phys. Rev. C **79**, 054009 (2009).

[Gio02] J. Giovinazzo et al., Phys. Rev. Lett. **89**, 102501 (2002).

[Got02] A. Gottdang et al., Nucl. Inst. and Methods B **190**, 177 (2002).

[Gri00] L.V. Grigorenko et al., Phys. Rev. Lett. **85**, 22 (2000).

[Gri01] L.V. Grigorenko et al., Phys. Rev. C **64**, 054002 (2001).

[HM61] S. Hinds and R. Middleton, Proc. Phys. Soc. **78**, 81 (1961).

[Hoy53] F. Hoyle et al., Phys. Rev. **92**, 1095 (1953).

[Hoy54] F. Hoyle, Astrophys. J. Suppl. Ser. **1**, 121 (1954).

[Hyl09a] S. Hyldegaard et al., Phys. Lett. B **678**, 459 (2009).

[Hyl09b] S. Hyldegaard et al., Phys. Rev. C **80**, 044304 (2009).

[Hyl10] S. Hyldegaard et al., Phys. Rev. C **81**, 024303 (2010).

[Ito04] M. Itoh et al., Nucl. Phys. A **738**, 268 (2004).

[Jac73] C. Jacquot et al., Nucl. Phys. A **201**, 247 (1973).

[Jep04] H. Jeppesen, *Low-energy nuclear reactions with the radioactive isotope ^9Li at REX-ISOLDE*, Ph.D. thesis, University of Aarhus, (2004).

[Joh03] B. John et al., Phys. Rev. C **68**, 014305 (2003).

[Kan07] Y. Kanada-En'yo, Prog. Theor. Phys. **117**, 655 (2007).

[Kir09] O.S. Kirsebom et al., Phys. Lett. B **680**, 44 (2009).

[Kno89] G.F. Knoll, *Radiation Detection and Measurement*, John Wiley & Sons, Inc., (1989).

[Kor90] A.A. Korsheninnikov, Sov. J. Nucl. Phys. **52**, 827 (1990).

[Kra88] K.S. Krane, *Introductory Nuclear Physics*, John Wiley & Sons, Inc., (1988).

[Len86] W.N. Lennard et al., Nucl. Inst. and Methods A **248**, 454 (1986).

[Leo87] W.R. Leo, *Techniques for Nuclear and Particle Physics Experiments*, Springer-Verlag Berlin Heidelberg, (1987).

[Lin98] E. Lin et al., Chinese Phys. Lett. **15**, 796 (1998).

[Mor56] H. Morinaga, Phys. Rev. **101**, 254 (1956).

[Mor66] H. Morinaga, Phys. Lett. **21**, 78 (1966).

[Nav07] P. Navrátil et al., Phys. Rev. Lett. **99**, 042501 (2007).

[Nie01] E. Nielsen et al., Phys. Rep. **347**, 373 (2001).

[Ohl65] G.G. Ohlsen, Nucl. Inst. and Methods **37**, 240 (1965).

[Pas04] C. Pascual Izarra, *Experimental determination of stopping forces for ions in matter*, Ph.D. thesis, Universidad Autonoma de Madrid, (2004).

[Pfu02] M. Pfutzner et al., Eur. Phys. J. A **14**, 279 (2002).

[Pie05] S.C. Pieper, Nucl. Phys. A **751**, 516 (2005).

[Pre03] Y. Prezado Alonso, *Study of the mechanism of multi-particle emission in $^{12}C^*$ and in the mirror transitions of the isobar A=9*, Ph.D. thesis, Universidade de Santiago de Compostela, (2003).

[Pri09] R.M. Prior et al., abstract available at http://meetings.aps.org/link/BAPS.2009.HAW.LG.8.

[RAM] RAMEM S.A., http://www.ramem.com.

[Rei70] F.D. Reisman et al., Nucl. Phys. A **153**, 244 (1970).

[RRP71] M.A. Reynolds, D.E. Rundquist, and R.M. Poichar, Phys. Rev. C **3**, 442 (1971).

[Sab03] A. Sabían Iglesias, *Diseño y montaje de una línea en el acelerador de 5 MV de la UAM para física nuclear experimental*, Master's thesis, Universidad Complutense de Madrid, (2003).

[Sal52] E.E. Salpeter, Astrophysical Journal **115**, 326 (1952).

[Sal07] E.E. Salpeter, arXiv:0711.3139v1 (2007).

[Sat80] G.R. Satchler, *Introduction to Nuclear Reactions*, The Macmillan Press LTD, (1980).

[SB65] W.A. Schier and C.P. Browne, Phys. Rev. **138**, B857 (1965).

[Sch93] D. Schardt et al., Z. Phys A **345**, 265 (1993).

[Tan85] I. Tanihata et al., Phys. Rev. Lett. **55**, 2676 (1985).

[Ten04] O. Tengblad et al., Nucl. Inst. and Methods A **525**, 458 (2004).

[TG70] N. De Takacsy and S. Das Gupta, Phys. Lett. B **33**, 556 (1970).

[Toh01] A. Tohsaki et al., Phys. Rev. Lett. **87**, 192501 (2001).

[TUN] TUNL, http://www.tunl.duke.edu/.

[Ueg79] E. Uegaki et al., Prog. Theor. Phys. **62**, 1621 (1979).

[Uni] http://www.pas.rochester.edu/∼cline/Research/.

[Vol06] V.I. Volosov, Nucl. Fusion **46**, 820 (2006).

[von00] P. von Neumann-Cosel et al., Nucl. Phys. A **669**, 3 (2000).

[von06] W. von Oertzen, Eur. Phys. J. A **29**, 133 (2006).

[Wag66] M.A. Waggoner et al., Nucl. Phys. **88**, 81 (1966).

[YS04] T. Yamada and P. Schuck, Phys. Rev. C **69**, 024309 (2004).

[Zem64] C. Zemach, Phys. Rev. **133**, B1201 (1964).

[Zie03] J.F. Ziegler et al., *The stopping and range of ions in solids*, SRIM **New York**, Pergamon Press (2003).